



Delft University of Technology

**Document Version**

Final published version

**Citation (APA)**

Padmakumar, G. (2026). *Engineering advanced front textures for high-performance thin-film silicon photovoltaics*. [Dissertation (TU Delft), Delft University of Technology]. <https://doi.org/10.4233/uuid:91287ad2-01d8-49a0-b33f-383d1e3f21ca>

**Important note**

To cite this publication, please use the final published version (if applicable). Please check the document version above.

**Copyright**

In case the licence states "Dutch Copyright Act (Article 25fa)", this publication was made available Green Open Access via the TU Delft Institutional Repository pursuant to Dutch Copyright Act (Article 25fa, the Taverne amendment). This provision does not affect copyright ownership. Unless copyright is transferred by contract or statute, it remains with the copyright holder.

**Sharing and reuse**

Other than for strictly personal use, it is not permitted to download, forward or distribute the text or part of it, without the consent of the author(s) and/or copyright holder(s), unless the work is under an open content license such as Creative Commons.

**Takedown policy**

Please contact us and provide details if you believe this document breaches copyrights. We will remove access to the work immediately and investigate your claim.

*This work is downloaded from Delft University of Technology.*

# Engineering Advanced Front Textures for High-Performance Thin-Film Silicon Photovoltaics



**ENGINEERING ADVANCED FRONT TEXTURES FOR  
HIGH-PERFORMANCE THIN-FILM SILICON  
PHOTOVOLTAICS**



# **ENGINEERING ADVANCED FRONT TEXTURES FOR HIGH-PERFORMANCE THIN-FILM SILICON PHOTOVOLTAICS**

## **Dissertation**

for the purpose of obtaining the degree of doctor  
at Delft University of Technology  
by the authority of the Rector Magnificus, Prof. dr. ir. .H. Bijl,  
chair of the Board for Doctorates  
to be defended publicly on  
Monday 20, April 2026, at 12:30

by

**Govind PADMAKUMAR**

This dissertation has been approved by the promotor.

*Composition of the doctoral committee:*

Rector Magnificus,	chairperson
Prof. dr. ir. A.H.M. Smets,	Delft University of Technology, <i>promotor</i>
Dr. R.A.C.M.M. van Swaaij,	Delft University of Technology, <i>promotor</i>

*Independent members:*

Prof. dr. ir. M. Popov	Delft University of Technology
Prof. dr. A. W. Weeber	Delft University of Technology
Prof. dr. R. Saive	University of Twente
Prof. dr. B. Stannowski	Berlin University of Applied Sciences and Technology, Germany
Dr. T. de Vrijer	Delft University of Technology / LiFT PV BV



*Printed by:* Ridderprint | [www.ridderprint.nl](http://www.ridderprint.nl)

*Cover:* Pattern formed on a plane by a red laser light beam in transmission mode through a periodic hexagonal patterned glass. Photograph by the author.

Copyright © 2026 by G. Padmakumar

ISBN 978-94-6537-420-8

An electronic copy of this dissertation is available at  
<https://repository.tudelft.nl/>.

*"As usual, nature's imagination far surpasses our own, as we have seen from the other theories which are subtle and deep."*

Richard P Feynman



# Contents

<b>Preface</b>	<b>xi</b>
<b>Summary</b>	<b>xiii</b>
<b>Samenvatting</b>	<b>xv</b>
<b>List of Acronyms</b>	<b>xvii</b>
<b>1. Introduction</b>	<b>1</b>
1.1. "The Crisis" . . . . .	1
1.2. Breaking the 'intrinsic link' . . . . .	2
1.3. Thin film silicon - single junction and multi junction solar cells . . . . .	4
1.4. Substrate/superstrate/hybrid configurations . . . . .	5
1.5. Light-trapping . . . . .	6
1.6. Textures on glass . . . . .	9
1.7. The Questions . . . . .	10
1.8. Thesis Outline . . . . .	11
<b>2. Optimisation of a-Si:H and nc-Si:H Intrinsic Absorbers</b>	<b>13</b>
2.1. Experimental Details . . . . .	15
2.1.1. Photoactive layer deposition parameters . . . . .	15
2.1.2. a-Si:H to nc-Si:H transition . . . . .	15
2.1.3. a-Si:H absorber optimisation . . . . .	16
2.1.4. nc-Si: H absorber optimisation . . . . .	17
2.1.5. Solar cell characterisation . . . . .	18
2.2. Results and Discussion . . . . .	19
2.2.1. a-Si:H to nc-Si:H transition . . . . .	19
2.2.2. a-Si:H optimisation on nano-sized textured Asahi superstrates . . . . .	21
2.2.3. nc-Si:H optimisation on micro-textured glass superstrates . . . . .	23
2.3. Conclusion . . . . .	28
<b>3. Thin-film Silicon Solar cells on Superimposed Sacrificial Textured Glass</b>	<b>31</b>
3.1. Introduction . . . . .	32
3.2. Materials and Methods . . . . .	34
3.2.1. ITO sacrificial layer texturing - $SLT_{ITO}$ . . . . .	34
3.2.2. i-ZnO sacrificial layer texturing - $SLT_{IZO}$ . . . . .	34
3.2.3. Superimposed sacrificial texturing - $SIT$ . . . . .	34
3.2.4. Characterisation of textures . . . . .	35
3.2.5. Solar cells on textures . . . . .	37

3.3.	Results and Discussion . . . . .	39
3.3.1.	Physical characterisation of $SLT_{ITO}$ , $SLT_{IZO}$ and $SIT$ . . . . .	39
3.3.2.	Diffused transmission of $SLT_{ITO}$ , $SLT_{IZO}$ and $SIT$ . . . . .	44
3.3.3.	AID of $SLT_{ITO}$ , $SLT_{IZO}$ and $SIT$ . . . . .	45
3.3.4.	Total transmission of $SLT_{ITO}$ , $SLT_{IZO}$ and $SIT$ . . . . .	46
3.3.5.	Solar cells on textures . . . . .	46
3.4.	Conclusion . . . . .	50
<b>4.</b>	<b>Engineering of Hexagonal Micro-textures on Glass</b>	<b>53</b>
4.1.	Introduction . . . . .	54
4.2.	Materials and methods . . . . .	55
4.2.1.	<b>Generating hexagonal textures on Glass</b> . . . . .	55
4.2.2.	<b>Design of experiment</b> . . . . .	57
4.2.3.	<b>Characterisation methodology</b> . . . . .	60
4.3.	Results and discussion . . . . .	61
4.3.1.	Mechanism of etching . . . . .	61
4.3.2.	Physical characterisation of textures . . . . .	61
4.3.3.	Effective orifice diameter ( $D_e$ ) . . . . .	63
4.3.4.	Baseline processing . . . . .	63
4.3.5.	Influence of cleaning method . . . . .	64
4.3.6.	Influence of pre-coating bake temperature . . . . .	65
4.3.7.	Influence of HMDS exposure duration . . . . .	65
4.3.8.	Influence of hard bake temperature . . . . .	66
4.3.9.	Influence of PR thickness . . . . .	67
4.3.10.	Influence of periodicity . . . . .	68
4.3.11.	Sensitivity of processes, $D_{e,P}$ . . . . .	69
4.3.12.	Potential of hexagonal textures on glass . . . . .	70
4.4.	Conclusion . . . . .	72
<b>5.</b>	<b>Thin-film Silicon solar cells on Hexagonal Microtextured Glass</b>	<b>75</b>
5.1.	Introduction . . . . .	76
5.2.	Materials and Methods . . . . .	76
5.2.1.	<b>Generating Hexagonal Textures on Glass</b> . . . . .	76
5.2.2.	Physical characterisation of hexagonal microtextures . . . . .	77
5.2.3.	Transmission characterisation of hexagonal microtextures . . . . .	78
5.2.4.	Angular intensity distribution (AID) measurement of hexagonal microtextures . . . . .	78
5.2.5.	Fabrication of solar cells . . . . .	80
5.2.6.	Characterisation of solar cells . . . . .	80
5.3.	Results and Discussion . . . . .	81
5.3.1.	Surface profile of hexagonal craters . . . . .	81
5.3.2.	Optical interaction of hexagonal textures . . . . .	83
5.3.3.	Solar cells on honeycomb textures . . . . .	87
5.4.	Conclusion . . . . .	92

---

<b>6. Interface and Grain Scattering in Thin-film Silicon Multijunction Solar cells</b>	<b>95</b>
6.1. Introduction . . . . .	96
6.1.1. Deposition of layers in a-Si:H/nc-Si:H tandem solar cells . . . . .	98
6.1.2. Design of Experiment . . . . .	98
6.1.3. Texture and Solar cell characterisation . . . . .	101
6.2. Results and Discussion . . . . .	102
6.2.1. Inspection of interfaces and i-ZnO grains . . . . .	102
6.2.2. a-Si:H / nc-Si:H tandem solar cells on random textures . . . . .	103
6.2.3. a-Si:H / nc-Si:H tandem solar cells on periodic textures . . . . .	104
6.3. Grain scattering with wide-bandgap SnO . . . . .	108
6.4. Conclusion . . . . .	109
<b>7. Conclusion</b>	<b>111</b>
7.1. Perspectives from the thesis . . . . .	113
<b>Bibliography</b>	<b>115</b>
<b>Appendices</b>	<b>133</b>
<b>Acknowledgements</b>	<b>143</b>
<b>List of Publications</b>	<b>147</b>

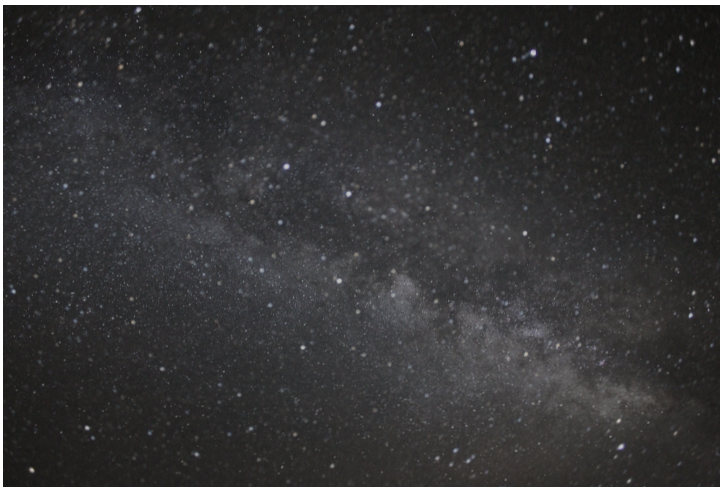


# Preface

The rule is simple: 'survival of the fittest'. Nature has generously equipped all life forms with the tools to thrive, adapt, and evolve. Yet, as humanity's progress turned, it steered us headlong into a crisis: climate change. With the climate crisis added to the context, the stakes have shifted dramatically — being fit demands not just physical traits, but also a sharp intellect and deep emotional resilience. As engineers and researchers, it is our moment to act by pooling the knowledge, intellect, and relentless drive to forge a sustainable future. This thesis is my bold contribution to that epic fight — a personal pledge to our global community. We shall save humanity, crafting a legacy so powerful that, 200 years from now, our descendants will spin tales of the generation that tamed its greed and staged a heroic comeback from the brink of the climate tipping point.

What follows is an exciting journey through this dissertation — I hope you enjoy the read!

*Govind Padmakumar*



From the 'pale blue dot' on Orion Spur, 2026. Photograph by the author.



# Summary

In this dissertation, light management techniques with front textures for thin-film silicon superstrate configuration solar cells are presented. Specifically, the textures are developed on glass to act as light scatterers at interfaces in thin-film devices. The thesis aims to study textures made on glass with a broader idea of transferring it to aluminium folie for fabricating pre-textured transparent conductive oxide (TCO)s in the roll-to-roll fabrication by LiFT PV B.V. This thesis aims to answer a main question:

**How to engineer a front glass texture with which high-performing thin-film silicon superstrate solar cells can be fabricated?**

This main question is addressed through four different key questions in five different chapters: The optimisation of thin-film silicon deposition conditions is presented in **Chapter 2**. Amorphous silicon and nanocrystalline silicon layers are deposited at very high frequency conditions to obtain device-grade photoactive silicon. The processing conditions optimised in this chapter are used to fabricate silicon absorber layers in subsequent chapters 3,4, and 5 of the thesis to study light trapping by glass textures.

In **Chapter 3**, the glass surface is textured with randomly scattered texturing shapes (craters or protrusions), without an explicit placement rule. The textures are referred to as “random textures”. This chapter addresses the sub-question *How does light interact with glass textures featuring nano-scale structures superimposed on micro-scale textures, and how does the resulting morphology influence nano-crystalline silicon growth?* This chapter demonstrates that a sequential wet etching technique can superimpose nano-sized craters on micro-sized craters on glass, with a higher optical performance and efficiency in solar cells when compared to both micro- and nano-textures individually.

Textures characterised by a repeating pattern of shapes at fixed, regular intervals are considered “periodic textures”. **Chapter 4** specifically addresses the question *How to design a periodic glass texture composed of micro-scale hexagonal craters to maximise light scattering efficiency?* To answer this, photolithography is used as a technique to make hexagonal-shaped micrometre-scale craters on the glass surface. The hexagonal textures increased the light scattering capability with deeper craters and higher periodicity value. Glass with hexagonal micro-textures demonstrated a diffusivity as high as 50% in the near infrared light.

Once the design of periodic textures is completed, the recipe to generate hexagonal shapes with different feature sizes is known. **Chapter 5** answers the question: *How does a hexagonal periodic texture on glass influence light interaction, and how do its*

*morphological characteristics affect the performance of thin-film silicon superstrate solar cells?* The hexagonal periodic textures made on glass are studied in detail for their light scattering and diffraction effects. Additionally, nanocrystalline silicon single-junction solar cells are fabricated on these textures with different feature sizes and studied for their electrical and optical performance. An optical performance of  $28.60 \text{ mA/cm}^2$  was achieved for the single junction nc-Si:H solar cells without any external antireflective measures, indicating a high potential for hexagonal textures on glass in multijunction thin-film solar cell applications.

**Chapter 6** explores light scattering of the developed textures when implemented on multijunction solar cells. The challenge of Fabry-Pérot interference in multilayers with contrasting refractive indices is identified in multijunctions, limiting their optical performance. This study addresses the sub-question: *What impact do interface and bulk scattering have on the optical performance of multijunction cells, and which strategies can effectively mitigate interference effects caused by optical micro-cavities?* For this, light scattering in bulk TCO grains, combined with random and periodic textures, is studied in detail. Hexagonal craters on glass, combined with a 0.9 micrometre thick i-ZnO layer, effectively mitigated fringes formed by all optical cavities in the device. The design principles discussed in this work are not restricted to amorphous silicon/nanocrystalline silicon tandem devices but can be extended to any thin-film multijunction solar cell that constitutes layers with contrasting refractive indices.

# Samenvatting

In dit proefschrift worden lichtmanagementtechnieken met voorzijdetexturen voor dunne-film silicium zonnecellen in een superstraatconfiguratie gepresenteerd. De texturen worden specifiek ontwikkeld op glas, met als doel lichtverstrooiing aan de interfaces in dunne-film apparaten te bevorderen. Het onderzoek richt zich op het creëren van texturen op glas, met het bredere doel deze over te brengen op aluminium voor de productie van voorgetextureerde TCO's in de rol-tot-rol productie van LiFT PV B.V. Dit proefschrift tracht de centrale onderzoeksvraag te beantwoorden:

## **Hoe kan een voorzijde glas texturen worden ontwikkeld waarmee hoogwaardige dunne-film silicium superstraat-zonnecellen kunnen worden vervaardigd?**

Deze centrale onderzoeksvraag wordt door beantwoordt door middel van vier subvragen over vijf verschillende hoofdstukken:

In **Hoofdstuk 2** wordt de optimalisatie van de depositie condities van dunne-film silicium besproken. Amorf en nanokristallijn silicium worden afgezet onder zeer hoge frequentiecondities om fotoactief silicium van hoogwaardig zonnecelkwaliteit. De geoptimaliseerde procescondities uit dit hoofdstuk worden vervolgens toegepast bij de vervaardiging van siliciumabsorberlagen in de hoofdstukken 3, 4 en 5, waarin lichtinval en -verstrooiing door glastexturen worden onderzocht.

In **Hoofdstuk 3** wordt het glasoppervlak voorzien van willekeurig verspreide textuurelementen (kraters of uitsteeksels), zonder specifieke plaatsingsregel. Deze structuren worden aangeduid als “willekeurige texturen”. Dit hoofdstuk behandelt de deelvraag: *Hoe interageert licht met een glastextuur wanneer nano-schaal kenmerken worden gesuperponeerd op micro-schaal texturen, en hoe beïnvloedt de resulterende morfologie de groei van nano-kristallijn silicium?* Hieruit blijkt dat een sequentiële nat-etsmethode in staat is nano-kraters op micro-kraters te superponeren, wat resulteert in een hogere optische prestatie en efficiëntie dan bij afzonderlijke micro- of nano-texturen.

Texturen die worden gekenmerkt door een herhalend patroon van vormen op vaste, regelmatige afstanden, worden beschouwd als “periodieke texturen”. **Hoofdstuk 4** richt zich specifiek op de vraag: *Hoe kan een periodieke glastextuur, bestaande uit micro-schaal hexagonale kraters, worden ontworpen om de lichtverstrooiingsefficiëntie te maximaliseren?* Om dit te realiseren wordt fotolithografie toegepast voor het vervaardigen van hexagonale microkraters op het glasoppervlak. De hexagonale texturen verhogen de lichtverstrooiingscapaciteit bij diepere kraters en een grotere periodiciteit. Glas met hexagonale microtexturen vertoonde een diffusiviteit tot wel

50% in het nabij-infrarode gebied.

Na de ontwikkeling van periodieke texturen is een reproduceerbaar proces verkregen om hexagonale vormen met verschillende afmetingen te genereren. **Hoofdstuk 5** behandelt de vraag: *Hoe beïnvloedt een hexagonale periodieke textuur op glas de lichtinteractie, en hoe beïnvloeden de morfologische eigenschappen de prestaties van dunne-film silicium superstraat zonnecellen?* De hexagonale texturen op glas worden uitgebreid bestudeerd wat betreft hun lichtverstrooiings- en diffractiekenmerken. Bovendien worden nanokristallijne silicium enkelvoudige zonnecellen op deze texturen vervaardigd en onderzocht op hun elektrische en optische prestaties. Een optische stroomdichtheid van  $28.60 \text{ mA/cm}^2$  werd bereikt zonder externe antireflectiemaatregelen, wat de grote potentie van hexagonale glastexturen voor meerlagige dunne-film zonnecellen aantoont.

**Hoofdstuk 6** onderzoekt de lichtverstrooiing van de ontwikkelde texturen wanneer deze worden toegepast in multi-junctie zonnecellen. Daarbij wordt de uitdaging van Fabry-Pérot-interferentie geïdentificeerd, die de optische prestaties beperkt. Dit hoofdstuk behandelt de deelvraag: *Welke invloed hebben interface- en bulkverstrooiing op de optische prestaties van multijunctiezonnecellen, en welke strategieën kunnen interferentie-effecten veroorzaakt door optische micro-caviteiten effectief beperken?* Hiertoe wordt de lichtverstrooiing in bulk TCO-korrels, gecombineerd met willekeurige en periodieke texturen, in detail bestudeerd. Hexagonale kraters op glas, gecombineerd met een 0,9 dikke i-ZnO-laag, bleken de interferentiefrajes afkomstig van optische caviteiten in het apparaat effectief te onderdrukken. De ontwerprichtlijnen die in dit werk worden besproken, zijn niet beperkt tot amorf/nano-kristallijn silicium-tandemcellen, maar kunnen worden toegepast op elk type dunne-film meerlagige zonnecel.

*Revised by Youri Blom*

# List of Acronyms

Acronym	Expansion
<b>Materials, Chemicals, and Solar Cell Compounds</b>	
1. Ag	Silver
2. Al	Aluminium
3. a-Si:H	Hydrogenated amorphous silicon
4. AZO	Aluminium doped zinc oxide
5. B <sub>2</sub> H <sub>6</sub>	Diborane (Dopant gas)
6. BHF	Buffered hydrofluoric acid
7. BZO	Boron-doped zinc oxide
8. CdTe	Cadmium telluride
9. CIGS	Copper Indium Gallium Selenide
10. Cr	Chromium
11. c-Si	Crystalline silicon
12. FTO	Fluorine-doped tin oxide
13. GZO	Gallium doped zinc oxide
14. HF	Hydrofluoric acid
15. HMDS	Hexamethyldisilazane
16. HNO <sub>3</sub>	Nitric acid
17. IOH	Hydrogenated indium oxide
18. ITO	Indium-doped tin oxide
19. i-ZnO	Unintentionally doped (intrinsic) zinc oxide
20. nc-Si:H	Hydrogenated nanocrystalline silicon
21. NH <sub>4</sub> F	Ammonium fluoride
22. OPV	Organic photovoltaics
23. PGMEA	Propylene glycol methyl ether acetate
24. PH <sub>3</sub>	Phosphine (Dopant gas)
25. PMDS	Polydimethylsiloxane
26. PR	Photoresist
27. PVK	Perovskites
28. SiO <sub>2</sub> / SiOx	Silicon dioxide / Silicon oxide
29. SnO	Tin oxide
30. TCO	Transparent conductive oxide
<b>Device Structures and Morphology</b>	
1. ARC	Anti-reflection coating
2. BL	Bi-layer (IOH/i-ZnO stack front electrode configuration)
3. BR	Back reflector
4. FLAT	Flat glass
5. HC	Honeycomb (periodic hexagonal microtextures)
6. MST	Modulated surface texturing
7. OC	Optical cavity
8. p-i-n	p doped HTL-intrinsic-n doped ETL sequence
9. PV	Photovoltaic
10. SIT	Superimposed sacrificial texturing

11.	$SLT_{ITO}$	Sacrificial layer texturing using ITO
12.	$SLT_{IZO}$	Sacrificial layer texturing using i-ZnO
13.	TRJ	Tunnelling recombination junction
14.	2-D	Two-dimensional
15.	3-D	Three-dimensional

#### Experimental Techniques and Processes

1.	4PP	Four-point probe
2.	AFM	Atomic Force Microscopy
3.	APCVD	Atmospheric pressure chemical vapour deposition
4.	ARTA	Automated reflectance/transmittance analyser
5.	BSR	Backside rinse
6.	CVD	Chemical vapour deposition
7.	DC	Direct current
8.	DI	Deionised
9.	LPCVD	Low pressure chemical vapour deposition
10.	MOCVD	Metal-organic chemical vapour deposition
11.	NIL	Nanoimprint lithography
12.	PECVD	Plasma-enhanced chemical vapour deposition
13.	PVD	Physical vapour deposition
14.	RF	Radio-frequency
15.	SEM	Scanning Electron Microscopy
16.	UV	Ultraviolet
17.	VHF	Very high-frequency

#### Parameters, Metrics, and Physical Properties

1.	AID	Angular intensity distribution
2.	AR	Aspect ratio
3.	$D/D_e$	Diameter / Effective orifice diameter
4.	ELSM	Extremely low stretching modes
5.	$EQE / QE$	External quantum efficiency / Quantum efficiency
6.	$E_{Tauc}$	Tauc bandgap energy
7.	$f$	Excitation frequency
8.	FF	Fill factor
9.	$F_{SiH_4}$	Silane flow rate
10.	$F_{H_2}$	Hydrogen flow rate
11.	$H_{exp}$	Expected texture height
12.	$H_r / H_g$	Peak height of the R-axis or G-axis
13.	HSM	High stretching mode
14.	$J_{sc}$	Short-circuit current density
15.	J-V	Current density-voltage measurement
16.	LSM	Low stretching mode
17.	MSM	Medium stretching mode
18.	NHSM	Narrow high stretching modes
19.	$p$	Chamber pressure
20.	$P$	Periodicity (Orifice or Texture)
21.	$PD$	Power density
22.	PSD	Power spectral density
23.	SC	Silane concentration
24.	SM	Stretching mode
25.	$T_D$	Diffused transmittance
26.	$T_{TOT}$	Total transmission
27.	$T_{sub}$	Substrate temperature
28.	$V_{oc}$	Open-circuit voltage
29.	WCA	Water contact angle
30.	$\chi_c$	Crystalline phase fraction

31.	$\eta$	Power conversion efficiency
32.	$\lambda$	Wavelength
33.	$\sigma_{RMS}$	Root-mean-square roughness

### Sample Identification IDs

1.	HC-BL	HC substrate with a bi-layer, i.e., IOH (150 nm)/i-ZnO TCO
2.	HC-BL1	HC substrate with a bi-layer, i.e., IOH (150 nm)/i-ZnO(200 nm) TCO
3.	HC-BL2	HC substrate with a bi-layer, i.e., IOH (150 nm)/i-ZnO(400 nm) TCO
4.	HC-BL3	HC substrate with a bi-layer, i.e., IOH (150 nm)/i-ZnO(600 nm) TCO
5.	HC-BL4	HC substrate with a bi-layer (IOH/i-ZnO(900 nm) TCO
6.	HC-IOH	HC substrate with a single IOH layer
7.	HC-SnO	HC substrate using Tin oxide (1000 nm) as a grain scatterer
8.	HP3	HC textured glass with 3 $\mu\text{m}$ periodicity
9.	HP4	HC textured glass with 4 $\mu\text{m}$ periodicity
10.	HP5	HC textured glass with 5 $\mu\text{m}$ periodicity
11.	NHP3	nc-Si:H Cell with 3 $\mu\text{m}$ periodicity (highest in terms of current)
12.	NHP4	nc-Si:H Cell with 4 $\mu\text{m}$ periodicity (highest in terms of current)
13.	NHP5	nc-Si:H Cell with 5 $\mu\text{m}$ periodicity (highest in terms of current)
14.	SIT-BL	SIT substrate with a bi-layer, i.e., IOH (150 nm)/i-ZnO(1500 nm) TCO
15.	SIT-IOH	SIT substrate with a single IOH layer
16.	$SLT_{ITO-1}$	Glass sample textured with ITO sacrificial layer $\sigma_{RMS} = 958\text{nm}$
17.	$SLT_{ITO-2}$	Glass sample textured with ITO sacrificial layer $\sigma_{RMS} = 656\text{nm}$
18.	$SLT_{ITO-3}$	Glass sample textured with ITO sacrificial layer $\sigma_{RMS} = 186\text{nm}$
19.	$SLT_{IZO-1}$	Glass sample textured with i-ZnO sacrificial layer $\sigma_{RMS} = 318\text{nm}$
20.	$SLT_{IZO-2}$	Glass sample textured with i-ZnO sacrificial layer $\sigma_{RMS} = 221\text{nm}$
21.	$SLT_{IZO-3}$	Glass sample textured with i-ZnO sacrificial layer $\sigma_{RMS} = 73\text{nm}$



# 1

## Introduction

*"Crisis is a messenger"*

Bryant McGill

### 1.1. "The Crisis"

At this point, humanity faces two important challenges: climate change and increasing energy demand. The root cause triggering these issues is overpopulation and improving living standards.

The rapidly growing global energy demand has been a concern over the past few decades, driven by exponential population growth, lifestyle changes, energy-intensive raw material demands (such as those in the construction and steel industries) and urbanisation. Additionally, with the emergence of new energy-intensive technologies such as blockchain and artificial intelligence, the electricity demand of data centres is expected to double (be around 1000 TWh) in the next 5 years [1]. The continued dependence on fossil fuels is unsustainable due to their finite nature. Energy resources such as oil and coal are limited and are expected to be depleted over time. This constraint necessitates a transition toward renewable and low-carbon energy systems to ensure a long-term energy supply. Meeting the world's high energy demand also poses a challenge due to the disproportionate distribution of energy reserves worldwide and the limited contribution from clean energy sources.

Climate change is frequently discussed and projected as the most critical, directly challenging life forms on Earth. Reliance on fossil fuels to meet demand accounts for 74.5% of global GHG emissions in the form of carbon dioxide (methane made up another 17.9%, and 4.8% consisted of nitrous oxide along with 2.8% by fluorinated gases) in 2024 [2]. This trend is accelerating climate change, causing extreme weather events, and slowly pushing some regions of our planet towards humanly uninhabitable conditions. In addition, the uneven global distribution of fossil fuel reserves creates energy dependence and geopolitical risks. Economically, countries that rely on fossil fuel imports to meet their energy needs face vulnerabilities, as shortages can disrupt industries and economies, hindering global competitiveness and development in their agricultural and manufacturing sectors. The transition to domestically available renewable energy sources can reduce this dependence,

enhance energy independence, and support sustainable economic growth. Socially, the lack of affordable, clean energy can lead to health problems, increased social inequality and forced migrations.

As long as the energy requirements of the growing world population are not met with renewable energy, the energy demand and climate crisis remain **intrinsically linked** to each other.

## 1.2. Breaking the ‘intrinsic link’

To address the interlink between energy demand and climate crises sustainably, a rapid, high-volume transition from fossil fuels to ‘cleaner’ renewable energy is urgently required. This transition would require the planned retirement of existing fossil fuel infrastructures and the scaling up of renewable energy sources, such as solar and wind. These energy sources are also cheaper than fossil fuels [3]. Models predicting 100% renewable energy in 2050 consider photovoltaics (PV) as a prime candidate with 69% of generated power (followed by wind power contributing  $\approx 18\%$ ) to replace non-renewable energy technologies [4]. PV manufacturing, installation, and the implementation of adequate storage technology are among the best routes for countries to achieve energy self-reliance. It is also very important that this expansion of PV industry happens in a climate-friendly manner. The extensive transition from existing energy technologies to solar energy and wind energy requires significant energy investments, which, in the current situation, will be met mainly through conventional energy sources.

Figure 1.1 represents a moderately ambitious scenario for the European Union by Breyer *et al.* where the current fossil fuel power plants are retired by 2050, and no new nuclear power plants are considered [5]. As seen in Figure 1.1, the final energy consumption in different sectors is in the form of electricity, heat and synthetic fuels. In this scenario, solar energy, wind energy, and energy based on hydropower constitute 74% of total primary energy sources by 2050. Additionally, synthetic fuels contribute  $\approx 15\%$  of total final consumption in industrial and transportation sectors, and renewable electricity production is expected to be a major contributor to synthetic fuel production, too.

In the past few decades (at the time of this thesis), solar-energy research has mainly focused on improving the light-to-electricity conversion efficiency of photovoltaic (PV) devices and on scaling up the cost-effective manufacturing of PV modules. As a result, 27.81% conversion efficiency is achieved for a monocrystalline silicon solar cell in a research facility [6]. This is admirably close to the Auger-limited efficiency of about 29.4% [7]. At module level, LONGi has reported 26.0% heterojunction back contact (HBC), and Trina Solar reports 25.4% in heterojunction technology (HJT) [8]. An alternative family of PV technologies called thin-film solar cells is characterised by their significantly thinner light-absorbing layers. The efficiency of thin-film cell technologies is lower than that of c-Si wafer-based technologies, except for GaAs [9]. The approximate range of efficiency varies as follows: 15.8% for organic photovoltaic (OPV) cells, 14% for triple-junction thin-film silicon, 23% for copper indium gallium selenide (CIGS) and copper indium selenide (CIS), 21% for cadmium telluride

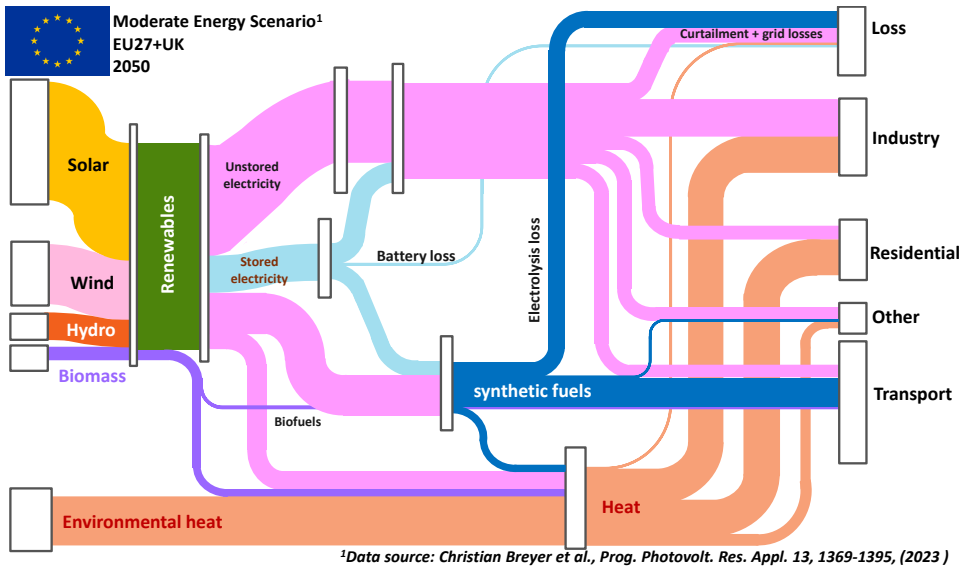


Figure 1.1.: Sankey diagram illustrating a moderately ambitious pathway predicting a 100% renewable energy future of the European Union. The diagram illustrates flows of energy between different energy sources and consumption in sectors (with different intermediate stages), the width of each flow is proportional to its magnitude (i.e. wider flows indicate larger quantities, while narrower flows represent smaller quantities).

(CdTe), 29% for single-junction gallium arsenide (GaAs), 35% for three-junction GaAs (non-concentrated), and over 47% for certain concentrated photovoltaic (CPV) cells [8, 10].

Thin-film silicon technologies, such as amorphous silicon and nanocrystalline silicon, once held a notable share of the market with their advantages, including scalable production techniques and lower material requirements than wafer-based PV technologies [11]. Eventually, they lost competitiveness in the market because they could not keep pace with efficiency and cost reductions at the module/system level in crystalline-silicon cells, and with the efficiency improvements achieved by other thin-film technologies [9]. However, the technology is still viewed as complementary to mainstream c-Si wafer technology as it can potentially capitalise on niche markets where the scope of existing wafer-based PV technology is limited. Thin-film silicon has been industrially adopted to produce flexible, lightweight modules [12, 13] that are typically encapsulated with polymers, resulting in a high energy yield per functional area. Such flexible, lightweight, and polymer-encapsulated modules are well-suited for specific applications, such as retrofitting structures that cannot support heavy systems. Additionally, minimal glare from the polymer encapsulation also supports cases with glare constraints—like airports—where the usage of glass encapsulated cells is limited (unless an external antiglare foil or glass texture

is implemented) [14]. In solar-fuel applications, PV devices require a flexible voltage source to drive the desired electrochemical reduction reaction. Thin-film photoactive materials can accommodate this need for a flexible output voltage and increased performance through multijunction devices. Thin-film silicon has been demonstrated as an active layer that can be combined with different materials, such as nanocrystalline silicon (nc-Si:H), organic PV, germanium, germanium-tin alloy, and narrow-bandgap perovskites [15–20].

### 1.3. Thin film silicon - single junction and multi junction solar cells

As discussed in the previous section, thin-film silicon (TF-Si) solar-cell materials like hydrogenated amorphous silicon (a-Si:H) and nc-Si:H have been vital in thin-film PV technology, utilised as intrinsic absorber layers and increasingly in heterojunction with intrinsic thin-film (HIT) solar cells [21]. In HIT solar cells, a-Si:H layers—typically measuring less than 10 nm—is integrated onto a c-Si substrate to function as both an emitter and a passivation interface, suppressing carrier recombination while enabling efficient charge transport. Deposition of these materials has been demonstrated using different techniques, including the hot-wire method [22, 23], expanding thermal plasma [24–26], radio-frequency (RF) plasma-enhanced chemical vapour deposition (PECVD), and very high-frequency (VHF) PECVD. Among these techniques, only RF PECVD and VHF PECVD have been industrially up-scaled successfully [12, 27, 28]. At an industrial scale, silicon thin-film solar cells were developed and manufactured by a range of companies, including LG [29, 30], Sharp [31], Kaneka [32], United Solar Ovonic LLC. [33], Applied Materials [34], Oerlikon Solar (later Tokyo Electron) [35], Solarex [36], ARCO Solar [13], LiFT PV (formerly HyET Solar) [12]. While most of these entities have since ceased production or shifted their focus away from this specific technology, LiFT PV remains actively engaged in the research and manufacturing of silicon thin-film cells.

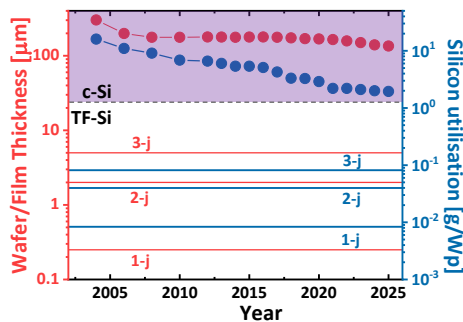


Figure 1.2.: Film thickness and material utilisation of various silicon PV technologies.

Higher efficiencies can be achieved by stacking different absorber layers forming multi-junction solar cells. In multijunctions, the band gap of active layers

progressively decreases, from the illuminated side to the rear side. This approach gives the advantages of higher output voltage, reduced thermalisation losses of light-excited charge carriers and reduced non-absorption of photons. A comparison between absorber thickness and silicon utilisation for both TF-Si and c-Si is shown in Figure 1.2. In theory, the maximum achievable efficiency of a solar cell rises with the number of junctions featuring different band gaps. However, in practice, each additional junction introduces losses: optical losses from parasitic absorption in the doped layers and electrical losses at the recombination junctions between subcells [15]. Performance of world-record-efficiency thin-film silicon single-junction and multijunction solar cells is summarised in Table 1.1. Additionally, Triple-junction solar cells with configurations other than a-Si:H/nc-Si:H/nc-Si:H stack or any quadruple-junction solar cell configurations could not yet outperform the efficiencies reported in Table 1.1.

## 1.4. Substrate/superstrate/hybrid configurations

Due to the low hole mobility and high defect density in thin-film silicon layers, charge collection driven by diffusion is insufficient for employing p-n junction thin-film silicon solar cells. Instead, a drift current driven by the built-in electric field, created by p- and n-type doped layers sandwiching the intrinsic a-Si:H or intrinsic nc-Si:H absorber layer, is required to assist charge collection. Although most of the incident photons are absorbed in the photoactive layers (generating light-excited electron-hole pairs), a small fraction of light is lost as parasitic absorption losses in the thin p- and n-type-doped layers. Deposition of the thin-film solar cell layers on a substrate material can begin on either the p-side (p-i-n deposition) or the n-side (n-i-p deposition). The illumination of the solar cell is typically done from the p-doped layer's side to generate most electron-hole pairs near the p-i interface, which aids in hole collection as the mobility of holes is lower than the mobility of electrons.

The solar-cell architecture in which the substrate forms the front window of the solar cell is called a superstrate configuration, as shown in Figure 1.3(A). When the substrate forms the rear side of a solar cell, the configuration is referred to as substrate configuration, as in Figure 1.3(B). To facilitate illumination from the p-doped side, superstrate configuration solar cells are often deposited in p-i-n order on transparent substrates that can withstand the high temperatures of the deposition process. This is the reason why all p-i-n solar modules, except those from LiFT PV, were manufactured on glass substrates [37]. In contrast, the n-i-p configuration can accommodate opaque substrates and is often used with flexible materials, such as stainless steel or polymers.

On a production scale, the configurations are chosen based on the unique technology of each manufacturing line. In the past, the majority of module manufacturers, such as Sharp, Kaneka, Sanyo, Oerlikon Solar, made in a p-i-n configuration solar cells on glass, featuring either a single or tandem junction with an a-Si:H top cell and an nc-Si:H bottom cell, but there were notable exceptions. Schott Solar produced tandem a-Si:H/a-Si:H solar cells with glass on both the front

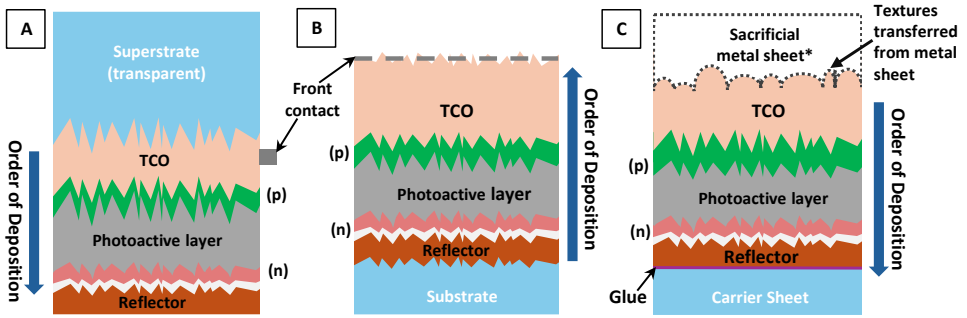


Figure 1.3.: (A) Superstrate configuration with glass at the illuminated side, (B) Substrate configuration, (C) Hybrid configuration. \*The sacrificial metal sheet is removed through wet etching and is not a part of the final product. Arrows show the order of deposition adopted in each configuration.

and rear sides [37]. United Solar created flexible triple-junction solar cells in an n-i-p configuration, with a top cell of a-Si:H and middle and bottom cells made of hydrogenated amorphous silicon-germanium alloys (a-SiGe<sub>x</sub>:H). United Solar had also reported exploring of other potential layer stacks, including those with nc-Si:H, but did not adopt them for production [33].

LiFT PV employs a hybrid method, depositing a solar cell in a p-i-n configuration on aluminium with TCO, which is later transferred to a flexible carrier with glue [12, 27]. The schematic of the final product (unencapsulated) is given in Figure 1.3(C). This hybrid technique is realised on a roll-to-roll (R2R) production line in which an aluminium sheet roll (marked in Figure 1.3(C) as sacrificial metal sheet) is unwound through an atmospheric pressure chemical vapour deposition (APCVD) for deposition of transparent conductive oxide (TCO), through a plasma enhanced chemical vapour deposition (PECVD) for deposition of silicon alloys, and through an RF sputtering chamber for deposition of the back contact in sequence. This intermediate product is glued to a carrier polymer as the next step. In the final step, the aluminium metal sheet is etched away completely with NaOH or KOH solutions. The removal of the aluminium layer leaves behind a pre-textured TCO on the illuminated side of the solar cell. This industrial R2R manufacturing has the advantages of easy scaling up and the potential to control absorber layer properties. Moreover, with the necessary adjustments in processing conditions, this technique is effectively extendable to other thin-film technologies.

## 1.5. Light-trapping

Light trapping in solar cells is required to make high efficiency thin film silicon cells because the absorption coefficient of nc-Si:H is small near the bandgap wavelength ( $\sim 100 \text{ cm}^{-1}$  at 1000 nm). An optically thick absorber layer is required to absorb

Category	Config.	$\eta$ [%]	$V_{oc}$ [V]	$J_{sc}$ [mA/cm <sup>2</sup> ]	FF[%]	Year	Institute[Ref.]
Single junction [a-Si:H]		9.47	0.859	17.52	63.0	2004	IMT [38]
	(p-i-n)	10.09	0.877	17.28	66.6	2009	Oerlikon [39]
	(p-i-n)	10.11	0.906	16.06	69.5	2013	AIST [40]
	(p-i-n)	10.22	0.896	16.36	69.8	2014	AIST [19]
	(p-i-n)	10.30	0.891	17.20	67.0	2015	Jülich [41]
Single junction [nc-Si:H]	-	10.10	0.539	24.35	76.8	1999	Kaneka [42]
	(p-i-n)	10.30	0.568	25.50	71.3	2006	Jülich [43]
	(n-i-p)	10.50	0.521	28.17	71.6	2013	AIST [44]
	(p-i-n)	10.69	0.549	26.55	73.3	2013	IMT [45]
	(n-i-p)	10.80	0.523	28.24	73.8	2013	AIST [46]
	(n-i-p)	10.97	0.542	27.44	73.8	2014	AIST [47]
	(n-i-p)	11.40	0.535	29.07	73.1	2014	AIST [48]
	(n-i-p)	11.77	0.548	29.39	73.1	2015	AIST [49]
	(n-i-p)	11.90	0.550	29.72	75.0	2018	AIST [50]
				$J_{sc}(J_{Tot,init})$ [mA/cm <sup>2</sup> ]			
Double junction [a-Si:H/nc-Si:H]	-	11.70	5.462	2.99 (-)	71.3	2004	Kaneka <sup>a</sup> [51]
	(p-i-n)	11.91	1.346	12.92 (26.6)	68.5	2010	Oerlikon [52]
	-	12.16	-	-	-	2011	Oerlikon <sup>b</sup> [53]
	-	12.20	-	-	-	2011	Sanyo <sup>b</sup> [54]
	(p-i-n)	11.90	1.322	13.02 (26.7)	69.0	2012	AIST [55]
	(p-i-n)	12.00	1.330	12.92 (27.1)	70.0	2013	AIST [40]
	(p-i-n)	12.10	1.411	12.60 (>25.2)	67.8	2013	HZB [56]
	-	12.30	1.365	12.93 (-)	69.4	2013	Kaneka [57]
	(p-i-n)	12.63	1.382	12.82 (26.8)	71.3	2014	IMT [58]
	(p-i-n)	12.69	1.342	13.45 (27.6)	70.2	2015	AIST [19]
Triple junction [a-Si:H/nc-Si:H/nc-Si:H]	-	12.00	1.840	8.54 (>25.65)	76.2	2004	Kaneka [59]
	(n-i-p)	12.41	1.936	8.96 (28.24)	71.5	2011	United Solar [60]
	(p-i-n)	13.44	1.963	9.52 (>28.57)	71.9	2013	LG [61]
	(p-i-n)	13.46	1.967	9.84 (30.0)	69.6	2015	TEL Solar [62]
	(n-i-p)	13.60	1.901	9.92 (31.3)	72.1	2015	AIST [63]
	(n-i-p)	14.00	1.922	10.39 (31.4)	73.4	2016	AIST [18]

Table 1.1.: Summary of record efficiencies for a-Si:H, nc-Si:H, and multijunction thin-film silicon solar cells reported in literature. Tabulation inspired by [37].

<sup>a</sup>Submodule, aperture area 14.23 cm<sup>2</sup>

<sup>b</sup>Only efficiency is reported

long-wavelength photons. At the same time, thin-film silicon solar cells require an electrically thin absorber layer to maintain a strong electric field for efficient charge collection. Light management techniques mainly focus on three effects: (i) reduction in surface reflection to increase the input energy to solar cells, (ii) reduction of the parasitic absorption in non-active layers, (iii) increase in light absorption due to an increase in optical path length by scattering, refraction or diffraction, and (iv) enhancement of internal/ rear reflection. The latter two effects are vital for increasing light absorption at higher wavelengths.

Traditional light-trapping strategies in solar cells rely on increasing the optical path length through geometric designs. This includes scattering incident light into multiple angles via surface texturing and reflecting the unabsorbed light back to the absorber at rear side of a cell. A Lambertian scatterer is a perfectly rough surface that scatters light in all directions [9]. When a Lambertian front surface is combined with a lossless Lambertian back reflector, the effective optical path length within the absorber can theoretically be increased up to a factor of  $4n^2$  relative to a flat surface, where  $n$  denotes the refractive index of the material [64]. Unlike many other crystalline materials, a-Si:H and nc-Si:H can be deposited highly conformally, enabling their use on rough textured substrates.

Random textures consist of surface morphology with randomly scattered texturing shapes (craters or protrusions). Random textures exhibit a specific range of feature sizes that determine how the light interacts with the interface between two media (reflection, transmission, and absorption). The nature of the incoherent scattering mechanisms and the coherent refraction of light by these textured interfaces lies in their geometry and dimensions relative to the wavelength ( $\lambda$ ) of the light [65]. The type of interaction is determined by the shape and size ( $S$ ) of a surface feature in reference to the  $\lambda$ . For small sizes of surface features and roughness, incoherent Rayleigh scattering ( $S \ll \lambda$ ) and Mie scattering ( $S \sim \lambda$ ) occur. In contrast, coherent refraction at an interface takes place at large ‘macro’ -sized features ( $S \gg \lambda$ ) [66]. Since the textures must maximise scattering over a broad spectral range (equivalent to the optical response of the thin-film absorber from the UV to the IR), the shape and dimensions of the texture features should be present accordingly. Different textures, shapes, and sizes must coexist on a surface to maximise the optical gain.

Periodic textures are characterised by a repeating pattern of shapes at fixed, regular intervals. The periodic textures can be characterised by the distance at which each shape recurs (periodicity) and the height of craters. For achieving high performance in solar cells with periodic texturing, two-dimensional (2D) gratings are preferable to one-dimensional (1D) designs because 2D structures provide a greater number of diffraction channels [67, 68]. Additionally, gratings couple incident light more effectively when they are tapered, as the gradual variation in optical density improves coupling [69]; on front surfaces, this tapering can also reduce reflection losses [70]. If the periodicity of the texture is too small, the light cannot resolve the structural features, resulting in weak diffraction. Conversely, if the periodicity exceeds the wavelength considerably, higher-order reflection modes beyond the zeroth order can emerge, which lowers absorption. In such cases, light becomes poorly confined within the film and can escape through these higher-order channels [71]. Despite

numerous studies, the question of whether periodic structures or random textures benefit solar cells the most remains unresolved [72, 73]. Notably, most of the world's record-high spectral-utilisation single junction nc-Si:H solar cells (above 28.0 mA/cm<sup>2</sup>) to date have used a periodic-structured n-i-p substrate configuration (Table 1.1).

Other than the direct texturing approach of the interfaces, bulk scattering or grain scattering is also employed on thin-film solar cells. Polycrystalline materials do not have uniform optical properties because of residual porosity, secondary phases, and/or crystalline anisotropies [74]. These optical inhomogeneities cause scattering in the bulk, which varies with layer thickness and grain size [75]. In solar cells, grain scattering is achieved with thick TCO layers that act as contact electrodes as well as light scatterers with their grain structure. Some examples of thick TCOs used as grain scatterer in solar cells are zinc oxide [45, 76], boron-doped zinc oxide (BZO) [19, 20, 28], and thick FTO layers [12].

Another method to facilitate light trapping is by integrating thick TCOs with surface textures [77]. This method combines interface scattering and grain scattering to boost optical performance in the cell. The hybrid manufacturing route adopted by LiFT PV enables the use of this technique with pre-textured TCO layers as described in Section 1.4. The texture on the sacrificial aluminium layer determines the TCO's front texture that causes interface scattering.

A general challenge for integrating textured interfaces into thin-film PV devices is that texture features may induce inhomogeneities, defects, cracks or pinholes in the PV-active materials. This might deteriorate the film's electrical quality by enhancing Shockley-Read-Hall recombination of light-excited charge carriers. The relation between substrate roughness and the accompanying additional electrical losses is often reflected in reduced open circuit voltage ( $V_{oc}$ ) and fill factor (FF) of the solar cells as described in detail in [78–82]. This demonstrates that there is a delicate interplay between increasing optical yield using textured interfaces and preserving electrical performance [12, 83–86].

## 1.6. Textures on glass

On a laboratory scale, making a textured interface on glass is a straightforward approach to evaluate the interface scattering of a morphology. A texture made on glass can be realised and transferred to an aluminium roll-to-roll flexible aluminium substrate with methods such as wet etching with chemicals like NaOH or KOH [87] or using a simple mechanical embossing technique [88]. The Figures 1.4(A) shows a wet-etched surface of aluminium foil in a lab-scale chemical bath, and 1.4(B) shows a periodic texture embossed on the aluminium surface prepared on a lab-scale roller press. Both these techniques can be incorporated into an R2R production line with a chemical bath chamber or an embossing roller.

Light-trapping and light-coupling using random and periodic textures for thin-film silicon solar cells have been explored extensively over the years by industry and research groups, for substrate and superstrate configurations. Despite this, the literature contains limited examples of multiscale random textures implemented

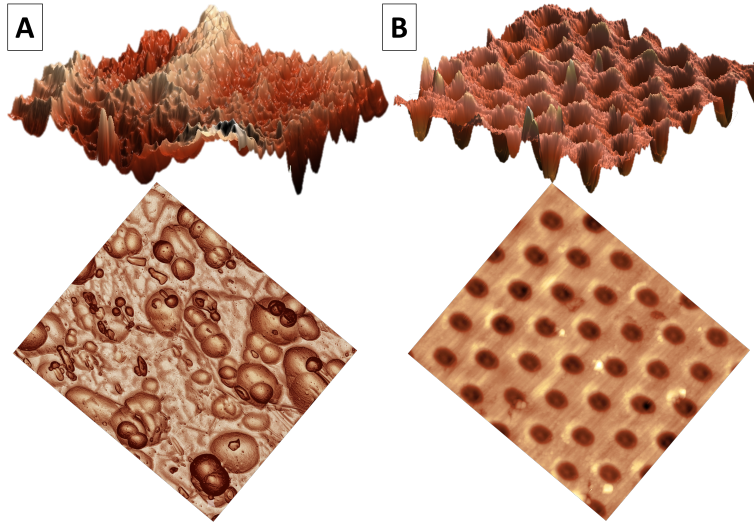


Figure 1.4.: Atomic force microscopy images of aluminium surfaces with (A) random textures made with wet etching and (B) periodic textures made with the embossing technique. The top row isometric images are  $30\ \mu \times 30\ \mu$ .

directly on glass i.e., without the aid of TCO grains. This direct approach is essential for roll-to-roll manufacturing, particularly when utilising sacrificial layers, as demonstrated by LiFT PV. This thesis explores this route. Furthermore, while periodic textures are typically fabricated on silicon wafers for lab-scale substrate-configuration solar cells, this research identifies the critical parameters required to translate these periodic structures onto glass superstrates for practical device integration. In this thesis, to support the further optimisation of enhancing the light management performance and processing of high electrical quality thin-film silicon solar cells, all the texturing concepts are explored and demonstrated on glass using chemical etching. The focus is specifically on p-i-n superstrate architecture solar cells made on glass.

## 1.7. The Questions

The primary objective of this thesis is to design a scattering front window for solar cells. This structure at the front should enhance the light management performance and enable the processing of high-quality thin-film silicon layers on top of it. To realise this, we need to answer the following main scientific question:

**How to engineer a front glass texture with which high-performing thin-film silicon superstrate solar cells can be fabricated?**

This main scientific question is broken down into four key research questions:

1. How does light interact with glass textures featuring nano-scale structures

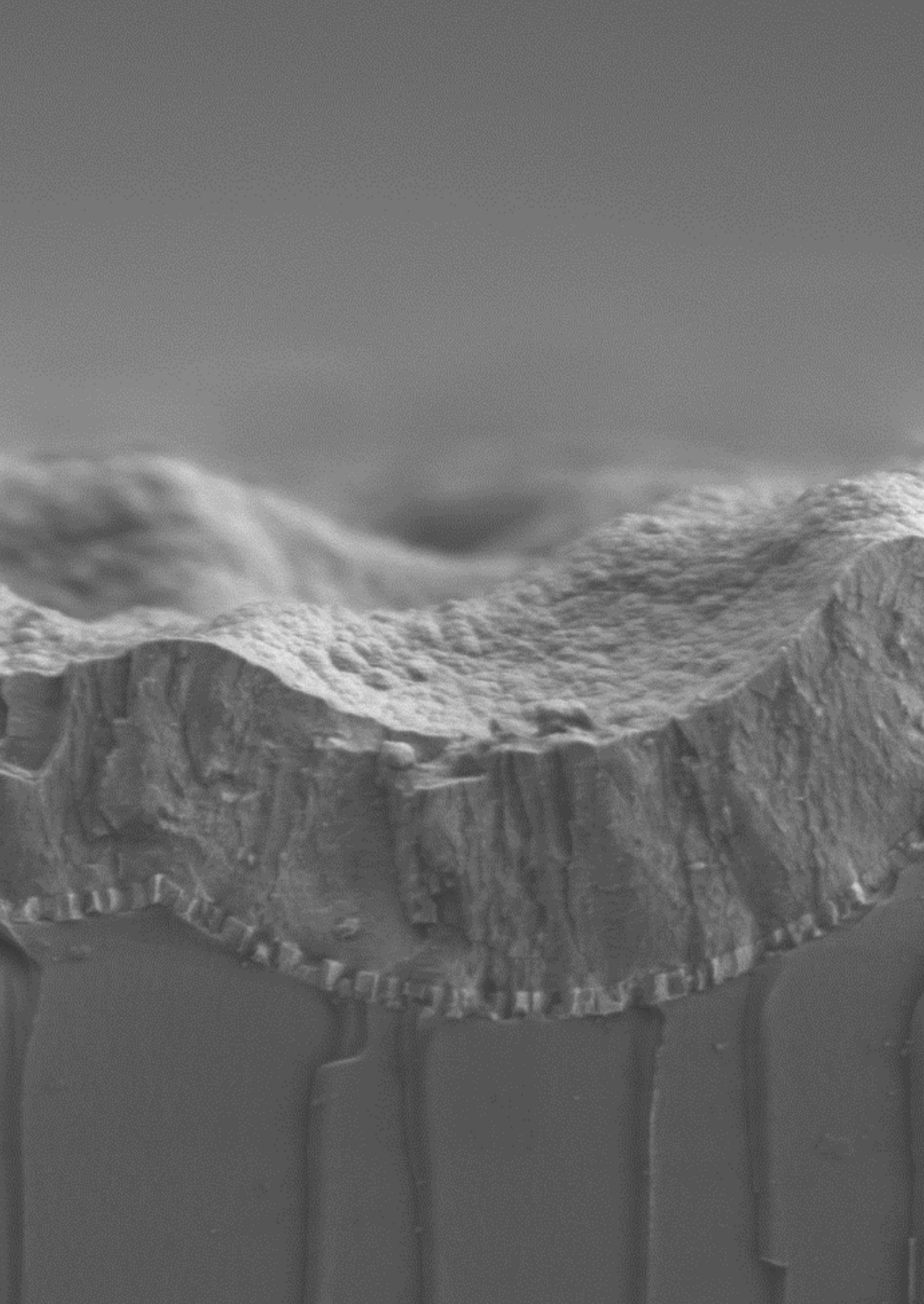
superimposed on micro-scale textures, and how does the resulting morphology influence nano-crystalline silicon growth?

2. How to design a periodic glass texture composed of micro-scale hexagonal craters to maximise light scattering efficiency?
3. How does a hexagonal periodic texture on glass influence light interaction, and how do its morphological characteristics affect the performance of thin-film silicon superstrate solar cells?
4. What impact do interface and bulk scattering have on the optical performance of multijunction cells, and which strategies can effectively mitigate interference effects caused by optical micro-cavities?

## 1.8. Thesis Outline

This thesis contributes to a broader bilateral agreement between Lift PV and TU Delft PVMD. The project's overarching milestones were divided into distinct sub-projects, with this specific study designed to be complemented by two parallel streams of research: first, the work of Dr. Paula Perez-Rodriguez and Federica Saitta on low band gap alloys, TCO development, and opto-electrical modelling; and second, the research by Peer Sluijs and Dr. Sreejith K.P. regarding PV module reliability testing, characterisation methods, and environmental impact analyses.

The thesis is structured into seven chapters, each introduced with a dedicated preface and conclusion to guide the reader through the research progression. **Chapter 2** presents the optimisation of the laboratory-scale deposition process for amorphous silicon (a-Si:H) and nanocrystalline silicon (nc-Si:H) thin films using a PECVD multichamber system. The photoactive absorber layers employed in subsequent chapters are fabricated under the optimised conditions established in this study. Key Questions 1, 2, 3, and 4 are addressed in Chapters 3, 4, 5, and 6, respectively. **Chapter 3** investigates three random surface texturing techniques and their implementation in solar cells, demonstrating improved spectral utilisation in indirect-band-gap silicon-based solar cell materials. **Chapter 4** introduces and optimises a novel fabrication process for generating periodic hexagonal microtextures on glass substrates. **Chapter 5** explores the interaction between light and periodic hexagonal gratings, evaluating the optical behaviour and performance of nc-Si:H solar cells deposited on these textured surfaces. **Chapter 6** focuses on the application of light scattering approaches in multi-junction silicon solar cells. Both random and periodic surface textures are analysed for their ability to suppress interference fringes caused by Fabry–Perot optical cavities within the device. **Chapter 7** provides the overall conclusions and summarises the key findings of the thesis.



# 2

## Optimisation of a-Si:H and nc-Si:H Intrinsic Absorbers

Manuscript in preparation<sup>1</sup>

*Thin film silicon photovoltaic technology has the potential to act as a complementary technology to mainstream crystalline silicon wafer technology. Industrially demonstrated roll-to-roll technology with plasma-enhanced chemical vapour deposition is a method for manufacturing thin film silicon solar cells on a large scale. Conventionally, in roll-to-roll processing, amorphous silicon (a-Si:H) depositions in PECVD are conducted at an input voltage operating at radio frequency (RF) and nanocrystalline silicon (nc-Si:H) depositions at very high frequency (VHF) in dedicated chambers. This chapter explores the feasibility of depositing both device-grade a-Si:H and nc-Si:H in the same PECVD chamber with the same VHF generator. This work reports optimised deposition conditions for wide bandgap a-Si:H single junction cells with a band gap energy of 1.90 eV in VHF conditions. In the same chamber, deposition of crystalline nc-Si:H layer is conducted at conditions optimised for 62% crystallinity phase fraction to obtain device-grade absorber material.*

---

<sup>1</sup>G. Padmakumar, O. Eringfeld, S.M. Ghayeni, S.M. Karthikeyan, T. De Vrijer, F. Saitta, P. Perez-Rodriguez, R.A.C.M.M. van Swaaij, Arno H.M. Smets, 'Optimisation of Amorphous and Microcrystalline Silicon in VHF Deposition Conditions'

Over the past 40 years, thin-film silicon solar cells have been seen as a complementary technology to mainstream crystalline silicon solar cells, offering benefits such as reduced raw material use, suitability for large-scale production, and adaptability for lightweight, flexible modules [11]. Thin-film photoactive materials such as amorphous silicon, nanocrystalline silicon, Copper Indium Gallium Selenide (CIGS), cadmium telluride (CdTe), III-V technology, organic PV (OPV) and Perovskites (PVK) are deposited as thin layers with thickness up to 2-4 micrometres. Enhancing device conversion efficiency through multijunction architectures is commonly implemented with at least one thin-film PV junction. PVK/c-Si, GaAs/c-Si, PVK/CIGS, InGaP/GaAs/Ge, a-Si:H/a-Si:H/nc-Si:H are some examples. In this work, we focus on a-Si:H/nc-Si:H tandem solar cell.

With a relatively wide band gap, a-Si:H (bandgap tunable between 1.70 and 1.95 eV) has the potential to be combined with nc-Si:H (bandgap energy between 1.0 to 1.1 eV), germanium, germanium-tin alloy, narrow-bandgap perovskites or OPV [15–20, 89]. The properties of a-Si:H and nc-Si:H materials are heavily dependent on their deposition conditions [90–92]. Performance optimisations for thin-film silicon-based devices have been extensively published [15, 93–100]. These previous reports describe a-Si:H and nc-Si:H depositions using different techniques, including the hot-wire technique, expanding thermal plasma, radio-frequency (RF) plasma-enhanced chemical vapour deposition (PECVD), and very high-frequency (VHF) PECVD. Among these techniques, only RF PECVD and VHF PECVD have been industrially up-scaled successfully [12, 27, 28].

At an industrial scale, silicon thin-film solar cells were developed and manufactured by LG [29, 30], Sharp [31], Kaneka [32], United Solar Systems Corp. [33], Applied Materials [34], Oerlikon Solar (later Tokyo Electron) [35], Solarex [36], ARCO Solar [13], LiFT PV (formerly HyET Solar) [12]. While most of these entities have since ceased production or shifted their focus away from this specific technology, LiFT PV remains actively engaged in the research and manufacturing of silicon thin-film cells.

Conventionally, in industries like LiFT PV (formerly HyET Solar) that utilise a p-i-n deposition sequence, a-Si:H depositions in PECVD are conducted at an input voltage operating at RF and nc-Si:H depositions at very high frequency (VHF) in dedicated chambers [12, 27]. This study explores the feasibility of depositing both device-grade a-Si:H (wide-bandgap and  $V_{OC} > 900$  mV) and nc-Si:H in the same PECVD chamber with the same VHF generator without dedicated conditioning. When realised, this approach is beneficial for the industrial production of a-Si:H, nc-Si:H and a-Si:H/nc-Si:H tandem solar cells [20]. Eventually, such an adjustment can reduce capital expenditure, as the a-Si:H and nc-Si:H absorbers, as well as their grading, can be fabricated using the same electrical generator and chamber.

The experiments in this chapter map the processing parameters of a solar cell in relation to its performance parameters. Optimisations of a-Si:H and nc-Si:H materials are conducted individually on single-junction p-i-n superstrate configurations to ensure device-quality layers can be fabricated in the same chamber. The objective of this study is to deliver standard recipes for depositing a-Si:H and nc-Si:H absorber layers in VHF conditions.

## 2.1. Experimental Details

### 2.1.1. Photoactive layer deposition parameters

The solar cells reported in this chapter are all made on textured glass with a p-i-n substrate configuration. The overview processing conditions that influence the material properties of thin film silicon and specific parameters selected in this study are as follows:

**i. Silane Concentration, (SC)** is given as the ratio of the silane flow rate ( $F_{\text{SiH}_4}$ ) to the hydrogen flow rate ( $F_{\text{H}_2}$ ),  $SC = F_{\text{SiH}_4}/(F_{\text{SiH}_4} + F_{\text{H}_2})$  [101].  $SC$  is a measure of the composition of precursor gases in the deposition chamber and plasma. **ii. Excitation frequency, ( $f$ )** is the frequency of voltage applied across deposition electrodes. Consequently,  $f$  determines the time over which an ion is accelerated in the plasma sheath.  $f$  can be RF 13.56 MHz or VHF at 40.68 MHz. This chapter explores  $f = 40.68$  MHz, which falls within the VHF range. At VHF frequencies, high-power deposition is possible without amorphizing the layer because the maximum ion bombardment energy is lower. As a result, nc-Si:H can be deposited at high deposition rates without compromising material quality [100, 102]. **iii. Chamber Pressure, ( $p$ )** inside the chamber is controlled using a throttle valve in the chamber.  $p$  has a direct influence on the residence time of the species in the chamber [103, 104]. An increase in  $p$  at constant power density will reduce the ion-bombardment energy towards the substrate surface due to increased ion-neutral collisions (decreasing the mean free path) in the plasma sheath. **iv. Power density ( $PD$ )** coupled into the Plasma region determines the energy carried by the ions and electrons in the plasma. The increase in power results in an increase in the deposition rate, provided there are sufficient  $\text{SiH}_4$  precursor molecules present in the volume to dissociate [103–105]. Additionally, parameters such as the electrode gap (the gap between the substrate holder and the excited electrode) and the substrate temperature ( $T_{\text{sub}}$ ) influence material properties. In this chapter, the electrode gap is kept constant at 13 mm and  $T_{\text{sub}}$  is maintained at 170 °C throughout the deposition.

In a PECVD process, the effects of the parameters mentioned above are often interlinked, and material properties are determined by multiple parameters simultaneously.  $p$ ,  $PD$  and total precursor flow have a complex interplay and have been explored extensively before [98, 100, 101, 105, 106].

### 2.1.2. a-Si:H to nc-Si:H transition

As discussed in Section 2.1.1, multiple process parameters determine the material properties of silicon deposited on solar cell superstrates. Most processing condition changes can cause a transition from nc-Si:H to a predominantly amorphous material within the bulk,  $SC$  is generally reported to be most influential. An elevated precursor flux of atomic hydrogen in reference to dissociated  $\text{SiH}_4$  precursor products in the plasma results in nc-Si:H growth [94, 107]. For this reason, in this experiment, the influence of silane flow and hydrogen flow conditions on the performance of single-junction p-i-n superstrate silicon devices (with either a-Si:H or nc-Si:H absorbers) is investigated. This experiment determines the processing window within

which further optimisation of absorbers can be conducted.

The deposition and solar cells in this experiment are made on commercially available Asahi UV-type substrates. The TCO on these commercially available glass is predeposited FTO with a thickness of 650 nm. The device structures are given in the Figure 2.1 (A) and (B). The deposition of intrinsic nc-Si:H absorbers and a-Si:H was made in a PECVD multichamber tool at very high frequency (40.68 MHz) and 170 °C substrate temperature. Using  $B_2H_6$  and  $PH_3$  as dopant gases, a boron-doped p-silicon oxide (p-SiO<sub>x</sub>) layer (16 nm) -used as hole transport layer- and a phosphorus-doped n-silicon oxide (n-SiO<sub>x</sub>) layer (20 nm) -used as electron transport layer- were deposited at RF (13.8 MHz) and 180 °C substrate temperature in dedicated chambers. The back reflector consists of sputtered i-ZnO (60 nm) and an evaporated silver (300 nm) layer. An aluminium strip (500 nm) serves as the front contact for these solar cells, and the back contact consists of 5 mm × 5 mm square-shaped chromium (30 nm) and aluminium (500 nm) dots. This results in a solar cell structure of FTO (650 nm) / p-nc-SiO:H (16 nm) / Si Alloy / n-nc-SiO:H (20 nm) / i-ZnO (60 nm) / Ag (300 nm).

A thin seed layer ( $F_{SiH_4} = 1$  sccm,  $F_{H_2} = 120$  sccm) is used for facilitating nucleation sites [108] during the depositions. The results of variations in  $F_{SiH_4}$ , processed at a constant  $F_{H_2}$  of 120 sccm, are presented in Figure 2.2(A).  $F_{SiH_4}$  is varied from 2.4 sccm ( $SC = 1.96\%$ ) to 4.0 sccm ( $SC = 3.22\%$ ) initially. The deposition times of these conditions are adjusted such that all nc-Si:H absorbers have a constant thickness of  $\approx 2.5$   $\mu\text{m}$ . The investigation is further extended to another batch of solar cells, with  $F_{SiH_4}$  varying from 6.0 sccm ( $SC = 4.76\%$ ) to 7.0 sccm ( $SC = 5.51\%$ ). These solar cells, specified under the latter conditions, are further re-fabricated without the incubation layer and with the material thickness controlled (configuration in Figure 2.1(B)). The reason for this step is detailed in the results in Section 2.2.1.

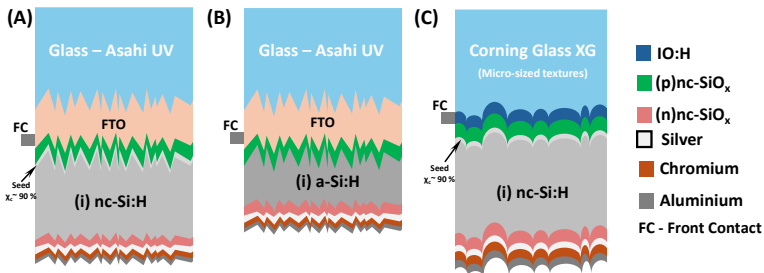


Figure 2.1.: Solar cell architectures of (A) a-Si:H on Asahi glass used for VHF silicon deposition and a-Si:H absorber optimisation, (B) nc-Si:H on Asahi glass used for VHF silicon deposition, (C) nc-Si:H on micro-textured glass used for VHF silicon deposition.

### 2.1.3. a-Si:H absorber optimisation

Optimisation of processing conditions for wide-bandgap a-Si:H is conducted on Asahi glass in a p-i-n configuration. The a-Si:H absorber is 300 nm thick, deposited in PECVD multichamber at VHF and a substrate temperature of 170 °C. The front and back

contacts, doped layers, and back reflector stack have specifications identical to those mentioned in Section 2.1.2. The resulting solar cell architecture is given to Figure 2.1(B). In this experiment,  $p$  is varied from 4 mBar to 9 mBar with an interval of 1 mBar, and  $PD$  is varied from  $0.10 \text{ W/cm}^2$  to  $0.4 \text{ W/cm}^2$  with an interval of  $0.1 \text{ W/cm}^2$ . I.e., a total of 30 different settings are used. A solar cell was fabricated under each processing condition, during which the plasma was observed to remain stable and deposited a spatially uniform layer. An additional solar cell was made at 5 mBar and  $0.28 \text{ W/cm}^2$  to narrow down the variation in the optimised window. In total, 28 solar cells were fabricated in this experiment (each of these  $p - PD$  combinations is explicitly marked in the summary plot in upcoming section 2.2.2 using hexagonal-shaped dots).

The conventionally used optimised recipe (optimisation not shown here) for a-Si:H using the RF input voltage in the same multichamber tool is as follows.

Layer	SiH <sub>4</sub> [sccm]	H <sub>2</sub> [sccm]	$p$ [mBar]	$PD$ [W/cm <sup>2</sup> ]	$T_{sub}$ [°C]	Deposition rate [Å/s]
(i) a-Si:H Narrow band-gap	40.0	0.0	0.7	0.028	180	2.8
(i) a-Si:H Wide band-gap	3.0	200.0	10	0.095	130	0.1

Table 2.1.: Deposition conditions of different silicon layers in RF conditions. The distance between the RF electrode and the grounded electrode is 13 mm for all p-doped layer depositions, 13 mm for all intrinsic layer depositions, and 21 mm for all n-doped layer depositions.

#### 2.1.4. nc-Si: H absorber optimisation

The solar cells used for optimising the nc-Si:H absorber layer use glass with micro-sized craters as superstrates. A 90 nm thick 90% crystalline seed layer ( $SC = 1\%$ ) is used for facilitating nucleation sites in all solar cells [108]. The growth of nc-Si:H conglomerate layers often leads to shading effects, crack formation, and poor passivation of crystallites [11]. As the layers are made thicker, the probability of crack formation also increases on nano-sized Asahi superstrates [109]. So it is ideal to optimise the conditions for micro-sized features. Similar superstrate approaches have been previously used in [96, 110] to study the deposition and properties of nc-Si:H. For this chapter, micro-textures on glass are created using a 300 nm-thick indium-doped tin oxide (ITO) sacrificial layer. This layer is etched using HF to produce textured glass. The process is explained in detail elsewhere [111]. The single-junction nc-Si:H solar cells included in this study have an absorber thickness of 2.5  $\mu\text{m}$ . The solar cells have hydrogenated indium oxide (IOH) as the front electrode TCO. IOH is RF magnetron sputtered from a ceramic indium oxide ( $\text{In}_2\text{O}_3$ ) target in  $\text{Ar}/\text{O}_2/\text{H}_2\text{O}$  mixtures at room temperature. The resulting solar cell architecture is given in Figure 2.1(C).

The solar cells were designed to sweep across crystalline phase fraction ( $\chi_c$ ) from 30% to 90%. 54 samples were fabricated with combinations of randomly varied  $F_{\text{H}_2}$ ,  $p$ , and  $PD$  at  $F_{\text{SiH}_4} = 3.2 \text{ sccm}$ . These samples depicted a variety of  $\chi_c$  values.  $p$  is varied from 3.0 mBar to 5.0 mBar,  $F_{\text{H}_2}$  is varied from 100 to 200 sccm. A deposition series with  $PD$  varied between 0.34 and  $0.47 \text{ W/cm}^2$  at  $p = 4.0 \text{ mBar}$ ,  $F_{\text{H}_2} = 120 \text{ sccm}$  is also made. This

set of samples is referred to as “power-series” henceforth.

### 2.1.5. Solar cell characterisation

The open-circuit voltage ( $V_{oc}$ ) and fill factor (FF) of solar cells were measured by a WACOM-class AAA xenon-halogen dual lamp continuous AM1.5G spectral simulator at 25 °C. The short-circuit current density ( $J_{sc}$ ) values were calculated based on the external quantum efficiency (EQE) measurement of solar cells. This helps to prevent the effect of any mismatch between the solar simulator spectrum and the AM1.5 spectrum. Also, it eliminates any overestimation of current caused by errors in estimating the active cell area in small-area solar cells. EQE measurement is conducted at a short-circuit condition of 0 V and a reverse bias condition of -2 V. The total reflection of the solar cell is also recorded using a LAMBDA 1050+ UV/Vis/NIR Spectrophotometer with a 150 mm InGaAs integrating sphere from PerkinElmer.

$\chi_c$  of the solar cells was characterised using a Renishaw Raman spectrometer equipped with a 633 nm excitation laser. The devices, configured in a superstrate p-i-n structure, were probed from the rear side (n-doped  $\text{SiO}_x$  layer). The Raman spectra were deconvoluted into Gaussian components centred around  $520 \text{ cm}^{-1}$ , attributed to the crystalline silicon (c-Si) phase, and near  $510 \text{ cm}^{-1}$ , corresponding to a transitional or partially ordered phase. Additional Gaussian peaks observed at 160, 320, 390, and  $480 \text{ cm}^{-1}$  are associated with the amorphous silicon ( $480 \text{ cm}^{-1}$ ) [112] and silicon oxide matrix within the bulk absorber. Although there are subtle differences in how to determine  $\chi_c$  from a Raman spectrum [113], in this study, the degree of crystallinity is quantified using the relation [114, 115]:

$$\chi_c = \frac{A_{520} + A_{510}}{(0.8A_{480}) + A_{520} + A_{510}} \quad (2.1)$$

where  $A_{520}$ ,  $A_{510}$ , and  $A_{480}$  represent the integrated intensities of the respective Raman peaks. 0.8 is a correction factor to account for the different scattering cross-sections from crystalline and amorphous phases in the bulk. Extended Raman measurements were carried out under the same configuration to investigate the hydride ( $\text{Si-H}_x$ ) stretching mode (SM) region in nc-Si:H. These stretching modes typically appear within the range of  $1800\text{--}2300 \text{ cm}^{-1}$ . Gaussian functions were fitted to the spectra to identify characteristic hydride bonding configurations in the bulk. The low stretching mode (LSM) peaks, located between  $1980$  and  $2010 \text{ cm}^{-1}$ , and the high stretching mode (HSM) peaks, positioned between  $2070$  and  $2100 \text{ cm}^{-1}$ , originate from a-Si:H regions within the bulk material [116, 117].

In nc-Si:H, the HSM region broadens with additional features at  $2120$  and  $2150 \text{ cm}^{-1}$ , which are attributed to contributions from dihydride and trihydride species associated with amorphous tissue in the nc-Si:H bulk. Furthermore, three narrow HSM components (NHSMs) appearing at  $2083$ ,  $2103$ , and  $2137 \text{ cm}^{-1}$  correspond to monohydride, dihydride, and trihydride bonds on crystalline surfaces, respectively. These NHSMs are indicative of hydrogen termination at crystalline grain boundaries within the bulk [112, 117, 118].

## 2.2. Results and Discussion

### 2.2.1. a-Si:H to nc-Si:H transition

Figure 2.2(A) maps the variation in solar cell performance with a change in  $F_{\text{SiH}_4}$  from 2.0 sccm to 7.0 sccm at  $F_{\text{H}_2}$  kept constant at 120 sccm. A secondary horizontal axis is included in the plot, marking the corresponding  $\chi_c$  values for the samples. It is noted that change in  $\chi_c$  is not linear with  $F_{\text{SiH}_4}$ . Figure 2.2(B) shows the Raman spectra normalised about the intensity of  $520 \text{ cm}^{-1}$ , measured from the n-side. The c-Si peak at  $520 \text{ cm}^{-1}$  relatively decreases in reference to the amorphous silicon transverse optic mode at  $480 \text{ cm}^{-1}$ , with increasing  $F_{\text{SiH}_4}$ . This decrease of the  $\chi_c$  with increasing SC has been well established [95, 101, 102, 113, 119]. A significant and rapid change in  $\chi_c$  can be observed when  $F_{\text{SiH}_4}$  is varied from 3.4 sccm to 3.6 sccm. Even though the change in SC is only 0.20%, a significant change in the  $\chi_c$  of about 28% absolute is observed. This very sharp transition from a-Si:H to nc-Si:H for minor changes in the SC is in agreement with earlier reports [93, 98, 101]. The transition from the dominant crystalline to the amorphous phase of silicon significantly impacts the characteristics of solar cells.

It can be observed in Figure 2.2(A) that with an increase in  $F_{\text{SiH}_4}$ , the amorphous fraction in the bulk absorber increases (ie,  $\chi_c$  decreases), which results in a gradual rise in  $V_{\text{oc}}$ . The  $V_{\text{oc}}$  values range from 400 mV to 940 mV. Beyond the crystalline to amorphous transition regime, a significant  $J_{\text{sc}}$  drops by  $12 \text{ mA/cm}^2$ . The FF also drops rapidly once the material transitions into an amorphous-dominated phase. The overall trend of  $J_{\text{sc}}$ , FF drop accompanied by  $V_{\text{oc}}$  increase with increase in  $F_{\text{SiH}_4}$  is due to the rise in amorphous fraction of the solar cell [120].

The EQE spectra in 2.2(C) further explain the  $J_{\text{sc}}$  variation. For  $F_{\text{SiH}_4} < 3.0$ , significant loss occurs in the collection of high-energy photons (blue part of the spectrum, wavelengths ( $\lambda$ ) below 500 nm). The least loss occurs for  $F_{\text{SiH}_4} = 3.0$ , and it has the highest  $J_{\text{sc}}$  value in the series, for the  $F_{\text{SiH}_4} > 3.2$  major  $J_{\text{sc}}$  loss occurs in the infrared ( $\lambda > 700 \text{ nm}$ ) part of the spectrum, which is in line with [97, 101]. The loss in the infrared is likely due to the dominance of the higher band gap a-Si:H, and fewer narrow band gap nc-Si:H grains are incorporated in the bulk. A drop in  $\chi_c$  results in a decrease in the average absorption probability for the low-energy infrared photons. A corollary of this is seen in Figure 2.2(D), which plots the specific EQE response value at  $\lambda = 400 \text{ nm}$  and  $\lambda = 950 \text{ nm}$ . The red response increases with crystalline phase fraction in the absorber. For a  $\chi_c > 70\%$ , the red response also drops. For  $\chi_c = 10\%$ , photo-response is low in both the blue ( $\lambda < 600 \text{ nm}$ ) and in near infrared ( $\lambda > 800 \text{ nm}$ ). The loss in the blue part of the spectrum is likely due to poor charge-carrier (both hole and electron) collection. Generally, the defect density in the amorphous tissue is much higher than that of the crystalline phase, and consequently, the recombination probability in an  $\chi_c = 9\%$  absorber is relatively high. Considering that the majority of the high-energy blue photons will be absorbed near the i/p-interface, the poor collection efficiency of electron-hole pairs generated upon blue-photon absorption can be understood to be significantly reduced in these relatively thick, predominantly amorphous absorber layers.

For  $F_{\text{SiH}_4} > 6.0 \text{ sccm}$ , the absorber layer is completely amorphous. The transition to a fully amorphous phase significantly increases the deposition rate, thereby making very thick a-Si:H layers severely suffer from charge-carrier collection. This leads to a very

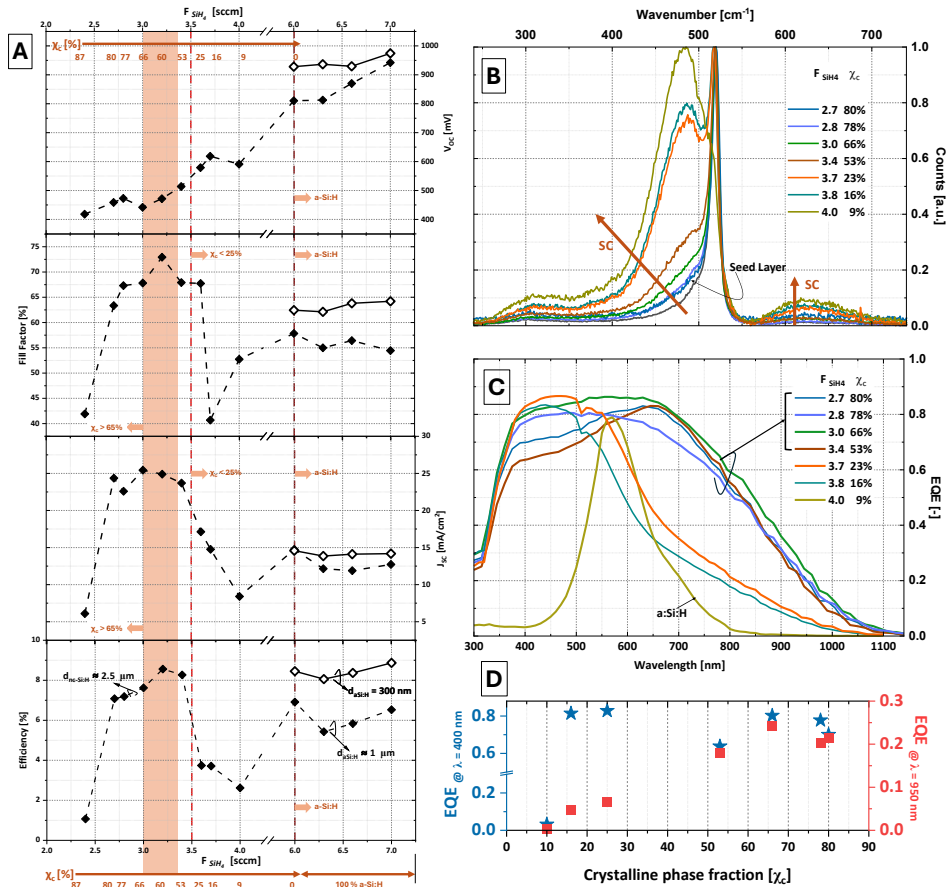


Figure 2.2.: Single junction thin film silicon solar cells made at different SC. (A) External parameters of the solar cells. (B) Raman spectroscopic analysis of the crystalline fraction was done on cells from the rear side. (C) EQE of the cells with the absorber deposited at different SC. (D) QE values at  $\lambda = 400 nm$  and  $\lambda = 950 nm$ .

low FF and  $J_{sc}$ . At the same time,  $V_{oc}$  follows the trend and increases with  $F_{SiH_4}$ . For a fair comparison with other solar cells in the experiment, new samples are prepared with 300 nm a-Si:H absorber layers, a typical absorber thickness for single-junction solar cells. This adjustment reduced losses associated with thickness. The highest-performing sample in this batch demonstrated a  $V_{oc}$  of 970 mV, an FF of 65%, and a power conversion efficiency ( $\eta$ ) of 8.9%.

From this variation of SC at VHF PECVD depositions, the processing window of the a-Si:H absorber is identified with an  $F_{SiH_4} > 6.0$  sccm and  $F_{H_2} = 120$  sccm. For crystalline dominated phase  $F_{SiH_4} < 3.5$  sccm and  $F_{H_2} = 120$  sccm is identified. These two deposition regimes are explored in detail and optimised for input PD and inlet pin

the upcoming sections 2.2.2 and 2.2.3.

### 2.2.2. a-Si:H optimisation on nano-sized textured Asahi superstrates

The experiment is conducted over various  $p - PD$  combinations to identify the plasma conditions that lead to the best-performing solar cells. All solar cells are made at  $F_{\text{SiH}_4} = 6$  sccm and  $F_{\text{H}_2} = 120$  sccm. Figure 2.3 maps the plasma stability and the external parameters of a-Si:H single junction solar cells fabricated at different  $p - PD$  combinations. The EQE data of each solar cell is broken down into values at three different  $\lambda$ : 405 nm, 505 nm, and 705 nm. From the experiment, it is observed that to maintain a stable plasma, the required  $PD$  input increases with increasing  $p$ . A flickering plasma zone is also marked in the figure, where the  $p$  is barely enough to ignite the plasma, but cannot maintain a stable plasma. The  $p$  for plasma ignition scales with Paschen's law.

The contour plots in Figure 2.3 (A), (B) map the  $V_{\text{oc}}$  and FF of all the 27 single junction a-Si:H solar cells made against a  $p - PD$  grid. The  $V_{\text{oc}}$  is the highest at a low- $p$ , high- $PD$  region. This is due to the high deposition rate ( $\approx 0.8$  nm/s) under this condition. The high  $PD$  results in high deposition rate, subsequently resulting in less dense material with high volume deficiencies. A FF of 68% is attained at 5 mBar and  $PD = 0.30$  W/cm<sup>2</sup> at a deposition rate  $\approx 0.4$  nm/s. Figure 2.3 (C), (D) shows that both  $\eta$  and  $J_{\text{sc}}$  exhibit similar trends, marking a sudden drop in performance for  $p > 5$  mBar.

The EQE spectra of samples were extracted into three components at  $\lambda = 405$  nm,  $\lambda = 505$  nm,  $\lambda = 705$  nm in Figure 2.3 (E), (F), (G). The QE plot at  $\lambda = 405$  nm (Figure 2.3 (E)) indicates that the cells experience a conversion loss in the blue region of the spectrum under low- $p$ , high- $PD$  deposition conditions. However, this loss of blue response is not observed in any RF-deposited a-Si:H single junctions with the same p-doped nc-SiO:H window layers (EQEs not shown in this chapter). It is previously reported that vigorous deposition conditions for intrinsic a-Si:H cause a boron impurity diffusion (via etching of existing p-doped layer and redeposition at the p-i interface) in the initial growth phase of the intrinsic a-Si:H single junctions [121, 122].  $f$  is a critical parameter in determining the ion energy distribution in the plasma. Assuming a collisionless Child-Langmuir space charge sheath, the energy distribution of ions bombarding the substrate follows a broad and bimodal distribution at 13.56 MHz RF [99, 123]. In RF, the ions tend to respond instantaneously to varying sheath voltage values as the ion transit time to cross the plasma sheath is smaller than the RF cycle. With an increase in  $f$ , as discussed in this experiment, for VHF 40.68 MHz, the distribution of the ions reacts only to an average sheath voltage value, resulting in a narrow energy distribution [123]. This variation in ion energy distribution in a VHF plasma, when compared to RF, is cited as a contributing factor to boron impurity diffusion at low- $p$ . By fine-tuning the  $p - PD$  combination, this boron tailing can be avoided. A 'pressure surplus' processing region near the unstable (flickering) plasma zone results in an  $EQE > 0.75$  at  $\lambda = 405$  nm. This can be attributed to an increase in ion-neutral collisions in regions of higher  $p$  and lower  $PD$  [99]. EQE at  $\lambda = 705$  nm is an indicator of the bandgap of the material. At the high  $PD$  and low- $p$  combination region, the bandgap of deposited a-Si:H is high (as noticed from the  $V_{\text{oc}}$ ), which causes a diminished EQE response at ( $\lambda = 705$  nm).

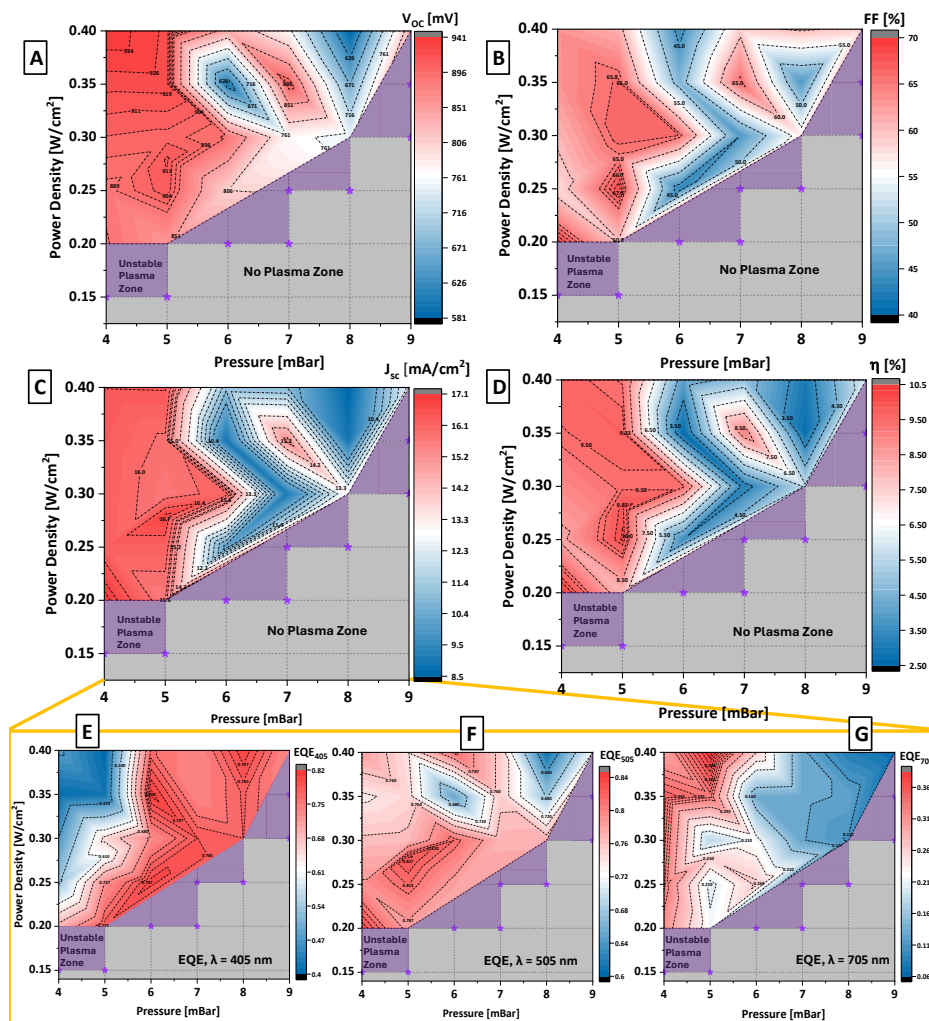


Figure 2.3.: External parameters of a-Si:H single junction solar cell. (A)  $V_{OC}$ , (B) FF (C)  $J_{SC}$  and (D)  $\eta$ . The  $\lambda$  specific QE values are extracted from EQE data to make the bottom box, (E)  $\lambda = 405$  nm, (F)  $\lambda = 505$  nm, (G)  $\lambda = 705$  nm

Figure 2.4 shows a summary of the processing conditions taking into account blue response, red response and  $V_{OC}$  of the solar cells with an absorber thickness of 300 nm fabricated at those processing conditions. Different zones are numbered in the  $p$ - $PD$  grid. Zone 1 belongs to the region where the input power is insufficient to ignite the plasma at the given  $p$ . The boundary of this region, marked with stars, marks the values at which the plasma seemed unstable (flickering). Zone 2 and Zone 3 (neighbourhood of unstable plasma zone) have a  $V_{OC}$  value of around 0.80 V. Zone 4 further decreases the

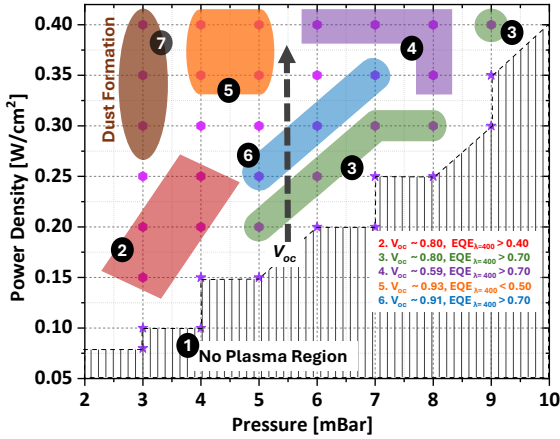


Figure 2.4.: Summarised plot of the a-Si:H deposition outcome (mainly  $V_{oc}$ , and specific QE value at  $\lambda = 400$  nm) at various  $p - PD$  combinations arranged to 7 different groups.

$V_{oc} \approx 600$  mV. Zones 5 and 6 yield a  $V_{oc} > 910$  mV, but Zone 5 exhibits a poor blue response. Zone 7 of the grid - the low  $p$  and high  $PD$  conditions, start forming silicon dust particles as a result of silane polymerisation [124]. The region between zones 5 and 6 has the highest  $\eta$  with  $V_{oc} \approx 934$  mV, FF = 68 and a blue response  $QE > 0.70$  combined with red response  $QE > 0.29$ . The Tauc bandgap energy ( $E_{Tauc}$ ) of a-Si:H deposited under these conditions is  $1.90 \text{ eV}^2$ . The  $p - PD$  grid mapping is significant as it demonstrates the feasibility of achieving varied band gaps in deposited a-Si:H films under identical precursor gas flow conditions, which is crucial for the fabrication of bandgap-graded solar cells.

To add context to the optical performance of a-Si:H at VHF, the EQE spectra of a-Si:H single junction solar cell deposited at RF (optimised processing conditions mentioned in Table 2.1) on the same multichamber deposition tool are also added to Figure 2.5. The influence of an increase in the material bandgap is clearly visible as the drop in EQE response at long wavelength ranges of the spectrum.

### 2.2.3. nc-Si:H optimisation on micro-textured glass superstrates

In Section 2.2.1, it is observed that a  $F_{SiH_4} < 3.7$  sccm and  $F_{H_2} = 120$  sccm had resulted in deposition of crystalline absorber  $\chi_c > 25\%$  on Asahi UV superstrates. Additionally, we observed that the change in performance is mainly correlated with the crystalline phase fraction of the deposited material. It is widely reported that device quality nc-Si:H is obtained for plasma conditions near the crystalline-to-amorphous "transition regime" [98, 101, 106, 119, 127–129] and that this particular transition regime is usually within a very narrow processing window [106, 129].

<sup>2</sup>This value is directly obtained from the Tauc-Lorentz model fit of spectroscopic ellipsometry data.  $E_{Tauc}$  is reported as it is close to the actual electrical band-gap of amorphous materials [125, 126].

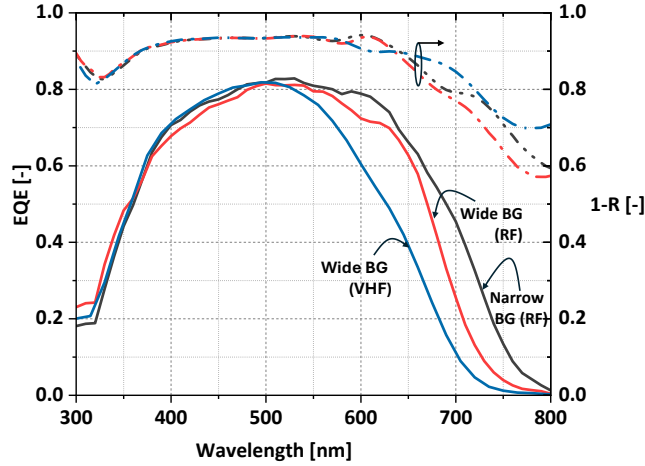


Figure 2.5.: EQE of VHF PECVD wide band gap a-Si:H compared to RF PECVD wide BG a-Si:H, and RF PECVD narrow BG a-Si:H.

Figure 2.6(A),(B),(C) and (D) plots the external parameters and resistances (series and parallel) of the solar cells. The cells made in power series are overlaid on the plot with semi-open data points and dotted lines. As observed from the plots, the power series is a good representative of the effect of  $\chi_c$  variation in solar cells.

**General trend:** In Figure 2.6(A), the  $V_{oc}$  drops continuously with increasing crystalline volume fraction. This is previously observed in detail for different processing techniques by Droz et al. [130]. The FF shows a general increasing trend and drops sharply beyond  $\chi_c = 67\%$ . This drop in FF is primarily attributed to a steep decrease in parallel resistance as observed in Figure 2.6 (C). High crystallinity can result in cracks and pinholes and consequently shunt paths through the absorber bulk. The a-Si:H phase fraction is insufficient to passivate the grain boundaries under these conditions. At the same time, a mild drop in series resistance is also observed with very high  $\chi_c$  values as more microcrystalline conglomerates are available in the bulk for conduction [15, 102]. The density variation with crystallinity is discussed in the last paragraph of this section. Figure 2.6 (C) plots the  $V_{oc} \times FF$  product, which is a good representation of the electrical performance of thin-film silicon cells [131, 132] against  $\chi_c$ .  $V_{oc} \times FF$  peaks at around 58 to 65% and declines sharply beyond  $\chi_c = 65\%$ . The  $J_{sc}$  scatters between 22 and 24 mA/cm<sup>2</sup> for  $\chi_c > 50\%$  as the  $J_{sc}$  for these crystallinities is majorly determined by the dominant light scattering mechanism (interface scattering or TCO bulk scattering). Owing majorly to a  $V_{oc} \times FF$  trend, the  $\eta$  shows peak values for nc-Si:H cells with absorber  $\chi_c$  between 61 and 64%.

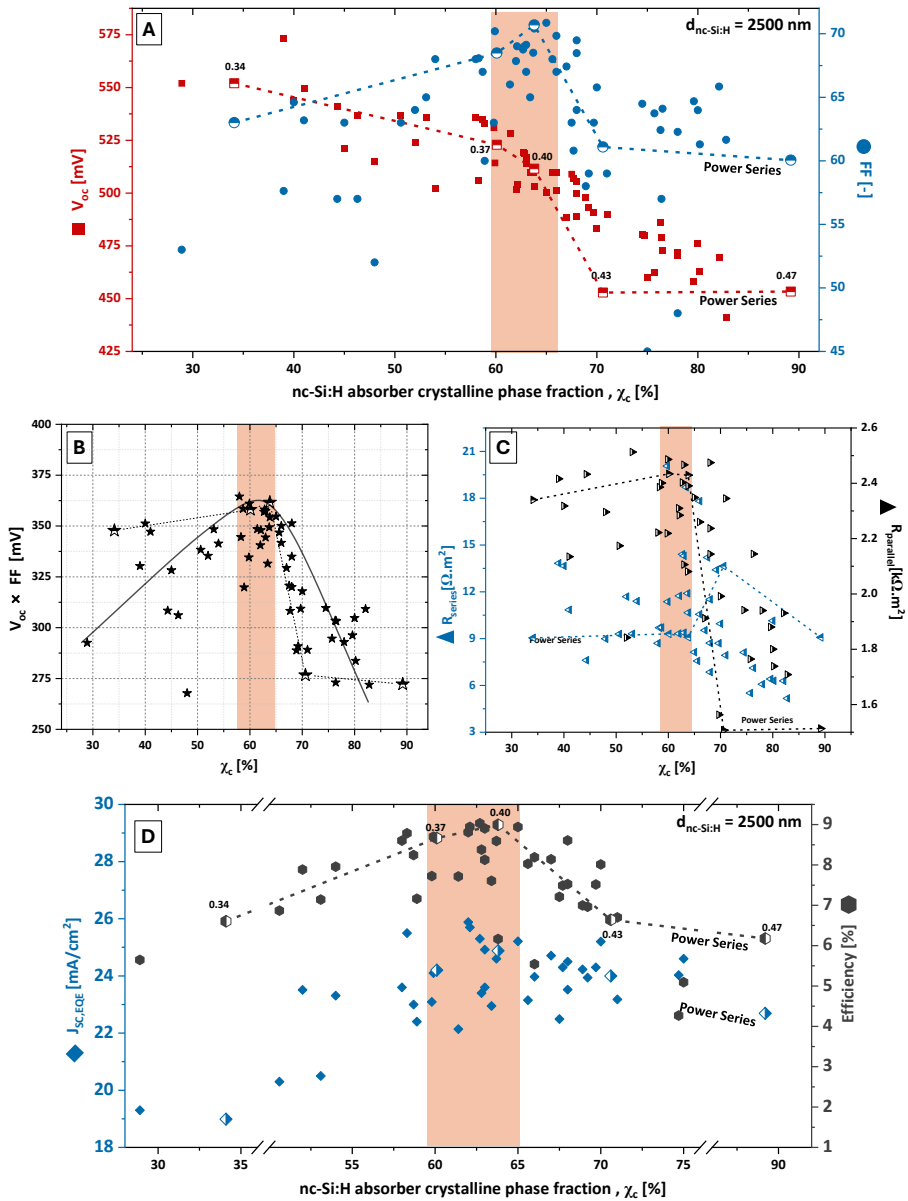


Figure 2.6.: External parameters (A)  $V_{oc}$  and FF, (B)  $V_{oc} \times FF$  (solid line is guide to the eye) (C) Series and parallel resistances and (D)  $J_{sc}$  and  $\eta$  plotted for nc-Si:H optimisation samples and power series fabricated on micro-sized superstrate glass. NOTE: The dashed lines represent power series, not a fit or guide to the eye.

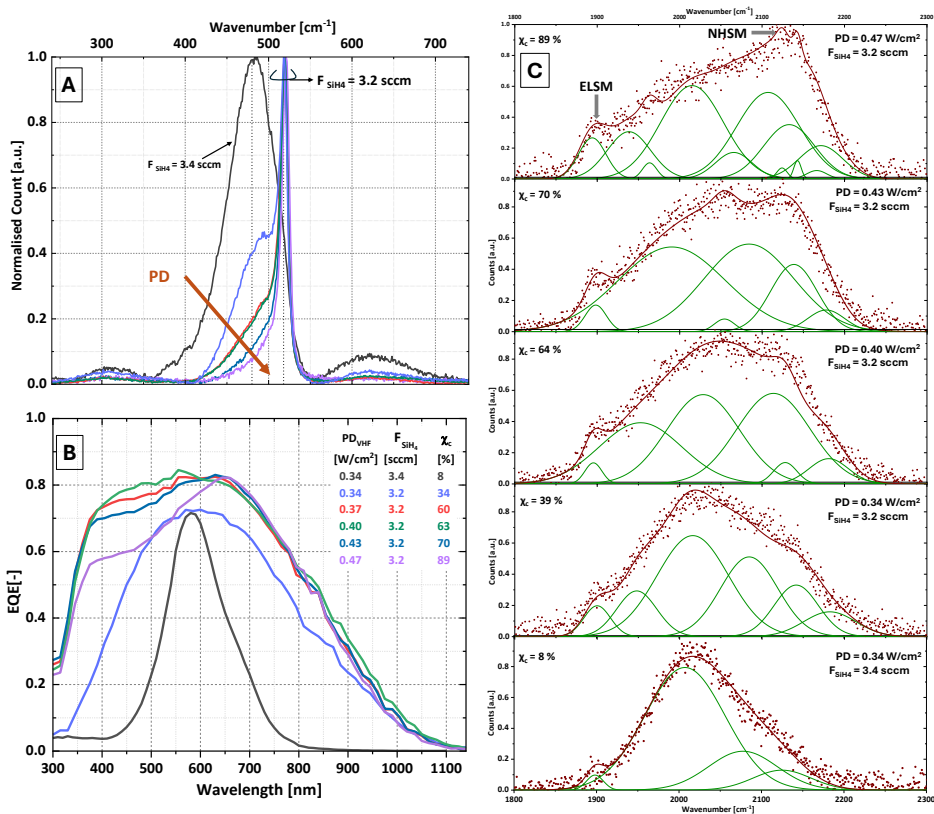


Figure 2.7.: (A) Stretching modes obtained from Raman spectroscopy measurements of nc-Si:H solar cells. (B) Increase in crystallinity variation in nc-Si:H absorber with increase in power. (C) EQE of solar cells from power series.

**Power series:** Figure 2.7(A), (B) and (C) give the crystallinity from Raman spectra, EQE and the extended Raman spectra of the solar cells in the power series. The Raman spectra show that the  $\chi_c$  increases with  $PD$ , which is in agreement with earlier observations by [100, 101]. Again, for a  $0.03 \text{ W/cm}^2$  change in  $PD$  near the transition regime, the  $\chi_c$  decreases steeply by approximately 25%. This demonstrates the sensitivity of this transition threshold to minor variations in the applied  $PD$ , similar to SC. Figure 2.7 (B) gives the EQE of the samples; a transition to amorphous-dominated absorbers shows significant losses in the blue and near infrared part of the EQE spectrum, explaining the substantial  $J_{sc}$  decrease that was mentioned in the previous paragraph. For  $PD = 0.40$ , the charge collection and red response is highest, which, when combined with the light trapping of micro-texture, gives  $J_{sc} = 25 \text{ mA/cm}^2$ . The best performing solar cells from the power series are the ones with nc-Si:H bulk absorber (with 90 nm thick seed layer) processed at  $F_{SiH4} = 3.2 \text{ sccm}$ ,  $F_{H2} = 120 \text{ sccm}$ ,  $p = 4 \text{ mBar}$ ,  $PD = 0.40 \text{ W/cm}^2$  with  $\chi_c \approx 63\%$ . This solar cell has a  $V_{oc} = 512 \text{ mV}$ ,  $FF = 70.2\%$ .  $J_{sc} = 25.0$  and  $\eta = 9.0\%$ .

The signature stretching modes of high device quality nc-Si:H are discussed in [100, 112]. Narrow high stretching modes (NHSM) are observed at 2083, 2103, and 2137  $\text{cm}^{-1}$ . These peaks represent the mono-, di-, and tri-hydrides on the crystalline surfaces [118]. These are generally present in low-density nc-Si:H with very high  $\chi_c$  and will undergo post-deposition oxidation over time [112]. The best nc-Si:H cell performance is usually observed for the  $\chi_c$  without any NHSM after deposition and sharp extremely low stretching modes (ELSM) peaks. The nc-Si:H deposited at  $PD = 0.43$  and  $0.40 \text{ W/cm}^2$  do not show NHSM peaks. This denotes a dense bulk matrix with thin, hydride-dense a-Si:H tissue passivating the crystalline grain boundaries, resulting in a high-quality absorber bulk. The transition to amorphous suppresses the stretching modes further, and only the ELSM (the ELSM peak at  $\chi_c = 0.08$  is considerably small in reference to low stretching mode (LSM) and high stretching mode (HSM)), LSM and HSM components are present in the Raman spectra at  $PD = 0.34 \text{ W/cm}^2$  and  $F_{\text{SiH}_4} = 3.2$  sccm. The stretching modes of amorphous-dominated bulk deposited at  $PD = 0.34 \text{ W/cm}^2$  and  $F_{\text{SiH}_4} = 3.4$  sccm in Figure 2.7(C) demonstrate an LSM, MSM (divacancies) and HSM (trivacancies) peaks. Medium stretching mode (MSM) peaks in the spectra indicate hydrogenated multivacancies in the bulk, which increase the material's band gap [133, 134].

It can be observed that for both the  $F_{\text{SiH}_4}$  series and  $PD$  series, the highest conversion efficiencies are achieved for the transition regime, which is located around  $\chi_c \approx 60\%$ . It is speculated that a slightly higher value of optimised  $\chi_c$  in micro-sized textures compared to Asahi superstrates is due to the shallow angles of micro-sized textures favouring crack-free growth of nc-Si:H [110]. Therefore, to maximise the performance of nc-Si:H absorbers, the processing window should be closely monitored and controlled. The crystallinity has to be chosen as close to the transition regime as equipment-dependent control and sample-to-sample fluctuations allow.

The optimised processing conditions of a-Si:H and nc-Si:H absorber materials are summarised in Table 2.2. Table 2.3 gives the performance parameters of the best-performing samples obtained from the optimisations discussed in this chapter.

Layer	SiH <sub>4</sub> [sccm]	H <sub>2</sub> [sccm]	$p$ [mBar]	$PD$ [W/cm <sup>2</sup> ]	Thickness [nm]	Deposition rate [Å/s]	$\chi_c$ [%]	$V_{oc}$ [mV]	FF [%]
(i) a-Si:H	6	120	5	0.30	320	4.0	0	934	68.0
(i) nc-Si:H (seed)	1.1	120	4	0.4	90	2.25	90	-	-
(i) nc-Si:H (bulk)	3.2	120	4	0.4	2500	4.82	62	512	70.0

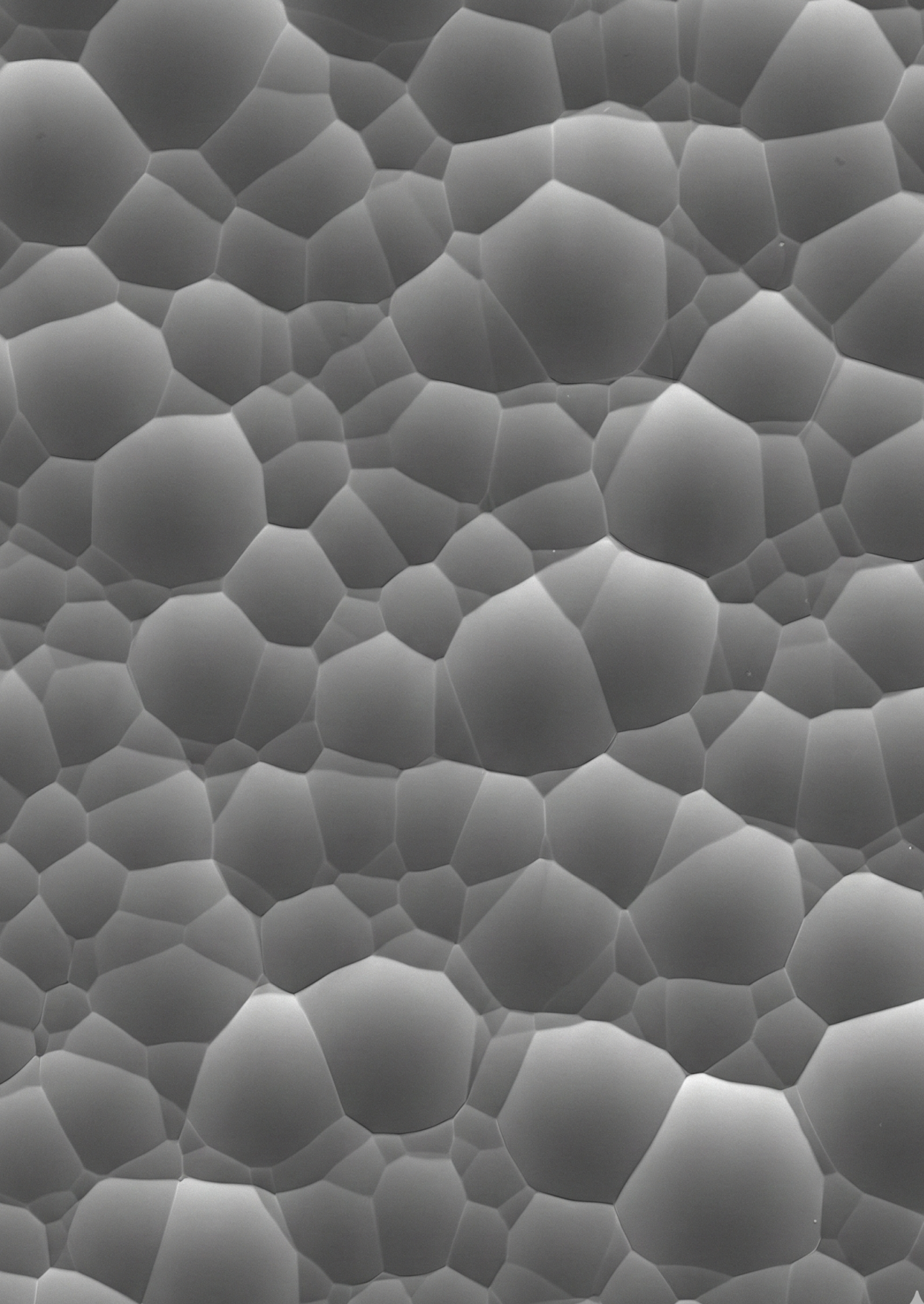
Table 2.2.: Optimised deposition conditions at VHF of different silicon layers in the solar cell. The distance between the RF electrode and the grounded electrode is 13 mm for all p-doped layer depositions, 13 mm for all intrinsic layer depositions, and 21 mm for all n-doped layer depositions.

<i>f</i>	Absorber Material	$\chi_c$ [%]	$V_{oc}$ [mV]	$J_{sc}$ [mA/cm <sup>2</sup> ]	$FF$ [%]	$R_s$ [ $\Omega.cm^2$ ]	$R_p$ [k $\Omega.cm^2$ ]	$\eta$ [%]
RF	Narrow band-gap a-Si:H	0	855	16.0	71.7	13	6.2	9.8
RF	Wide band-gap a-Si:H	0	902	14.6	68.0	17	4.74	8.9
VHF	Wide band-gap a-Si:H	0	934	12.7	68.0	13	4.4	7.9
VHF	nc-Si:H	63	512	25.0	70.0	9	2.42	9.0

Table 2.3.: External parameters of a-Si:H solar cells deposited at RF and VHF chambers. Standard deviation ( $\sigma_d$ ) of measurements are as follows: root-mean-square error of  $J_{sc} = 0.8\%$  (absolute)  $\sigma_d(V_{oc}) \approx 3$  mV,  $\sigma_d(FF) \approx 0.7\%$ ,  $\sigma_d(R_s) \approx 0.2 \Omega.cm^2$ ,  $\sigma_d(R_p) \approx 0.2 k\Omega.cm^2$ .

### 2.3. Conclusion

The fabrication of device-grade nc-Si:H and a-Si:H absorber material is realised in VHF conditions using the same chamber. The performance of nc-Si:H absorber is the best at a crystallinity near the amorphous to nanocrystalline transition regime ( $\chi_c \approx 60$  to 65%). Fine-tuning of this value depends on the surface morphology of superstrates. For a micro-textured glass highest performing cells were made at 40.68 MHz VHF, chamber pressure of 4 mBar, power density of 0.4 W/cm<sup>2</sup>, silane flow of 3.2 sccm and hydrogen flow of 120 sccm (resulting silane concentration: 2.6%). Wide bandgap a-Si:H single junction cells with band gap energy of 1.90 eV,  $V_{oc} = 934$  mV and fill factor of 68% were deposited at VHF conditions, at a pressure of 5 mBar, power density 0.30 W/cm<sup>2</sup>, silane flow 6 sccm, and hydrogen flow 120 sccm (resulting in a silane concentration of 4.8%). These will be used as the standard recipes in this thesis.





# 3

## Thin-film Silicon Solar cells on Superimposed Sacrificial Textured Glass

This chapter is based on the publication:

G. Padmakumar, M. Criel, T. Kashyap, F. Saitta, P. Perez-Rodriguez, R.A.C.M.M. van Swaaij, A.H.M Smets, “Superimposed Sacrificial Texturing to Enhance the Optical Performance in Thin Film Solar Cells”, *Progress in Photovoltaics*, 34, 465–481, 2026 DOI: 10.1002/pip.70046

*Techniques to facilitate excellent optical yield are required to manufacture high-performing solar cells. In thin film solar cells, light scattering with the help of textured interfaces increases the absorption path length of photons and reduces the reflection of the photovoltaic active layer. These textures should also facilitate the growth of crack-free thin film layers, ensuring high efficiency in multi-junction devices. This work explores three texturing methods for glass that have the potential to be integrated into solar cells in a superstrate configuration. A detailed study of sacrificial texturing on glass using i-ZnO (SLT<sub>IZO</sub>) and indium-doped tin oxide (SLT<sub>ITO</sub>) is presented. The optical interaction of these textures is correlated to their root-mean-square (RMS) roughness ( $\sigma_{rms}$ ). It is demonstrated that high optical scattering can be achieved for both SLT<sub>ITO</sub> and SLT<sub>IZO</sub> but at different  $\sigma_{rms}$  regimes. A novel texture with superimposed morphology, named superimposed sacrificial texturing (SIT), is created by combining SLT<sub>ITO</sub> and SLT<sub>IZO</sub> through sequential wet etching. The SIT exhibits exceptional transmission and light scattering properties. Nanocrystalline silicon (nc-Si:H) single-junction solar cells were fabricated in a superstrate configuration to investigate the impact of these textures on indirect bandgap thin-film solar cells. The efficiency of solar cells on SIT is nearly 0.57% and 1.52% (absolute) more than SLT<sub>ITO</sub> and SLT<sub>IZO</sub> solar cells, respectively. By superimposing two textures, solar cells can combine the advantages of enhanced optical performance with high-quality nc-Si:H material growth.*

### 3.1. Introduction

Progress in the conversion efficiencies of photovoltaic (PV) technologies requires a reduction of the fundamental optical, electrical, and thermodynamic conversion loss mechanisms in solar cell devices. The introduction of textured interfaces in PV device architectures is a successful light management technique that improves the optical performance of solar cells. It enhances the PV-active absorption by enhancing the absorption path length of the light [135]. Texturing of interfaces is an integral process step in the manufacturing of various thin-film PV technologies, including CIGS, perovskites, amorphous-nanocrystalline silicon, and wafer-based crystalline silicon (c-Si) PV technologies [136–138]. Thin-film silicon PV devices are often fabricated in a substrate or superstrate configuration. For thin-film PV modules, texturing the front window based on glass in a superstrate configuration or texturing the back reflector in a substrate configuration is typical to maximise light trapping.

The random surface texture and its surface features can be physically characterised by the root-mean-square roughness ( $\sigma_{rms}$ ), lateral correlation length ( $L_{corr}$ ) and aspect ratios (AR) [65]. Random textures exhibit a specific range of feature sizes that determine how the light interacts with the interface between two media (reflection, transmission, and absorption). The nature of the incoherent scattering mechanisms and the coherent refraction of light by these textured interfaces lies in their geometry and dimension in reference to the wavelength ( $\lambda$ ) of the light [65]. The type of interaction is determined by the shape and size ( $S$ ) of a surface feature in reference to the  $\lambda$ . As illustrated in Figure 3.1, Rayleigh scattering scatters light equally forward and backwards, whereas Mie scattering is generally much stronger in the forward direction. For small sizes of surface features and roughness, incoherent Rayleigh scattering ( $S \ll \lambda$ ) and Mie scattering ( $S \sim \lambda$ ) occur. In contrast, coherent refraction at an interface takes place at large ‘macro’-sized features ( $S \gg \lambda$ ) [66]. Since the textures present on the glass must maximise scattering over a broad spectral range (equivalent to the optical response of the thin-film absorber from the UV to the IR region), the shape and dimensions of the texture features should be present accordingly. Different textures, shapes, and sizes must coexist on a surface to maximise the optical gain. This article helps determine the type of texture and which texture sizes result in the highest transmission and light scattering, thereby increasing absorption in a solar cell.

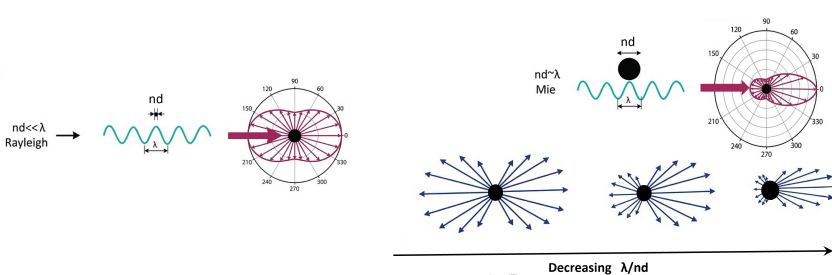


Figure 3.1.: Rayleigh vs Mie scattering. Illustration inspired by [9].

A general challenge for integrating textured interfaces into thin-film PV devices is that texture features may induce inhomogeneities, defects, cracks or pinholes in the PV-active materials. This might deteriorate the film’s electrical quality by enhancing Shockley-Read-Hall recombination of light-excited charge carriers. The relation between substrate roughness and the accompanying additional electrical losses is often reflected in reduced open circuit voltage ( $V_{oc}$ ) and fill factor (FF) of the solar cells as described in detail in [78–82]. This demonstrates that there is a delicate

interplay between increasing optical yield using textured interfaces and preserving electrical performance [12, 83–86].

Glass is an amorphous solid with a random network of silicon and oxygen atoms [139]. The absence of both well-defined lattice structure and a suitable etching process makes glass texturing extremely challenging, especially for large-area applications. Methods such as photolithography [140, 141] and wet etching of sacrificial aluminium [142] or sacrificial transparent conductive oxide (TCO) layers [143, 144] on top of glass substrates are commonly employed to create craters on glass. Photolithography is an expensive and time-intensive process, especially for large-area processing [145]. For wet chemical etching using a sacrificial layer, a polycrystalline TCO layer like indium-doped tin oxide (ITO) [144], aluminium doped zinc oxide (AZO) [146], or gallium doped zinc oxide (GZO) [147] acts as a 'leaking' mask that is partly or wholly removed during a chemical wet-etching process. The etching solution penetrates the easiest through pinholes and pores around grain boundaries in the TCO material [77]. As the sacrificial TCO layer dissolves, the glass is etched inhomogeneously, resulting in a random surface texture. In previous studies, ITO has often been used as a sacrificial TCO layer to add micro-scale texture and AZO as a sacrificial layer to impart nano-scale textures to glass.

To demonstrate the potential of multi-scale features coexisting on glass, a modulated surface texturing (MST) concept was implemented by Isabella *et al.* for substrate configuration. The MST combined etched glass ( $\sigma_{rms} = 200$  nm) with AZO-induced sacrificial textures ( $\sigma_{rms} = 82$  nm) [65]. Later, the MST concept was extended to nano-textures generated with partially etched AZO in a superstrate configuration solar cell device by Tan *et al.* and Yang *et al.* [77, 79, 144]. But these methods had the drawback of parasitic UV light absorption by the retained AZO or ZnO when implemented in a superstrate configuration. This report presents an extensive sample-size study of nano-scale and micro-scale textures for the first time, aiming to determine the design rules for optimal modulated texturing conditions. A novel texturing method is required to address these issues for implementing the MST concept in superstrate thin-film devices. In solar cells, nanocrystalline silicon is an ideal material to illustrate the performance of textures because it behaves as an indirect bandgap material in the spectral range of 800–1100 nm and requires light trapping concepts to enhance the absorption in this wavelength range [44, 46].

This work focuses on undoped zinc oxide (i-ZnO) as a novel sacrificial TCO material for creating small-sized craters on glass. We also explore in detail the conventional method of using ITO as a TCO sacrificial layer to make large-scale textures. In addition, multiple-step etching of the glass is identified as a route to create modulated surface textures at the glass surface. The properties and thickness of the sacrificial TCO layers are varied to make an extensive range of surface features and texture sizes. Through a comprehensive study of this sample set, the relation between light scattering, quantified in terms of diffused transmission ( $T_D$ ) and  $\sigma_{rms}$ , has been revealed. This empirical relation serves as a guideline for developing superimposed textured surfaces (SITs) with a broad spectral range of light scattering. The optical performance of textured glass substrates in solar cells is demonstrated using hydrogenated nanocrystalline silicon (nc-Si:H) single-junction PV devices. The nc-Si:H single-junction solar cell devices are fabricated in a superstrate configuration to compare the impact of all three developed textures on optical and electrical device performance. An identical solar cell architecture is fabricated on flat glass to observe the optical response when light scattering is negligible. The thin-film nc-Si:H absorber layers adopt the morphology of the textured glass when they are processed in a superstrate configuration. It is demonstrated that exceptional optical performance can be combined with good electrical performance using SIT.

## 3.2. Materials and Methods

Corning XG glass, 0.7 mm thick with  $\sigma_{rms} < 10$  nm [148, 149] is used as a substrate throughout this study to develop textures. In the study presented here, two different TCO masking materials have been selected, namely ITO and i-ZnO. Three different texturing approaches are presented in this work: (i) ITO sacrificial layer texturing ( $SLT_{ITO}$ ), (ii) i-ZnO sacrificial layer texturing ( $SLT_{IZO}$ ), and (iii) superimposed sacrificial texturing ( $SIT$ ), which uses both ITO and i-ZnO for texturing. Varying several processing parameters alters the crystallinity ( $\chi_c$ ), density, and thickness of these sacrificial TCO layers, resulting in the creation of textures with different shapes and dimensions [150, 151].

3

### 3.2.1. ITO sacrificial layer texturing - $SLT_{ITO}$

$SLT_{ITO}$  is developed using ITO deposited on glass. A flowchart of the processing method is presented in Figure 3.2. The first five steps represent  $SLT_{ITO}$  texturing. In step 1, Corning XG glass is cleaned in ultrasonic baths of acetone and 2-propanol for 10 minutes each. During step 2, ITO is deposited as a sacrificial TCO layer using magnetron sputtering at elevated temperatures. The properties of the deposited layer are controlled by varying the physical parameters of power, pressure, and temperature [152, 153]. In subsequent steps 3 and 4, the layer deposited on the flat glass is wet-etched. Step 3 is the phase in which the TCO is being etched up to the moment the etchant reaches the glass-TCO interface. Step 4 corresponds to the phase in which both TCO and glass are being etched. During steps 3 and 4, the TCO deposited over the glass is removed and dissolved into the bath, and the textures referred to as  $SLT_{ITO}$  are visible on the glass surface. The etchant solution used in this study is HF(40%): H<sub>2</sub>O<sub>2</sub>(31%): H<sub>2</sub>O in the ratio 1:2:10. After step 4, the textured samples are cleaned by dipping in HNO<sub>3</sub>(69.9%) for 3 minutes (step 5). This step removes any possible remaining ITO residues.

**Design of experiment:** To vary the properties of the ITO layer, the deposition conditions are varied over different combinations of RF power, temperature, and thickness. The deposition temperature ranges between 200 °C and 300 °C. Deposition power density varies between 1.35 W/cm<sup>2</sup> and 2.45 W/cm<sup>2</sup>. The thickness of the deposited ITO layer ranged from 150 nm to 400 nm. In this specified range of deposition conditions, 35 different conditions have been explored to create different  $SLT_{ITO}$  textures.

### 3.2.2. i-ZnO sacrificial layer texturing - $SLT_{IZO}$

A similar approach as in section 3.2.1 is employed for  $SLT_{IZO}$ . The flowchart of the processing method is given in Figure 3.2 steps 1 to 5. During step 2, an i-ZnO layer is deposited as a sacrificial layer using magnetron sputtering. These layers are subsequently wet-etched using a HF (40%) solution and HNO<sub>3</sub> (69.9%) solution in a 1:8 ratio in steps 3 and 4. The residual TCO is cleaned by dipping in HNO<sub>3</sub> (69.9%) for 3 minutes in step 5.

**Design of experiment:** The i-ZnO layer deposition temperature varies between 25 °C and 400 °C. The deposition power density varies between 0.5 W/cm<sup>2</sup> and 4.0 W/cm<sup>2</sup>. The resulting thickness of i-ZnO is between 120 nm and 300 nm. 26 conditions were explored within this specified range of deposition conditions.

### 3.2.3. Superimposed sacrificial texturing - $SIT$

$SIT$  is developed by superimposing  $SLT_{IZO}$  on  $SLT_{ITO}$  using two cycles (step 1-5 and step 6-10) of sacrificial etching as shown in Figure 3.2 in sequence. For this, the deposition conditions

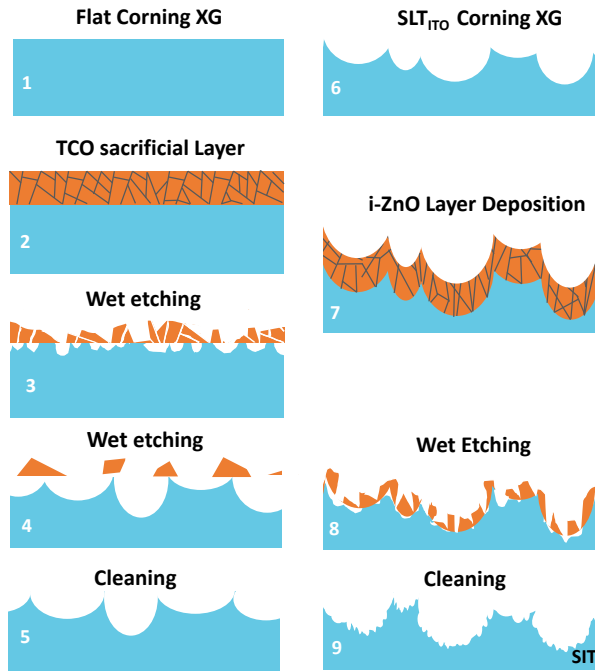


Figure 3.2.: Flowchart of the sacrificial texturing approach. steps 1-5 are the development of  $SLT_{ITO}$  or  $SLT_{IZO}$  depending on the TCO layer. Steps 6-9 are representations of the superposition of  $SLT_{IZO}$  over  $SLT_{ITO}$ . The processing steps 1–9 are referenced in the text. Step 3 illustrates an intermediate phase that occurs shortly after the etchant has reached the glass, and Step 4 shows the result after the required time has elapsed, resulting in craters and the complete removal of the sacrificial layer.

resulting in the highest diffused transmission  $SLT_{ITO}$  and  $SLT_{IZO}$  (will be discussed in Section 3.3.2) were utilised to make  $SIT$ . In step 2 (first cycle),  $SLT_{ITO}$  sacrificial layer of 360 nm thickness is deposited at 230 °C temperature and 2.1 W/cm<sup>2</sup> power density on cleaned glass. This is subsequently etched as mentioned in section 3.2.1 to make craters of  $SLT_{ITO}$  (steps 3 to 5). In step 7, during the second cycle, a 140 nm thick layer of i-ZnO is deposited at 200 °C, 4 W/cm<sup>2</sup>, and 2.6 micro bar pressure on the textured side of  $SLT_{ITO}$ . This is followed by wet etching (step 8) of the i-ZnO layer by similar processes explained in section 3.2.2. The residual TCO layers were removed, and samples were cleaned by dipping in HNO<sub>3</sub> (69.9%) for 3 minutes (step 9).

The textures made and their summary of characterisation techniques are given as a flow chart in Figure 3.3. The characterisation methods are detailed in the upcoming sections.

### 3.2.4. Characterisation of textures

Atomic Force Microscopy (AFM) is carried out to examine the surface morphology of developed textures using a Bruker AFM FastScan in the FastScan closed-loop scanner head modus.

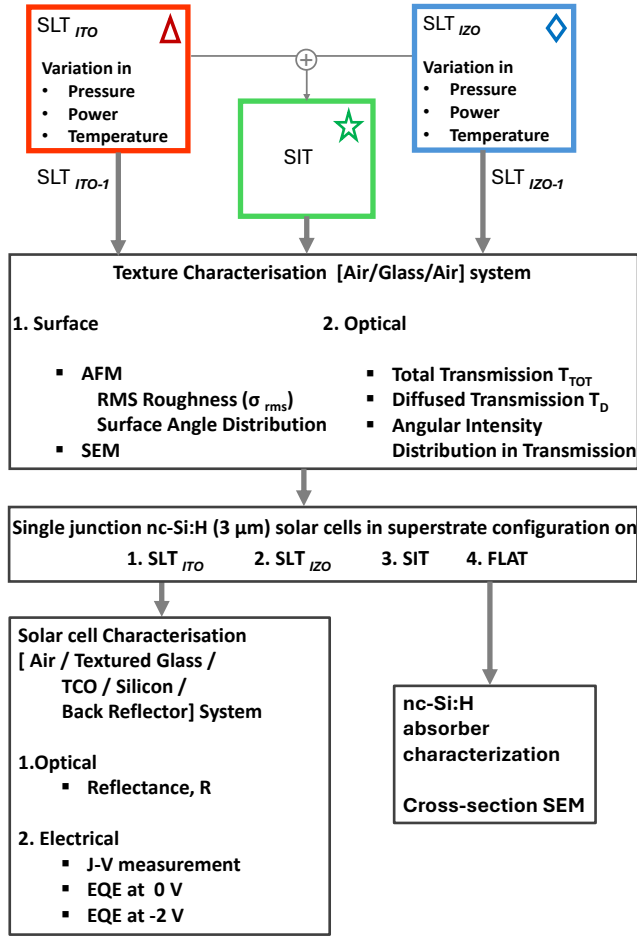


Figure 3.3.: Flow chart representing the design of the experiment and characterisation steps.

Scanning sizes of a  $16 \mu\text{m} \times 16 \mu\text{m}$  and a  $30 \mu\text{m} \times 30 \mu\text{m}$  were chosen for analyzing the differently sized textures. In cases when small area scans ( $16 \mu\text{m} \times 16 \mu\text{m}$ ) were not enough to capture all typical feature sizes and their fractal nature, larger area scans were opted for ( $30 \mu\text{m} \times 30 \mu\text{m}$ ). The surface parameters  $\sigma_{rms}$ , Power Spectral Density (PSD), and slope distribution were extracted from the AFM data using the NanoScope Analysis software from Bruker. PSD is used to represent the morphology of textures quantitatively. PSD of the height variation on the surface is a spatial frequency (in  $\mu^{-1}$  units) representation of the surface based on a discrete 2-dimensional Fourier transform of the height-height correlation function [154, 155]. NanoScope analyses the surface slopes based on the normalised occurrence distribution of angles subtended by surface vectors with the vertical plane. Further, the textures were analysed for their increase in effective surface area, which is defined as the ratio (in percentage) of the real surface area of the texture to the projected area. The effective surface area analysis is completed using Gwyddion software

(version 2.63). In addition, the surface textures have been analysed using Scanning Electron Microscopy (SEM) with a Hitachi Regulus 8230 at an acceleration voltage of 1.5 kV.

To characterise textures optically, the transmission of all glass samples was measured with probing light on the flat side as shown in Figure 3.4(a). Optical transmission measurements were performed using a LAMBDA 1050+ UV/ Vis/ NIR Spectrophotometer equipped with a 150 mm InGaAs integrating sphere from PerkinElmer. The Angular Intensity Distribution (AID) of transmitted light was examined using the 180 mm automated reflectance/ transmittance analyser (ARTA22) accessory on a LAMBDA 950 PerkinElmer unit. Measurement methods of AID for transparent objects can be found in [156, 157]. The percentage of light transmitted in any direction other than normal is quantified as diffused transmittance ( $T_D$ ).  $T_D$  values at different wavelengths were considered the prime metric for quantifying the optical scattering performance of the textured glass in this work.

### 3.2.5. Solar cells on textures

Finally, the impact of textures on the optical and electrical performance of solar cells, as well as their effect on absorber crystal growth, was investigated. Solar cells were made on selected substrates of *SLTITO*, *SLTIZO*, *SIT*, and also on non-textured Corning XG glass (FLAT) for reference. Hydrogenated nano-crystalline silicon (nc-Si:H) single p-i-n junction solar cells were made in a superstrate configuration with an area of 5 mm × 5 mm. The solar cell architecture is shown in Figure 3.4(b).

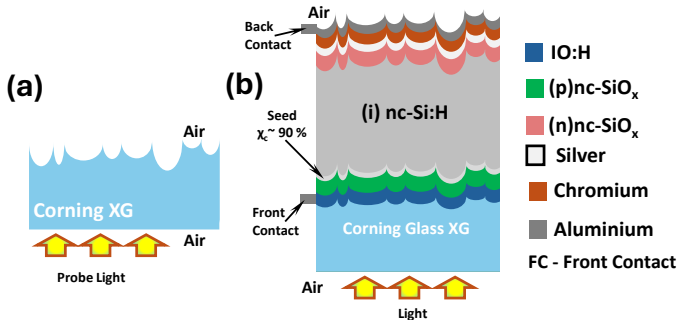


Figure 3.4.: (a) Representation of air/ textured glass/ air system probed from the flat side. (b) Schematic diagram of a 5 mm × 5 mm solar cell made on a glass superstrate configuration. Probing direction is also shown for the air/ textured glass/ IOH/ silicon solar cell/ back reflector system.

The solar cells have hydrogenated indium oxide (IOH) as the front electrode TCO. IOH is RF magnetron sputtered from a ceramic indium oxide ( $\text{In}_2\text{O}_3$ ) target in  $\text{Ar}/\text{O}_2/\text{H}_2\text{O}$  mixtures. The introduction of water vapour prevents crystalline growth of IOH, and the resulting IOH deposited at room temperature is amorphous [158, 159]. This choice of IOH is made because it is flat by nature and omits the possibility of any added roughness and light scattering by TCO grains [160, 161]. The silicon alloy deposition was done on a Plasma-Enhanced Chemical Vapour Deposition (PECVD) multi-chamber tool with dedicated processing chambers for the boron-doped hydrogenated nano-crystalline silicon oxide p-layer (B-doped (p)nc-SiO:H), intrinsic hydrogenated nanocrystalline silicon ((i)nc-Si:H) and phosphorus-doped hydrogenated nano-crystalline silicon oxide n-layer ((n)nc-SiO:H). The B-doped nc-SiO:H layer (16 nm thick)

and p-doped nc-SiO:H n-layer (20 nm thick) were deposited using radiofrequency (13.8 MHz) in the PECVD tool at 180 °C substrate temperature and using B<sub>2</sub>H<sub>6</sub> and PH<sub>3</sub> as dopant gasses, respectively. The (i)nc-Si:H absorber layer was deposited at very high frequency (40.68 MHz) at 170 °C substrate and deposition rate of 4.9 Å/s. The solar cells have a back reflector consisting of sputtered i-ZnO (60 nm) and an evaporated silver (300 nm) layer. The front contact is an aluminium strip with a thickness of 500 nm, and the back contact consists of chromium (30 nm) and aluminium (500 nm). The solar cell area is defined by 5 mm × 5 mm squares. This results in a solar cell structure of IOH (150 nm) / (p)nc-SiO:H (16 nm) / (i)nc-Si:H (3000 nm) / (n)nc-SiO:H (20 nm) / i-ZnO (60 nm) / Ag (300 nm). No external front anti-reflective coatings were applied to the solar cells presented in this study.

The specific deposition parameters are included in Table 3.1. The deposition rates, refractive indices (n), and extinction coefficients (k) of the mentioned layers (except the nc-Si:H absorber) were measured using spectroscopic ellipsometry, and the data are included in the Appendix Figure A.3. The deposition parameter optimisation of the 3200 nm thick nc-Si:H bulk photoactive layer is conducted on micro-textured glass, with  $\chi_c$  as the optimised parameter. The deposition conditions are optimised to attain a  $\chi_c$  between 55% and 65% to ensure the use of high-quality material [96, 98, 101]. The deposition rate of nc-Si:H was determined with SEM cross-section imaging. The n and k values of nc-Si:H are determined by postprocessing spectroscopic ellipsometry measurements through the effective medium approximation method.

Layer	SiH <sub>4</sub> [sccm]	H <sub>2</sub> [sccm]	Dopant Gas [sccm]	CO <sub>2</sub> [sccm]	Pressure [mBar]	Power [W/cm <sup>2</sup> ]	Elec. Gap [mm]	Depo. rate [Å/s]
(p)nc-SiO:H	0.8	170	10 0.02% B <sub>2</sub> H <sub>6</sub> in H <sub>2</sub>	1.2	2.2	0.12	13	0.33
(i)nc-Si:H (seed)	1.1	120	-	-	4	0.4	13	2.3
(i)nc-Si:H (bulk)	3.2	120	-	-	4	0.4	13	4.9
(n)nc-SiO:H	1	170	2 2% PH <sub>3</sub> in H <sub>2</sub>	1.6	1.5	0.11	21	0.16
TCO	Ar [sccm]		H <sub>2</sub> O PP		Pressure [μBar]	Power	T <sub>sub</sub> °C	Depo. Rate [Å/s]
IOH (Front electrode)	50	-	0.06	-	5.7	1.5	27	0.98
i-ZnO (Back Reflector)	20	-	-	-	2.6	2.0	130	0.87

Table 3.1.: Deposition conditions of different layers in the solar cell. PP is the partial pressure.

The  $V_{oc}$  and  $FF$  of solar cells were measured by a WACOM-class AAA xenon-halogen dual lamp continuous AM1.5G spectral simulator at 25 °C. The short-circuit current density ( $J_{sc}$ ) values were calculated based on the external quantum efficiency (EQE) measurement of solar cells ( $J_{sc,EQE}$ ).

This helps to prevent the effect of any mismatch between the solar simulator spectrum and the AM1.5 spectrum. Also, it eliminates any overestimation of current caused by errors in estimating the active cell area in small-area solar cells. EQE measurement is conducted at a short-circuit condition of 0 V and a reverse bias condition of -2 V. The total reflection of the solar cell is also recorded, with the help of LAMBDA 1050+ UV/Vis/NIR Spectrophotometer with a 150 mm InGaAs integrating sphere from PerkinElmer.

### 3.3. Results and Discussion

Sacrificial layers of TCOs, each different from the others, were deposited on flat glass and etched to develop random textures on the glass using the sacrificial method successfully. When observed under SEM, the i-ZnO exhibits a columnar crystal growth, whereas ITO exhibits bulky growth for its crystals, as shown in Figure 3.5. Wet etching of ITO and i-ZnO sacrificial layers deposited by varying power, pressure and temperature produced surface textures over a wide range of  $\sigma_{rms}$  values. In the upcoming sections, the discussions will be based on two optical systems: (i) air/glass/air and (ii) air/glass/IOH/nc-Si:H solar cell/silver. The former system provides insights into the physical and optical behaviour of developed textures, while the latter offers conclusions on their impact when employed in a solar cell. The optical properties of textures in one system are not one-to-one translatable to the other because the Fresnel reflection and transmission coefficients differ. Additionally, the system (ii) exhibits multiple reflections at the interfaces.

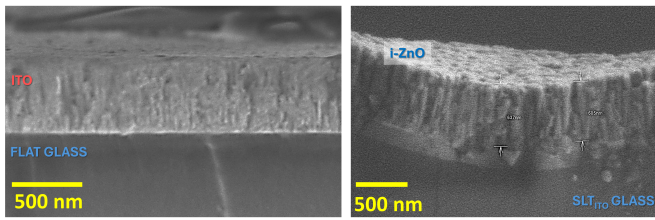


Figure 3.5.: ITO and i-ZnO crystal structure observed with SEM on flat glass. ITO demonstrates a bulky growth on glass while i-ZnO has a columnar growth of the crystals.

#### 3.3.1. Physical characterisation of $SLT_{ITO}$ , $SLT_{IZO}$ and $SIT$

The shape of craters made using the sacrificial texturing method was observed with SEM and AFM. Data of  $SLT_{ITO}$ ,  $SLT_{IZO}$  and  $SIT$  samples are shown in Figure 3.6, 3.7, and 3.8, respectively. The image suggests that  $SLT_{ITO}$  possesses sharp boundaries with a polygonal shape on the glass surface, compared to  $SLT_{IZO}$ , which has more circular borders. Another interesting visual observation is that  $SLT_{ITO}$  possesses a larger fraction of hexagon-shaped craters, whereas  $SLT_{IZO}$  has a larger fraction of tetragon- and pentagon-shaped craters.  $SIT$  was successfully made by wet etching i-ZnO layer deposited on  $SLT_{ITO}$  texture. Upon executing this sequential etching step on  $SLT_{ITO}$ , a superimposed version of craters is identified on the glass surface as shown in Figure 3.8. This is made possible as the sputtered i-ZnO films have more frequent boundaries compared to ITO to act as a 'leaking mask'. This columnar structure of i-ZnO allows multiple paths for the etchant to reach the glass surface and create craters within the large craters

of  $SLT_{ITO}$ . This phenomenon occurs uniformly across the entire surface. Multiple leak paths for the chemical also result in a quicker removal of the deposited i-ZnO mask (in comparison with ITO) from the surface, which also limits the depth of  $SLT_{IZO}$  craters (compared to  $SLT_{ITO}$ ).

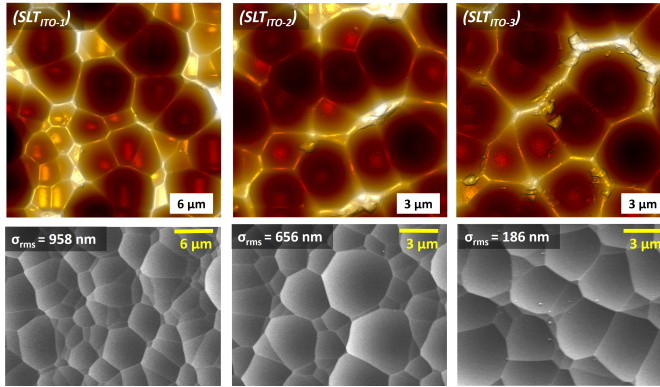


Figure 3.6.: AFM images (top row) and SEM image (bottom) of  $SLT_{ITO}$  samples. From left to right, the samples have a decrease in  $\sigma_{rms}$  and are named as  $SLT_{ITO-1}$ ,  $SLT_{ITO-2}$ ,  $SLT_{ITO-3}$ . N.B. Area of  $SLT_{ITO-2}$  and  $SLT_{ITO-3}$  is  $16 \mu\text{m} \times 16 \mu\text{m}$  and  $SLT_{ITO-1}$  is a  $30 \mu\text{m} \times 30 \mu\text{m}$ .

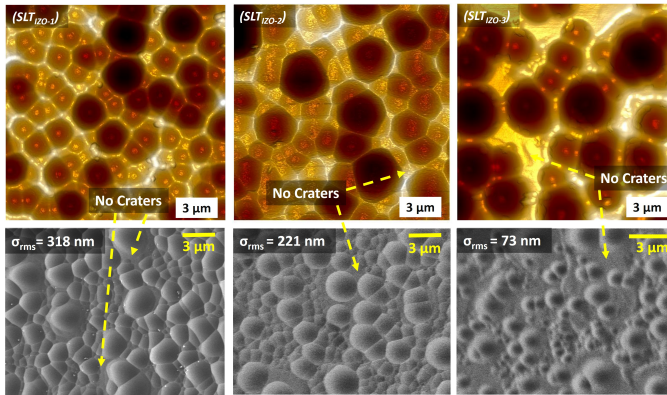


Figure 3.7.: AFM images of  $SLT_{IZO}$  samples (top row), and SEM image of  $SLT_{IZO}$  samples. From left to right, the samples are named as  $SLT_{IZO-1}$ ,  $SLT_{IZO-2}$ ,  $SLT_{IZO-3}$  indicating decrease in  $\sigma_{rms}$  and an increase in flat regions.

The surface profiles extracted from AFM data of the samples  $SLT_{ITO-1}$ ,  $SLT_{IZO-1}$ ,  $SIT$  are given in Figures 3.9 (a), (b) and (c), respectively. To visualise the signature shape of craters in 3 dimensions (3D), an isometric view ( $15 \mu\text{m} \times 15 \mu\text{m}$ ) of surfaces is shown in the inset. The isometric view for  $SLT_{ITO}$  (Figure 3.9 (a)) shows an ‘inverted U’ shape, suggesting that it resembles spherical sectors. The surface craters of  $SLT_{IZO}$  (Figure 3.9 (b)) show an ‘inverted V’ shape at the edge, suggesting the dips resemble inverted cones. While adding the surface morphologies,  $SLT_{ITO}$

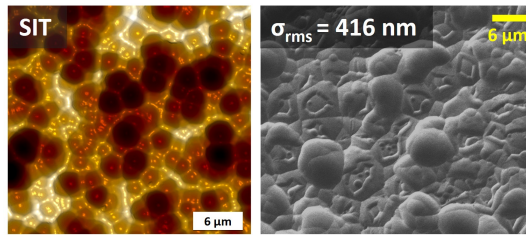


Figure 3.8.: AFM data (left) and SEM images (right) of *SIT*.

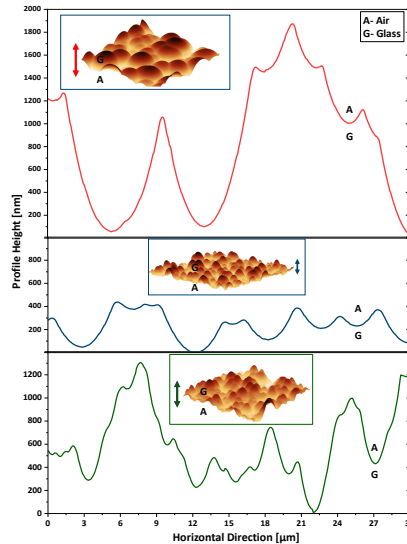


Figure 3.9.: Surface profile over 30  $\mu\text{m}$  length (all graphs in the same scale) of **top:** *SLT<sub>ITO-1</sub>* sample, **middle:** *SLT<sub>IZO-1</sub>* sample, **bottom** *SIT* sample and their isometric views (inset). The surface is the glass (G)/air (A) interface, with media as indicated for each image. N.B. The inset images are flipped vertically to display their features.

accommodates small cones of *SLT<sub>IZO</sub>* in its wide spherical craters to form *SIT* (Figure 3.9 (c)-inset). Interestingly, the *SIT* maintains the polygonal-shaped borders inherited from *SLT<sub>ITO</sub>* on its surface. The amplitude of the extracted profile of the *SLT<sub>IZO</sub>* sample is 0.5  $\mu\text{m}$ , and that of *SLT<sub>ITO</sub>* is 2  $\mu\text{m}$ . The second etching step in *SIT* fabrication reduces the amplitude of *SIT* to 1.3  $\mu\text{m}$  from the high amplitude of *SLT<sub>ITO</sub>*. After etching, the textures show an increase in effective surface area by 8.0% for *SLT<sub>ITO</sub>*, 2.5% for *SLT<sub>IZO</sub>* and 6.8% for *SIT* when compared to FLAT.

### 3.3.1.1. Slope distribution of the surfaces

Slope analysis of the textures obtained from their respective AFM scans is given in Figure 3.10. The conical shape of *SLT<sub>IZO</sub>* results in a concentrated slope distribution in the range  $0^\circ$  to  $38^\circ$  (*maximum*  $\approx 7^\circ$ ) in contrast to spherical sector-like *SLT<sub>ITO</sub>* with wider angle distribution

from  $0^\circ$  to  $55^\circ$  ( $maximum \approx 16^\circ$ ). Upon superimposition, the slope distribution of *SIT* resembles the shape of the slope distribution of *SLT<sub>ITO</sub>*, but at the same time shows a shift in peak. The range of surface slope for *SIT* is determined by the largest-sized textures (of *SLT<sub>ITO</sub>*), whereas covering the whole area by small conical features (of *SLT<sub>IZO</sub>*) shifts the peak occurrence value to the left ( $maximum \approx 12^\circ$ ). The texture regions contributing to shallow angles (taken as  $12^\circ$  here) are depicted in Figure 3.11. The wider shallow angle region (greyscale) at crater boundaries of *SIT* compared to *SLT<sub>ITO</sub>* implies that the sharp peaks of *SLT<sub>ITO</sub>* are marginally rounded in *SIT* during the second etching step.

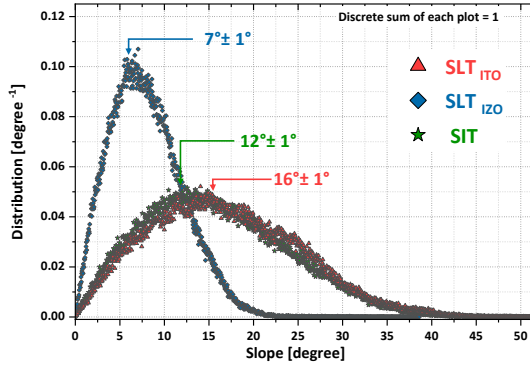


Figure 3.10.: Surface normal distribution curves of *SLT<sub>ITO</sub>*, *SLT<sub>IZO</sub>* and *SIT* in terms of angle. The occurrence value is normalised such that the total of each curve adds up to 1. Different angle ranges are identified in the Appendix Figure A.1.

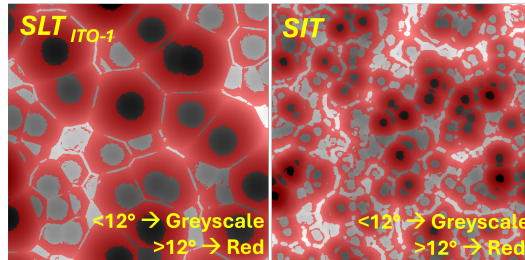


Figure 3.11.: Surface angle distribution of *SLT<sub>ITO</sub>* and *SIT*. The occurrence of angles less than and greater than  $13^\circ$  is specified. The areas of both AFM scans are  $30 \mu\text{m} \times 30 \mu\text{m}$ .

### 3.3.1.2. PSD analysis of the textures

Figure 3.12 is a PSD analysis of three surfaces *SLT<sub>ITO-1</sub>*, *SLT<sub>IZO-1</sub>* and *SIT*. PSD is plotted against spatial frequency (in units of  $\mu\text{m}^{-1}$ ). The PSD of a texture at low frequencies (Zone 1) characterises the features with large lateral and vertical dimensions. The high-frequency (Zone 2)

represents small-scale texture features. The influence of feature sizes on light scattering has been widely discussed with PSD as a tool [65, 162]. It is ideal to have features from both Zone 1 and Zone 2 in a solar cell, enabling light scattering across a broad wavelength range. Spectrum scattering by the discussed features in Zone 1 is coherent scattering, which can be understood using ray optics models. Whereas Zone 2 features (where  $S \leq \lambda$ ) can be understood with Mie scattering and incoherent diffraction [65, 163]. The highest occurrence for large features is for  $SLT_{ITO}$ , and the lowest is for  $SLT_{IZO}$ . This implies that the scattering mechanism of  $SLT_{ITO}$  is predominantly coherent refraction. The small features occur the most in  $SIT$ , followed by  $SLT_{IZO}$ . The fact that  $SIT$  has most small-scale features is highly likely a combined result of small textures inherited from  $SLT_{IZO}$  and pre-existing crater boundaries of  $SLT_{ITO}$ . This also implies that  $SIT$  is not a perfect superposition of  $SLT_{IZO}$  and  $SLT_{ITO}$ . These observations predict that  $SIT$  can be active in interacting with light over the wide range of spectrum from 300-1100 nm.

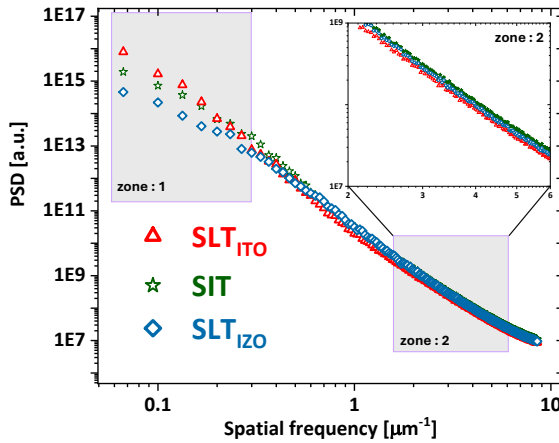


Figure 3.12.: PSD function versus spacial frequency of  $SLT_{ITO-1}$ ,  $SLT_{IZO-1}$  and  $SIT$ . Zone 1 corresponds to large feature sizes, and Zone 2 corresponds to small feature sizes.

### 3.3.1.3. Roughness of the textures

Due to the self-affinity of the random textured surfaces, general fractal scaling laws show that the scan size needs to be much larger than the typical feature sizes ( $L \gg S$ ) to accurately determine  $L_{corr}$  [164]. The AFM scan size is smaller than the required size for features considered in this work. Therefore, in the remainder of this article, we will plot the optical properties as a function of  $\sigma_{rms}$  to demonstrate the empirical relation between parameters.

For  $SLT_{ITO}$ , the obtained  $\sigma_{rms}$  value ranges from 186 to 1124 nm. SEM images (Figure 3.6) imply that the cause of the increase of  $\sigma_{rms}$  for  $SLT_{ITO}$  is a result of the increased crater depths. For  $SLT_{IZO}$ , the attained  $\sigma_{rms}$  value ranges between 73 nm and 336 nm. Also,  $SLT_{IZO}$  can result in flat regions on the glass, which can reduce its  $\sigma_{rms}$  (Figure 3.7,  $SLT_{IZO-3}$ ). A wide range of  $\sigma_{rms}$  values across  $SLT_{IZO}$  samples explicitly shows that the variation in i-ZnO's deposition conditions can be used to tune the texture properties. This is similar to observations on nano-scale sacrificial texturing using AZO layers [143, 144]. The  $\sigma_{rms}$  of  $SIT$  determined from

the 2D AFM scan area  $30 \mu\text{m} \times 30 \mu\text{m}$  is  $416 \text{ nm}$ . This  $\sigma_{rms}$  is intermediate to the roughness of its two constituent morphologies.

### 3.3.2. Diffused transmission of $SLT_{ITO}$ , $SLT_{IZO}$ and $SIT$

**$T_D$  data of  $SLT_{ITO}$ :** In Figure 3.13,  $T_D$  for each  $SLT_{ITO}$  sample is shown as the percentage of total transmitted light. The diffusivity of transmitted light gradually increases with  $\sigma_{rms}$  for  $\sigma_{rms} < 500 \text{ nm}$ . For  $500 \text{ nm} < \sigma_{rms} < 800 \text{ nm}$ , there is a steeper increase in  $T_D$ .  $T_D$  saturates for  $\sigma_{rms} > 950 \text{ nm}$ . Three samples of  $SLT_{ITO}$ , namely  $SLT_{ITO-1}$ ,  $SLT_{ITO-2}$ , and  $SLT_{ITO-3}$ , are marked on the plot  $T_D$  vs  $\sigma_{rms}$ . The mechanism of scattering in  $SLT_{ITO}$  is refractive - governed by the refractive properties of the medium at the interface. For this reason, deep textures like  $SLT_{ITO-1}$  effectively scatter light. Whereas, for  $SLT_{ITO-3}$  with shallow craters, the diffusivity is limited.

The observed  $T_D$  for  $SLT_{ITO-1}$  at  $\lambda = 400 \text{ nm}$ ,  $600 \text{ nm}$ ,  $800 \text{ nm}$ ,  $1000 \text{ nm}$  are 84%, 80%, 79% and 78% respectively.  $SLT_{ITO-1}$  was made from a  $360 \text{ nm}$  thick sputtered ITO sacrificial layer deposited at a temperature of  $230^\circ\text{C}$ , power density of  $2.1 \text{ W/cm}^2$ , chamber pressure  $16 \text{ micro bar}$  and an argon flow of  $45 \text{ sccm}$ .

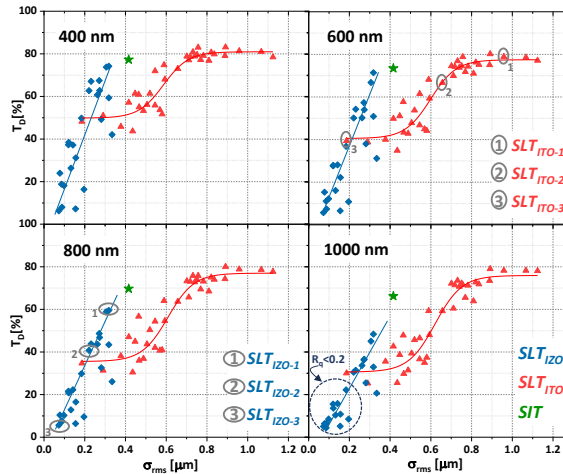


Figure 3.13.: Diffused Transmittance values in percentage of different sacrificial textures,  $SLT_{ITO}$  (red and triangle),  $SLT_{IZO}$  (blue and diamond), and  $SIT$  (green and star) at wavelengths  $400 \text{ nm}$ ,  $600 \text{ nm}$ ,  $800 \text{ nm}$ , and  $1000 \text{ nm}$ . The lines are a guide to the eye.

**$T_D$  data of  $SLT_{IZO}$ :**  $T_D$  values for each  $SLT_{IZO}$  sample were recorded as the percentage of total transmitted light in Figure 3.13. The increase in  $T_D$  is monotonous with the increase in  $\sigma_{rms}$ . Three samples of  $SLT_{IZO}$ , namely  $SLT_{IZO-1}$ ,  $SLT_{IZO-2}$ , and  $SLT_{IZO-3}$  are highlighted in the data plot in Figure 3.13. The scattering mechanism in  $SLT_{IZO}$  is mainly incoherent diffraction, which is related to the S of texture. The best scatterers in the set of  $SLT_{IZO}$  samples are glass samples with uniformly distributed and well-developed craters, similar to those in  $SLT_{IZO-1}$ . The small  $\sigma_{rms}$  samples like ( $SLT_{IZO-3}$ ) have intermediate regions without any craters (as observed in Figure 3.7). This explains the limited scattering ability of  $SLT_{IZO-3}$  over all  $\lambda$ .

In this experiment, the highest value of  $T_D$  is attained at  $\sigma_{rms} = 318 \text{ nm}$ . This sample -  $SLT_{IZO-1}$ , was etched from the glass with a  $140 \text{ nm}$  thick layer of i-ZnO deposited at  $200^\circ\text{C}$ , 4

$W/cm^2$ , 2.6 micro Bar pressure and 20 sccm argon flow. The  $T_D$  values are 75%, 71%, 67%, and 55% at  $\lambda=400$  nm, 600 nm, 800 nm, and 1000 nm, respectively.

**$T_D$  of  $SIT$ :** The data point at  $\sigma_{rms} = 416$  nm in Figure 3.13 (the green star) represents  $T_D$  of  $SIT$ . The processing conditions of the ITO layer and the i-ZnO layer in  $SIT$  correspond to those of  $SLT_{ITO-1}$  and  $SLT_{IZO-1}$ , respectively.  $SIT$  displays a  $T_D$  higher than all  $SLT_{IZOs}$  but lower than the best  $SLT_{ITOs}$ .

Figure 3.13 demonstrates that at  $\lambda = 400$  nm, 600 nm, 800 nm, and 1000 nm,  $SIT$  diffuses 77%, 73%, 70%, and 66% of transmitted light, respectively.  $SIT$  at relatively small  $\sigma_{rms}$  shows a high  $T_D$  which is nearly equal to  $T_D$  of  $SLT_{ITO-1}$ . For  $\lambda=400$  and 600, the data point of  $SIT$  appears similar to an extrapolated point of  $SLT_{IZO}$ , suggesting a scattering mechanism similar to  $SLT_{IZO}$ . For  $\lambda > 600$ ,  $SIT$  shows a minor drop in  $T_D$  - a behaviour similar to  $SLT_{ITOs}$ .

In the upcoming sections, names  $SLT_{ITO}$  and  $SLT_{IZO}$  refer to the sample with the highest observed  $T_D$  of the set, i.e.,  $SLT_{ITO-1}$  and  $SLT_{IZO-1}$ , respectively.

### 3.3.3. AID of $SLT_{ITO}$ , $SLT_{IZO}$ and $SIT$

AID of  $SLT_{ITO}$ ,  $SLT_{IZO}$ , and  $SIT$  for four different  $\lambda$  are compared in Figures 3.14.  $SLT_{ITO}$  scatters the light over wider angles for all  $\lambda$  compared to  $SLT_{IZO}$  and  $SIT$ . AID of  $SLT_{ITO}$  is the highest for near infrared ( $\lambda = 850$  nm) and red ( $\lambda = 700$  nm), where the wavelength is comparable to  $\sigma_{rms}$  of  $SLT_{ITO}$ .  $SLT_{IZO}$  shows the highest AID for  $\lambda = 400$  nm, where  $\lambda$  is comparable to its  $\sigma_{rms}$ . The scattered light intensity for  $\lambda = 850$  nm steeply drops beyond 40 °angles and reaches zero at 65 °. The diffractive scattering nature of  $SLT_{IZO}$  is the reason for the quick drop of  $T_D$  for  $\lambda = 850$  nm. This same effect is also observed in Figure 3.13 in the form of accumulated data points for  $\lambda = 800$  nm and 1000 nm at  $\sigma_{rms} < 0.2$  (highlighted with a circle in the graph).  $SIT$  exhibits an intermediate AID of its constituent textures. The diffused transmittance trends in Figure 3.15 also demonstrate the same.  $SIT$  exhibits good angular scattering for  $\lambda = 400$  nm and 850 nm, presumably because the constituent features of  $SLT_{ITO}$  and  $SLT_{IZO}$  are closest comparable to these values.

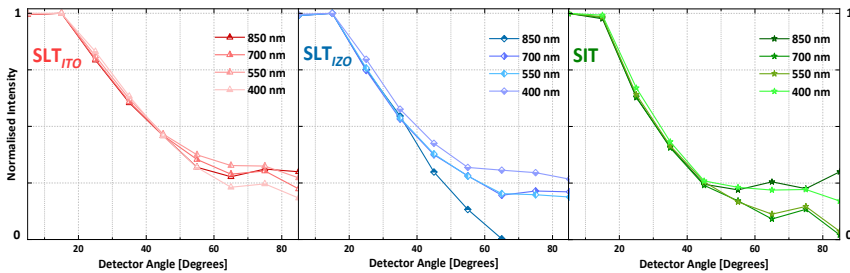


Figure 3.14.: Angle dependent transmission properties of  $SLT_{ITO}$ ,  $SLT_{IZO}$ , and  $SIT$ : (a) Normalised intensity as a function of scattering angles (5° to 85°). Normalisation is performed with respect to the maximum intensity. N.B. To interpret intensity normalised AID graphs of a specific texture at a particular wavelength, use the corresponding  $T_D$  [%] values of that texture at that wavelength in Figure 3.15.

### 3.3.4. Total transmission of $SLT_{ITO}$ , $SLT_{IZO}$ and $SIT$

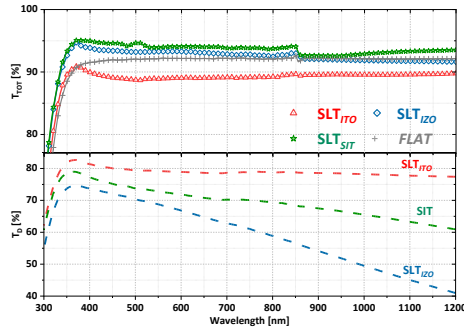


Figure 3.15.: Total transmission spectra (solid line with symbols) and diffused transmission spectra (dashed lines) of  $SLT_{ITO}$ ,  $SLT_{IZO}$  and  $SIT$ .

The total transmission ( $T_{TOT}$ ) spectra (solid line with symbols) and diffused transmission spectra (dashed line) of different textures when probed from the flat side are shown in Figure 3.15.  $SLT_{ITO}$  (red curve) shows a lower transmission for all wavelengths compared to FLAT. This suggests that when we introduce a texture with  $S \gg \lambda$  on a flat glass, the transmission at the glass/air interface of the sample decreases. The light incoming from the non-textured side of the glass interacts with the curved interface of  $SLT_{ITO}$  as “locally flat” due to its feature diameter. The interaction of micro-textured glass at this interface follows coherent reflection and obeys Fresnel’s relations of reflection coefficients for light entering an optically rarer medium at angles  $> 0^\circ$  [9]. With an increased surface area, this texture reflects more light than a flat surface. Interestingly, a weak interference fringe appears for all  $SLT_{ITO}$  samples around 350 nm, which is absent in the transmission measurement of FLAT. The small textures of  $SLT_{IZO}$  reduce reflection at the glass/air interface when compared to FLAT. For  $SLT_{IZO}$ , the small features ( $S \sim \lambda$ ) aid in breaking the coherence at the glass/air interface. The light scattering is based on incoherent diffraction and follows the Mie scattering mechanism. The total transmission of  $SLT_{IZO}$  is greater than that of both  $SLT_{ITO}$  and FLAT. When the small features of  $SLT_{IZO}$  are superimposed over  $SLT_{ITO}$ , a diffractive nature is added to the optical response. The resultant surface (i.e.,  $SIT$ ) no longer acts as “locally flat” (in comparison with  $SLT_{ITO}$ ). As observed in Figure 3.12 Zone 2,  $SIT$  possess the highest amount of small-scale features among the three textures. For  $SIT$ , the incoherent diffraction scattering dominates the transmission mechanism and as a result,  $SIT$  exhibits the highest transmission spectrum among the three textures.

The interaction of light with textures is determined by their  $\sigma_{rms}$ , surface vector angles, and crater shapes. These observations suggest that to combine two textures, the large and small craters should have distinct, well-defined roughness ranges for which they perform best individually. These ranges must belong to optically refractive and diffractive regimes. As observed in this work, optically, this approach yields the least reflectance while also facilitating effective light diffusion.

### 3.3.5. Solar cells on textures

The performances of nc-Si single-junction solar cell devices fabricated on  $SLT_{ITO}$ ,  $SIT$  and  $SLT_{IZO}$  in superstrate configuration are compared. A solar cell is also made on FLAT as a reference to the textured glass. The performance of solar cells on different textures is shown in

Figure 3.16 (a), (b) and (c). The performance parameters of each superstrate solar cell are summarised in Table 3.2. The tabulated values represent the average performance of the top ten solar cells (out of 30) for each sample. Selected solar cells, their position on the superstrate and standard deviation (SD) are included in Appendix A of this thesis. The SD of  $\sigma_{rms}$  and the external parameters suggest that the texture properties and their effect on cell performances are homogeneous over the glass strip (3 cm  $\times$  10 cm) used in this experiment. *SIT* solar cells showed the highest power conversion efficiency ( $\eta$ ) among the differently textured solar cells. The  $\eta$  of *SIT* solar cells is 0.57%, 1.52% and 2.71% (absolute) more than *SLT<sub>ITO</sub>*, *SLT<sub>IZO</sub>* and *FLAT* solar cells, respectively.  $J_{sc,EQE}$  of *SIT* solar cells was significantly higher than the other two textured solar cells. *SIT* sample outperforms the next best (*SLT<sub>ITO</sub>*) by 0.94 mA/cm<sup>2</sup>. Interestingly,  $V_{oc}$  and  $FF$  values of *SIT*, *SLT<sub>ITO</sub>* are in the same range, whereas  $V_{oc}$  and  $FF$  values of *SLT<sub>IZO</sub>* and *FLAT* were considerably lower. The efficiency of *FLAT* is lower than the reported values for n-i-p substrate cells on flat glass, as seen in [143]. While the  $V_{oc}$  and  $J_{sc}$  values are comparable, the performance drop is primarily due to a low  $FF$ . The values of  $FF$  reported here on superstrate configuration solar cells in this study, for 3  $\mu$ m thick nc-Si:H single junction solar cells, are close to the observed values by Tan *et al.* for identical p-i-n configuration and thickness [144]. The electrical losses through series resistances can be further reduced with a thicker IOH as the front electrode.

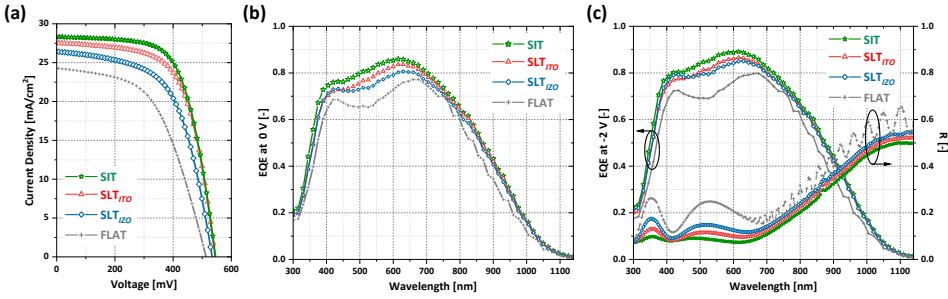


Figure 3.16.: (a) Current density versus Voltage characterisation of solar cells on each texture, (b) EQE at 0 V bias, (c) EQE at 2 V reverse bias and reflectance (R) as a function of wavelength for the solar cells.

### 3.3.5.1. Photocurrent Density

The optical properties of textures explained in the previous Sections 3.3.2, 3.3.3 and 3.3.4 account for the reflection of the air/ glass/ air system with two interfaces. In the solar cells, the refractive index of the layers is graded. Four intermediate interfaces of air/ glass/ IOH/ nc-Si:H solar cell/ silver architecture are decisive in determining the reflection spectrum of a solar cell. Figure 3.16 (c) shows the reflectance spectrum of the solar cells. Two major optical Fabry-Perot cavities [165] were observed in the solar cell stack, giving rise to interference fringes in the spectra [166, 167]. (i) The fringe in the visible wavelengths and (ii) fringes in the near-IR wavelength.

(i) The fringes with minima at 350 nm and 525 nm are related to the interference in the TCO layer (by reflection at the IOH/silicon interface). We observe that with changes in the thickness of the IOH, the minima of this fringe shift (Appendix Figure A.2). This is shown in Appendix A of this thesis. Cross-sectional SEM images of solar cell (Figure 3.17) suggest that at the mentioned deposition conditions, the 150 nm layer of sputtered IOH is conformal, and does not influence

Sample	$\sigma_{rms}$ [nm]	$V_{oc}$ [mV]	$\chi_c$ [%]	$J_{SC,EQE(0V)}$ [mA/cm <sup>2</sup> ]	$J_{SC,EQE(-2V)}$ [mA/cm <sup>2</sup> ]	$\Delta J_{SC,EQE}$ [mA/cm <sup>2</sup> ]	FF [%]	$R_S$ [ $\Omega \cdot \text{cm}^2$ ]	$R_P$ [ $\text{k}\Omega \cdot \text{cm}^2$ ]	$\eta$ [%]
SLT <sub>ITO</sub>	958 ± 22	540	57	25.8	26.8	1.03	63.2	11.0	2.8	8.8
SLT <sub>IZO</sub>	318 ± 12	534	58	25.1	26.5	1.45	58.7	13.9	1.7	7.9
SIT	416 ± 8	544	57	26.8	27.7	0.94	64.5	9.0	2.7	9.4
FLAT	–	521	63	23.1	24.1	1.02	55.5	13.7	1.0	6.7

Table 3.2.: External parameters of solar cells deposited on different textured glass samples. The reported values are calculated from ten cells on each textured substrate which has the highest  $V_{OC} \times FF$  value. The standard deviation of superstrate  $\sigma_{rms}$  is calculated from four different AFM scan areas on the same sample. The standard deviation of external parameters are included in Appendix A Table A.1.

the crater shape. Examining the interfaces as discrete changes in refractive indices ( $n_{IOH} - n_{glass}$  and  $n_{silicon} - n_{IOH}$ ), the IOH/silicon interface makes the dominant contribution to the reflection losses. The superstrate  $\sigma_{rms}$  with respect to the thickness of the IOH front electrode determines the R and amplitude of interference fringes in the visible spectrum for these solar cells [166]. For SLT<sub>ITO</sub>, the  $\sigma_{rms} \gg$  IOH thickness. For SIT the  $\sigma_{rms} >$  IOH thickness. Whereas for SLT<sub>IZO</sub>,  $\sigma_{rms} \sim$  IOH thickness, which implies the interface is relatively flat for SLT<sub>IZO</sub>. In solar cells, the overall reflection losses (R) and fringe amplitude follow the same order as  $\sigma_{rms}$ : Flat > SLT<sub>IZO</sub> > SLT<sub>ITO</sub> > SIT.

(ii) The Fabry-Perot interference beyond 700 nm in the near IR region is correlated to reflections in the nc-Si:H bulk absorber layer. Compared to FLAT, all three textures on glass have almost nullified the fringes induced by the nc-Si:H. This is because the solar cells on FLAT have flat interfaces for the absorber layer and back reflector, which are unable to break the optical cavity formed. With the introduction of textures to solar cells, the specular component decreases considerably, quenching the interference fringes in EQE and R.

SIT improves the QE in near UV, visible and near IR ranges in comparison with other textures (Figure 3.16 (b)). The gain is primarily due to the reduction in R combined with the scattering properties of features. The overall response of the solar cell can be further improved using an external anti-reflection coating [11, 168]. The spectral utilisation at long wavelengths near IR is affected by the back reflector properties. From the SEM image in Figure 3.17, it is observed that the back reflector surface morphology is rather flat and not an exact repetition of the textures on glass after a deposition of a very thick nc-Si:H layer. The spectral utilisation in the near IR can be further increased with increasing  $\chi_c$  [98], but this often causes a drop in  $V_{oc}$ . Sai *et al.* and Guha *et al.* have reported an EQE of  $\approx 0.3$  at  $\lambda = 1000$  nm for their record devices at high  $\chi_c$  values with a  $V_{oc} \approx$  of 480 mV [168, 169].

To add results into perspective, Tan *et al.* had reported the highest  $J_{sc}$  for the superstrate configuration single texture at  $\sigma_{rms} = 126$  nm, achieving 27.7 mA/cm<sup>2</sup>, but at the cost of FF and  $V_{oc}$ , resulting in  $\eta = 7.4\%$  [77]. Also,  $\eta = 10.2\%$  is reported in the same paper at a  $\sigma_{rms} = 370$  nm and a  $J_{sc}$  of 25.6 mA/cm<sup>2</sup> [77]. For a TCO (5  $\mu\text{m}$  thick)-based pyramidal texture approach on flat glass ( $\sigma_{rms}$  not available), the highest reported  $\eta$  is 10.9% at a  $J_{sc}$  of 27.5 mA/cm<sup>2</sup> [45] by EPFL. A similar TCO-based MST approach on periodic honeycomb textures on glass has also been reported for two-junction tandem solar cells, with a total spectral utilisation of approximately

26.0 mA/cm<sup>2</sup> [170]. For a periodic honeycomb texture on glass with IOH (150 nm), a spectral utilisation of 28.6 mA/cm<sup>2</sup> is reported by TU Delft [171] in superstrate p-i-n configuration. It has been a point of long discussion whether the substrate or the superstrate configuration is beneficial from a conversion efficiency perspective [172, 173]. Still, from an optical standpoint, the substrate configuration has an inherent advantage in that it does not have a smooth glass (or similar transparent material) acting as an extra reflective layer at the front of solar cells. In the substrate n-i-p configuration, the main component to be optimised is the back reflector texture. The highest reported  $\eta$  values on the substrate n-i-p nc-Si:H solar cells are 11.9% with  $J_{sc} = 28.74$  by AIST, Japan [17, 50] on honeycomb textures developed on wafers with moth eye anti-reflection coatings [168]. Additionally, a very high  $J_{sc}$  of 32.9 mA/cm<sup>2</sup> is reported on a honeycomb textured wafer [11].

### 3.3.5.2. nc-Si:H absorber quality

Cross-section SEM images of solar cells are shown in Figure 3.17. For a 3  $\mu$ m thick nc-Si:H absorber, we observe a few cracks (or voids) near the back contact of the solar cells. Cracks are formed in the crystalline absorber due to the shadowing effect at narrow funnel-shaped growth regions [11, 174]. This crack formation is dependent on the thickness of the cell and the slope of the superstrate, at which silicon is deposited [78]. These cracks act as sites for charge carrier recombination and low parallel resistance, leading to low  $FF$ .

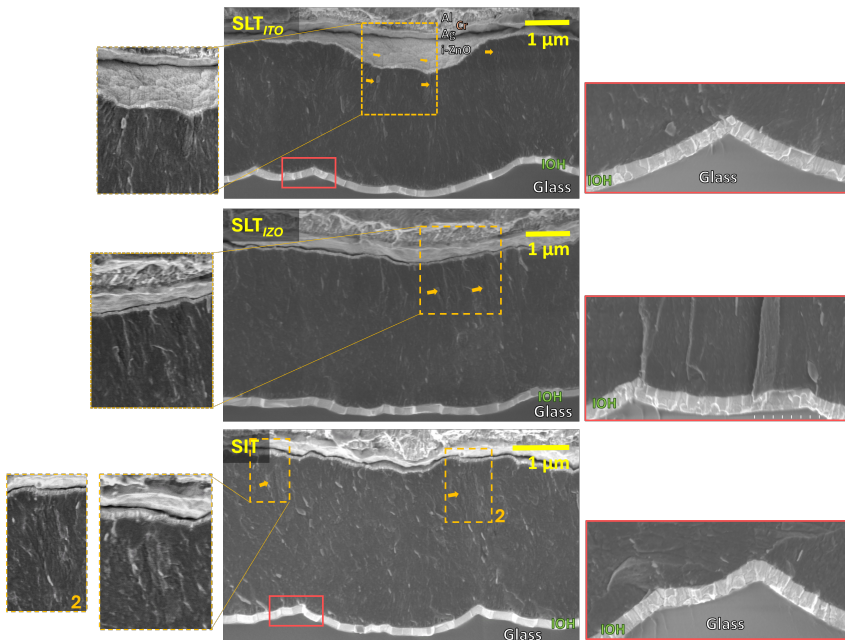
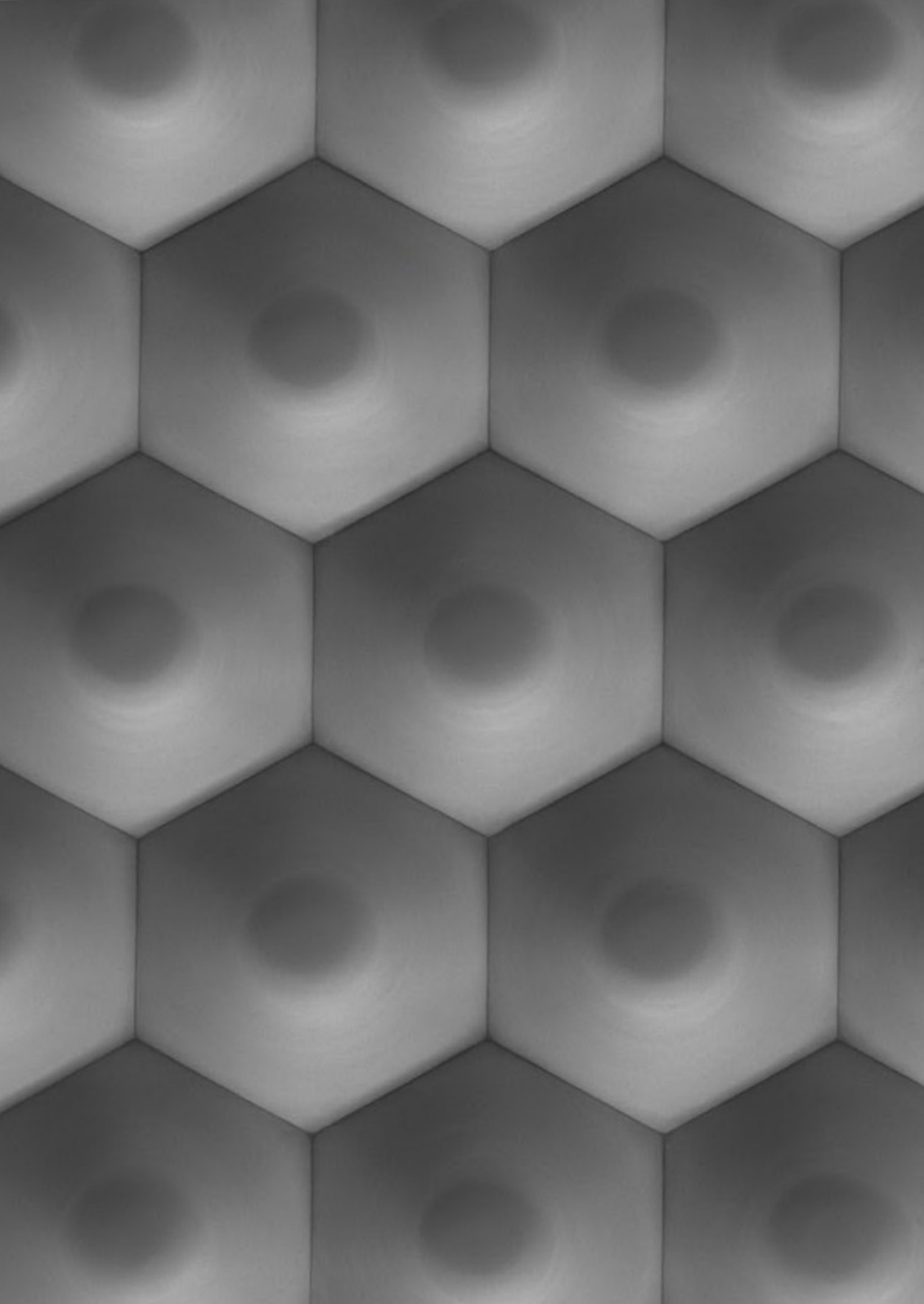


Figure 3.17.: Cross-sectional images of superstrate p-i-n solar cells made on  $SLT_{ITO}$ ,  $SLT_{IZO}$ ,  $SIT$ . The direction of cell deposition is from the glass (marked) to the top. Defective filaments in the nc-Si bulk are identified and marked with arrows (gold) and zoomed in (gold boxes). IOH conformality is qualitatively examined at different crater shapes and zoomed in (red boxes).

Figure 3.16 (b) shows the EQE of solar cells at 0 V and Figure 3.16 (c) shows EQE of solar cells at a reverse bias voltage of 2 V. The absolute difference between EQE measurements at 0 V and -2 V bias is representative of the recombination losses in the at defect rich filaments in solar cell [175]. From the  $\Delta J_{sc, EQE(-2V, 0V)}$  values tabulated in the Table 3.2,  $SLT_{IZO}$  has the most recombination losses in the bulk, this is presumably because of the sharp angles of  $SLT_{IZO}$  with its 'V shape' craters. The  $\Delta J_{sc}$  is significant in the blue response as well, indicating an electron recombination in the vicinity of the p/i interface of the cell. These recombinations lead to low  $V_{oc}$  values. As a consequence of the bulk defects,  $V_{oc}$  and  $FF$  values also follow the order of angle distribution:  $SIT > SLT_{ITO} > SLT_{IZO} > FLAT$ . Python *et al.* have made a similar discussion on how the U-type superstrate mitigates crack formation when compared to Asahi V-type superstrates [109]. We speculate that  $SIT$  has the added advantage of smoother crater boundaries owing to the double etching step involved in making  $SIT$ . This suppresses the density of recombination centres in the solar cell [80]. However, to make a conclusion on this effect in  $SIT$ , more statistics are required.

### 3.4. Conclusion

This work presents a detailed sample study of three sacrificial random texturing approaches on glass utilising two different sacrificial TCO layers, namely indium-doped tin oxide (ITO) and intrinsic (not intentionally doped) zinc oxide (i-ZnO). i-ZnO is a novel TCO material used in texturing glass. The chapter presents observations on the physical properties of the created textures and their interaction with light. Using the ITO layer for sacrificial texturing ( $SLT_{ITO}$ ) resulted in large craters with spherical 'inverted U' shapes with peak RMS roughness ( $\sigma_{rms}$ ) of 958 nm. Using the i-ZnO sacrificial layer ( $SLT_{IZO}$ ) created small craters with conical 'inverted V' shapes and peak attained  $\sigma_{rms} = 318$  nm. A correlation is observed between the  $\sigma_{rms}$  of the textures and their diffused transmission. Large-size textures of  $SLT_{ITO}$  follow coherent refraction, while  $SLT_{IZO}$  nano textures follow incoherent Mie scattering. The best-performing  $SLT_{ITO}$ ,  $SLT_{IZO}$  resulted in  $\eta$  of 8.81% and 7.38% with  $J_{sc}$  25.81, 25.08 mA/cm<sup>2</sup>, respectively. The processing conditions of optically best-diffusing textures from each sample set are combined to make a superimposed texturing -  $SIT$ .  $SIT$  has features resembling its constituent morphologies ( $\sigma_{rms} = 418$  nm) and exhibits combined scattering characteristics of both diffractive and refractive scattering regimes across a broad wavelength.  $SIT$  exhibits excellent optical properties in terms of reflectance and scattering. The nc-Si:H single-junction solar cells made on  $SIT$  resulted in the highest-performing solar cell in terms of external quantum efficiency (EQE) with  $J_{sc}$  of 26.75 mA/cm<sup>2</sup> and  $\eta = 9.38\%$  among the mentioned textures.





# 4

## Engineering of Hexagonal Micro-textures on Glass

This chapter is based on the publication:

G. Padmakumar, A. Balaji, M. Criel, F. Saitta, G. Limodio, P. Perez-Rodriguez, R.A.C.M.M. van Swaaij, A.H.M. Smets, "Engineering of Hexagonal Microtextures on Glass" *ACS Applied Optical Materials*, 3(10), 2360-2372, 2025. DOI: 10.1021/acsaom.5c00328

*Textured glass is utilised in a wide range of applications to enhance optoelectrical performance, including photovoltaics, biosensing, microfluidics, and photonics. Honeycomb textures have demonstrated excellent performance in optical devices using crystalline silicon wafer substrates. As a pathway to translate these advantages to superstrate configuration, hexagonal-shaped micro-sized craters (honeycombs) are made on glass in this study. We use photolithography combined with wet etching for this process. The relationship between photoresist mask design, glass-photoresist adhesion, wet etching steps, and the mechanism of honeycomb formation is studied. It is demonstrated that the higher the isotropic nature of etching achieved, the deeper the hexagonal craters will be. The potential of hexagonal textures on the glass to significantly reduce reflection losses to <8% over the entire spectral range is observed. Finally, hexagonal micro-textures with 5  $\mu\text{m}$  periodicity and 1.01  $\mu\text{m}$  depth that effectively diffuses 50% of total transmitted light at near-infrared (1100 nm) wavelength are developed.*

## 4.1. Introduction

Texturing of glass is extensively used in applications where active interaction with light is required. In photovoltaics (PV) applications, textured glass surfaces enhance light trapping to improve efficiency; in biosensing, textures on glass improve sensitivity and detection capabilities [176, 177]; in photonics, textures manipulate light generating colours and adding haze [178–180]; in microfluidics, textures make channels for devices [181]. Two broad classifications of textures are (i) random shapes with random distribution over the surface and (ii) periodically distributed shapes on the surface.

Wet etching with a deposited crystalline sacrificial layer is an effective method to develop random textures on glass. The crystals over glass act as a selective mask to form crater-like structures on glass. This ‘leaking’ mask is partly or wholly removed during a chemical wet-etching process step [182, 183]. The etching solution penetrates the easiest through pinholes and pores around grain boundaries in the layer. As the sacrificial layer is dissolved, the glass is inhomogeneously etched, resulting in a random texture at the surface [77, 184].

To make a periodic texture on any surface, the constituent geometric shape should cover the plane with no gaps or overlaps. This property is called tessellation. The three regular polygons that can form regular tessellation are triangles, squares, and hexagons [185]. Regular hexagons have the smallest perimeter for a given area among all shapes that can tessellate. This property, referred to as ‘honeycomb conjecture’, makes hexagons the most efficient shape for enclosing and separating spaces [186]. For crystal depositions, honeycomb-shaped textures minimise the length of sharp boundaries caused by texture borders, which can otherwise interfere with crystal structure, causing cracks [187]. For this reason, hexagonal textures (alias ‘honeycomb textures’) are of special interest in thin-film PV applications. Commonly adopted methods to make periodic hexagonal textures are nanoimprint lithography (NIL) [188], laser ablation [189], and photolithography [190]. NIL is a method of physically pressing polydimethylsiloxane (PMDS) mould with a targeted pattern onto a substrate coated with a thin polymer layer. The polymer layer with the impressed pattern is cured under ultraviolet (UV) light as the next step. Upon removal of the PMDS stamp, the complementary pattern is made on the substrate [191, 192]. A nano-imprinted resist layer can also be used as a three-dimensional etching mask to obtain a hexagonal pattern in the c-Si absorber surface by reactive ion etching [193]. To make hexagons on metals, laser ablation is utilised. A nano-pulsed fibre laser beam travels in a hexagonal pattern on the substrate surface to remove a material partially through vaporisation or sublimation [194].

Photolithography uses polymer-based materials known as photoresists (PR). The PR layer clones a desired pattern with the help of either X-ray or UV light transmitted through a photomask [195]. When exposed to these high-energy wavelengths, the PR degrades. These degraded areas are removed in the following step called ‘development’. In the final step of pattern generation, the glass substrate with PR masks is dipped in an etchant to remove material from its surface. Since PR-covered regions act as a shield for etching, selective etching through the PR-less areas creates patterns on the substrate. Photolithography is generally used to make patterns on silicon wafers [196, 197]. Lithography with row-wise distributed and alternatively spaced orifices for wet etching can make hexagonal patterns [198, 199]. In this method, a silicon dioxide ( $\text{SiO}_2$ ) layer is grown on the wafer surface and subsequently patterned with orifices. The wafer is subsequently wet etched isotropically using ( $\text{HNO}_3:\text{HF}:\text{CH}_3\text{COOH}$ —25:1:10) acid solution or BHF to obtain hexagonal features [46, 47, 187, 200]. Texturing methods on glass differ from texturing on silicon wafers. Glass is an amorphous solid with a random network of silicon and oxygen atoms [139]. To develop honeycomb textures on glass wafers, a similar photolithography mask technique can be employed. This can be done without an additional  $\text{SiO}_2$  layer [201, 202]. However, upon direct translation of photolithography and subsequent etching steps to glass, the resultant textures suffer from flat bottom regions [141]. The detailed

optimisation of the steps involved in photolithography to create honeycomb textures on glass has not yet been explored. Hexagonal textures with flat bottom regions cannot actively scatter light itself and require additional scattering mechanisms [203] when used in PV applications.

The work presented in this article aims to develop a fabrication process for making honeycomb textures on glass with rounded bases. We have taken the process of making honeycomb textures on silicon [187] as a starting point and optimised it to achieve the desired rounded features on glass. For the first time, this work identifies challenges specific to developing honeycomb textures on glass using photolithography. The underlying wet etching mechanism and its implications on surface morphology are explored in detail. Further, process parameters based on the shape and height of the hexagons are optimised. We define a term ‘effective orifice diameter’ as a parameter to quantify the isotropism involved in the generation of hexagonal textures on glass. Finally, we demonstrate the potential of hexagonal textures on glass to enhance total transmittance while ensuring excellent light scattering.

## 4.2. Materials and methods

### 4.2.1. Generating hexagonal textures on Glass

The methodology adopted to create hexagonal textures on glass is similar to that described in [187, 204]. The glass substrates used in this study are Corning glass XG Boro-alumino-silicate glass wafers of 4 inches in diameter and 0.7 mm thickness with a primary flat [148, 149]. The basic process for obtaining the honeycomb textures using photolithography on the glass superstrates is depicted in Figure 4.1. Each step in Figure 4.1 is detailed in the following subsections.

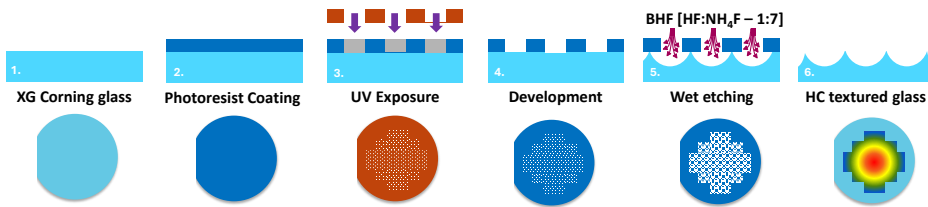


Figure 4.1.: The schematic diagram of all steps involved in generating hexagonal textures on glass (top row). The bottom row shows the Corning glass wafers after the corresponding steps.

#### 4.2.1.1. Step 1: Superstrate preparation

The glass wafers are composed of silicon oxide, which makes them extremely hydrophilic. In Step 1, the glass wafer undergoes a non-acidic cleaning step to remove organic impurities from its surface. This includes 10 minutes of ultrasonic cleaning in an acetone bath followed by 10 minutes in an isopropyl alcohol bath [205, 206]. The cleaned glass is dried with nitrogen flow and loaded for further processing. It is essential to conduct these steps with minimal delay to prevent the hydroxyl groups from getting attached to the surface from the atmosphere [206].

#### 4.2.1.2. Step 2: Coating of PR on superstrate

Following cleaning, the next step is to coat the PR onto the glass superstrate. An EVG120 coater machine is used for this step.

**Pre-coating bake:** In a pre-baking step inside the EVG 120 coater, the substrate is annealed at 100 °C for 600 s. This is an extra step to decrease the surface density of hydroxyl groups attached to the surface as much as possible.

**Hexamethyldisilazane (HMDS) exposure:** After prebaking, the wafer is vapour-primed with HMDS on a hotplate in order to suppress any remaining hydroxyl groups. HMDS priming of the surface before coating PR significantly affects PR adhesion on the surface [206]. The reaction between the OH group on the surface and methyl groups boosts the hydrophobicity of the surface. HMDS forms a strong bond with hydroxyl groups on the wafer surface, thereby bridging the inorganic wafer and the organic photoresist [206, 207]. EVG120 exposes the samples to HMDS with N<sub>2</sub> as the carrier in a separate priming chamber. This process is carried out at 130 °C for 50 seconds.

**PR coating:** The PR used in this work is Shipley SPR3012 positive PR. 1.4 µm thick SPR3012 is coated on glass. The coater tool dispenses 2600 µl of PR at a rate of 1000 µl/s onto a wafer spinning at 600 rpm. Afterwards, an acceleration of 2500 rpm/s is applied until the wafer reaches a rotational speed of 3450 rpm, which is maintained for 30 seconds. Resist can flow around the wafer edges, or the resist may splatter from the coater bowl, too. Both cases can land the PR on the back side of the glass wafer and can eventually cause issues in later processing steps (such as contaminating hotplates or introducing flatness errors during exposure). Then, the backside of the wafer is rinsed (BSR) with propylene glycol methyl ether acetate (PGMEA) for 2 s at a rotational speed of 1700 rpm. At the end of this step, the rotational speed increases to 2500 rpm to remove the PGMEA.

**Post-coating bake:** Once the PR is coated on the wafer, it is soft-baked (or post-coating bake) for 90 seconds at 90 °C. This step ensures that a monolayer of the PR is formed on the superstrate surface [208]. The formed monolayer ensures that the pattern's accuracy is maintained post-development, aiding in the formation of a precise PR mask on the superstrate. The optimum annealing duration and temperature suggested in the technical datasheet offered by Merck [209] is used in the EVG120 recipe. This is conducted in a dedicated chamber at 90 °C for 90 s. Afterwards, the wafer is cooled down on a cooling plate for 20 s.

#### 4.2.1.3. Step 3: Exposure of coated superstrates

The subsequent step after PR coating is the exposure of the coated PR to UV light. The UV exposure is conducted using the ASML PAS5500/80 Waferstepper. For 1.4 µm thick PR coated wafers, exposure is done at 150 MJ/cm<sup>2</sup>. The chromium reticle used for obtaining the hexagonal textures has a pattern of orifices spaced out at a particular periodicity along the horizontal direction. Around each orifice, six adjacent orifices occur spaced out at 60° angles. Figure 4.2 shows an SEM image of this orifice distribution on PR mask.

#### 4.2.1.4. Step 4: Development of exposed superstrates

In the final step of the photolithography, the exposed superstrates are developed in the EVG120 Developer. The superstrate is spun at 5 rpm in the developer rack with the developer solution poured onto the surface. Slow spin speed ensures a uniform layer of the developer solution, which reacts with the exposed parts of the PR and dissolves them. Then, the superstrate is spun at high speeds ranging from 2000 to 3000 rpm and washed with DI water to remove the dissolved PR from the wafer surface. At this step, the PR mask formation is complete with a diameter ( $D$ )  $1000 \pm 11$  nm and an orifice periodicity ( $P$ )  $3000 \pm 13$  nm. The standard deviation of  $D$  and  $P$  reported in this article are based on multiple measurements of orifice diameter and periodicity after development of PR.

**Hard baking:** Following this, the superstrate with the developed pattern is baked at 100 °C for

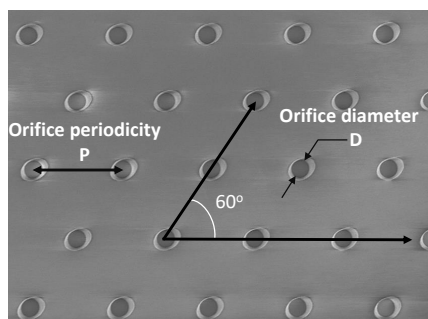


Figure 4.2.: SEM image of the 2D distribution of orifices on the PR imparted using chromium reticle.

90 s to evaporate excess PR and developer present on the superstrate. This step hardens the PR and causes crosslinking.

#### 4.2.1.5. Step 5: Wet etching of patterned superstrates

The glass superstrate with the patterned PR is to be chemically etched to obtain the hexagonal texturing on the surface. This is done in a sequence of two steps. The first step involves a 1-minute dip in a 1:5000 aqueous Triton X-100 ( $[C_{14}H_{22}O(C_2H_4O)_n]: H_2O = 1:5000]$ ) bath. The main purpose of this bath is to improve the wettability of the surface by the etchant. The Triton X-100 acts as a surfactant, lowering the surface tension and enabling better contact between the solid and the aqueous medium [210].

As the next step, the glass wafer is dipped as a whole in the etchant to make patterns. The non PR coated side of the wafer is not shielded from etching during the process. For glass etching, hydrofluoric acid (HF) offers an etching rate of around 833 nm/min at 40 % concentration [148, 149, 211]. However, the usage of HF increases the peeling off of the PR due to the influx of the  $F^-$  ions through the PR [212, 213]. To gain better control over the etching rate and etch step, in this work, we use premade buffered hydrofluoric acid (BHF), comprised of ammonium fluoride ( $NH_4F$ ) (40%): hydrofluoric acid (HF) (49%) in ratio 7:1. In BHF, the buffer results in an increase in the concentration of  $F^-$  ions and due to their high electronegativity, tends to form  $HF_2^-$  ions. The PR is more resistant to the diffusion of these ions due to their larger size. This helps to protect the PR from the impact of HF and aids in better selectivity in the etching of the glass [212, 213].

#### 4.2.1.6. Step 6: Cleaning of textured superstrates

The remaining photoresist on glass is removed with PVA TePla Microwave Plasma system asher. The cleaned glass is dipped in ultrasonic baths of acetone, followed by isopropyle alcohol for 10 minutes each [205, 206]. The cleaned glass is dried with nitrogen flow.

### 4.2.2. Design of experiment

Experiments in this work are conducted in three phases. An overview of the design of experiments is depicted in the flowchart in Figure 4.3. The crater height of a completely developed hexagon is the metric chosen to define the texture quality throughout the experiments. To clarify the term height of texture, Figure 4.4 is included.

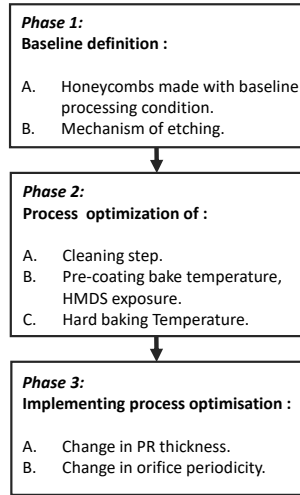


Figure 4.3.: Design of experiment flowchart. The experiments in this manuscript are divided into three phases.

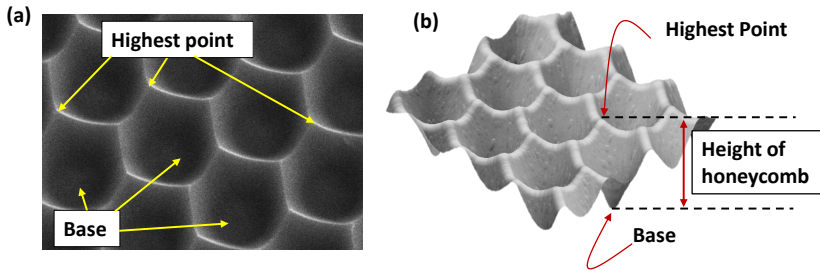


Figure 4.4.: Image of a completely developed honeycomb. (a) SEM image - tilted view. (b) Concept of height of the honeycomb as defined in the text.

**Phase 1 - Baseline definition:** To define a baseline for the processing conditions, with the processing steps elaborated in Section 5.2.1, an etching duration series of 18 to 30 minutes with 2-minute steps was conducted. This experiment was carried out to observe the properties of hexagonal textures on glass and identify the challenges involved in processing.

**Phase 2 - Process optimisation:** In this phase, the experiments are designed to optimise the processes involved in substrate cleaning and preparation (2.1.1), coating on PR on superstrate (2.1.2), and development of exposed superstrates (2.1.4). The experiments in these three sections are optimised based on the adhesion between PR and glass.

**2.A.** Four different cleaning procedures are attempted to identify a suitable surface cleaning procedure for photolithography on Corning XG glass. *i.* Non-acidic cleaning with IPA and acetone in an ultrasonic bath. *ii.* Acidic cleaning by dipping the wafers in  $\text{HNO}_3$  (30%) bath for 3 minutes at room temperature. *iii.* Acidic cleaning by dipping the wafers in  $\text{HNO}_3$  (69.5%) at room temperature for 3 minutes. *iv.* Acidic cleaning by dipping the wafers in  $\text{HNO}_3$  (99%) bath and

then followed by  $\text{HNO}_3$  (69.5%) bath for 3 minutes each. All baths used for cleaning have dimensions 15 cm x 15 cm x 15 cm.  $\text{HNO}_3$  was selected for its feasibility, as it is the standard cleaning solution available in the lab where these experiments were conducted. These wafers are cleaned in a deionised running water bath in each procedure. After rinsing, the samples were dried using the spin dryer. For each cleaning procedure, two wafers were coated with 1.4  $\mu\text{m}$  PR and wet etched for 24 minutes, and their height was analysed with atomic force microscopy (AFM) data.

**2.B.** To optimise PR coating on superstrate, variation in pre-coating bake temperature and HMDS exposure is conducted, staying within the limits of the EVG 120 Coater tool. The maximum duration for the pre-baking was fixed at 10 minutes since the dipod arm in the EVG120 cannot handle hot superstates. If the superstrates were to be heated longer, they had to be cooled again before being used in the EVG120. This delay could offer enough time for the surface to re-adsorb water. To determine the optimum pre-coating bake temperature, the samples were heated at temperatures ranging from 100 °C to 140 °C, in 10 °C increments. This temperature range was suggested by the manual provided by Microchemicals for sample preparation [208]. HMDS exposure time varies from 0 to 150 seconds in 50-second increments. For these two experiments, the hydrophobicity of the surface is studied to identify the influence of each step in PR adhesion on glass (the measurement procedure is described in Section 4.2.3.1).

**2.C.** To study the effect of the development steps, the influence of hard baking temperature is studied. Hard baking is generally done to physically and chemically stabilise the PR material. The thermal softening and rounding of PR3012 occurs at a temperature around 110 - 130 °C called reflow temperature [214, 215]. The two options considered for this experiment include hard baking at temperatures similar to and above the reflow temperature of PR [216]. The first trial is to heat the superstrates at 110 °C for 30 minutes. The second option is hard-baking the PR at 140 °C for 30 minutes. It was also necessary to etch the samples to visualise the effect of the hard baking experiment. The samples were etched using the procedure mentioned in Section 4.2.1.5 over an etching duration series conducted for 14 to 30 minutes at 2-minute intervals. At each time value, one wafer was processed and etched. These samples were processed using the parameters optimised in Section 4.3.5 to 4.3.7. The physical properties of each wafer were studied by AFM scan of multiple spots on the wafer to ensure spatial uniformity of textures.

**Phase 3 - Implementing optimised process:** In phase 3 of the experiments, the parameters optimised through the experiment conducted at phase 2 are implemented. The experiments in Phase 3 do not impact Phase 2 as the conditions optimised in Phase 2 address the PR-glass adhesion, which is kept the same for Phase 3.

**3.A.** To study the effect of variation of PR thickness, the thickness of PR SPR3012 is increased to 2.1  $\mu\text{m}$ . An etching duration series for 14 to 26 minutes for each PR thickness is conducted. This work does not attempt to use a chemically different PR because such a change might require re-optimising parameters explored in Phases 1 and 2. For a 2.1  $\mu\text{m}$  thickness, a 3000  $\mu\text{l}$  volume of PR is dispensed at 750  $\mu\text{l/s}$  on a spinning wafer at 600 rpm. Then, an acceleration of 1000 rpm/s is introduced to reach a speed of 1575 rpm, which is kept constant for 30 seconds. The backside of the wafer is rinsed with PGMEA for 2 seconds at 1500 rpm. At the end of this step, the rotational speed increases to 2500 rpm to remove PGMEA. Since the UV exposure dose for a sample is determined based on the thickness of the PR used, a UV exposure dosage of 315  $\text{MJ/cm}^2$  is required for 2.1  $\mu\text{m}$  thick PR.

**3.B.** To study the effect of orifice periodicity on etching, PR masks corresponding to periodicity 3  $\mu\text{m}$ , 4  $\mu\text{m}$ , and 5  $\mu\text{m}$  were used. An etching duration series between 14 and 24 minutes is made for each periodicity.

At each phase of this work, the observed patterns are physically correlated to the etching

process utilising matrices defined in the upcoming Section 4.3.3. It has to be noted that the wafers were etched one at a time, as the author's attempts to etch multiple wafers simultaneously in one bath [dimension: 15cm x 15cm x 15cm] had adverse effects on texture uniformity due to the re-deposition of the peeled-off PR onto adjacent wafers.

### 4.2.3. Characterisation methodology

#### 4.2.3.1. Hydrophobicity of glass wafers

The surface energy or the hydrophobicity of the surface could be related to the contact angle of a water droplet dropped onto the surface. This could be measured from the superstrate's water contact angle (WCA). WCA is the contact angle formed by a water droplet on the surface. This measurement is conducted with DataPhysics-OCA200. 1  $\mu\text{l}$  of water was dropped on five different spots on the superstrate. The droplet's left and right contact angle with the superstrate is calculated with a microscopic image of the droplet profile as illustrated in Figure 4.5. The mean value of the five measurements indicates the hydrophobicity of the surface.



Figure 4.5.: Illustration of water contact angle measurement. L and R represent the tangential angles formed by water with glass at left and right contact points.

#### 4.2.3.2. Physical characterisation

To examine the surface morphology of developed textures with AFM, a Bruker AFM FastScan with a FastScan closed loop scanner head is utilised. Scanning areas of a 16  $\mu\text{m} \times 16 \mu\text{m}$  were chosen for analyzing the differently sized textures. The surface parameters, such as maximum height and slope distribution, were extracted from the AFM data using Bruker's NanoScope Analysis software. The standard deviation in height measurement of texture was reported based on multiple AFM measurements of the same wafer. The practical surface area analysis and angle distribution are completed using Gwyddion software (version 2.63). Gwyddion analyses the surface slopes based on normalised occurrence curves of angles subtended by surface vectors with the vertical plane. The Scanning Electron Microscopy (SEM) analysis of the surface was conducted on Hitachi Regulus 8230 at an acceleration voltage of 1.5kV.

#### 4.2.3.3. Optical characterisation

Optical transmission measurements were carried out using a LAMBDA 1050+ UV/Vis/NIR Spectrophotometer with a 150 mm InGaAs integrating sphere from PerkinElmer. All glass samples were probed with light on the flat side for this measurement. The percentage of light transmitted in any direction other than normal is quantified as diffused transmittance ( $T_D$ ).  $T_D$  values at different wavelengths were considered the prime metric for quantifying the optical scattering performance in this work. The total transmission ( $T_{TOT}$ ) and  $T_D$  of flat glass (acid-cleaned glass wafer) are also added as a reference.

## 4.3. Results and discussion

### 4.3.1. Mechanism of etching

The different steps involved in forming hexagonal textures through wet etching are schematically illustrated in Figure 4.6. The circular patterns formed on the glass surface intersect to form a hexagon due to the spatial placement of orifices on the PR mask.

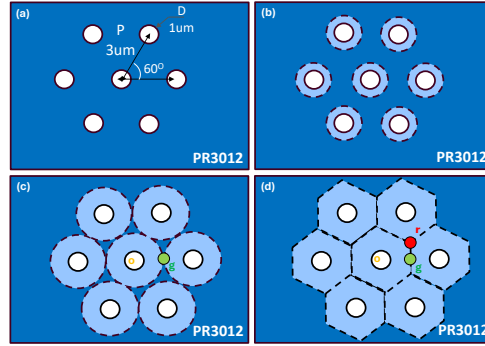


Figure 4.6.: Demonstration of hexagon formation during etching with BHF (a) Position and spacing of orifices to make hexagonal textures. (b) The initial etching stage is when BHF enters through the orifice and initiates crater propagation. (c) Initial intersection points of craters (green dot, marked as g). (d) Completion of honeycomb formation (red dot, marked as r).

The centre of the orifice can be considered the origin of the etching process, which is marked as (o) in Figure 4.6. The distance between the orifices on PR is translated to the periodicity (P) of the resultant texture. The etchant penetrates through the orifice and etches glass vertically and laterally. The lateral etching exhibits a circular behaviour centred at (o). The first intersection point of the formed circles is marked (g) in Figure 4.6 (c). The circle's boundary propagates radially outward and eventually merges with that of its neighbours, as demonstrated in Figure 4.6 (d). The point (r) marks the completion of merging and formation of hexagonal shapes. Removal of glass in the vicinity of (g) continues until the hexagon formation is completed. By geometry, (g) is at a distance of  $P/2$  from the origin (o) and (r) is at a distance  $P/\sqrt{3}$  from the origin (o). Figure 4.7 (a) shows the schematic top view of hexagons on glass. Figure 4.7 (b) shows the top view of a unit hexagon. The hexagons have an edge with a  $P/\sqrt{3}$  length.

### 4.3.2. Physical characterisation of textures

A regular hexagon is symmetric at 60° rotations and asymmetric at 30° rotations. The surface profile of wet-etched hexagonal textures differs in two directions with a phase difference of 30°. Figure 4.7 explicitly shows the two directions. Two surface profiles in these directions can describe the entire surface topology of each hexagon. The two directions are named Red axis (R-axis) and Green axis (G-axis) for convenience. The G-axis represents an imaginary centre-to-centre line perpendicular to the edge of the hexagons. The R-axis represents the centre-to-centre line parallel to the edges of the hexagons. This is demonstrated in 4.8(a).

The height profile along the G and R axes is plotted on the same scale in Figure 4.8 (b). The observed peak height of the R-axis ( $H_r$ ) is more than that of the peak height of the G-axis ( $H_g$ ).

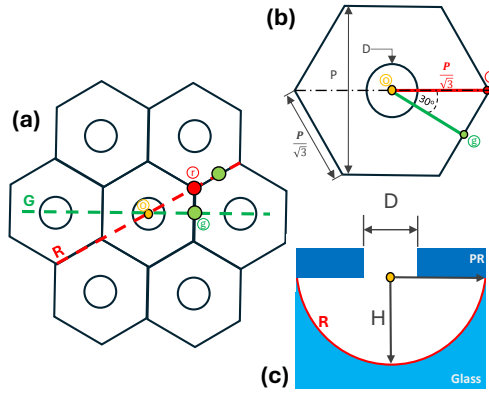


Figure 4.7.: (a) Top view of hexagonal microtextures after final cleaning. (b) Dimensions of one hexagon unit in terms of periodicity,  $P$ . (c) The cross-sectional representation of etched glass with PR assuming isotropic etching with BHF. The axes are marked R and G.

Both profiles are periodic in nature, with periodicity  $P$  along the G axis and  $\sqrt{3}P$  along the R axis. This arises from the fact that  $\textcircled{r}$  marks the point of completion of the honeycomb and is located at a longer distance than  $\textcircled{g}$  from  $\textcircled{o}$ .

From Figure 4.7 (b) and (c), for the isotropic etching mechanism, the expected texture height ( $H_{exp}$ ) can be related to the orifice diameter ( $D$ ), and texture periodicity ( $P$ ) by the equation,

$$H_{exp} = \frac{P}{\sqrt{3}} - \frac{D}{2} \quad (4.1)$$

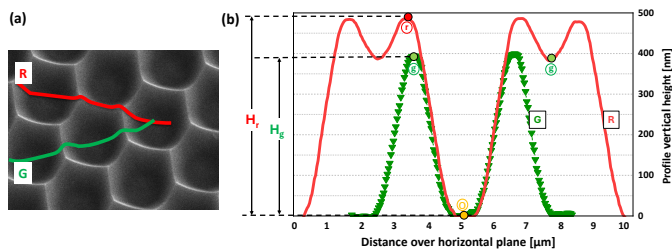


Figure 4.8.: (a) Demonstration of the asymmetric axes (G and R-axis) of the honeycomb texture on honeycomb texture (SEM image). (b) Extracted AFM profiles over the R-axis profile (solid line, marked R) and the G-axis profile (lines with triangles, marked G). Points with encircled letters are the same as in Figure 4.7 (a). The Profiles are extracted from AFM data with a  $3 \mu\text{m}$  periodic texture.

### 4.3.3. Effective orifice diameter ( $D_e$ )

To quantify the extent of isotropism resulting from etching, we define the term effective orifice diameter ( $D_e$ ).  $D_e$  for a specific periodicity is the orifice diameter at which the texture height is achieved with isotropic etching. A decrease in the numerical value of  $D_e$  signifies enhanced directional uniformity in the etching. For any peak height,  $H_r$  measured,  $D_e$  is given as,

$$D_e = 2 \left[ \frac{P}{\sqrt{3}} - H_r \right] \quad (4.2)$$

The term  $\sqrt{3}D_e/2P$  gives a ratio of effective orifice diameter to the diagonal length of the honeycomb. This term is referred to as  $D_{e,P}$  from now on in this work.  $D_{e,P}$  can quantify the isotropism of a processing step irrespective of texture periodicity. This term is also a measure of the texture's sensitivity towards a sub-process. The aspect ratio (AR) of hexagons on glass can be defined in terms of  $D_{e,P}$  as

$$AR = \frac{H_r}{P} = \frac{1}{\sqrt{3}} [1 - D_{e,P}] \quad (4.3)$$

### 4.3.4. Baseline processing

The measured peak profile heights  $H_r$  and  $H_g$  with AFM are plotted against etching durations in Figure 4.9. As explained in Section 4.3.1, the lateral propagation of etching leads to the formation of hexagons. Once the circles join completely, the honeycomb formation is complete. For baseline definition time series, this event occurs at 24 minutes. Glass wafers etched below this duration are under-etched and etched above this duration are over-etched.

The presented time series starts at 18 minutes. For etch durations below 18 minutes, the situation resembles Figure 4.6(b). For this case, the height of the two profiles is the same  $H_r = H_g$ . Above 18 minutes, the circles intersect along the G-axis, but are still distinct along the R-axis (as in Figure 4.6(c)). SEM image in Figure 4.10 represents this scenario. From Figure 4.10 (b), it is clear that  $H_r > H_g$  once etching starts at point (g). Both  $H_r$  and  $H_g$  increase with etching duration up to 24 minutes and decrease if over-etched. The highest value of  $H_r$  in this time series is  $0.34 \pm 0.01 \mu\text{m}$ , when the hexagons are completely developed.

The value of  $H_r - H_g$  increases over time and is highest for completely developed hexagons (etch time = 24 minutes). Beyond 24 minutes, when over-etched, etching at (r) is quicker than (g) as the conical structures at (r) are etched from all sides. This gradually decreases  $H_r - H_g$  and starts flattening out the peaks.

According to the Equation 4.1, for an orifice diameter of 1000 nm and periodicity 3000 nm,  $H_{exp} = 1230 \text{ nm}$ . Whereas  $H_r$  in baseline processing is  $0.34 \pm 0.01 \mu\text{m}$ , which is significantly smaller than the expected value. This diminishing height effect is caused by PR peel-off as demonstrated schematically in Figure 4.11 (c). During the wet etching, the orifice diameter does not stay constant at 1000 nm, but increases with the etching duration. As the orifice diameter increases, the lateral etching is faster. Etching continues up to a critical level of PR peel-off, causing a flat region at the base of the honeycomb. The SEM image of texture in Figure 4.11 (a) shows this. Similar cases of flat bottoms are reported elsewhere in the making of hexagonal textures [141, 187, 203]. The PR peel-off is mainly determined by the adhesion of the PR to the glass surface [212].

The  $D_e$  of baseline processing is  $2.80 \pm 0.02 \mu\text{m}$ . This implies that the effective diameter for etching is much higher than the intended diameter of  $1.00 \pm 0.01 \mu\text{m}$ . The corresponding  $D_{e,P}$  is  $0.80 \pm 0.01$ , and AR is  $11.2 \pm 0.1 \%$ .

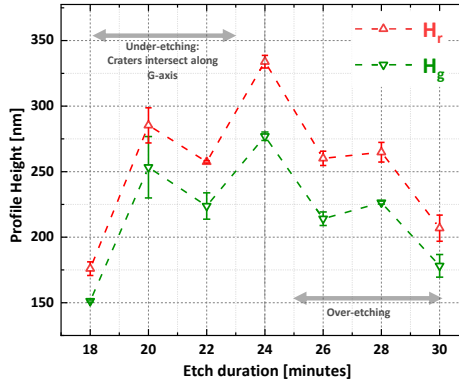


Figure 4.9.: Profile height of G-axis (green) and R-axis (red) for wafers processed with baseline conditions for different etch durations.

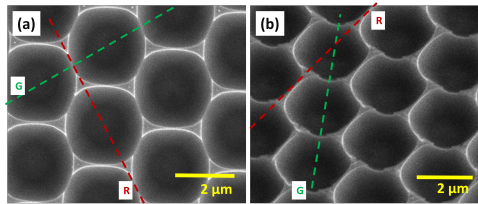


Figure 4.10.: SEM images of under-etched glass wafer (corresponding to etching time for 22 minutes in Figure 4.9). (a) Top view. (b) Tilted view.

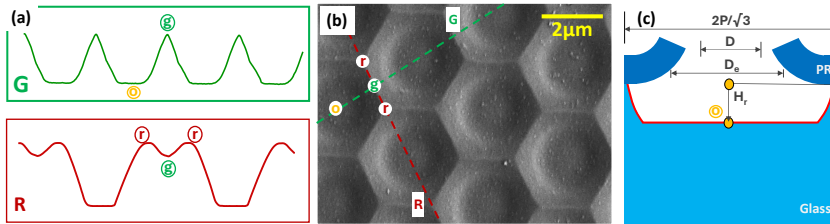


Figure 4.11.:  $3\ \mu\text{m}$  periodic hexagonal textures with a flat base. The sample corresponds to baseline processing conditions etched for 24 minutes. (a) The 2D surface profile along the G and R-axis as extracted from AFM (profiles are not to scale). (b) SEM image. The encircled letters are given to aid in the interpretation of the SEM image. (c) Conceptual drawing of PR peel-off and effective orifice diameter  $D_e$  leading to a flat base.

#### 4.3.5. Influence of cleaning method

The effect of different cleaning steps on texture heights  $H_r$  and  $H_g$  is plotted in Figure 4.12. Acidic cleaning with a 30%  $\text{HNO}_3$  solution shows an increase in  $H_r$  and  $H_r - H_g$  value compared to the

non-acidic baseline cleaning step. This implies that the non-acidic method is insufficient to clean the wafer surface. With an acid cleaning method, the adhesion between the PR and the glass is stronger [206]. As a result, the lateral etching is slowed down, implying that the vertical depth will be higher by the time PR peels off. However, for glass substrates, a further increase in the concentration of the acidic bath from 30% to 69.5% and 99%  $\text{HNO}_3$  decreases texture height. The nitric acid cleaning affects the surface of Corning glass, altering the chemical composition of the glass [217], combined with mild surface etching. This minute surface structure change can cause capillary action and pinning, changing material adhesion [218]. The local surface composition changes during acid etching affect the surface free energy of the wafer. For concentrated baths, the composition changes are vigorous enough to affect PR-Glass adhesion negatively. This explains the decrease in profile height.

Increasing the acidic concentration improves the uniformity of texture over the substrate area. The standard deviation ( $\sigma$ ) = 40 nm for 30%  $\text{HNO}_3$  and  $\sigma$  = 10 nm for 69.5%  $\text{HNO}_3$ . This would imply that the cleaning methodology based on the 30%  $\text{HNO}_3$  has a good adhesive nature, resulting in the deepest textures, but is insufficient to texture the 4-inch wafer area uniformly. For this reason, 69.5%  $\text{HNO}_3$  is selected as an optimised condition in this work.

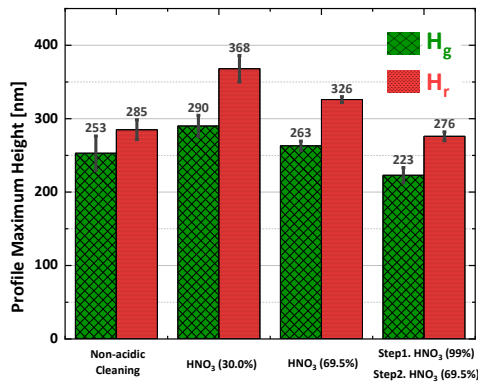


Figure 4.12.: Influence of different cleaning methods on hexagonal texture height. G-axis height ( $H_g$ ) and R-axis height ( $H_r$ ) are plotted. The standard deviation represents the uniformity across the wafer surface area.

#### 4.3.6. Influence of pre-coating bake temperature

Figure 4.13 represents the WCA measured for the glass wafer surface before HMDS exposure and PR coating at different pre-treatment temperatures. The mean WCA peak value is at  $85^\circ$  for the samples pre-coat baked at a temperature of  $110^\circ\text{C}$ . For any temperature above  $110^\circ\text{C}$  physically absorbed hydroxyl groups are removed from the glass. In the optimised processing recipe,  $110^\circ\text{C}$  temperature is used.

#### 4.3.7. Influence of HMDS exposure duration

Figure 4.14 shows the effect of the exposure duration on the PR adhesion. The WCA of wafers primed with HMDS for different periods, from 50 to 150 s, in steps of 50 s at  $130^\circ\text{C}$ , is depicted in the plot. Right after the wafer cleaning step - without HMDS treatment, the WCA is  $45^\circ$ . However,

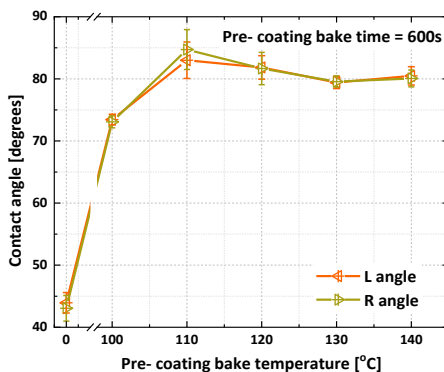


Figure 4.13.: Variation of contact angle with pre-coating bake temperature. Contact angle at Left (L) and Right (R) of the water droplet.

the WCA increases with an increase in exposure duration of HMDS, with a maximum value of  $80^\circ$  attained at 150 s of HMDS priming. The presence of non-polar trimethylsilyl groups on the glass surface [219, 220] decreases the wettability of the surface and, as a result, enhances PR adhesion to the glass.

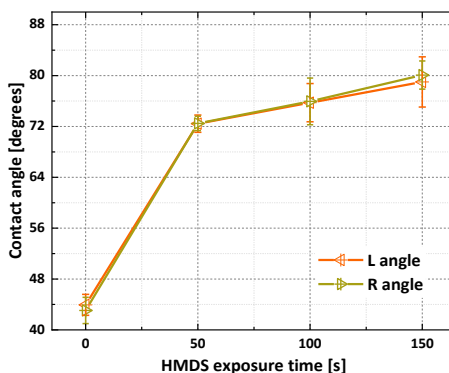


Figure 4.14.: Variation of contact angle with HMDS exposure duration. Contact angle at water droplet's left (L) side and right (R) side.

#### 4.3.8. Influence of hard bake temperature

After developing the coated PR, we observe that the hard baking of wafers results in a change in a pattern called "roundening". Around reflow temperature, the PR softens, and the top surface of the PR changes to a blunt orifice border due to the evaporation of the PR from these parts [215, 216]. The top diameter of orifices has become larger due to the rounding effect, channelling the etchant to the glass surface. Simultaneously, a thermal cross-linking of the PR occurs at the PR-glass interface at elevated temperatures. Compared to baseline processing conditions, the texture height increases with hard baking.

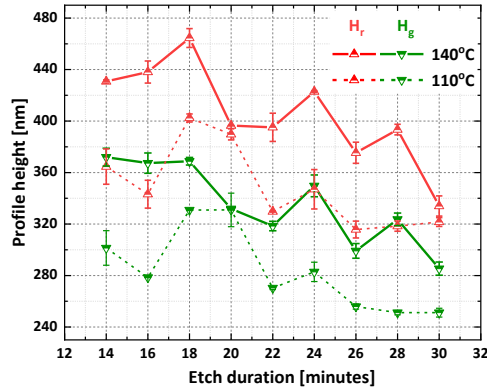


Figure 4.15.: Influence of hard bake temperature on texture height. G-axis height ( $H_g$ ) and R-axis height ( $H_r$ ) are plotted for each time stamp.

Figure 4.15 indicates the texture height along the G and R axes obtained for different etch durations at 110 °C and 140 °C hard baking. After 18 minutes of etching in both hard bake conditions, the maximum texture height is attained. Hard baking at 140 °C results in a deeper texture than at 110 °C for all etch durations. Visually observed, the PR sediment inside the solution significantly reduces for hard-baked samples. This indicates the improved stability of the PR mask in etchant.

The value of  $D_{e,p}$  for hard baking at 110 °C and 140 °C are  $0.78 \pm 0.02$  and  $0.73 \pm 0.02$ , respectively. The drop in  $D_{e,p}$  implies the etching is approaching an isotropic nature, forming the crater with reduced PR peel-off. However, hard baking at such high temperatures can also result in crack formation in the PR, which could allow the etchant to seep in during the wet etching process. This situation causes broken periodicity and unexpected spots on patterns on glass wafers [216]. Changes in PR around reflow temperatures can also shut off some orifices. After etching, such regions appear as unpatterned patches on wafers. This is an after-effect of the nonuniform heating of wafers.

#### 4.3.9. Influence of PR thickness

The samples prepared using the optimised recipe were etched for a time series with 2-minute intervals ranging from 14 to 26 minutes. The variation of texture height along the G and R axes for 2.1  $\mu\text{m}$  and 1.4  $\mu\text{m}$  PR thicknesses is shown in Figure 4.16. After 18 minutes of etching, 2.1  $\mu\text{m}$  PR coating makes deeper hexagons than a 1.4  $\mu\text{m}$  PR coating. The gain in  $H_r$  is a consequence of the protected etching of the honeycomb edges, which is indicated by the same  $H_g$  of 1.4 and 2.1  $\mu\text{m}$  thick PR. We speculate that the thicker coating reduces the influx of etchant ions through the PR. The PR peel-off starts at 16 minutes of etching, but the thickness slows the effect. Beyond 18 minutes, the advantage of using 2.1  $\mu\text{m}$  PR vanishes as the hexagon formation is complete. At 20 minutes, the  $H_r$  value is the same for 1.4 and 2.1  $\mu\text{m}$  thick PR. This is because the etching is prominent for peaks at the R-axis and not for the crest of the G-axis. Other  $H_r$  and  $H_g$  values between 16 and 22 minutes coincide, indicating the etch mechanism is the same once the hexagon formation is complete.

Another significant observation of this experiment is that using 2.1  $\mu\text{m}$  PR avoids unpatterned

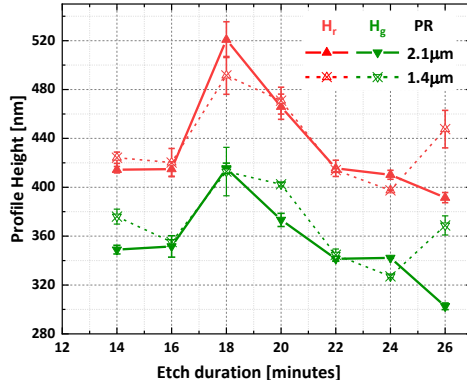


Figure 4.16.: Influence of PR thickness on texture height. G-axis height ( $H_g$ ) and R-axis height ( $H_r$ ) are plotted for each time stamp.

areas on wafers (caused as a result of hard baking 1.4 μm PR at elevated temperatures). This suggests that at 140 °C temperature, the 2.1 μm thick PR does not reflow to the extent that it affects the developed orifice pattern. The  $D_{e,P}$  values of process for 1.4 μm PR and 2.1 μm PR are  $0.73 \pm 0.02$  and  $0.71 \pm 0.02$  respectively.

The optimised processing steps for generating hexagonal microtextures on glass is given in Figure 4.17.

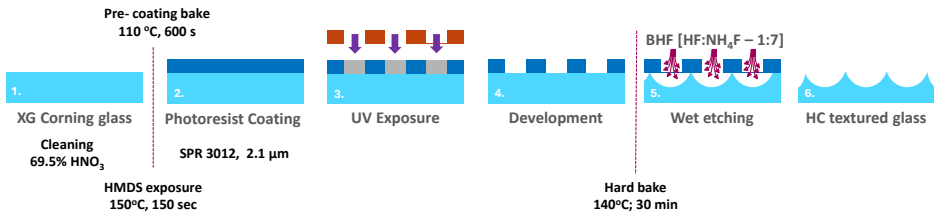


Figure 4.17.: The schematic diagram of optimised processing steps involved in generating hexagonal textures on glass from the conducted experiments.

#### 4.3.10. Influence of periodicity

Figure 4.18 shows the variation in height by changing the orifice periodicity. This figure shows that the profile height increases with the orifice periodicity. The  $H_r = 0.52 \pm 0.01$  μm for 3 μm periodicity,  $H_r = 0.75 \pm 0.01$  μm for 4 μm periodicity, and  $H_r = 1.010 \pm 0.005$  μm for 5 μm periodicity. This implies that the increase in periodicity plays a significant role in increasing the texture's height. The increase of texture height with orifice periodicity across all the etching durations is because point (r) is located farther away from the orifice (o) when P increases. This can also explain why 2 extra minutes are required for complete honeycomb formation for orifice periodicities of 4 μm and 5 μm than for 3 μm.

The  $D_{e,P}$  decreases as the periodicity increases. The  $D_{e,P}$  value for 3 μm orifice periodicity is

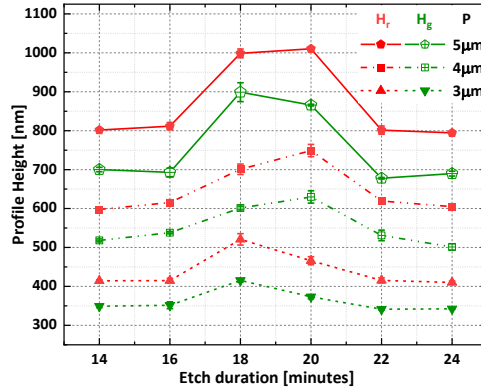


Figure 4.18.: The influence of orifice periodicity on texture height. G-axis height ( $H_g$ ) and R-axis height ( $H_r$ ) are plotted for each time stamp.

$0.70 \pm 0.03$ ; for  $4 \mu\text{m}$  orifice periodicity, it is  $0.67 \pm 0.01$ ; and for  $5 \mu\text{m}$  orifice periodicity, it is  $0.65 \pm 0.01$ . The orifice periodicity of  $5 \mu\text{m}$  makes the hexagonal texture with the highest aspect ratio of  $20.2 \pm 0.1\%$  among all samples used in this study.

#### 4.3.11. Sensitivity of processes, $D_{e,P}$

The effective orifice diameter values,  $D_e$  and  $D_{e,P}$  are recorded in Table 4.1. The magnitude of the drop of  $D_{e,P}$  value for a step implies the increase in isotropism imparted by the corresponding step. The final optimised recipe (refer Figure 4.17) changes  $D_{e,P}$  from  $0.80 \pm 0.01$  to  $0.73 \pm 0.02$  i.e., a decrease in  $D_{e,P}$  by  $0.10 \pm 0.04$ . Hard baking is the critical parameter in this optimisation, which contributed to 70% of this  $D_{e,P}$  decrease. This implies that hard braking is the most critical step in the total process. Further, an increase in periodicity enhances isotropism involved in etching by approximately 3% for every  $1 \mu\text{m}$  increase.

The AFM profile and SEM analysis of honeycomb texture for orifice periodicity  $5 \mu\text{m}$  developed with the optimised recipe is shown in Figure 4.19 (a) and (b). It shows the hexagons have changed from craters with flat bases under the baseline recipe in Figure 4.11 (b), (c), to craters with curved bases under optimised processing conditions.

Process	$H_r$ [nm]	$D_e$ [nm]	$D_{e,P}$ [-]	AR [%]
Baseline	$336 \pm 4$	$2800 \pm 15$	$0.80 \pm 0.01$	$11.2 \pm 0.1$
Hard Baking $110^\circ\text{C}$	$370 \pm 5$	$2720 \pm 17$	$0.78 \pm 0.02$	$12.3 \pm 0.2$
Hard Baking $140^\circ\text{C}$	$460 \pm 8$	$2540 \pm 20$	$0.73 \pm 0.02$	$15.3 \pm 0.3$
PR Thickness = $1.4 \mu\text{m}$	$491 \pm 12$	$2480 \pm 26$	$0.71 \pm 0.02$	$16.3 \pm 0.4$
Opt. Recipe, P = $3 \mu\text{m}$	$521 \pm 13$	$2420 \pm 26$	$0.70 \pm 0.03$	$17.3 \pm 0.6$
Opt. Recipe, P = $4 \mu\text{m}$	$748 \pm 10$	$3120 \pm 23$	$0.67 \pm 0.01$	$18.8 \pm 0.2$
Opt. Recipe, P = $5 \mu\text{m}$	$1010 \pm 3$	$3750 \pm 14$	$0.65 \pm 0.01$	$20.2 \pm 0.1$

Table 4.1.: Texture height, effective orifice diameter, and the associated parameters of each etching duration series presented in this manuscript.

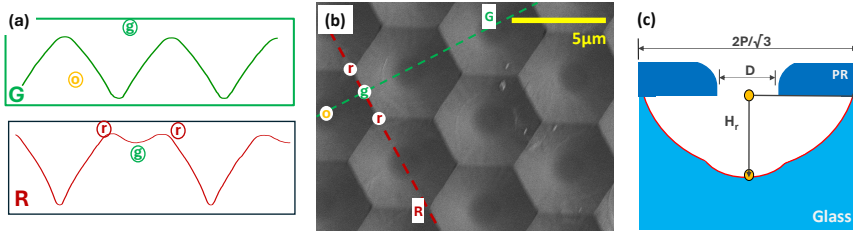


Figure 4.19.: Honeycomb textures with optimised processing conditions (etching time of 20 minutes) with  $H_r = 1.010 \pm 0.005 \mu m$ . (a) The 2D surface profile along the G-axis and R-axis, as extracted from AFM (the profiles are not to scale). (b) SEM image. The encircled letters are added to aid in interpreting the image. (c) Conceptual drawing of the cross-section with hard-baked PR

4

#### 4.3.12. Potential of hexagonal textures on glass

Figure 4.20 shows the distribution of surface angles of hexagonal microtextures made on glass with 3 μm, 4 μm, and 5 μm periodicity. The isometric views of AFM scans are shown in the inset. The distribution of surface normal values of hexagons shows two major peaks. As elaborated in Figure 4.21, the first peak occurring between 5° and 15° represents crater bases and honeycomb boundaries. This peak's intensity and absolute value combined represent the honeycombs' flatness. The second peak beyond the 15° angle represents the curved surface of the honeycomb textures. The intensity of this peak is representative of the steepness of the honeycomb. With an increase in periodicity, both peaks shift toward smaller angles.

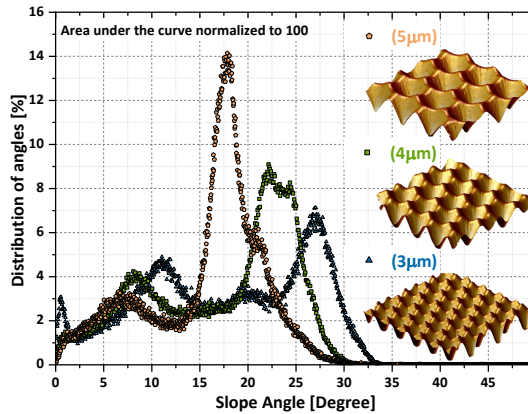


Figure 4.20.: Distribution of surface vectors of the deepest obtained honeycomb texture for different periodicities, in terms of percentage of occurrence. The isometric view of AFM (scan size  $16 \mu m \times 16 \mu m$ ) is shown inset.

Figure 4.22 shows the total and diffuse transmittance corresponding to these samples. The total transmission ( $T_{TOT}$ ) increases with periodicity, specifically for long wavelengths. Below 800 nm, a periodicity increase of 1 μm shows a gain of 1% in total transmission. Beyond 850 nm, 4 μm,

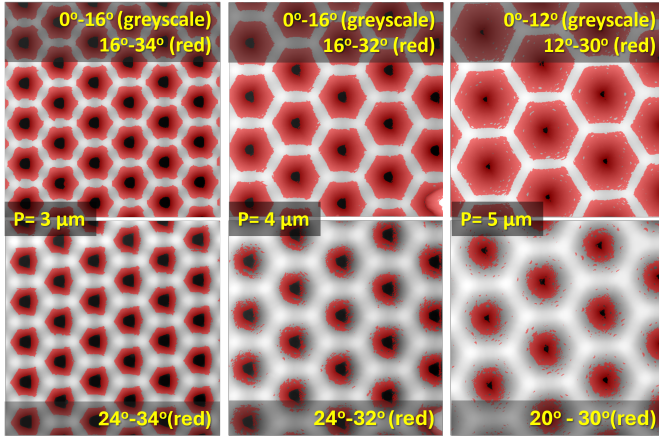


Figure 4.21.: Surface slopes of honeycomb textures for different periodicity. The angle ranges in each image correspond to peaks in Figure 4.20.

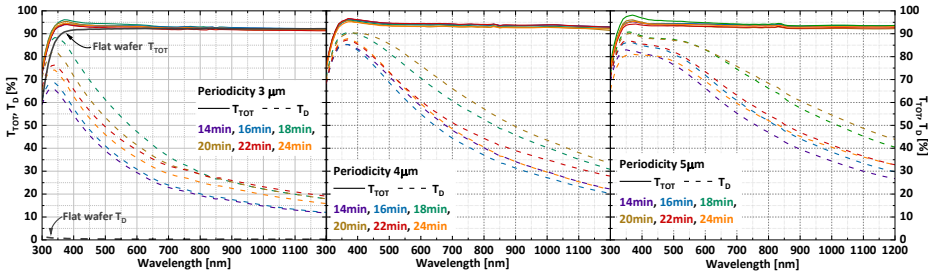


Figure 4.22.: Total transmission (solid lines) and diffused transmission (dashed lines) spectra of hexagonal textures with periodicity 3  $\mu\text{m}$  (top), 4  $\mu\text{m}$  (middle) and 5  $\mu\text{m}$  (bottom). Each periodicity has six samples for an etching time of 14 to 24 minutes with 2-minute intervals.

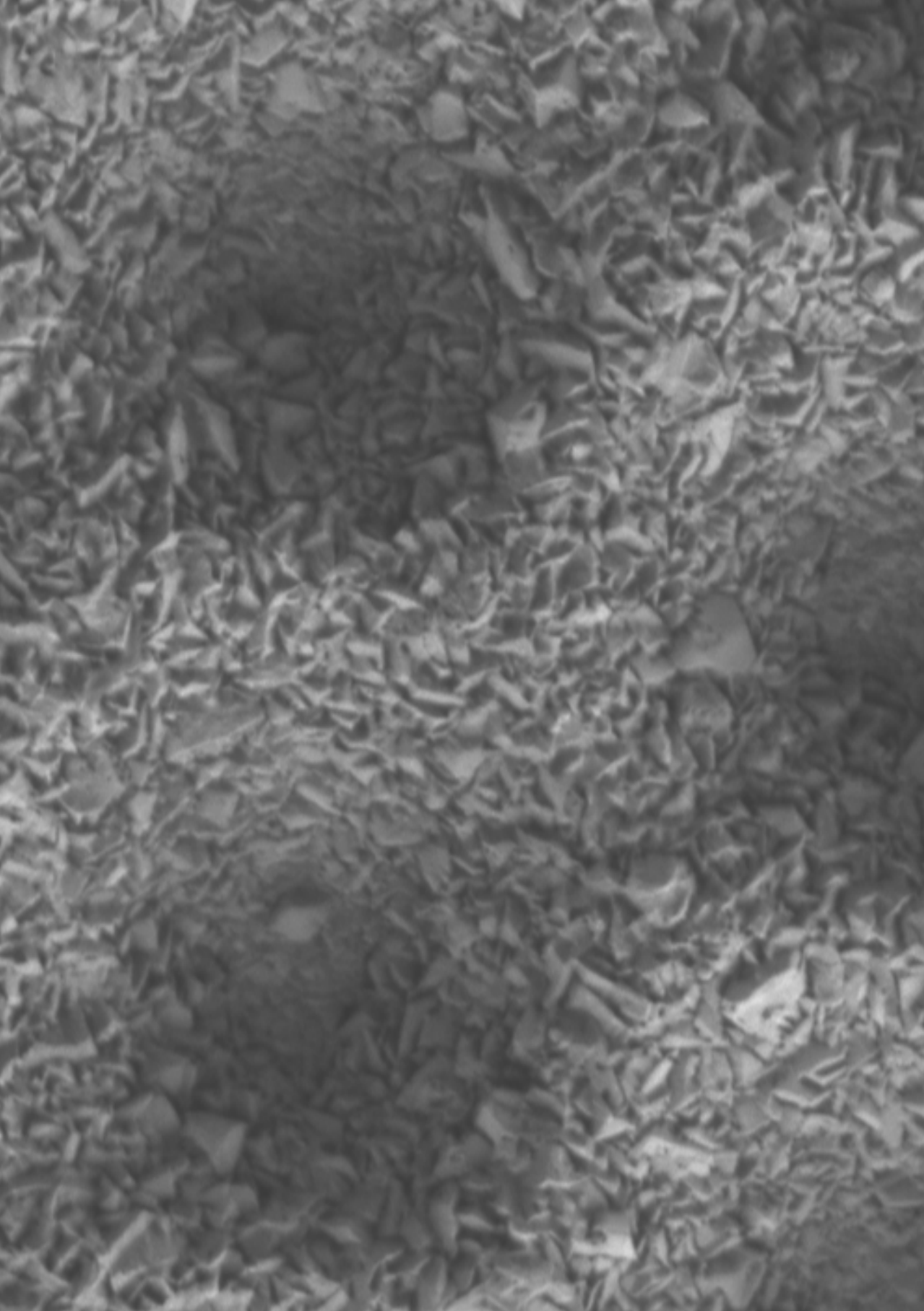
and 5  $\mu\text{m}$  periodicity show similar transmission with an increase of 2% compared to 3  $\mu\text{m}$  texture. The diffused transmittance ( $T_D$ ) of hexagonal textures increases with periodicity. This observation correlates to the smaller surface angles of 5  $\mu\text{m}$  hexagons. The hexagonal textures scatter short-wavelength light the best and show a drop in  $T_D$  for longer wavelengths. The drop is steepest for 3  $\mu\text{m}$  periodicity, followed by 4  $\mu\text{m}$  and 5  $\mu\text{m}$ , respectively. The diffusive nature of the hexagonal texture on glass depends on the crater height. It can be observed that the highest transmittance spectra of each time series for  $\mu\text{m}$ , 4  $\mu\text{m}$  and 5  $\mu\text{m}$  periodicities correspond to the deepest sample in the set. In general, hexagonal features with higher periodicity values and deeper texture exhibit high optical transmission and scattering properties.

## 4.4. Conclusion

A detailed analysis of the processes used to make honeycomb textures in glass superstrates has been conducted. The influence of these processing parameters, especially their effect on texture depth, is studied in detail.

Glass wafer surfaces require acidic cleaning to facilitate proper adhesion between glass and PR. This was done by cleaning the glass superstrates with 69.5%  $\text{HNO}_3$  followed by a running water dip and spin-drying. Pre-baking of wafers at 110 °C for 10 minutes before coating with PR ensured the removal of any amount of adsorbed water from the surface. Additionally, it was noted that during the coating step, priming the surface with HMDS at 150 °C for 150 s best removes the polar hydroxyl groups to improve the surface adhesion towards PR. Using a 2.1  $\mu\text{m}$  for SPR3012 reduces the diffusion of the etchant ions through the PR. Post development, the samples were hard-baked at 140 °C for 30 minutes to enhance PR adhesion via cross-linking. Using these parameters, honeycombs were made on glass wafers with varying periodicities of 3  $\mu\text{m}$ , 4  $\mu\text{m}$  and 5  $\mu\text{m}$ . At 5  $\mu\text{m}$ , hexagonal microtextures with 1010 nm absolute depth are obtained.

Hexagonal texturing on glass does not exhibit perfectly isotropic etching, a property dedicated to the spatial distribution of orifices. A parameter,  $D_{e,P}$ , is defined, successfully quantifying the extent of isotropism exhibited by the texturing process. The total transmission and scattering of light by hexagonal textures depends on their angle distribution. As the periodicity and height of the texture increase, hexagonal microtextures exhibit enhanced transmission and scattering properties.





# 5

## Thin-film Silicon solar cells on Hexagonal Microtextured Glass

This chapter is based on the publication:

G. Padmakumar, A. Balaji, F. Saitta, P. Perez-Rodriguez, R.A.C.M.M. van Swaaij, A.H.M. Smets, "Hexagonal Microtextured Glass to Achieve High Optical Performance in Thin-Film Silicon Solar Cells" *Solar Energy*, 306 (2026), 114292. DOI:10.1016/j.solener.2025.114292

*Periodic hexagonal microtexture arrays (also known as honeycombs) are successfully implemented for the first time in a superstrate glass configuration. Hexagonal textures on glass demonstrate an anti-reflective effect when compared to flat glass. It is shown that the light scattering increases at the honeycomb interfaces with an increase in texture height and periodicity. The performance of the textures is demonstrated using thin-film single-junction PV devices based on an indirect bandgap semiconductor material, nanocrystalline silicon (nc-Si:H), which requires light trapping in the infrared region of the spectrum. Inspecting the nc-Si:H bulk absorber suggests a conformal, crack-free growth of crystals on the hexagonal arrays. Short-circuit current density ( $J_{SC}$ ) increases with an increase in aspect ratio of the superstrate, without compromising on voltage and fill factor. The  $J_{SC}$  enhancement is attributed to a combined benefit of (i) the anti-reflective nature of developed textures, (ii) trapping light within the absorbing layer through multiple order diffraction at the front and (iii) reflection from a back reflector with adapted hexagonal morphology. With the above observations, a  $J_{SC}$  of  $28.6 \text{ mA/cm}^2$  (photovoltaic conversion efficiency of 9.3%) is achieved for a  $5\mu\text{m}$  periodic texture with a height of  $1\mu\text{m}$  (aspect ratio = 0.21). This is the highest reported  $J_{SC}$  for a single-junction nc-Si:H solar cell in a superstrate configuration without an external anti-reflection coating.*

## 5.1. Introduction

For thin-film solar cell technologies, such as copper indium gallium selenide, cadmium telluride, amorphous silicon, nano-crystalline silicon and perovskite, minimising absorber-layer thickness offers multiple benefits, including high production throughput, lower production costs, improved stability against light-induced degradation and enhanced carrier collection. To achieve high efficiency with thin layers, these photovoltaic (PV) devices require enhanced optical performance, which is accomplished by increasing light coupling and light trapping [221]. This is typically achieved using random or periodic textures that scatter light at the interfaces. This extends the light path length, thereby improving photoconversion efficiencies [64, 72, 198, 221, 222]. Random textures have been extensively explored and correlated with an enhanced optical performance [77, 79, 144, 223]. In recent years, periodically textured substrates have been extensively studied as an alternative route and have been reported to achieve current densities higher than those conventionally used with randomly distributed textures [47, 67, 73, 224].

Typically employed periodic textures are either pyramidal in shape or two-dimensional (2-D) gratings. However, thin-film PV technologies with a crystalline phase in the absorber are not compatible with the steep slopes of the pyramidal shape [46, 110, 144]. In contrast, a 2-D grating shape facilitates high-quality crystal growth [46]. The periodic shape that can cover an area with the least perimeter is a hexagon [186]. For crystal depositions, hexagon-shaped textures (also known as honeycomb (HC) textures) minimise the length of sharp boundaries created by texture borders, thereby reducing defect formation [187]. Different methods to make hexagonal-shaped periodic textures on potential solar cell substrates include nanoimprint lithography [188, 193], laser ablation (for sheet metals) [189, 194], or photolithography [187, 190, 225]. HC textures have been previously implemented in monocrystalline silicon solar cells [222, 226], as well as in thin-film solar cell technologies [193, 227]. In wafer-based technology, HC textures are implemented on the illuminated side of wafer substrates [198, 222, 226]. In thin-film technology, hexagonal periodic arrays are typically employed on opaque substrates on the reflective side [11, 18, 168, 187, 227]. The photoactive layers are subsequently deposited on these arrays. In such cases, the morphology features flatten out when multiple layers are stacked on top of it. This means that the morphology of the illuminated cell surface is not a replica of the hexagons [204] and fails to capitalise on the full light-management potential of texture. On the contrary, superstrate configuration enables us to implement textures on the illumination side of a solar cell, typically on transparent superstrates [77, 228]. Thus, the initial light scattering before entering the photoactive layers in the superstrate configuration is independent of layer conformality. A feasible method for creating HC textures on glass is to use photolithography [140, 213]. The optical properties of hexagonal textures on glass and their implementation in superstrate-configuration solar cells have not been extensively explored yet and are the primary focus of this article.

For the first time, this article presents a comprehensive optical characterisation of hexagonal micro-sized textures on glass. The optical interaction is correlated with the physical height and surface features of the hexagons. Finally, we explore the effect of periodic front-textured glass on solar cell performance. The HC-textured glass is utilised as a superstrate for an indirect band-gap material, such as hydrogenated nanocrystalline silicon (nc-Si:H), to fabricate single-junction solar cells. Additionally, we examine the quality of silicon crystal growth on the texture.

## 5.2. Materials and Methods

### 5.2.1. Generating Hexagonal Textures on Glass

This study uses Corning glass XG Boro-alumino-silicate glass wafers, with a 4-inch diameter and 0.7 mm thickness, featuring a primary flat side [148, 149]. UV photolithography is used to generate

HC textures on the glass superstrates. A flowchart of this approach is presented in Figure 5.1. In Step 1, the Corning glass wafer is cleaned with 69.5%  $\text{HNO}_3$  for 3 minutes. The wafer is dried and annealed in Step 2 at 110 °C for 10 minutes (pre-coating bake). In the subsequent Step, the wafer is exposed to hexamethyl disilazane (HMDS) for 150 seconds at 150 °C, using nitrogen as the carrier gas. In Step 4, 2.1  $\mu\text{m}$  of Shipley SPR3012 positive photoresist is spin-coated. An extra annealing (post-coating bake) is then performed at 100 °C for 90 s. In Step 6, UV exposure is conducted using a chromium reticle with periodically distributed holes. The periodicity ( $P$ ) of hexagonal textures is directly determined by the orifice periodicity of photoresist masks produced by UV lithography. Step 7 involves pattern development, in which the exposed areas of the photoresist are removed. The photolithography technique implemented on glass requires an additional hard-bake (Step 8 - post-development bake) at 140°C for 30 minutes. In Step 9, the pattern is transferred from the mask to the Corning glass wafer through a 20-minute dip in premade buffered hydrofluoric acid (BHF), comprised of ammonium fluoride ( $\text{NH}_4\text{F}$ ) (40%): hydrofluoric acid (HF) (49%) in ratio 7:1. The wafer is then rinsed with deionised (DI) water, and the remaining photoresist is removed. The processing parameters in the flowchart shown are optimised so that the etched hexagonal shapes beneath the photoresist mask are well-defined and not over-etched. The detailed concepts and optimisation of the steps involved in creating hexagonal textures on glass are discussed elsewhere [140]. An image of these HC textures obtained by atomic Force Microscopy (AFM) is given in Figure 5.2.

For the physical and optical characterisation of HC in this study, 75 different hexagonal microtextured glass wafers were fabricated. Each sample has a surface that is geometrically different from the others. This ensures an extensive sample set of hexagonal patterns on glass, which has not been attempted in the literature. Of the 75 glass wafers, 61 samples exhibit a periodicity of 3  $\mu\text{m}$ , with heights ranging from 150 nm to 521 nm. Seven samples were created with periodicities of 4  $\mu\text{m}$  and 5  $\mu\text{m}$ , having height ranges of 590 to 748 nm and 802 to 1012 nm, respectively. The sample with maximum attained height for 3  $\mu\text{m}$ , 4  $\mu\text{m}$  and 5  $\mu\text{m}$  periodicity is named HP3, HP4 and HP5, respectively.

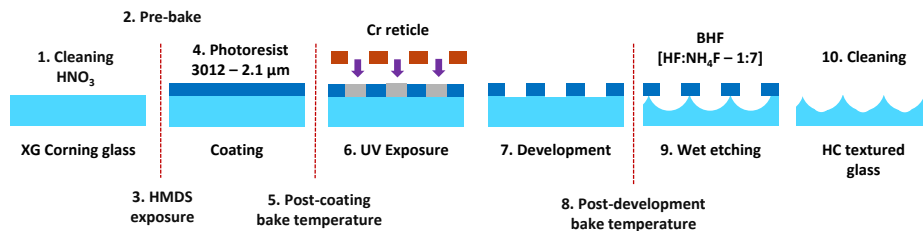


Figure 5.1.: Process flow for generating hexagonal microtextures (HC) using UV photolithography on Corning glass superstrates.

### 5.2.2. Physical characterisation of hexagonal microtextures

AFM maps the surface morphology of HC textures using a Bruker AFM FastScan in FastScan closed-loop scanner head mode. Scanning areas of 16  $\mu\text{m} \times 16 \mu\text{m}$  are used. Extraction of feature

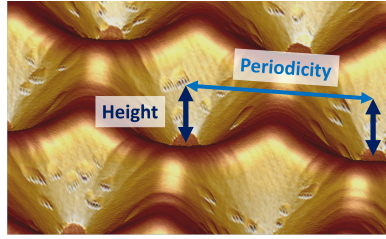


Figure 5.2.: AFM image of hexagonal microtextures developed on glass. Height and periodicity of the textures are also demonstrated. Other significant dimensions related to hexagons are given in Appendix B, Figure B.2.

heights from AFM images was conducted using NanoScope Analysis (version 2.0) software from Bruker. The distribution of angles subtended by surface vectors with respect to the vertical plane is used as a metric to analyse surface angles ( $\theta_s$ ) in Gwyddion (version 2.63). The 2D power spectral density (PSD) plot is a quantitative measure of surface features. PSD is a spatial frequency representation of the morphology based on the discrete 2-dimensional Fourier transform of the height-height correlation function [65, 154, 155].

After the deposition of the front electrode IOH, the sheet resistance ( $R_{sheet, IOH}$ ) is determined using the four-point probe (4PP) method. This measurement is carried out at 23 °C with an AIT CMT-SR2000N system, which uses four contacts arranged linearly and equidistant with a 1 mm gap.

### 5.2.3. Transmission characterisation of hexagonal microtextures

For measuring transmission, all glass samples were probed with light on the flat side, as shown in Figure 5.3 (a). The LAMBDA 1050+ UV/Vis/NIR spectrophotometer, equipped with a 150 mm InGaAs integrating sphere from PerkinElmer, is used to record the optical transmission. This measurement was performed over a wavelength ( $\lambda$ ) range of 300 to 1200 nm in 10 nm increments. The total transmission ( $T_{TOT}$ ) is measured as a percentage ratio of transmitted light to total incident light. The diffused transmittance ( $T_D$ ) is measured as a percentage ratio of the non-specular component of light to the total transmitted light.

### 5.2.4. Angular intensity distribution (AID) measurement of hexagonal microtextures

A wafer with periodic hexagonal microtextures exhibits diffractive patterns under white light. Figure 5.3(B) shows a textured wafer under a TL lamp viewed with bare eyes. To determine the extent of angular scattering of the HC textures, the AID of transmitted light was recorded using the 180 mm automated reflectance/transmittance analyser (ARTA) accessory on a LAMBDA 950 PerkinElmer unit. A schematic diagram of the setup is shown in Figure 5.4(A). Measurement details of AID for transparent objects can be found elsewhere [157, 228]. The ARTA detector moves in a cylindrical plane with the sample at the centre. The sample is positioned in a plane perpendicular to the direction of the incoming light ray. The motion of the detector is shown in Figure 5.4(A). The AID measurement was performed over a  $\lambda$  range of 300 nm to 1000 nm. The AID is measured in transmission mode, and the angle values range from 0 to 90°, where the angles indicate the position of the detector with respect to the surface normal of the sample. It is to be noted that only a quarter of the transmission sphere is required, as the AID curve is symmetric.

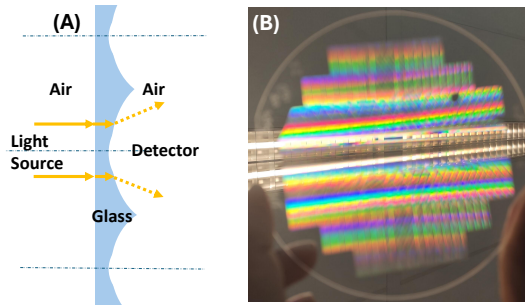


Figure 5.3.: (A) Orientation of textured wafers with respect to the light source and detector for optical measurement. (B) A wafer with hexagonal microstructures viewed under a tube-luminescent lamp. The 2D hexagonal periodicity of the hole positions drives the rainbow effect.

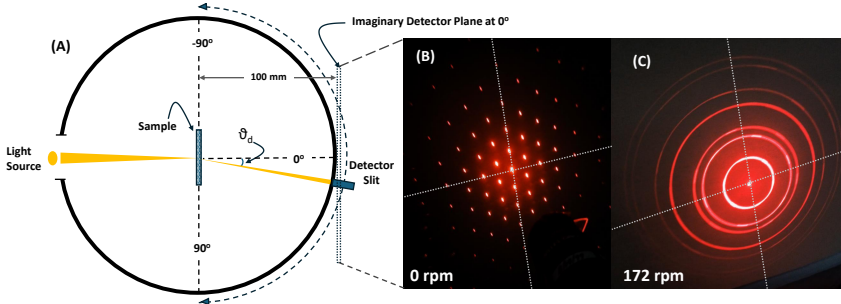


Figure 5.4.: (A) Top view of ARTA accessory on a LAMBDA 950 PerkinElmer unit. The direction of the sweep, the sample position, and the light ray are depicted in the picture. (B) Far-field diffraction pattern of hexagonal microtextures interacting with a 635 nm laser. The hexagonal array of diffraction orders mirrors the symmetry of the surface craters. (C) The pattern in (B) was transformed into circles at a rotation speed of 172 rpm.

When analysing the results of the ARTA tool, it was assumed that a texture serves as a random scatterer, which challenges the measurement of 2D surface gratings that exhibit multiple diffraction peaks in a 2D plane. Figure 5.4 (B) is the photograph of the far-field pattern (in transmission mode) generated by the HC textured wafer when probed with a 635 nm laser on a plane parallel to the wafer. The six-fold symmetrical texture of the sample yields a pattern featuring first, second, third, up to an  $n^{\text{th}}$  order spots, as illustrated. To account for light spots, which are otherwise located at an angle to the horizontal plane in the measurements, the wafer is rotated at of 172 rotations per minute (rpm) about its vertical axis. This rotation, in turn, converts all the light spots into rings representing the maxima and minima of the patterns, as shown in Figure 5.4 (C). In this approach, light ring intensities are incident on the detector over a sufficient time and the values are recorded.

### 5.2.5. Fabrication of solar cells

The optical characterisation conducted on the texture is in an air/glass/air system, where the incident light ray at glass/air interface has a higher to lower refractive index variation. A solar cell has an air/glass/silicon/back-reflector system, where the incident light ray at glass/silicon interface has a lower to higher refractive index variation. This difference makes the study on air/glass/air system not one-to-one translatable to solar cells. Therefore, to evaluate the potential of textured interfaces, multiple solar cells are fabricated with following specifications on different texture heights and periodicities.

The solar cell architecture employed in this study is shown in Figure 5.5. Solar cells were fabricated on hexagonal-textured wafers with periodicities of 3  $\mu\text{m}$ , 4  $\mu\text{m}$ , and 5  $\mu\text{m}$ . Single-junction nc-Si:H solar cells were fabricated in a superstrate configuration. The solar cells have hydrogenated indium oxide (IOH) as the front transparent conductive oxide (TCO). IOH is RF magnetron sputtered from a ceramic indium oxide ( $\text{In}_2\text{O}_3$ ) target in  $\text{Ar}/\text{O}_2/\text{H}_2\text{O}$  mixtures. The trace of water vapour suppresses crystal growth of IOH, which results in deposition of amorphous IOH [158, 229]. 150-nm thick IOH layer has  $R_{\text{sheet},\text{IOH}} = 21 \pm 0.7 \Omega/\text{sq}$ . The silicon alloy deposition was done in a plasma-enhanced chemical vapour deposition (PECVD) multi-chamber tool with dedicated processing chambers for the boron-doped hydrogenated nano-crystalline silicon oxide p-layer (B-doped (p)nc-SiO<sub>x</sub>:H), intrinsic hydrogenated nanocrystalline silicon ((i)nc-Si:H) and phosphorus-doped hydrogenated nano-crystalline silicon oxide n-layer (P-doped (n)nc-SiO<sub>x</sub>:H). The B-doped nc-SiO<sub>x</sub>:H layer (16 nm thick) and P-doped nc-SiO<sub>x</sub>:H n-layer (20 nm thick) were deposited using radiofrequency (13.8 MHz) in the PECVD tool at 180 °C substrate temperature and using  $\text{B}_2\text{H}_6$  and  $\text{PH}_3$  as dopant gasses, respectively. The (i)nc-Si:H absorber layer was deposited at very high frequency (40.68 MHz) at a deposition rate of 0.49  $\text{\AA}/\text{s}$  at 170 °C substrate temperature. In PECVD processing, the deposition rate on textured surfaces is lower than on flat glass. This deposition rate scales down by a factor equivalent to the effective surface area change by texturing [230]. Based on this value, the deposition rates of all layers in the aforementioned solar cells are adjusted to achieve similar layer thicknesses across different textures. The solar cells have a back reflector consisting of i-ZnO (60 nm) sputtered at a substrate temperature of 200 °C and an evaporated silver (300 nm) layer. i-ZnO acts as a suppressor for the surface plasmon resonance at the silver-silicon layer interface [231]. The front contact is a 500 nm thick aluminium layer (not shown in the figure 5.5), and the back contact comprises chromium (30 nm) and aluminium (500 nm). The solar cell area is defined by 5 mm  $\times$  5 mm squares. This results in a solar cell structure of IOH (150 nm) / (p)nc-SiO<sub>x</sub>:H (16 nm) / (i)nc-Si:H (3200 nm) / (n)nc-SiO<sub>x</sub>:H (20 nm) / i-ZnO (60 nm) / Ag (300 nm) for single junction solar cells. No anti-reflective coating was used at the front of any of the solar cells presented in this study.

### 5.2.6. Characterisation of solar cells

The solar cells are characterised by their current density-voltage (J-V) performance and external quantum efficiency (EQE). J-V measurements are conducted at 25 °C using a WACOM-class AAA xenon-halogen dual-lamp continuous solar simulator, mimicking AM1.5G illumination (100  $\text{mW}/\text{cm}^2$ ). EQE was measured using an in-house-developed tool with monochromatic light. EQE measurements are performed at a short-circuit condition of 0 V and at a reverse bias condition of -2 V in some cases. Short-circuit current density ( $J_{\text{SC}}$ ) was calculated by integrating the EQE measurements of solar cells against the AM1.5G spectrum, denoted  $J_{\text{sc},\text{EQE}}$  henceforth. This helps to prevent the over- or underestimation of current caused by any mismatch between the solar spectrum and the WACOM solar simulator. This approach also eliminates errors in estimating the active cell area in small-area solar cells. The total absorptance of the solar cell ( $1 - R$ ) is derived from reflectance ( $R$ ), which is also recorded using a UV/Vis/NIR

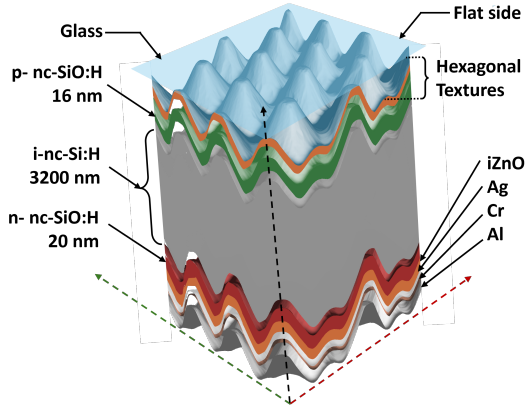


Figure 5.5.: Cell architecture and layers of an nc-Si:H single-junction solar cell.

Spectrophotometer. Renishaw inVia Raman microscope is used to determine the crystallinity ( $\chi_c$ ) of the nc-Si:H absorber with a 633 nm red laser. In addition, scanning electron microscopy (SEM) with Hitachi Regulus 8230 at an acceleration voltage of 1.5 kV is used to create cross-sectional images of solar cells on glass.

## 5.3. Results and Discussion

### 5.3.1. Surface profile of hexagonal craters

An isometric view of the hexagonal textures on a Corning glass wafer, along with its characteristic dimensions, is given in Figure 5.6 (A). The two axes, named as R-axis and G-axis, represent the innate 30° asymmetry of the surface morphology in HC. AFM images of HP3, HP4 and HP5 are shown in Figure 5.6 (B), (D) and (F) respectively and the corresponding extracted surface profile data are given in 5.6 (C), (E) and (G). The observed nature of craters is typically spherical, with no flat bases. We observe that, for a fully developed hexagonal pattern on a glass superstrate, the maximum height along the R-axis (referred to as  $H_r$  henceforth) and the maximum height in the G-axis (referred to as  $H_g$  henceforth) are different. We consider  $H_r$  as the characteristic height of the texture and define the aspect ratio (AR) as  $H_r/P$  as conventionally used in literature [47, 198, 204, 225, 232]. For the same processing conditions, all three parameters —  $H_r$ ,  $H_g$  and AR — increase with HC periodicity. An inverted conical protrusion, with a saddle point, is present at the intersection point of three hexagons. Each saddle point is located at a distance of  $P/2$  from the adjacent saddle points. The R-axis is chosen so that the saddle points (and conical features) are positioned along this axis. The height difference between the two axes,  $H_r - H_g$ , represents the height of the saddle. This idea of  $H_r - H_g$  is illustrated in 5.6 (C), (E) and (G).

The summary of all height parameters shown in these images is presented in Table 5.1.  $H_r$ ,  $H_r - H_g$  and AR increase with an increase in periodicity. For the cross-section profiles along the G and R axes, the surface profiles can be fitted to a good agreement with fragments of circles. These circles and corresponding radii of the fitted spheres are shown in Appendix B, Figure B.5. In total, four significant height features are present in the hexagonal textures, in descending order:  $P$ ,  $H_r$ ,  $H_g$ , and  $H_r - H_g$ .

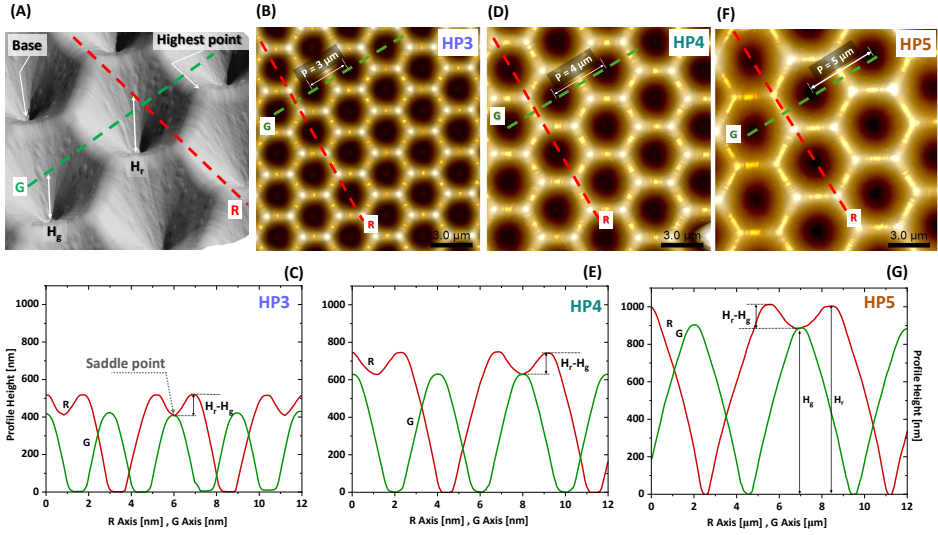


Figure 5.6.: AFM data visualised for hexagonal microtextures on glass. The 30° asymmetrical directions are highlighted by two lines, namely the R-axis and the G-axis. (A) The isometric view of HC. The highest point of the texture, the base of the crater and two defined axes, the R-axis and G-axis, are illustrated. Top view of (B) HP3 and (C) the corresponding R and G axes profiles (D) HP4 and (E) the corresponding R and G axes profiles, (F) HP5 and (G) the corresponding R and G axes profiles.

Superstrate	$P$ [ $\mu\text{m}$ ]	$H_r$ [nm]	$H_g$ [nm]	$H_r - H_g$ [nm]	AR [%]	Surface Area (of $16 \mu\text{m} \times 16 \mu\text{m}$ projected area) [ $\mu\text{m}^2$ ]
HP3	3	521	412	109	17.3	272.7
HP4	4	748	628	120	18.8	270.9
HP5	5	1012	865	147	20.2	267.8

Table 5.1.: Height and area parameters of the hexagonal textures.

### 5.3.1.1. Slope distribution of the craters

The occurrence distribution of  $\theta_s$  for HP3, HP4 and HP5 is recorded in Figure 5.7. For each sample, three sets of angles can be identified as follows. Set 1: angles  $< 3^\circ$  marking the inflexion points on the texture morphology. This includes crater boundaries, the saddle points and the bottom flatness of the hexagons. Set 2: angle between  $5^\circ$  and  $15^\circ$ . This region represents the neighbourhood of the inflexion regions. Set 3: angles  $> 15^\circ$  represents the walls of the hexagonal surface. This set of angles determines the tapering angle of the hexagonal grating. Set 3 has the highest contribution to the total  $\theta_s$  in all three samples.

An overall trend is observable for all three sets. For HP3, the peak in angle Set 1 indicates that

the flat regions are more pronounced in HP3 than in HP4 and HP5. HP3 has broader boundaries and flatter bases. Sets 2 and 3 show a shift of the peak towards smaller angles with increasing periodicity, indicating that the crater walls become less steep as the periodicity increases. This is an interesting observation, considering that the texture height follows the order  $HP5 > HP4 > HP3$ . Further, this observation implies that higher periodicity in hexagonal craters results in deeper textures and decreased steepness. For Set 3, HP5 has a concentrated peak occurrence when compared to HP3 and HP4, indicating a uniform taper for HP5 craters.

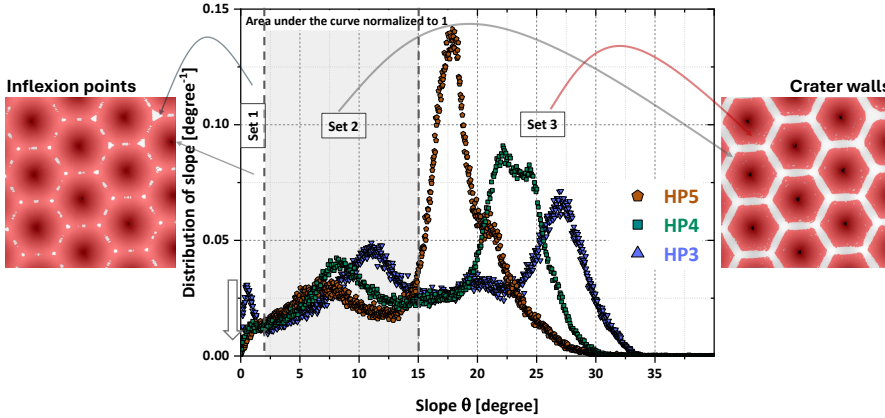


Figure 5.7.: Surface normal distribution curves of HP3, HP4 and HP5 in terms of angles. The occurrence value is normalised such that the total for each curve adds up to 1. Arrows mark different angle sets - HP5 is used for demonstration purposes. A detailed contribution of surface morphology to the angles is provided in Appendix B, Figure B.1.

### 5.3.1.2. Micro-scale and nano-scale features

PSD analysis of the HP3, HP4 and HP5 surfaces is presented in Figure 5.8. The PSD of a texture at low frequencies (Zone 1) indicates the presence of features with large lateral and vertical dimensions. The high-frequency zone (Zone 2) represents small features in the texture. Beyond Zone 2 is the decay zone where the fractal nature and noise come into effect [65, 154]. In Zone 1, the highest value of PSD occurs for HP5, followed by HP4 and HP3 at their respective  $P^{-1}$  values. The periodicity of the textures determines the most prominent features in the sample. The high PSD values in Zone 1 are indicative of the height  $H_r$ . The highlighted Zone 2 includes the spatial frequency of saddle points ( $2P^{-1}$ ) in the morphology. In this high-frequency zone, HP5 shows more small-scale features than HP4 and HP3.

## 5.3.2. Optical interaction of hexagonal textures

### 5.3.2.1. Hexagonal textures in Transmission

Figure 5.9 plots the  $T_D$  values in % versus  $H_r$  at  $\lambda$  of 300 nm, 400 nm, 600 nm, 800 nm, 1000 nm and 1200 nm for 21 samples (7 samples each for periodicities 3  $\mu\text{m}$ , 4  $\mu\text{m}$  and 5  $\mu\text{m}$ ) with well developed hexagonal shapes. The lines serve as guides for the eye to identify the effect of  $H_r$  and periodicity on  $T_D$  in Figure 5.9. The change in  $T_D$  is almost negligible for  $\lambda = 300$  nm. For  $\lambda = 400$  nm,  $T_D$  saturates at around 85%. As  $H_r$  and periodicity increase, the  $T_D$  increases linearly for

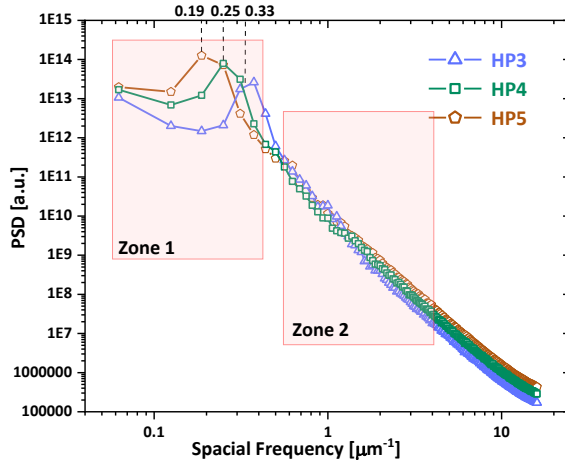


Figure 5.8.: PSD curves of HP3, HP4, and HP5 hexagonal microtextures. The reciprocal values of periodicity, i.e.,  $1/3$ ,  $1/4$  and  $1/5$  are marked on the horizontal axis.

5

all  $\lambda > 600$  nm. At  $\lambda = 1000$  nm,  $T_D \approx 50$  %. Based on the observed trend, the  $T_D$  of light for  $\lambda > 600$  nm could be further increased by increasing the texture height or periodicity. However, to conclude, an extended sample set is required. The scattering trend of short-wavelength light in this graph stands out as it does not show a direct relation with hexagonal feature sizes. This is explored further.

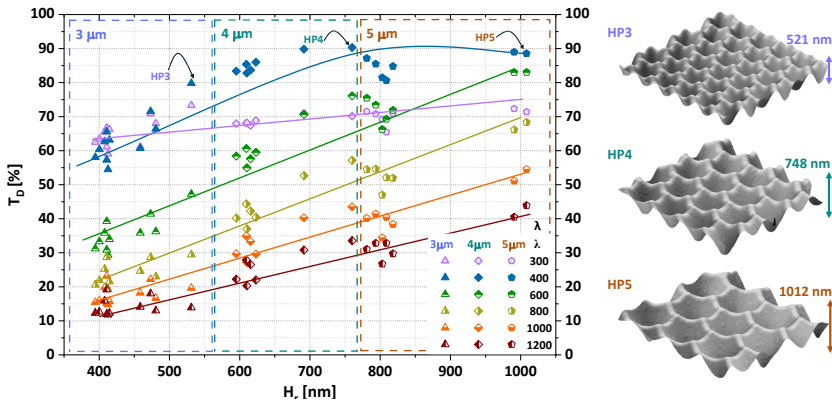


Figure 5.9.: Diffused transmission of different wavelengths versus profile height of  $3 \mu\text{m}$ ,  $4 \mu\text{m}$  and  $5 \mu\text{m}$  periodicity hexagonal micro textures (21 samples). The lines in the image are guides to the eye.

$T_D$  of hexagonal textured wafers is plotted against the height of the saddle region in Figure 5.10. The value  $H_r - H_g$  represents the height of the saddle region. The graph includes  $T_D$  values in % for  $\lambda$  at  $300$  nm,  $400$  nm,  $600$  nm,  $800$  nm,  $1000$  nm and  $1200$  nm for 75 glass wafers. The solid lines are meant to guide the eyes. Overall,  $T_D$  increases with increase of  $H_r - H_g$ . But the rate of increase

differs with the  $\lambda$  of light. For  $\lambda < 600$  nm, there is a rapid increase in scattering. For  $\lambda = 300$  nm,  $T_D$  steeply rises and saturates around  $H_r - H_g = 70$  nm and  $\lambda = 400$  nm saturates at around 120 nm  $H_r - H_g$ . For  $\lambda = 600$  nm,  $T_D$  shows a monotonous increase. For  $\lambda > 600$  nm, the rate of increase in  $T_D$  is mild. This suggests that the influence of small feature heights is not significant in interactions with  $\lambda > 600$  nm, implying that the scattering mechanism is not the same across the entire wavelength range considered. Most likely, the interaction with small features in the morphology is diffractive for  $\lambda < 600$  nm, and these features do not significantly impact  $T_D$  beyond  $\lambda = 600$  nm. As observed previously, texture height and periodicity play a primary role in scattering light with  $\lambda > 600$  nm, which is likely to exhibit refractive scattering.

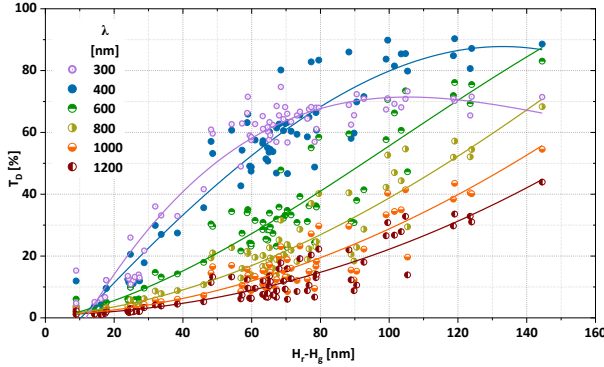


Figure 5.10.: Diffused transmission of different  $\lambda$  versus  $H_r - H_g$  values of 3  $\mu\text{m}$ , 4  $\mu\text{m}$  and 5  $\mu\text{m}$  hexagonal micro textures (75 samples). The lines in the image are guides to the eye.

Figure 5.11 (A) shows the  $T_{TOT}$  and  $T_D$  spectra corresponding to the HC textures HP3, HP4 and HP5. Corresponding values of flat glass are also added as a reference (the  $T_D$  of flat glass is almost zero).  $T_{TOT}$  spectra show an anti-reflective nature of HC textures. An increase in transmission compared to flat glass is attributed to the angles formed by craters at the glass-air interface [233]. This property is well known for opaque hexagonal textures on wafer substrates with hexagonal holes facing illumination in concave mode [200, 234–236]. It is worth noting that, in our study, the craters are positioned in a convex mode relative to the incident light as illustrated in Figure 5.11 (B).  $T_{TOT}$  rises with an increase in periodicity and AR. This is correlated with the  $\theta_s$  of the hexagonal textures, specifically Set 3, which represents the surface angles of crater walls ( $\theta_s > 15^\circ$ ). The uniform taper on the gratings results in a gradual optical density variation [69], which results in reduced reflection at the interface [70]. Additionally, a high total contribution of HP5 in Set 3, combined with its crater height, results in multiple reflections within the glass medium, enhancing its  $T_{TOT}$ . The  $T_D$  spectra of HP5 are highest, followed by HP4 and HP3, as already observed in Figure 5.9.

### 5.3.2.2. Diffraction patterns made by hexagonal microtextures

The glass wafer, tessellated with periodic craters featuring hexagonal edges, can be considered a 2D hexagonal grating in transmission mode, where the 2D periodicity determines the diffraction pattern [165]. When light is incident on the flat side of the glass wafer, each hexagonal microscale crater can act as a plano-concave lens. The hexagonal shape ensures six-fold symmetry in both near and far-field patterns, with the near-field exhibiting multiple HC shapes and the far-field

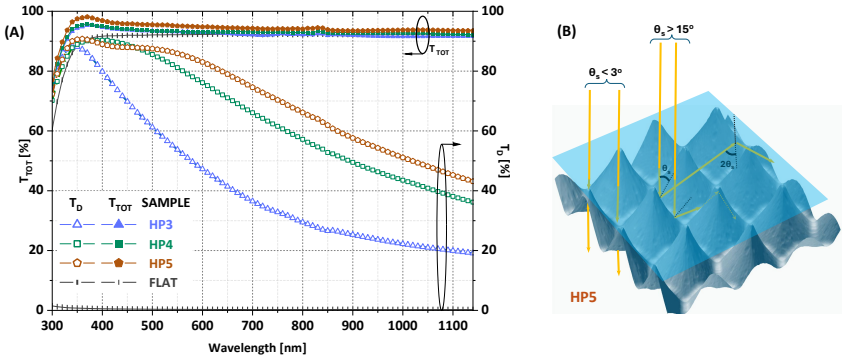


Figure 5.11.: (A) Total transmission spectra  $T_{TOT}$  and diffused transmission spectra  $T_D$  of hexagonal textured HP3, HP4, HP5 and non textured flat Corning glass wafers. (B) Illustration of the set of 3 angles of the crater, multiple reflections in the glass.

5

showing a reciprocal lattice [165, 237]. A near-field diffraction pattern at  $3 \mu\text{m}$  (simulated using the angular spectrum method) and far-field diffraction at 10 cm distance (simulated with fast Fourier transforms) are provided in Appendix B, Figure B.6. To observe the far-field pattern in the real world, the flat side was probed with a 635 nm collimated diode laser. The hexagonal-shaped array creates a pattern with a central maximum (zeroth-order) of the highest intensity. A hexagonal array of bright light spots surrounds this central spot. The pattern is consistent with the theoretically simulated far-field pattern shown in Appendix B.6. Additionally, the maxima surrounding the central peak are followed by weaker subsidiary maxima. The experimentally measured angular scattering intensity of white light by hexagonal textures is discussed in the following section.

### 5.3.2.3. AID of hexagonal microtextures

Far-field diffracted white light transmitted through HC patterns on glass, at a distance of 10 cm from the sample, is shown in Figure 5.12 (A). The diffracted orders, except for the central (zeroth) spot, will be coloured, as the light is dispersed into different wavelengths at various angles. To measure the angular scattering caused by the sample, the wafer was rotated at a speed of 172 rpm (as explained in Section 5.2.4). Coloured, discrete rings, as shown in Figure 5.12 (B), are formed at the detector plane.

The Figure 5.13 shows the intensity distribution of the transmitted light versus transmission angles. Intensity for  $\lambda = 300, 400, 600, 800$  and  $1000 \text{ nm}$  for HP3, HP4 and HP5 yields the following observations. (i) Among the plotted wavelengths, the specular component is the highest for  $\lambda = 1000 \text{ nm}$  (near  $0^\circ$  transmission angle), which agrees with the  $T_D$  in Figure 5.11. This minor prominence of long wavelength causes the central spot to appear red in Figure 5.12 (B). (ii) The subsequent orders depict the influence of wavelengths on scattered angles. For each set of maxima, the light is scattered at wider angles for longer wavelengths, due to which the patterns in Figure 5.12 (A) and (B) have coloured spots/rings in blue to red order in a radial outward direction. (iii) The amplitude of the first, second and subsequent-orders in the AID plots is highest for HP5, followed by HP4 and HP3. The intensity redistribution due to texture gets most pronounced with increasing periodicity. (iv) The scattering pattern (as well as the rings used for

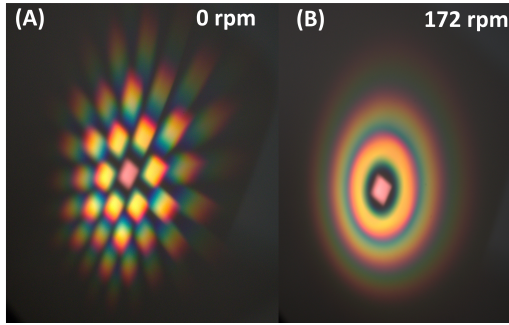


Figure 5.12.: (A) The far-field scattering of white light at 10 cm distance by hexagonal texture HP5. (B) Rings formed at the same distance with samples given 172 rpm.

the measurements here) becomes well defined with distinct peaks and zero intensity points with an increase in wavelength and periodicity. To summarise, the far-field diffraction pattern consists of hexagonally arranged diffraction spots, whose intensities are determined by the size and shape of the hexagonal microtexture.

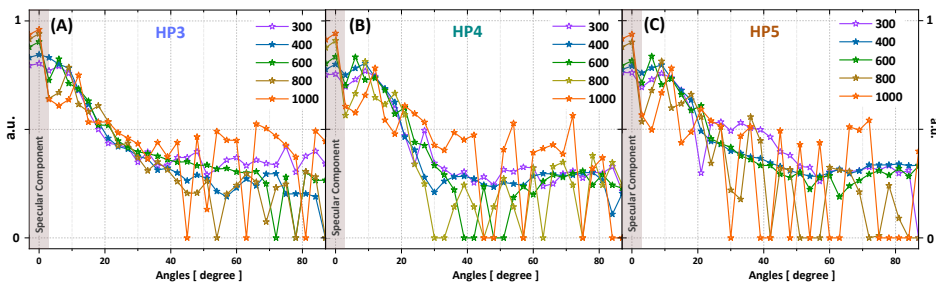


Figure 5.13.: Normalised Angular intensity distribution of hexagonal textures on glass for (a) HP3, (b) HP4 and (c) HP5.

### 5.3.3. Solar cells on honeycomb textures

Figure 5.14 presents the external solar cell parameters of nc-Si:H single-junctions plotted as a function of AR for the different periodicities. The  $J_{sc,EQE}$  increases directly with AR. This is a result of an increase in diffused transmission with total texture height and nano features as discussed in Section 5.3.2.1. It is also evident that the  $J_{sc,EQE}$  increases with periodicity. This can be explained from the discussion in Section 5.3.2.2 that an increase in periodicity results in stronger diffraction and amplitudes over broad angles, which enhance light absorption through higher order diffraction channels [71]. The open-circuit voltage ( $V_{oc}$ ) of the samples is independent of AR and periodicity of the texture. The fill factor is significantly low for samples with small AR with 3  $\mu\text{m}$  periodicity. This is a consequence of steep walls of 3  $\mu\text{m}$  periodic craters, contributing to shunt formation in silicon [78]. The solar cells exhibit similar fill factors for cells fabricated on 4  $\mu\text{m}$  and 5  $\mu\text{m}$ -periodic textures. A similar observation of near-constant electrical

properties has been previously reported for single-junction cells fabricated on a hexagonal substrate configuration by Sai *et al.* [225].

The efficiency of the solar cells increases with AR as a combined effect of  $J_{sc,EQE}$  and fill factor increase, reaching as high as 9.3% at AR = 0.21 for the HP5. Based on trends in  $J_{sc,EQE}$  and FF, the conversion efficiency could be further improved by increasing the AR and the periodicity. However, to draw a conclusive observation, an extensive sample set is required.

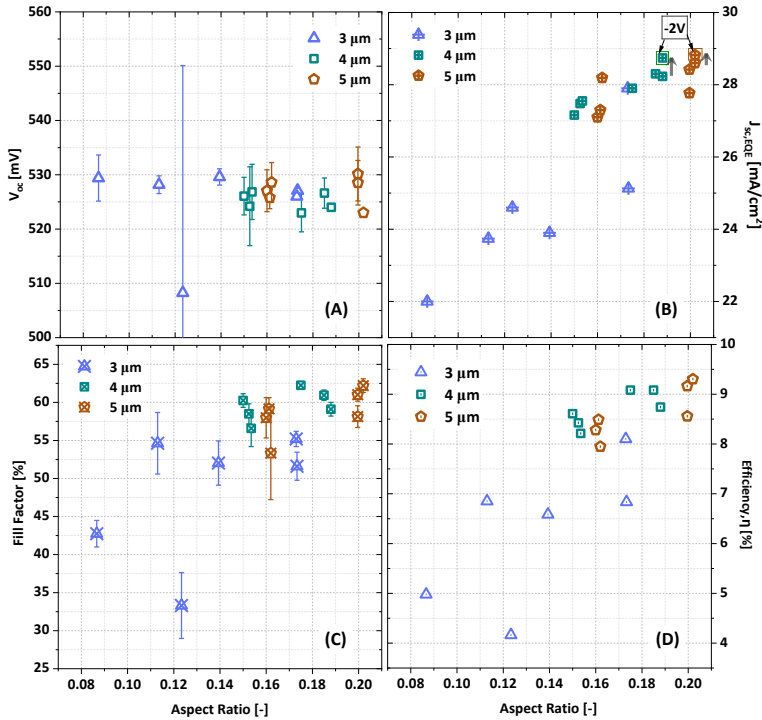


Figure 5.14.: The current-voltage parameters of 3200 nm (approximately) thick nc-Si:H single junction solar cells on superstrate configuration fabricated on hexagonal microtextures. The parameters (A)  $V_{oc}$ , (B)  $J_{sc,EQE}$  (values marked using the box are measured at a reverse bias of 2V), (C) fill factor and (D) efficiency are plotted as a function of AR for different periodicities.

The sections below discuss the solar cells with the highest short-circuit current density and conversion efficiency for each periodicity. Hereafter, the nc-Si:H single-junction solar cells fabricated on flat glass, HP3, HP4 and HP5 will be referred to as FLAT, NHP3, NHP4 and NHP5, respectively. All solar cell parameters of FLAT, NHP3, NHP4 and NHP5 are tabulated and recorded in Table 5.2. In Figure 5.15 (A), the J-V curve of the 3.2μm thick FLAT, NHP3, NHP4 and NHP5 nc-Si:H solar cells are plotted. The fill factor (FF) of the cells increases with periodicity. The low FF on FLAT is due to the low parallel resistances caused by crack formation in nc-Si:H absorber materials when deposited on flat surfaces [238]. The sheet resistance values of HP3, HP4, and HP5 show a subtle decrease with increasing periodicity. Which can be speculated that it is related

to the steepness of the hexagons as discussed in Figure 5.7. The steeper the walls, the greater the shadowing effect that can result in thin or non-uniform regions of the TCO layer, increasing the sheet resistance. The FF reported for NHP5 is typical for superstrate configuration (p-i-n) nc-Si:H single-junction solar cells with an absorber thickness of approximately 3200 nm and a thin TCO front electrode [119, 144, 239–241]. However, Tan *et al.* have reported 69% FF for superstrate configuration on random microtextured glass with ZnO:Al front TCO for a similar absorber thickness [144]. This suggests a possibility for increasing fill factor by increasing free carrier concentration in TCO [242] or increasing TCO thickness. An illustration of small-area solar cells distributed over glass substrates studied in this chapter is shown in Appendix A, Figure A.4. A further enhancement in series resistance can also be made by reducing the distance between the front contact and the cells. A summary of the reported highest fill factors and open-circuit voltages of thin-film silicon solar cells with different cell architectures is included in Appendix B, Figure B.4.

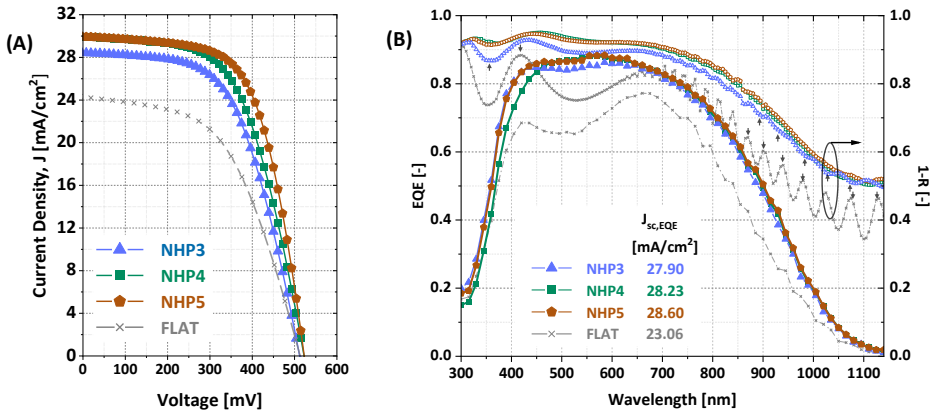


Figure 5.15.: (A) EQE spectra and (B) Current density versus voltage ( $J$ - $V$ ) characteristics of nc-Si:H single junction solar cells NHP3, NHP4, NHP5 fabricated on hexagonal microtextures with periodicity 3  $\mu\text{m}$  (HP3), 4  $\mu\text{m}$  (HP4) and 5  $\mu\text{m}$  (HP5) respectively. An nc-Si:H single-junction solar cell fabricated on FLAT is added for reference. All absorber nc-Si:H layers are 3200 nm thick. Arrows mark the  $1 - R$  peaks due to Fabry-Perot interference.

### 5.3.3.1. Photocurrent density

Figure 5.15 (B) gives the measured EQE spectra of NHP3, NHP4 and NHP5. The highest short-circuit current density of  $28.6 \text{ mA}/\text{cm}^2$  is achieved on NHP5 ( $H_r = 1012 \text{ nm}$  and  $\text{AR} = 20.2\%$ ). To the best of the author's knowledge, this is the highest reported  $J_{sc,EQE}$  for p-i-n superstrate silicon solar cells without external anti-reflection coating (Appendix B, Figure B.3). This is an increase of 24%  $J_{sc,EQE}$  in reference to FLAT. NHP5 followed by NHP4 with  $J_{sc,EQE} = 28.2 \text{ mA}/\text{cm}^2$  ( $H_r = 748 \text{ nm}$  and  $\text{AR} = 18.8\%$ ) and NHP3 with  $J_{sc,EQE} = 27.9 \text{ mA}/\text{cm}^2$  ( $H_r = 521 \text{ nm}$  and  $\text{AR} = 17.3\%$ ).

Over the entire spectrum, the total absorption ( $1 - R$ ) of the solar cell increases with increasing periodicity of the glass as a result of uniform tapering as previously reported by Chutinan *et al.* [69] and Sai *et al.* [70]. This additional transmission is directly translated to the EQE spectra of NHP5 when compared to NHP3 and NHP4. The high  $J_{sc,EQE}$  observed in the hexagonal microtextures when compared to flat glass arises from a combined effect of anti-reflective nature and enhanced

Sample	P [ $\mu\text{m}$ ]	$R_{sheet,IOH}$ [ $\Omega/sq$ ]	$J_{sc,EQE}$ [ $\text{mA}/\text{cm}^2$ ]	$V_{oc}$ [ $\text{mV}$ ]	FF [%]	$R_s$ [ $\Omega.\text{cm}^2$ ]	$R_p$ [ $\text{k}\Omega.\text{cm}^2$ ]	Eff [%]
FLAT	0	21	23.0	511	55.0	19.4	0.9	6.5
NHP3	3	25	27.9	526	55.2	18.1	1.9	8.1
NHP4	4	23	28.2	524	59.1	12.9	2.1	8.7
NHP5	5	22	28.6	523	62.2	9.6	1.9	9.3

Table 5.2.: solar cell parameters nc-Si:H single junction solar cells on textures of different periodicity. The standard deviation ( $\sigma_d$ ) for electrical performance parameters are calculated based on the 5 best performing cell of each substrate.  $\sigma_d(V_{oc}) \approx 3$  mV,  $\sigma_d(\text{FF}) \approx 0.7\%$ ,  $\sigma_d(R_s) \approx 0.1 \Omega.\text{m}^2$ ,  $\sigma_d(R_p) \approx 0.1 \text{k}\Omega.\text{m}^2$ .  $R_{sheet}$  is calculated based on 8 measurements on 150-nm thick IOH deposited over glass.  $\sigma_d(R_{sheet,IOH}) \approx 0.7 \Omega/sq$ .

light trapping in the solar cells. A similar discussion has been reported previously by Chong *et al.* correlating the rise in  $J_{sc,EQE}$  to gratings on the illuminated surface of the solar cell [234]. These surface gratings can diffract light into multiple orders, trapping it within the absorbing layer [67, 232]. Although the  $1 - R$  spectra of NHP5 and NHP4 are very similar, NHP4 shows a lower blue response than NHP5. This difference may arise from parasitic absorption in the (p)nc-SiO<sub>x</sub>:H layer of the solar cell due to unexpected variation in processing conditions.

Hexagonal microtextured superstrate glass significantly increases the EQE in the long-wavelength region compared to FLAT. This can be attributed to the high  $T_D$  exhibited by HC textures in transmission (Section 5.3.2). The hexagonal texture with sufficient  $H_r$  is capable of quenching Fabry-Perot interference in the nc-Si:H absorber in the near-IR region when compared with FLAT (marked by downward arrows in Figure 5.15 (B)). Interference fringes with diminished amplitudes appear in the  $1 - R$  of the NHP3 cell (marked by upward arrows) and some other solar cells fabricated on low AR wafers with 3  $\mu\text{m}$  periodicity (not shown in this work). This is speculated to be due to the less deep craters of the 3  $\mu\text{m}$  periodic textures when compared to other considered periodicities (refer to Figure 5.9).

The high values in the near-IR response are also due to the silver back reflector, which adapts to the hexagonal morphology, combined with the natural texture of the nanocrystalline material. Figure 5.16 (A) and (B) are the AFM scans and (C) and (D) are the SEM images representing before and after deposition of silicon layers on HP5 from the non-illuminated side of the absorber layer. In a PECVD-deposited thin-film silicon solar cell, the surface morphology is conventionally not externally guided but instead naturally formed through crystal growth. This flattens out the textures and reduces their amplitude [204]. Although the amplitudes and sharpness of the hexagons decrease when a 3200 nm thick silicon film is deposited, as evident from Figures 5.16 (B) and (D), the surface still resembles distinct hexagonal shapes. This suggests that the back reflector Ag layer forms a HC morphology with a height of 916 nm (AR = 0.14 and an RMS roughness of 278 nm). These Ag back reflectors with HC morphology are similar to back reflectors employed in thin-film silicon cells in substrate configurations, which are well known for enhancing near-IR responses [187, 204, 227].

### 5.3.3.2. nc-Si:H film growth

To inspect the growth of the nc-Si film on hexagonal microtextures, an SEM image of NHP4 is shown in Figure 5.17. The nc-Si growth appears to be conformal. The nc-Si absorber deposited on the hexagonal microtexture is of high quality with minimal defects. A crack is observed near

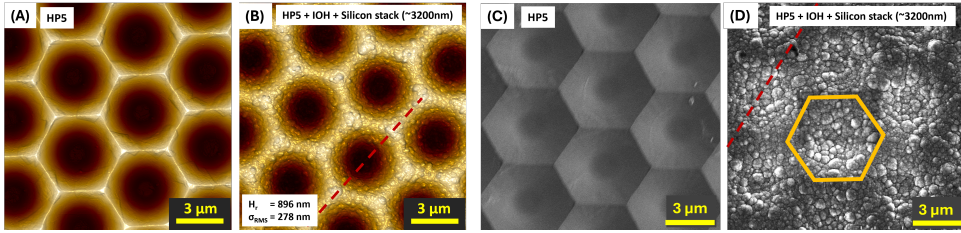


Figure 5.16.: nc-Si:H single junction solar cell characterised from the n-layer side before depositing the silver back reflector and back contact. (A) AFM and (B) SEM of bare textured glass (period = 4 μm). (C) AFM and (D) SEM of solar cell absorber after depositing IOH (150 nm)/(p)nc-SiO<sub>x</sub>:H (16 nm)/(i)nc-Si:H (3200 nm)/(n)nc-SiO<sub>x</sub>:H (20 nm).

the back contact in the bulk, away from the glass, which is highlighted and zoomed in. These kinds of defects can cause a drop in parallel resistance ( $R_p$ ) and, in turn, a decrease in FF in the solar cells, as observed in the cells presented in this chapter. Silicon crystals, when deposited on hexagonal textures, have been reported to develop cracks in the vicinity of an imaginary focal point of the curve due to shading effects [11, 46]. However, a 4.4 μm thick nc-Si:H ( $\chi_c \approx 60\%$ ) deposited on HP4 does not demonstrate any cracks of this type in the absorber bulk (HP4 yields a focal distance of 3.3 μm as depicted in Appendix B, Figure B.5). Hexagonal microtextures on glass with considered periodicity - AR combination can facilitate the formation of high-quality nc-Si:H filaments, eliminating shadowing effects.

5

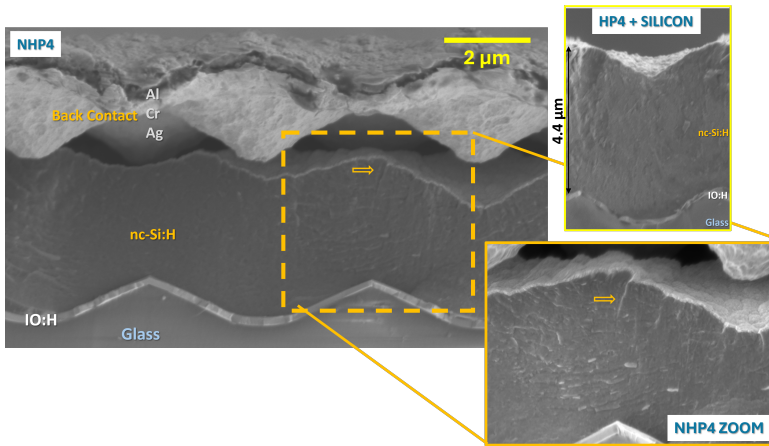
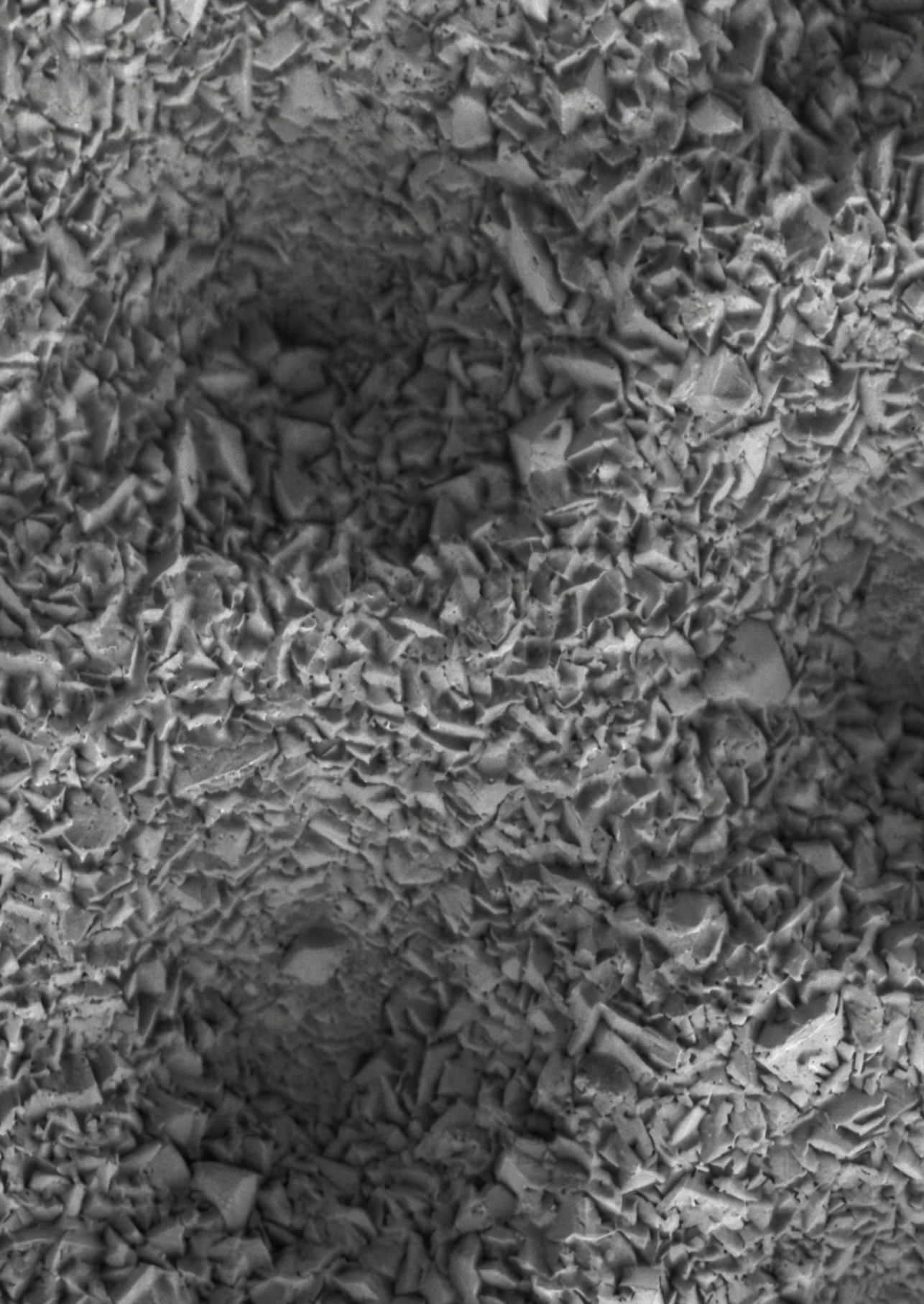


Figure 5.17.: SEM cross-sectional image of a 3.2 μm thick nc-Si:H cell on a 4 μm period hexagonal microtextured glass superstrate.

## 5.4. Conclusion

This chapter reports hexagonal microtextures on glass, their optical properties and their application in nc-Si:H solar cell devices. The surface morphology and optical properties of the textures are reported. Features of multiple size ranges characterise the HC surface morphology. Hexagonal textures exhibit enhanced light transmission across all wavelengths, with an increase in periodicity. Hexagonal textures exhibit enhanced light transmission across the entire wavelength range when the periodicity is increased. Hexagonal textures with deeper craters also display high diffused transmission and broad-angle scattering properties. These properties directly translate to EQE spectra of solar cells fabricated on the textures, increasing the photoresponse and efficiency with an increase in periodicity and aspect ratio of the hexagonal micro-textures. Hexagonal textures with a 5  $\mu\text{m}$  periodicity with a 20.2% AR yield a photocurrent of 28.6  $\text{mA}/\text{cm}^2$  and a photo conversion efficiency of 9.30%. It is also observed that the HC textures in the superstrate configuration glass can facilitate high  $V_{oc}$  and crack-free nc-Si:H crystal growth. This indicates a high potential for hexagonal textures on glass in multijunction thin-film solar cell applications.





# 6

## Interface and Grain Scattering in Thin-film Silicon Multijunction Solar cells

This chapter is based on the publication:

G. Padmakumar, F. Saitta, K.P. Sreejith, P. Perez-Rodriguez, R.A.C.M.M. van Swaaij, A.H.M. Smets, "Mitigating the Interference Effects Induced by Optical Cavities in Superstrate Thin Film Silicon Multi-junction Solar Cells" *Solar Energy*, 311 (2026), 114537 DOI: 10.1016/j.solener.2026.114537

*A major challenge in multijunction devices is reduced light incoupling caused by interference fringes from optical microcavities. This paper reports a potential route to mitigate the interference effects with an effective front-window design. The concepts of interface scattering and grain scattering are implemented at the front side of superstrate tandem solar cells. A random texturing and periodic-hexagonal texturing approach on glass is used as interface scatterers. However, applying an interface scatterer alone is insufficient to eliminate the interference effects of optical cavities completely. Use of sputtered unintentionally doped zinc oxide (i-ZnO) or tin oxide (SnO) as grain scatterers stacked over random and periodic glass textures quenches the interference effects significantly. For a random textured glass substrate, a 1.5- $\mu\text{m}$  thick i-ZnO layer could quench interference in the top cell, except for the effect of the optical cavity formed in the amorphous top cell. Hexagonal craters on glass, combined with a 0.9- $\mu\text{m}$  thick i-ZnO layer, effectively mitigate fringes formed by all optical cavities in the device. This sample demonstrates the highest incoupled photon flux with 86% of photons entering the device. Use of a wide-bandgap grain scatterer, such as SnO, reduces parasitic absorption of high-energy photons while mitigating optical cavities. The design principles discussed in this work can be applied to any thin-film multijunction solar cells consisting of layers with contrasting refractive indices.*

## 6.1. Introduction

In the energy transition, cost-effective yet efficient photovoltaics fabrication methods are required. Multijunction PV devices are considered a potential route to achieving these goals with low material utilisation and enhanced performance compared to conventional single-junction PV architectures [12, 15]. Thin-film photoactive materials such as amorphous silicon (a-Si:H), copper indium gallium selenide (CIGS), organic PV, III-V materials or perovskites are combined with crystalline silicon wafers or another of the above-mentioned thin-film layers in a tandem configuration to form a multijunction solar cell. The choice of absorber combination depends on band gaps corresponding to the individual spectral utilisation potential and applications.

The complexity of the many layers of materials stacked to form a multijunction can introduce additional optical challenges [241]. The thin layers, stacked one on top of the other, can have alternating high- and low-refractive-index materials. This results in multiple reflecting surfaces within the device. These layers with contrasting refractive indices can form multiple Fabry-Pérot microcavities in the solar cell [89, 243]. In an a-Si:H/nc-Si:H solar cell, the optical cavities (OC) can be identified as shown in Figure 6.1. The constructive and destructive interferences of the (partially) coherent light might limit the light incoupling and absorption in the absorber layer at specific wavelengths. Which wavelengths ( $\lambda$ ) interfere in which parts of the solar cell depends on how far light penetrates the stack of layers, determined by transmission and absorption at each  $\lambda$ . For example, an a-Si:H layer absorbs light up to  $\lambda$  corresponding to 1.8 eV and lets the remaining light pass through. This unabsorbed light is reflected between the layers. Multiple interference fringes within the spectral response can lead to parasitic absorption, potentially reducing the overall absorption of the photoactive layer unless the standing-wave pattern is quenched through averaging over incidence angles and optical thickness variations [244, 245]. Conversely, interference and cavity effects are also frequently employed to achieve constructive outcomes, such as the design of anti-reflective (AR) coatings or optical spacers, which serve to suppress unwanted reflections or localise field maxima at strategic positions.

Three simplified OCs are identified and marked in the Figure 6.1.  $OC_B$  is formed in the TCO and p-doped top layer, which has a low refractive index for wavelengths 300 - 550 nm ( $\lambda$ s starting from blue) compared to that of a-Si:H top cell.  $OC_G$  are caused mainly by the high refractive index a-Si:H layer sandwiched between two low refractive index layers for wavelengths around 550-800 nm ( $\lambda$ s starting from green), and  $OC_R$  is caused by the nc-Si:H silicon layer sandwiched between tunnelling recombination junction and nc-SiO:H/back reflector layer beyond 800 nm ( $\lambda$  corresponding to red and near infrared).

Standard techniques for mitigating interference in OCs are (i) light scattering via interface morphology (“interface-scattering”) and (ii) light scattering aided with grains or crystals (“grain-scattering”). Interface-scattering is implemented in solar cells by texturing the front side [144] or the rear side of the solar cells [168, 204], where the thin-film nature allows the other device interfaces to adopt the texture as well. Texturing increases the haze of the superstrates through effective scattering of light over broad wavelengths [65, 111, 225]. Grain scattering is implemented using transparent conductive oxides (TCO) layers with a thickness in the range of a few microns [45, 246]. Polycrystalline materials like TCOs do not have uniform optical properties because of residual porosity, secondary phases, and/or crystalline anisotropies [74]. These optical inhomogeneities cause scattering in the bulk. The use of thicker TCO layers enhances light trapping, as the grains within the bulk effectively scatter incident light in transmission [76, 247]. A combination of interface-scattering (from textured surfaces) and grain scattering (from thick TCO layers) at the front side has been employed in some of the highest-efficiency multijunction solar cells [49, 77, 248]. In this paper, we will study the extent to which a texture with or without grain scattering in the TCO bulk can mitigate coherent interference in the OCs in superstrate thin-film silicon solar cells.

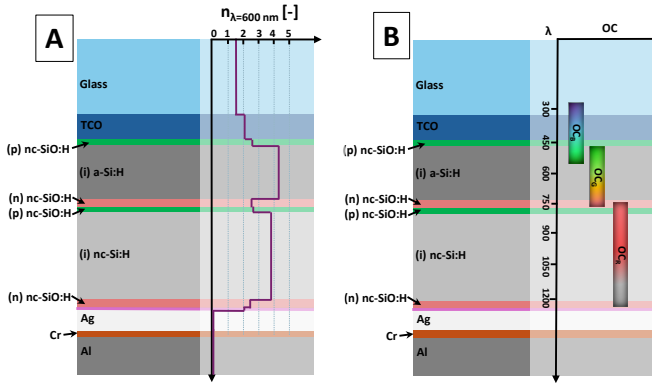


Figure 6.1.: Schematic representation of an a-Si:H/nc-Si:H double junction tandem solar cell. (A) The refractive index of each layer at a wavelength of 600 nm ( $n_{\lambda=600}$ ) is overlaid on the image. A detailed wavelength versus refractive indices graph is given in Figure 6.2. (B) The simplified demonstration of optical micro-cavities considering penetration depth of light with different wavelength is marked as  $OC_B$ ,  $OC_G$  and  $OC_R$ .

Chemical vapour deposition (CVD) techniques, such as low-pressure CVD (LPCVD), atmospheric pressure CVD (APCVD) and metal organic CVD (MOCVD) or physical vapour deposition (PVD) techniques like Radio frequency (RF) and direct current (DC) sputtering, are commonly used to deposit TCO layers [27, 77, 247]. The processing methods and deposition temperature determine the presence of grains, crystallinity, grain shape and size. The TCO alloy's band gap and tail states determine its parasitic absorption of blue light and the transmission spectrum, respectively. State-of-the-art TCOs used in solar cells have been reported in literature by Hänni *et al.* where a 5- $\mu\text{m}$  thick TCO layer is implemented on flat glass [45, 76] and a 2.3- $\mu\text{m}$  thick TCO layer by Tan *et al.* on micro-sized glass textures [77, 249]. Both these approaches used i-ZnO deposited with LPCVD in superstrate configurations. On the module level, Cashmore *et al.* have reported a 2- $\mu\text{m}$  boron-doped zinc oxide (BZO) grown using LPCVD as both front and rear electrodes [20, 28, 250]. These layers exhibit high-quality crystal growth but absorb UV light. PVD TCO deposition techniques, such as sputtering, result in TCO grain structure and properties very different from LPCVD-depositions [76, 251, 252]. Often, they show higher absorbance (parasitic absorption) for micron-thick TCO layers in the visible spectrum than LPCVD and MOCVD [247].

For the first time, this paper explores in detail the use of grain scattering with sputtered TCOs and compares it with interface-scattering techniques to mitigate cavity-induced interference fringes in OCs. Interface scattering is investigated by implementing random and periodic surface texturings on glass substrates. Additionally, this paper addresses the extent to which TCO thickness can be reduced to implement grain scattering successfully. Increasing the layer thickness enhances the scattering of light by grains and reduces the electrical sheet resistance, but also increases the parasitic absorption in this layer. In this paper, we study a low-temperature (below 100 °C) deposited unintentionally doped zinc oxide (i-ZnO) and tin oxide (SnO), both deposited by RF magnetron sputtering and integrated at the front side of a-Si:H/nc-Si:H tandem solar cells. Grain scattering by TCO bulk was evaluated using varying thicknesses of sputtered i-ZnO layers. We propose a combined interface bulk design strategy on glass to suppress optical

micro-cavity effects in a-Si:H/nc-Si:H tandem solar cells.

### 6.1.1. Deposition of layers in a-Si:H/nc-Si:H tandem solar cells

The a-Si:H/nc-Si:H tandem devices were co-deposited in a superstrate p-i-n top cell /p-i-n bottom cell architecture similar to Figure 6.1. All solar cells are measured without any external anti-reflection coating (ARC).

**Absorber layers:** The deposition of intrinsic hydrogenated nanocrystalline silicon ((i)nc-Si:H) and amorphous silicon ((i)a-Si:H) absorbers was made in a PECVD multichamber tool at very high frequency (40.68 MHz) and 170 °C substrate temperature. A thin seed layer (SC = 1%) is used for facilitating nucleation sites [108] during the nc-Si:H bottom cell depositions.

**Doped layers:** Using B<sub>2</sub>H<sub>6</sub> and PH<sub>3</sub> as dopant gases, boron-doped p-layer and phosphorus-doped n-layer were deposited at RF (13.8 MHz) and 180 °C substrate temperature in dedicated chambers. The p-doped layers at the front consist of a thin, heavily boron-doped silicon oxide contact layer ((p+)nc-SiO:H) and a boron-doped silicon oxide window layer ((p)nc-SiO:H). A similar configuration of p-layers is also used in the tunnelling recombination junction (TRJ) with a higher oxygen content in its layers. The n-doped TRJ consist of three layers: phosphorous-doped amorphous silicon ((n)a-Si:H), phosphorous-doped heavily oxygenated silicon oxide layer ((n)nc-SiO:H) and a phosphorous-doped nc-Si:H contact layer ((n)nc-Si:H). The nc-SiO:H layer in TRJ is 70 nm thick, acting as an intermediate reflectance layer as well [132, 253]. A similar order of n-doped layers is used for the rear side of the bottom cell. The nc-SiO:H layer at the rear side is 30 nm thick.

**Back reflector, contacts:** The back reflector (BR) consists of sputtered i-ZnO (60 nm) and an evaporated silver (300 nm) layer. An aluminium strip serves as the front contact for these solar cells, and the back contact consists of 5 mm × 5 mm square-shaped chromium (30 nm) and aluminium (500 nm) dots.

The above mentioned layers results in a solar cell structure: TCO front electrode/(p+)nc-SiO:H/(p)nc-SiO:H/(i)a-Si:H/(n)a-Si:H/(n)nc-SiO:H/(n)nc-Si:H/(p+)nc-SiO:H/(p)nc-SiO:H/(i)nc-Si:H/(n)a-Si:H/(n)nc-SiO:H/(n)nc-Si:H/BR. The deposition conditions of all layers for the a-Si:H/nc-Si:H tandem solar cells with their thicknesses are given in Table 6.1. The rows from top to bottom follow the order of deposition.

### 6.1.2. Design of Experiment

#### 6.1.2.1. Textured glass substrates:

The superstrate tandem solar cells are made on two different glass textures : (i) random texture, named superimposed texture (SIT), and (ii) periodic hexagonal-shaped textures, also known as honeycomb (HC) textures. Both textures are created directly on Corning borosilicate glass XG.

SIT is a type of multiscale texture developed directly on glass by generating nano-sized features on micro-sized textures through a sequential wet-etching process. The procedure of developing SIT is given in 7 steps as discussed. In step 1, Corning XG glass is cleaned in ultrasonic baths of acetone and 2-propanol for 10 minutes each. During step 2, ITO is deposited as a sacrificial TCO layer using magnetron sputtering at elevated temperature. In subsequent Step 3, the layer deposited on the flat glass is wet-etched with hydrofluoric acid (HF) (40%): H<sub>2</sub>O<sub>2</sub>(31%): H<sub>2</sub>O in the ratio 1:2:10. In this step ITO layer acts as a selective leaking mask and solution etches glass to make micrometer scale textures on the glass surface. The etching is continued till the ITO layer is completely removed. In next Step 5, i-ZnO layer is deposited as a sacrificial TCO layer over the textured surface using magnetron sputtering (at elevated temperature). In Step 6, the i-ZnO layer is wet-etched using a HF (40%) and nitric acid (HNO<sub>3</sub>) (69.9%) solution in a 1:8 ratio. In Step 7, the substrate is cleaned to remove any residual TCO by dipping in HNO<sub>3</sub> (69.9%) for 3

Table 6.1.: Deposition conditions of different silicon-based layers in the solar cell. The distance between the RF electrode and the grounded electrode is 13 mm for all p-doped layer depositions, 13 mm for all intrinsic layer depositions, and 21 mm for all n-doped layer depositions.

Layer	SiH <sub>4</sub> [sccm]	H <sub>2</sub> [sccm]	Dopant Gas [sccm]	CO <sub>2</sub> [sccm]	Pressure [mBar]	Power [W/cm <sup>2</sup> ]	Thickness [nm]	Depo. rate [Å/s]
(p+)nc-SiO:H (contact)	0.8	170	50 (0.02% B <sub>2</sub> H <sub>6</sub> in H <sub>2</sub> )	1.2	2.2	0.12	3	0.46
(p)nc-SiO:H (window)	0.8	170	10 (0.02% B <sub>2</sub> H <sub>6</sub> in H <sub>2</sub> )	1.2	2.2	0.12	13	0.39
(i)a-Si:H	6	120	-	-	5	0.30	280	4.0
(n)a-Si:H (TR)	40	0	11 (2% PH <sub>3</sub> in H <sub>2</sub> )	0	0.6	0.04	5	1.1
(n)nc-SiO:H (TR/RL)	1	120	2 (2% PH <sub>3</sub> in H <sub>2</sub> )	2.4	1.5	0.11	70	0.11
(n)nc-Si:H (TR)	1	120	2 (2% PH <sub>3</sub> in H <sub>2</sub> )	0	1.5	0.11	7	0.19
(p+)nc-SiO:H (TR)	0.8	170	50 (0.02% B <sub>2</sub> H <sub>6</sub> in H <sub>2</sub> )	2.2	2.2	0.12	3	0.46
(p)nc-SiO:H (TR)	0.8	170	10 (0.02% B <sub>2</sub> H <sub>6</sub> in H <sub>2</sub> )	2.2	2.2	0.12	15	0.39
(i)nc-Si:H (seed)	1.1	120	-	-	4	0.4	90	2.25
(i)nc-Si:H (bulk)	3.2	120	-	-	4	0.4	3200	4.82
(n)a-Si:H	40	0	11 (2% PH <sub>3</sub> in H <sub>2</sub> )	0	0.6	0.04	5	1.1
(n)nc-SiO:H	1	120	2 (2% PH <sub>3</sub> in H <sub>2</sub> )	1.6	1.5	0.11	30	0.22
(n)nc-Si:H (contact)	1	120	2 (2% PH <sub>3</sub> in H <sub>2</sub> )	1.6	1.5	0.11	7	0.19

minutes. The detailed procedure and properties are reported elsewhere [111]. The RMS roughness of SIT is approximately 400 nm. For this SIT, a total spectral utilisation potential of 26.7 mA/cm<sup>2</sup> is demonstrated on an nc-Si:H single-junction solar cell without ARC (after quenching fringes due to OCs in the device) [111].

HC textures are created on glass using photolithography (with specific masks) and wet etching in 9 subsequent steps. UV photolithography is used to generate HC textures on the glass superstrates. In Step 1, the Corning glass wafer is cleaned with 69.5% HNO<sub>3</sub> for 3 minutes. In step 2, the wafer is dried at 110 °C. In Step 3, the wafer is exposed to hexamethyl disilazane (HMDS) for 150 seconds at 150 °C, using nitrogen as the carrier gas. In Step 4, Shipley SPR3012 positive photoresist (2.1 μm thick) is spin-coated. In Step 5, UV exposure is conducted using a chromium reticle with periodically distributed holes. Step 6 involves pattern development, in which the exposed areas of the photoresist are removed. The photolithography technique implemented on glass requires an additional hard-bake at 140°C for 30 minutes as Step 7. In Step 8, the pattern is transferred from the mask to the Corning glass wafer through a 20-minute dip in premade buffered hydrofluoric acid, comprised of ammonium fluoride (NH<sub>4</sub>F) (40%): hydrofluoric acid (HF) (49%) in ratio 7:1. The wafer is then rinsed with deionised water, and the remaining photoresist is removed. The detailed procedure and process optimisation are detailed elsewhere [140]. The HC substrates used in this paper have a periodicity of 5-μm and a texture depth of 1-μm. For this HC, a 3200-nm thick nc-Si:H single-junction solar cell fabricated has demonstrated a potential to obtain 28.6 mA/cm<sup>2</sup> current (after quenching the fringes formed by OCs) [171, 254].

### 6.1.2.2. Front electrode design:

The TCO front electrode design is based on the bandgap of the TCOs and the phenomenon that we want to observe.

(i) To observe interface scattering : A single layer 150-nm thick hydrogenated indium oxide (IOH) electrode. IOH layer is amorphous, with no grain structures to contribute to any light

scattering inside its bulk. Amorphous IOH is a “flat” layer and adopts the texture of the substrate on which it is deposited [247]. For this reason, IOH is chosen to study interface scattering.

(ii) To study the grain scatterer which is a part of the front electrode: Sputtered i-ZnO has a low band gap. Which permits its use as a grain scatterer in a “bi-layer” (BL) configuration. BL front electrode stack comprises of thick i-ZnO layer deposited on top of amorphous IOH over glass. Both IOH and i-ZnO are deposited with RF magnetron sputtering. i-ZnO has a crystalline structure with columnar grains. It can facilitate light scattering at the bulk grains. It is added to the IOH layer that has a low sheet resistance. In this BL configuration, charge transport is expected to occur laterally in IOH layers and transversely through i-ZnO columns [247]. Varying the layer thickness of i-ZnO is expected to enhance grain scattering.

(iii) To study grain scatterer which is a part of the substrate: HC texture is also studied with a SnO layer to act as a grain scatterer. SnO is a wide bandgap TCO with very high sheet resistance. The presence of SnO in a silicon cell creates an energy barrier in the valence band for holes at the SnO/p-doped layer interface due to the very high bandgap relative to the (p)nc-SiO:H. The wide bandgap of SnO prevents its use in a bi-layer TCO configuration, unlike i-ZnO. To overcome this effect, the SnO layer is deposited directly on glass, making it a part of the substrate. The thick SnO layer is electrically isolated from the solar cell stack using a 100 nm thick silicon oxide layer deposited at 400 °C.

Deposition conditions and band gap of the TCO layers are specified in Table 6.2. Additionally, the refractive indices and extinction coefficient of all materials used in this study is given in Figure 6.2 (A) and Figure 6.2 (B) as a function of  $\lambda$ .

Table 6.2.: Deposition conditions of TCO front electrode and back reflector TCO layer.  $T_{sub}$  refers to substrate temperature. Band gap is determined from Tauc plot analysis of the TCO.

TCO	Ar [sccm]	H <sub>2</sub> O Partial Pressure	Pressure [ $\mu$ Bar]	Power [W/cm <sup>2</sup> ]	$T_{sub}$ [°C]	Thickness [nm]	Depo. Rate [Å/s]	Bandgap [eV]
IOH (Front electrode)	50	0.06	5.7	1.5	27	150	0.98	3.9
i-ZnO (Front electrode)	20	–	2.6	2.0	95	varied	0.87	3.1
i-ZnO (Back Reflector)	20	–	2.6	2.0	157	60	0.87	3.2
	Ar [sccm]	Ar/O <sub>2</sub> [sccm]						
SnO (Grain Scatterer)	10	10	2.6	1.5	95	60	0.7	3.9

The a-Si:H/nc-Si:H tandem solar cells made on SIT with only IOH as TCO layer are referred to as SIT-IOH. Tandem cells made on SIT, with IOH (150 nm)/i-ZnO (1500 nm) bi-layer TCO will be referred to as SIT-BL. The device structures are illustrated in Figures 6.3 (A), (B). Similarly, a-Si:H/nc-Si:H tandem solar cells made on HC with IOH TCO are referred to as HC-IOH, and tandem cells made on HC with IOH (150 nm)/i-ZnO bi-layer TCO are referred to as HC-BL. In this case, the amorphous top layer is expected to smooth the nano-features in the textures, and the bottom layer's spectral utilisation is maximised with micro-sized textures [77]. The device structures are illustrated in Figures 6.3 (C), (D). The tandem solar cell made on HC with electrically isolated SnO used as a grain scatterer is referred as HC-SnO. The structure of this device is illustrated in Figure 6.3 (E). Four experiments are performed in total, using nine solar cells with structures as summarised in Table 6.3.

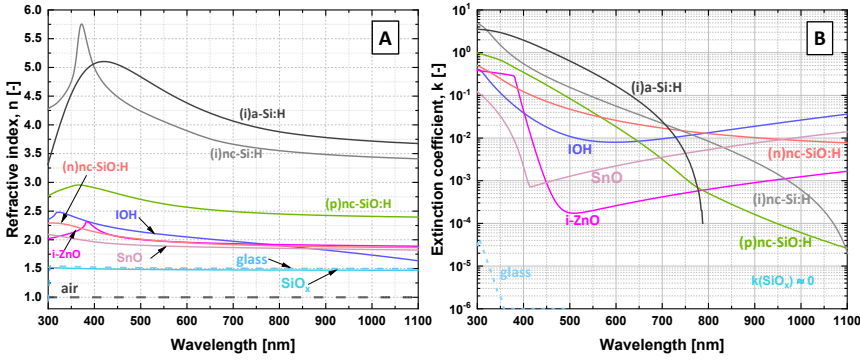


Figure 6.2.: The (A) refractive index -  $n$ , and (B) extinction coefficient -  $k$ , of materials in this study.

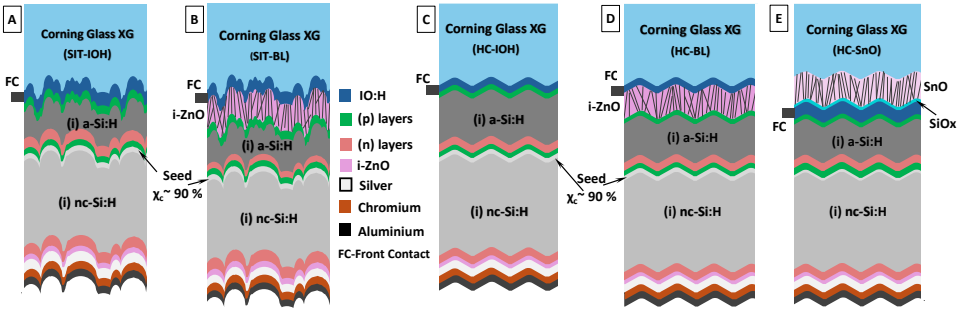


Figure 6.3.: a-Si:H/nc-Si:H superstrate tandem solar cells on (A) random textured glass: SIT-IOH (B) random textured glass with thick front i-ZnO: SIT-BL (C) periodic textured glass: HC-IOH (D) periodic textured glass with thick front i-ZnO: HC-BL (E) periodic textured glass with SnO/SiOx at front: HC-SnO.

### 6.1.3. Texture and Solar cell characterisation

The textures on glass are analysed using atomic force microscopy (AFM) with a Bruker AFM FastScan in FastScan closed-loop scanner head mode. Power spectral density of  $16\text{-}\mu\text{m} \times 16\text{-}\mu\text{m}$  is extracted using NanoScope Analysis (version 2.0) software from Bruker. In addition, scanning electron microscopy (SEM) with Hitachi Regulus 8230 at an acceleration voltage of 1.5 kV (to minimise charging of glass) is used to create cross-sectional images of solar cells on glass. The open-circuit voltage ( $V_{oc}$ ) and fill factor ( $FF$ ) of solar cells were measured by a WACOM-class AAA xenon-halogen dual lamp continuous AM1.5G spectral simulator at 25 °C. The short-circuit current density ( $J_{sc}$ ) values were calculated based on the EQE measurement by integrating over the AM 1.5G solar spectrum. In this way, the effect of any mismatch between the solar simulator spectrum and the AM1.5 spectrum is prevented. Also, it eliminates any overestimation of current caused by errors in estimating the active cell area in small-area solar cells. EQE measurements were performed using an in-house developed system equipped with monochromatic illumination and EQE calibration photodiode from Fraunhofer ISE. For multijunction solar cells, each subcell was characterised under carefully selected high-intensity bias light (LED sources)

Table 6.3.: List of samples, figures, substrates, and corresponding experimental objectives for tandem solar cell studies.

Serial Number	Sample	Figure	Substrate	i-ZnO thickness ( $\mu\text{m}$ )	Experiment
1	SIT-IOH	1(A)	Random	0	To study the difference in random textures interface and interface-grain combination scattering.
2	SIT-BL	1(B)	Random	1.5	
3	HC-IOH	1(C)	Periodic	0	To study the influence of grain scattering combined with periodic textures.
4	HC-BL1	1(D)	Periodic	0.2	
5	HC-BL2	1(D)	Periodic	0.4	
6	HC-BL3	1(D)	Periodic	0.6	
7	HC-IOH	1(C)	Periodic	0	To study the difference in periodic textures interface and interface-grain combination scattering.
8	HC-BL4	1(D)	Periodic	0.9	
				SnO thickness ( $\mu\text{m}$ )	Experiment
9	HC-SnO	1(E)	Periodic	1.0	To study the influence of wide band gap grain scatterers.

and at 0 V. The total reflection spectra (R) of the solar cell are recorded using a LAMBDA 1050+ UV/Vis/NIR Spectrophotometer with a 150-mm InGaAs integrating sphere from PerkinElmer for a 300 to 1200 nm  $\lambda$  range at 10-nm intervals.

In this paper, a parameter  $R'_{\lambda_1 < \lambda < \lambda_2}$ , signifying the fraction of total photons reflected in the wavelength range between  $\lambda_1$  and  $\lambda_2$  in the AM1.5 solar spectrum, is calculated following the equation:

$$R'_{\lambda_1 < \lambda < \lambda_2} (\%) = \frac{\int_{\lambda_1}^{\lambda_2} R(\lambda) \Phi(\lambda) d\lambda}{\int_{300}^{1200} \Phi(\lambda) d\lambda} \times 100\% \quad (6.1)$$

Where  $R(\lambda)$  is the measured reflectance of the solar cell and  $\Phi(\lambda)$  is the photon flux density of the AM1.5 spectrum, as a function of  $\lambda$ . For evaluating the effect of optical cavities -  $OC_B$ ,  $OC_G$  and  $OC_R$ , weighted average reflectance  $R'_{300 < \lambda < 540}$ ,  $R'_{550 < \lambda < 790}$  and  $R'_{800 < \lambda < 1200}$  were used respectively.

## 6.2. Results and Discussion

### 6.2.1. Inspection of interfaces and i-ZnO grains

Figure 6.4 shows the cross-section SEM images of SIT-IOH, SIT-BL, HC-IOH and HC-BL4, respectively. The growth of i-ZnO crystals on both substrates is similar. Additionally, the growth of i-ZnO crystals from small to large crystals with increasing thickness is evident in the SEM of SIT-BL. At the specific thickness of 0.9- $\mu\text{m}$  (marked in the image), the cross-sectional grain structure and size of i-ZnO on both types of textures (SIT-BL and HC-BL4) appear identical.

Figure 6.5(A) gives the power spectral density (PSD) of SIT-IOH and HC-IOH. Zone 1 represents the large-sized features in the texture morphology, while zone 2 represents the small features. In both zones, HC-IOH has a higher value than SIT-IOH, suggesting that HC-IOH has more features at micro- and nano-scale [65]. These features actively scatter light over a broad wavelength range. Figure 6.5(B) is the surface angle distribution of SIT-IOH and HC-IOH superstrates. HC-IOH shows a concentrated peak at 17°, whereas SIT-IOH shows a broad distribution with a peak at 12°. This sharp peak indicates that HC-IOH has a uniform taper, leading to gradual changes in optical density and improved light coupling [69, 255].

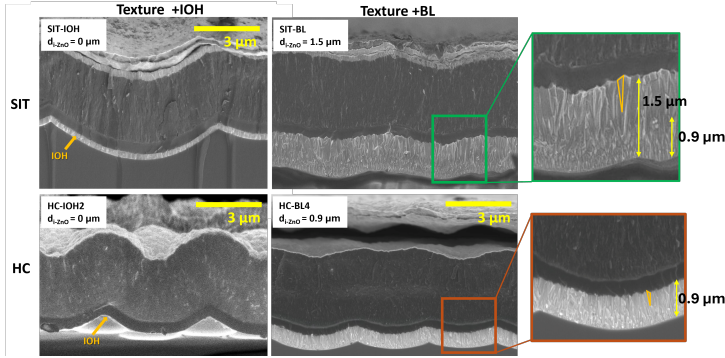


Figure 6.4.: Cross-sectional SEM images of a-Si:H/nc-Si:H tandem solar cells made on SIT-IOH, SIT-BL (1.5- $\mu\text{m}$  thick i-ZnO), HC-IOH and HC-BL4 (0.9- $\mu\text{m}$  thick i-ZnO). The i-ZnO layer is zoomed in with its heights marked, and one crystal is also marked (arbitrarily selected) to guide the reader. Note: The profile in HC solar cells in HC-BL4 differs from that in HC-IOH because the cut in the glass is not exactly through the lowest point of the hexagons.

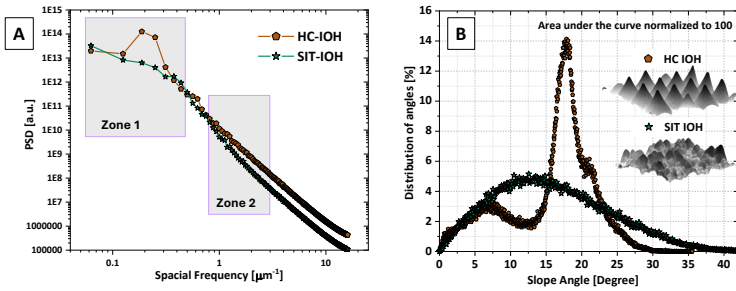


Figure 6.5.: (A) PSD of SIT and HC textures. (B) Slope distribution of SIT and HC textures, the 3D isometric view of the textures is given inset.

### 6.2.2. a-Si:H / nc-Si:H tandem solar cells on random textures

Figure 6.6(A) shows the EQE of tandem solar cells made on SIT. The interface-scattering in SIT is insufficient to mitigate the fringes in the solar-cell stack. Thus, SIT-IOH has the effect of  $OC_B$ ,  $OC_G$  and  $OC_R$  in the  $1 - R$  spectra, resulting in multiple fringes across the entire wavelength range. The effect of interference fringes is directly translated to the EQE spectra, leading to a loss of optical response. The top cell loses the response in  $OC_B$  at around 400 -500 nm, and  $OC_G$  reduces the bottom cell response at a wavelength of approximately 750 nm (marked with arrows). A total spectral utilisation ( $J_{SC,TOT}$ ) of a-Si:H / nc-Si:H tandem on SIT-IOH is 24.7 mA/cm<sup>2</sup>.

To study the optical effects of SIT combined with grain-scattering in multijunction solar cells, a 1.5- $\mu\text{m}$  thick i-ZnO layer is added to the front electrode, forming a bi-layer. Figure 6.6(B) shows the estimated bandgap and absorption coefficient ( $\alpha$ ) of i-ZnO. The estimated band gap of sputtered i-ZnO is 3.1 eV, which corresponds to  $\lambda = 399$  nm. Photons with energies above this threshold are absorbed in i-ZnO. Similarly, minor parasitic absorption loss is observed between  $\lambda = 400$  nm and

500 nm due to tail states in sputtered i-ZnO [247].

EQE spectra of SIT-BL in Figure 6.6(A) suggest that at the shorter wavelengths, the amplitude of interference fringes in the  $1 - R$  spectra due to  $OC_B$  were reduced with the bi-Layer TCO. The fringes resulting from the IOH/(p)SiO:H layer are reduced, showing that the light has become less coherent (also, a minor reduction in reflection at the TCO/silicon interface is also achieved by the introduction of i-ZnO due to graded refractive index values; however, this effect is not a significant factor here). This leads to the conclusion that grain-scattering is needed to mitigate interference fringes in  $OC_B$  in SIT. Yet, the SIT interface and grain-scattering combination is unable to break the  $OC_G$  formed by the flat a-Si:H top cell. Table 6.4 gives the  $R'$  values for SIT-IOH and SIT-BL. Both  $R'_{300 < \lambda < 550}$  and  $R'_{550 < \lambda < 790}$  are decreased when i-ZnO is incorporated into IOH as a TCO layer, indicating a better light incoupling as a result of reduced interferences in the layers.

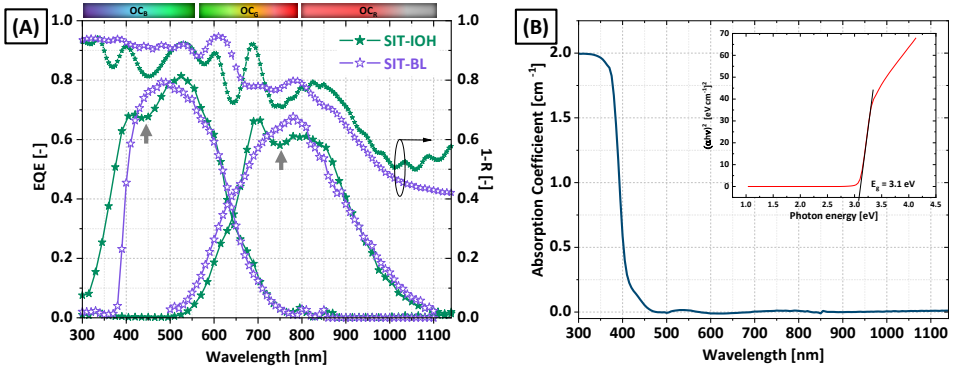


Figure 6.6.: (A) EQE and  $1 - R$  spectra of SIT-IOH and SIT-BL a-Si:H/nc-Si:H tandem solar cells (B) Absorbance of i-ZnO used in SIT-BL.

The benefit of light trapping in the solar cell with bi-layer TCO is nullified by the parasitic absorption losses of high-energy photons in i-ZnO. As a consequence,  $J_{SC,TOT}$  of SIT-BL is  $24.5 \text{ mA/cm}^2$  which is  $0.2 \text{ mA/cm}^2$  less than that of SIT-IOH. The sputtered i-ZnO with a thickness of  $1.5\text{-}\mu\text{m}$  is insufficient to completely mitigate the Fabry-Pérot interference effects in solar cells with random textures, unlike the LPCV-deposited i-ZnO reported in the literature [144]. This is due to the fact that CVD-grown TCOs have more crystal grains in the bulk. Moreover, these CVD-grown TCOs are optically more transparent and have higher electrical conductivity than RF magnetron-sputtered TCOs, as sputtering is heavily dependent on target quality [251, 252].

### 6.2.3. a-Si:H / nc-Si:H tandem solar cells on periodic textures

For studying a bi-layer TCO structure on HCs, i-ZnO layers with thicknesses of  $0.2 \mu\text{m}$ ,  $0.4 \mu\text{m}$ , and  $0.6 \mu\text{m}$  were incorporated, named HC-BL1, HC-BL2, and HC-BL3, respectively.

Figure 6.7(A) shows SEM images of the superstrate glasses before deposition. It can be observed that the size of TCO crystals increases with increasing layer thickness. This observation is consistent with what is reported by Faÿ *et al.*[76]. Solar cell active layer stack of HC-BL1, HC-BL2, and HC-BL3 was fabricated together with HC-IOH in a single batch to ensure comparability.

Figure 6.7(B) gives the  $1 - R$  of the solar cells. Considering the  $1 - R$  spectra, it is observed that, with increasing thickness and crystal size, the bi-layer TCO reduces the fringe amplitudes. Table 6.4 gives the  $R'$  values corresponding to different optical cavities for HC-IOH, HC-BL1, HC-BL2,

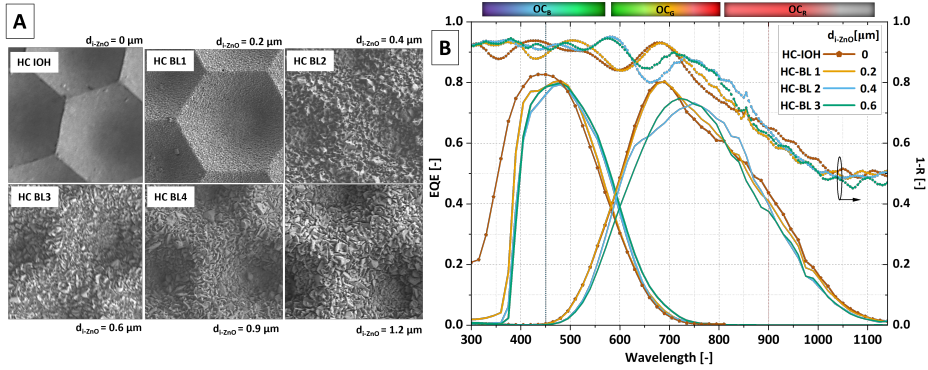


Figure 6.7.: (A) SEM images of different substrates used for HC-IOH ( covered glass), HC-BL1 (200 nm thick i-ZnO), HC-BL2 (400 nm thick i-ZnO), HC-BL3 (600 nm thick i-ZnO) and HC-BL4 (0.9- $\mu\text{m}$  thick i-ZnO). Additionally, 1.5- $\mu\text{m}$  thick i-ZnO layer on glass is shown to demonstrate the size difference in crystals. (B) EQE and  $1 - R$  spectra of a-Si:H/nc-Si:H tandem solar cells on these superstrates.

Table 6.4.: Weighted average reflectance values  $R'$  of different solar cells presented in this paper.

Sample	$R'_{300 < \lambda < 540}$ [%]	$R'_{550 < \lambda < 790}$ [%]	$R'_{800 < \lambda < 1200}$ [%]	$R'_{300 < \lambda < 1200}$ [%]
SIT-IOH	3.24	8.88	8.63	20.75
SIT-BL	2.24	7.47	10.03	19.74
HC-IOH	2.37	6.47	9.87	18.71
HC-BL1	2.19	6.06	10.49	18.74
HC-BL2	2.16	6.01	9.47	17.64
HC-BL3	2.10	5.40	10.11	17.61
HC-BL4	1.93	4.10	8.02	14.05
HC-SnO	1.58	5.29	10.15	17.01

and HC-BL3. HC-BL1 shows a minor shift of fringe from 350 to 420 nm because i-ZnO absorbs all photons below 380 nm completely. The interference fringe pattern in the  $1-R$  is approximately the same for HC-IOH and HC-BL1. For HC-BL2 and HC-BL3, the fringes formed by  $OC_B$  are totally quenched. This indicates that at least an i-ZnO thickness of 0.4- $\mu\text{m}$  (as in HC-BL2) is required to diminish the effect of  $OC_B$  in hexagonal micro-textures.  $R'_{300 < \lambda < 540}$  consistently decreases in value, indicating the decrease in reflected photon flux in the blue region. It is also observed that even a 0.6- $\mu\text{m}$  thick i-ZnO is not enough to mitigate the interference fringes caused by  $OC_G$ . However,  $R'_{550 < \lambda < 790}$  decreases by  $\approx 1\%$  absolute when 0.6- $\mu\text{m}$  i-ZnO layer is introduced. No tandem solar cells on the HC textures show major interference in the

Table 6.5.:  $J_{sc, TOT}$  and constituting component current values of solar cells on HC-IOH, HC-BL1, HC-BL-1 and HC-BL3 samples. NB: Subscripts - ToC refers to the top cell, and BoC refers to the bottom cell.

Sample	$d_{i-ZnO}$ [ $\mu\text{m}$ ]	$J_{\lambda < 450\text{nm}}$ [ $\text{mA}/\text{cm}^2$ ]	$J_{sc, ToC}$ [ $\text{mA}/\text{cm}^2$ ]	$J_{sc, BoC}$ [ $\text{mA}/\text{cm}^2$ ]	$J_{\lambda > 900\text{nm}}$ [ $\text{mA}/\text{cm}^2$ ]	$J_{sc, TOT}$ [ $\text{mA}/\text{cm}^2$ ]
HC-IOH	0	2.7	10.0	16.8	1.9	26.8
HC-BL1	0.2	2.1	9.1	16.7	1.7	25.8
HC-BL2	0.4	1.8	9.6	15.7	1.5	25.3
HC-BL3	0.6	1.9	9.6	15.1	1.5	24.7

near-infrared. This is either because the interface scattering of 5- $\mu\text{m}$  periodic HC with 1- $\mu\text{m}$  height profile can suppress the  $OC_R$ -induced interference fringes, or because the bottom cell thickness is sufficient to absorb all low-energy photons.

Figure 6.7(B) also gives the sub-cell EQEs. HC-IOH, HC-BL1, HC-BL2 and HC-BL3 have total spectral utilisations of 26.7  $\text{mA}/\text{cm}^2$ , 25.8  $\text{mA}/\text{cm}^2$ , 25.3  $\text{mA}/\text{cm}^2$  and 24.7  $\text{mA}/\text{cm}^2$  respectively. Table 6.5 gives the photoresponse at different  $\lambda$  ranges. The  $J_{SC, TOT}$  continuously decreases with an increase in i-ZnO thickness due to loss in blue response (related to bandgap) and parasitic absorption in the visible range by i-ZnO (related to tail states in i-ZnO). A loss of 0.6  $\text{mA}/\text{cm}^2$  is observed directly in  $J_{\lambda < 450\text{nm}}$  as parasitic absorption with the addition of 200-nm thick i-ZnO. The loss in the IR region is due to free carrier absorption (Drude absorption) [256].

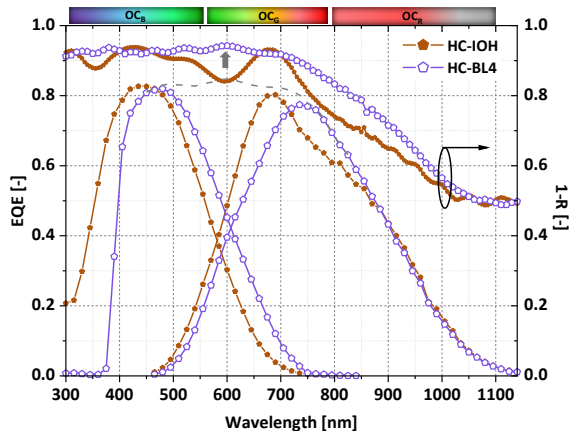


Figure 6.8.: EQE and  $1 - R$  spectra of HC-IOH and HC-BL4 a-Si:H/nc-Si:H tandem solar cells. Dotted lines represent the total spectral utilisation of HC-BL4.

Figure 6.8 gives the EQE and  $1 - R$  of tandem solar cells made on HC-IOH and HC-BL4. Initially, we consider the sole effect of the periodic and random interface scatterings by comparing HC-IOH with SIT-IOH (from Figure 6.6). In HC-IOH, the amplitude of fringes is significantly diminished compared to SIT-IOH. This is due to the morphological properties of HC-IOH shown in Figure 6.5 and discussed in Section 6.2.1. The presence of more feature sizes enhances scattering in HC-IOH compared to SIT-IOH. Additionally, light coupling via tapered

gratings reduces reflection in the cavities. Table 6.4 shows a gain of approximately 1% and more than 2% in  $R'_{300<\lambda<540}$  and  $R'_{550<\lambda<790}$  respectively for HC-IOH over SIT-IOH and an overall  $R'$  increase of 2% incoupled photon flux.

As discussed before, 0.4- $\mu\text{m}$  i-ZnO bi-layer suppresses the  $OC_B$  induced interference fringes in HC substrates. A further increase in i-ZnO thickness up to 0.9- $\mu\text{m}$  could suppress the interference resulting from  $OC_G$  as well (marked with arrow). HC-BL4 suggests that the OCs in HC superstrates can be nullified by scattering from smaller grains compared to SITs (refer to SEM image Figure 6.4). This can be attributed to the efficient interface-scattering property of HC, which, in turn, requires a smaller grain size to mitigate the interference effects of all OCs. From Table 6.4, an increase of 0.4%, 2.3% and 1.8% gain in photon flux is observed for  $R'_{300<\lambda<540}$ ,  $R'_{550<\lambda<800}$ ,  $R'_{800<\lambda<1200}$  respectively resulting an overall gain of 4.6% in photon flux in HC-BL4 compared to HC-IOH. Although the interference fringes are quenched, the sputtered i-ZnO exhibits parasitic absorption losses of high-energy photons — a trend similar to that observed in SIT-BL — which overshadows the gain. As a result, the total optical performance of the cell is reduced to 26.4  $\text{mA}/\text{cm}^2$  in HC-BL4 when compared to 26.8  $\text{mA}/\text{cm}^2$  for HC-IOH.

External parameters of single-layer and bi-layer solar cells are reported in Table 6.6. For random textures, SIT-IOH outperforms SIT-BL. A drop in  $V_{oc}$  and  $FF$  is observed for the bi-layer configuration. Both solar cells exhibit top cell current-limited behaviour. SIT-IOH has 1.2% (absolute) higher  $\eta$  compared to SIT-BL. For periodic textures, introducing a 0.9- $\mu\text{m}$  thick i-ZnO layer results in approximately the same  $V_{oc}$  and  $FF$ . An  $\eta = 9.2\%$  is measured for HC-IOH and 9.7% for HC-BL4. These are also a result of a heavily current-mismatched (top-cell-limited) situation. An increase in series resistance is observed upon introducing a sputtered i-ZnO layer for both bi-layer configurations. Notably, this increase in series resistance is almost double when using 1.5- $\mu\text{m}$  i-ZnO. This observation has not yet been reported in studies using LPCVD i-ZnO [77, 257] or BZO [76, 258]. It should be noted that the devices demonstrated in this study are not directly comparable to state-of-the-art a-Si:H/nc-Si:H configurations. Rather, the primary aim of these devices is to investigate and compare total spectral utilisation under conditions where optical interference effects are mitigated.

Table 6.6.: External parameters of solar cells deposited on SIT-IOH, SIT-BL, HC-IOH and HC-BL4 samples. The reported values are calculated from five cells on each textured substrate, which has the highest  $V_{oc} \times FF$  value. ToC refers to top cell and BoC refers to bottom cell. Standard deviation ( $\sigma_d$ ) of measurements are as follows: root-mean-square error of  $J_{sc} = 0.7\%$  (absolute)  $\sigma_d(V_{oc}) \approx 2$  mV,  $\sigma_d(FF) \approx 0.6\%$ ,  $\sigma_d(R_s) \approx 0.1 \Omega \cdot \text{cm}^2$ ,  $\sigma_d(R_p) \approx 0.1 \text{ k}\Omega \cdot \text{cm}^2$ .

Sample	$d_{i\text{-ZnO}}$ [ $\mu\text{m}$ ]	$V_{oc}$ [mV]	$J_{sc,ToC}$ [ $\text{mA}/\text{cm}^2$ ]	$J_{sc,BoC}$ [ $\text{mA}/\text{cm}^2$ ]	$J_{sc,TOT}$ [ $\text{mA}/\text{cm}^2$ ]	FF [%]	$R_s$ [ $\Omega \cdot \text{cm}^2$ ]	$R_p$ [ $\text{k}\Omega \cdot \text{cm}^2$ ]	$\eta$ [%]
SIT-IOH	0	1390	12.1	12.6	24.7	66.9	30.2	7.7	11.3
SIT-BL	1.5	1361	11.4	13.1	24.5	65.1	42.1	7.2	10.1
HC-IOH	0	1408	10.0	16.8	26.8	65.0	35.9	8.9	9.2
HC-BL4	0.9	1410	10.5	15.9	26.4	65.4	40.0	8.7	9.7
HC-SnO	1.0	1393	10.7	13.8	24.5	54.0	34.0	3.4	8.0

In summary, the optical performance of the solar cells on any texture with sputtered i-ZnO is a trade-off between the gain in photocurrent from reduced fringes and the loss of high-energy photons in the sputtered i-ZnO layer. A periodic texture combined with an i-ZnO stack with a

thickness below  $1\ \mu\text{m}$  (sample: HC-BL4) could mitigate fringe contributions of  $OC_B$ ,  $OC_G$ , and  $OC_R$ , which is much smaller than the  $\approx 2\text{-}\mu\text{m}$  thick LPCVD TCOs reported in the literature [19, 20, 28, 45, 49, 77]. On the contrary, grain scattering by a  $1.5\text{-}\mu\text{m}$  thick i-ZnO layer and larger crystals (sample: SIT-BL) was not as effective at removing the effects of  $OC_G$ . Since the target material influences the quality and optical absorption of the sputtered layer, the thickness that needs to be used is a compromise between parasitic absorption and light scattering. This means that a periodic hexagonal texture is the preferred combination for low-temperature sputtered i-ZnO. The reported total current density of  $26.4\ \text{mA}/\text{cm}^2$  can yield bottom-subcell current-limited cells with  $13.1\ \text{mA}/\text{cm}^2$  using internal reflection layer techniques and a thicker top cell.

### 6.3. Grain scattering with wide-bandgap SnO

Table 6.6 includes the performance of HC-SnO solar cells with a  $1.0\text{-}\mu\text{m}$ -thick SnO layer implemented as a grain scatterer. When the SnO/SiO<sub>x</sub>/IOH front electrode is used, the cell's electrical performance drops significantly due to a decrease in FF caused by low parallel resistance. We speculate that the lower parallel resistance is likely caused by the lack of a sufficient cleaning cycle between the SiO<sub>x</sub> deposition and IOH deposition, which happens in two different deposition tools and requires exposure to ambient between the processes. The SEM image and EQE of this solar cell are given in Figure 6.9. The SEM images given in the inset suggest that the SnO grains exhibit a columnar crystal growth with very minimal naturally grown texture at the interface. An important observation is that a thickness of  $1\text{-}\mu\text{m}$  is enough to mitigate all interference fringes caused by  $OC_B$ ,  $OC_G$ , and  $OC_R$ .

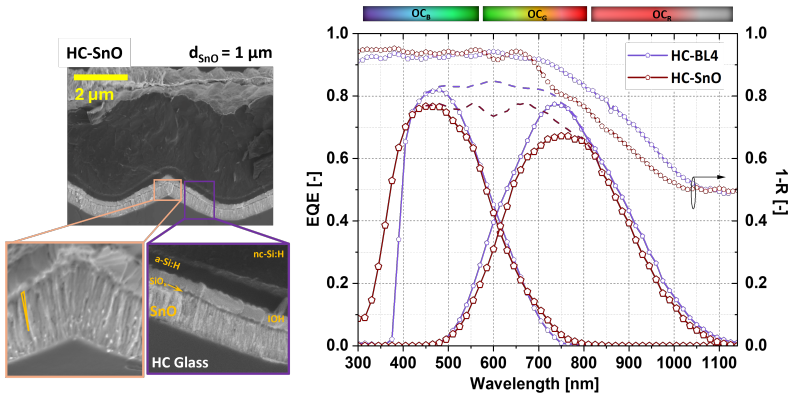


Figure 6.9.: EQE and  $1 - R$  spectra of HC-SnO and HC-BL4 a-Si:H/nc-Si:H tandem solar cells. Dotted lines represent the total spectral utilisation of each solar cell.

The high band gap of SnO resulted in an increase in the EQE response of the top cell between 300 and 450 nm in HC-SnO compared to HC-BL4. From Table 6.4, a small increase of 0.4% gain in photon incoupling is observed for  $R'_{300 < \lambda < 540}$ . The same cell also shows a drop of 1.2% and 2.1% in photon flux is observed for  $R'_{550 < \lambda < 800}$ ,  $R'_{800 < \lambda < 1200}$ , respectively. These together result in an overall drop of light incoupling by 3% in HC-SnO compared to HC-BL4. The major loss is between  $\lambda = 700\ \text{nm}$  and  $1000\ \text{nm}$  - similar to the HC-IOH in Figure 6.8. The higher reflection in the 700-1200 nm range is a result of the presence of the IOH/(p)SiO:H interface in HC-SnO and HC-IOH. As seen in Figure 6.2, above 700 nm IOH has the highest contrast in refractive indices

with the (p)SiO:H among all TCOs used. This means that the Fresnel reflection coefficient is higher for IOH/(p)SiO:H compared to the graded refractive indices in IOH/i-ZnO/(p)SiO:H stack. The SnO used in this demonstration exhibits heavy parasitic absorption, which reduces the total optical response of the solar cell. However, the SnO sputtering recipe can be optimised rigorously further in this case, as the TCO does not take part electrically in the cell performance. A SnO layer with high optical transmission and significantly low free carrier concentrations can be a promising route for high-performing front textures with little or no interference fringes in thin-film silicon solar cells.

## 6.4. Conclusion

This work uses a-Si:H/nc-Si:H tandem solar cells as a medium to study superstrate configuration multijunction cells with Fabry-Pérot micro-cavities. These optical micro-cavities limit the optimal light coupling in the subcells of a multijunction solar cell. Random or periodic texture demonstrates interface scattering in devices and partially mitigates the interference effect of optical cavities. However, applying textures to glass alone is insufficient to eliminate the interference effects of optical cavities completely. With interface scattering, a periodic hexagonal texture on glass breaks the coherence in light more than random textures. Furthermore, a light scattering mechanism with TCO grains is added to textures through low-temperature sputtered i-ZnO. With increasing thickness and crystal size, the amplitude of fringes decreases. For a random textured glass substrate, a 1.5- $\mu\text{m}$  thick i-ZnO layer could quench interference in the top cell, except for the effect of the optical cavity formed in the amorphous top cell. Whereas, hexagonal craters on glass, combined with a 0.9- $\mu\text{m}$  thick i-ZnO layer, effectively mitigated fringes formed by all optical cavities in the device. It is suggested that a periodic hexagonal texture is the preferred combination for low-temperature sputtered i-ZnO. Use of a wide bandgap TCO like SnO can effectively suppress cavity-induced interference fringes, simultaneously avoiding the parasitic absorption of high-energy photons, which is otherwise absorbed by i-ZnO. The design principles discussed in this work are not restricted to a-Si:H/nc-Si:H tandem but can be extended to any thin-film multijunction solar cells consisting of layers with contrasting refractive indices.



# 7

## Conclusion

In this dissertation, light-management techniques with front textures for thin-film silicon superstrate configuration solar cells are presented. Specifically, the textures are developed on glass to act as light scatterers at interfaces in thin-film devices. This thesis aims to create textures on glass with a broader idea of transferring them to aluminium for implementing them for pre-textured transparent conductive oxides (TCO) made by LiFT PV B.V. On a broader scale, this thesis aims to answer a main question:

### **How to engineer a front glass texture with which high-performing thin-film silicon superstrate solar cells can be fabricated?**

This main research question is divided into four key questions answered by studying random textures on glass, periodic textures on glass and fabricating multijunction thin-film silicon cells on glass textures.

Before addressing the key questions, an optimisation of thin-film silicon deposition in the multichamber plasma-enhanced chemical vapour deposition (PECVD) tool is presented. The fabrication of device-grade nanocrystalline silicon (nc-Si:H) and amorphous silicon (a-Si:H) absorber material is realised in very high frequency (VHF) conditions in the same chamber. The product of open-circuit voltage ( $V_{oc}$ ) and fill factor (FF) is highest for nc-Si:H single-junction solar cells at a crystallinity near the amorphous to nanocrystalline transition regime with crystallinity  $\approx 60$  to 65%. For micro-sized textures on glass, the highest-performing cells in terms of efficiency ( $\approx 9.0\%$ ) were made at 40.68 MHz VHF, at a chamber pressure of 4 mBar, a power density of  $0.4 \text{ W/cm}^2$ , a silane flow of 3.3 sccm, and a hydrogen flow of 120 sccm (resulting in a silane concentration of 2.6%). Wide bandgap a-Si:H with band gap energy of 1.90 eV and single junction cells with  $V_{oc} = 934 \text{ mV}$ , FF = 68%, short-circuit current density ( $J_{sc}$ ) of  $12.7 \text{ mA/cm}^2$  and efficiency ( $\eta$ ) of 7.9% were deposited at VHF, at a pressure of 5 mBar, power density  $0.30 \text{ W/cm}^2$ , silane flow 6 sccm, and hydrogen flow 120 sccm (resulting silane concentration of 4.8%).

Chapter 3 presents a detailed sample study of three sacrificial random texturing approaches on glass utilising two different sacrificial TCO layers, namely indium-doped tin oxide (ITO) and intrinsic (not intentionally doped) zinc oxide (i-ZnO). i-ZnO is a novel TCO material used in texturing glass. The chapter presents observations on the physical properties of the created textures and their interaction with light. Using the ITO layer for sacrificial texturing ( $SLT_{ITO}$ ) resulted in large craters with spherical 'inverted U' shapes with peak RMS roughness ( $\sigma_{rms}$ ) of 958 nm. Using the i-ZnO sacrificial layer ( $SLT_{IZO}$ ) created small craters with conical 'inverted V' shapes and peak attained  $\sigma_{rms} = 318 \text{ nm}$ . A correlation is observed between the  $\sigma_{rms}$  of the textures and their diffused transmission. Large-size textures of  $SLT_{ITO}$  follow coherent refraction, while  $SLT_{IZO}$  nano textures follow incoherent Mie scattering. The best-performing

$SLT_{ITO}$ ,  $SLT_{IZO}$  resulted in  $\eta$  of 8.81% and 7.38% with  $J_{sc}$  25.81, 25.08 mA/cm<sup>2</sup>, respectively. The processing conditions of optically best-diffusing textures from each sample set are combined to make a superimposed texturing -  $SIT$ .  $SIT$  has features resembling its constituent morphologies ( $\sigma_{rms} = 418$  nm) and exhibits combined scattering characteristics of both diffractive and refractive scattering regimes across a broad wavelength.  $SIT$  exhibits excellent optical properties in terms of reflectance and scattering. The nc-Si:H single-junction solar cells made on  $SIT$  resulted in the highest-performing solar cell in terms of external quantum efficiency (EQE) with  $J_{sc}$  of 26.75 mA/cm<sup>2</sup> and  $\eta = 9.38\%$  among the mentioned textures.

Chapter 4 presents a detailed analysis of the processes used to make periodic honeycomb (HC) textures in glass superstrates. The influence of these processing parameters, particularly their effect on texture depth, is studied in detail. Glass wafer surfaces require acidic cleaning to ensure proper adhesion between the glass and photoresist (PR). This was achieved by cleaning the glass superstrates with 69.5% HNO<sub>3</sub> followed by a running water dip and spin-drying. Pre-baking of wafers at 110 °C for 10 minutes before coating with PR ensured the removal of any amount of adsorbed water from the surface. Additionally, it was noted that during the coating step, priming the surface with hexamethyldisilazane at 150 °C for 150 seconds best removes the polar hydroxyl groups to improve the surface adhesion towards PR. Using a 2.1 μm for Shipley PR3012 reduces the diffusion of the etchant ions through the PR. Post development, the samples were hard-baked at 140 °C for 30 minutes to enhance PR adhesion via cross-linking. Using these parameters, honeycombs were made on glass wafers with varying periodicities of 3 μm, 4 μm and 5 μm. At 5 μm, hexagonal microtextures with 1010 nm absolute depth are obtained.

Hexagonal texturing on glass does not exhibit perfectly isotropic etching, a property dedicated to the spatial distribution of orifices. A parameter,  $D_{e,p}$  is defined, successfully quantifying the extent of isotropic etching exhibited by the texturing process. The total transmission and scattering of light by hexagonal textures depend on their angle distribution. As the periodicity and height of the texture increase, hexagonal microtextures exhibit enhanced transmission and scattering properties.

7

Chapter 5 reports periodic hexagonal microtextures on glass, their optical properties and their application in nc-Si:H solar-cell devices. The surface morphology and optical properties of the textures are reported. Features of multiple size ranges characterise the HC surface morphology. Hexagonal textures exhibit enhanced light transmission across the entire wavelength range when the periodicity is increased. Hexagonal textures with deeper craters also display high diffused transmission and broad-angle scattering properties. These properties directly translate to EQE spectra of solar cells fabricated on the textures, increasing the photoresponse and efficiency with an increase in periodicity and aspect ratio of the hexagonal micro-textures. Hexagonal textures with a 5 μm periodicity with a 20.2% aspect ratio yield a photocurrent of 28.6 mA/cm<sup>2</sup> and a photo conversion efficiency of 9.30%. It is also observed that the HC textures in the superstrate configuration glass can facilitate  $V_{oc}$  around 520 mV and crack-free nc-Si:H crystal growth. This indicates a high potential for hexagonal textures on glass in multijunction thin-film solar-cell applications.

Chapter 6 of this thesis presents a-Si:H/nc-Si:H tandem solar cells as a route to study superstrate configuration multijunction cells with Fabry-Pérot micro-cavities. These optical micro-cavities limit the optimal light incoupling in the subcells of a multijunction solar cell. We demonstrate the use of random or periodic texture to implement interface scattering in devices and partially mitigate the interference effect of optical cavities. However, applying textures to glass alone is insufficient to eliminate the interference effects of optical cavities completely. With interface scattering, a periodic hexagonal texture on glass breaks the coherence in light more

than random textures. Furthermore, a light-scattering mechanism with TCO grains is added to textures through low-temperature, cost-effective sputtered i-ZnO. For a random textured glass substrate, a 1.5- $\mu\text{m}$  thick i-ZnO layer could quench interference in the top cell, except for the effect of the optical cavity formed in the amorphous top cell. Hexagonal craters on glass, combined with a 0.9- $\mu\text{m}$  thick i-ZnO layer, effectively mitigated fringes formed by all optical cavities in the device. Use of a wide bandgap TCO like tin oxide (SnO) is useful in eliminating the optical cavities, simultaneously avoiding the parasitic absorption of high-energy photons, which are otherwise absorbed by i-ZnO. The design principles discussed in this work are not restricted to a-Si:H/nc-Si:H tandem but can be extended to any thin-film multijunction solar cells consisting of layers with contrasting refractive indices.

## 7.1. Perspectives from the thesis

The primary objective of this thesis is to design a scattering front window that enhances the light management performance and enables the processing of high-quality thin-film silicon layers on top of it. Beyond the specific results and conclusions detailed in Chapters 2 through 6, this thesis has generated several additional conceptual perspectives related to the primary research question. This section briefly outlines these emergent insights.

Chapters 3 and 5 compare single-junction nc-Si:H solar cells on random and periodic-hexagonal textures on glass. The best optical responses of a single junction nc-Si:H p-i-n superstrate solar cell processed on random and periodic textures in this thesis are 26.75 and 28.60  $\text{mA}/\text{cm}^2$ , respectively - refer Figure 7.1 (Left). The  $J_{sc}$  of 28.60  $\text{mA}/\text{cm}^2$  on 5  $\mu\text{m}$  periodic hexagonal micro-textures is one of the highest reported optical performances on a single junction nc-Si:H superstrate solar cells without any external anti-reflection measures.

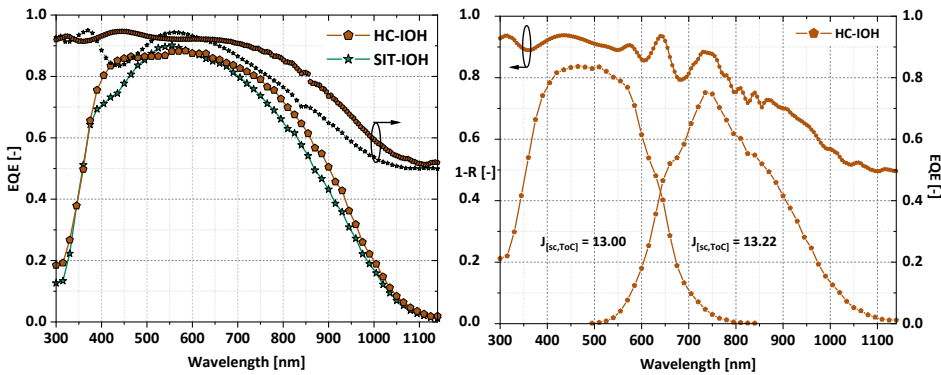


Figure 7.1.: EQE and  $1 - R$  spectra of: **Left:** nc-Si:H single junction solar cells on random (SIT-IOH) and periodic (HC-IOH) textures, **Right:** a-Si:H/nc-Si:H tandem solar cells on periodic texture (HC-IOH).

During this thesis, a-Si:H/nc-Si:H tandem solar cells were fabricated on the hexagonal microtextures to reach a  $\eta = 12.3\%$  for an approximately current-matched solar cell with top cell  $J_{sc} = 13.0 \text{ mA}/\text{cm}^2$  and bottom cell  $J_{sc} = 13.2 \text{ mA}/\text{cm}^2$  (total spectral utilisation of  $26.2 \text{ mA}/\text{cm}^2$ ) - refer Figure 7.1 (Right). This solar cell has  $V_{oc} = 1392 \text{ mV}$  and  $FF = 67.9$ . It has to be noted that the

cell is top-cell current-limited. Mitigating interference fringes in the  $1 - R$  spectrum with high-bandgap TCO grain scattering can enhance the optical performance of the solar cells.

**Grain scattering:** As an initial experiment, sputtered tin oxide is employed as a wide bandgap grain scatterer at the front side of an a-Si:H/nc-Si:H tandem configuration in Chapter 6. The SnO sputtering recipe can be further optimised rigorously for better performance. As the TCO does not take part electrically in the cell performance, the layer properties need to be optimised for high optical transmission with significantly low free carrier concentrations.

**Anti-reflection:** To further improve thin-film silicon solar cells' optical performances, two possible anti-reflection routes that can be explored are a  $\text{MgF}_2$  layer deposited and subwavelength anti-reflection structures glued to the front side of the glass. As a part of this thesis, a 70-nm-thick  $\text{MgF}_2$  layer was deposited at the front side of the solar cell; however, due to the flat nature of the layers, a new optical microcavity was developed around a 350-nm wavelength. A potential route to tackle this challenge is to introduce a nano-texture at the front flat side of the glass before  $\text{MgF}_2$  deposition. But it would require a special technique to shield the intended cell deposition side to protect the crater structures.

To enhance the electrical performance, it is essential to employ a thicker top cell or incorporate an internal reflective layer to ensure the bottom sub-cell functions as the current-limiting cell. Furthermore, the integration of an external anti-reflection coating on the front surface of the glass is required. This must be coupled with high-temperature deposition of the TCO, resulting in reduced parasitic absorption losses and contributing to refractive index grading within the window layer stack: Glass/IOH/i-ZnO/p-layer to attain record-best conversion efficiencies.

# Bibliography

- [1] International Energy Agency. *World Energy Outlook 2025*. English. Tech. rep. Paris: International Energy Agency, Nov. 2025. URL: <https://www.iea.org/reports/world-energy-outlook-2025>.
- [2] M. Crippa, D. Guizzardi, F. Pagani, M. Banja, and M. Muntean. *GHG emissions of all world countries*. Tech. rep. Luxembourg: Publications Office of the European Union, 2025, JRC143227. DOI: [10.2760/9816914](https://doi.org/10.2760/9816914). URL: <https://data.europa.eu/doi/10.2760/9816914>.
- [3] M. Victoria, N. Haegel, I. M. Peters, R. Sinton, A. Jäger-Waldau, C. del Cañizo, C. Breyer, M. Stocks, A. Blakers, I. Kaizuka, K. Komoto, and A. Smets. *Solar photovoltaics is ready to power a sustainable future*. May 2021. DOI: [10.1016/j.joule.2021.03.005](https://doi.org/10.1016/j.joule.2021.03.005).
- [4] D. Bogdanov, J. Farfan, K. Sadovskaia, A. Aghahosseini, M. Child, A. Gulagi, A. S. Oyewo, L. de Souza Noel Simas Barbosa, and C. Breyer. “Radical transformation pathway towards sustainable electricity via evolutionary steps”. In: *Nature Communications* 10.1 (Dec. 2019). ISSN: 20411723. DOI: [10.1038/s41467-019-08855-1](https://doi.org/10.1038/s41467-019-08855-1).
- [5] C. Breyer, D. Bogdanov, M. Ram, S. Khalili, E. Vartiainen, D. Moser, E. Román Medina, G. Masson, A. Aghahosseini, T. N. Mensah, G. Lopez, M. Schmela, R. Rossi, W. Hemetsberger, and A. Jäger-Waldau. “Reflecting the energy transition from a European perspective and in the global context—Relevance of solar photovoltaics benchmarking two ambitious scenarios”. In: *Progress in Photovoltaics: Research and Applications* 31.12 (Dec. 2023), pp. 1369–1395. ISSN: 1099159X. DOI: [10.1002/pip.3659](https://doi.org/10.1002/pip.3659).
- [6] *27.81%! LONGi Refreshes the World Record for the Efficiency of Monocrystalline Silicon Cells Again*. United States, Apr. 2025. URL: <https://www.longi.com/us/news/longi-world-record-efficiency-of-monocrystalline-silicon-cells/>.
- [7] A. Richter, M. Hermle, and S. W. Glunz. “Reassessment of the Limiting Efficiency for Crystalline Silicon Solar Cells”. In: *IEEE Journal of Photovoltaics* 3.4 (Oct. 2013), pp. 1184–1191. ISSN: 2156-3381. DOI: [10.1109/JPHOTOV.2013.2270351](https://doi.org/10.1109/JPHOTOV.2013.2270351).
- [8] M. A. Green, E. D. Dunlop, M. Yoshita, N. Kopidakis, K. Bothe, G. Siefer, X. Hao, and J. Y. Jiang. “Solar cell efficiency tables (version 66)”. In: *Progress in Photovoltaics* 33.NREL/JA-5900-94273 (2025).
- [9] A. H. Smets, K. Jäger, I. Olindo, M. Zeman, and R. A. van Swaaij. “Solar Energy: The physics and engineering of photovoltaic conversion, technologies and systems”. In: UIT Cambridge, 2016. ISBN: 1906860750,9781906860752.
- [10] Gaëtan Masson, Melodie de l’Epine, and Izumi Kaizuka. *Trends in Photovoltaic Applications 2024*. Tech. rep. International Energy Agency, 2024, p. 104. URL: [www.iea-pvps.org](http://www.iea-pvps.org).
- [11] T. Matsui, H. Sai, A. Bidiville, H.-J. Hsu, and K. Matsubara. “Progress and limitations of thin-film silicon solar cells”. In: *Solar Energy* 170.May (Aug. 2018), pp. 486–498. ISSN: 0038092X. DOI: [10.1016/j.solener.2018.05.077](https://doi.org/10.1016/j.solener.2018.05.077).
- [12] A. Gordijn, M. N. Van Den Donker, F. Finger, E. A. G. Hamers, G. J. Jongerden, W. M. M. Kessels, R. Bartl, A. M. B. Van Mol, J. K. Rath, B. Rech, R. Schlatmann, R. E. I. Schropp, B. Stannowski, H. Stiebig, M. C. M. Van De Sanden, R. A. C. M. M. Van Swaaij, and M. Zeman. “Flexible a-Si/ $\mu$ c-Si Tandem Modules in the Helianthos Project”. In: *2006 IEEE 4th World Conference on Photovoltaic Energy Conference*. IEEE, 2007, pp. 1716–1719. DOI: [10.1109/WCPEC.2006.279822](https://doi.org/10.1109/WCPEC.2006.279822).
- [13] NREL. *Research on Amorphous-Silicon-Based Thin-Film Photovoltaic Devices: Semiannual Subcontract Report, 1 July 1987 - 31 December 1987*. American English. 1988. URL: <https://www.nrel.gov/docs/legosti/old/3350.pdf>.

- [14] K. P. Sreejith, V. Venkatesh, G. Padmakumar, and A. H. Smets. “Comprehensive Glare Hazard Analysis of Ethylene Tetrafluoroethylene (ETFE) Based Frontsheet for Flexible Photovoltaic Applications”. In: *IEEE Journal of Photovoltaics* 14.6 (2024), pp. 930–936. ISSN: 21563403. DOI: [10.1109/JPHOTOV.2024.3463961](https://doi.org/10.1109/JPHOTOV.2024.3463961).
- [15] A. Shah. “Thin-film silicon solar cells”. In: *McEvoy's Handbook of Photovoltaics: Fundamentals and Applications*. Elsevier Inc., Nov. 2017, pp. 235–307. ISBN: 9780128103975. DOI: [10.1016/B978-0-12-809921-6.00008-2](https://doi.org/10.1016/B978-0-12-809921-6.00008-2).
- [16] F. Saitta, A. H. M. Smets, L. Kessels, R. Santbergen, P. Perez Rodriguez, and R. A. J. Janssen. “Optical modelling and performance assessment of thin-film silicon/perovskite tandem solar cells”. In: *Photonics for Solar Energy Systems X*. Ed. by L. Mazzarella, J. C. Goldschmidt, and A. N. Sprafke. SPIE, June 2024, p. 3. ISBN: 9781510681415. DOI: [10.1117/12.3017541](https://doi.org/10.1117/12.3017541).
- [17] H. Sai, T. Matsui, and K. Matsubara. “Key Points in the Latest Developments of High-Efficiency Thin-Film Silicon Solar Cells”. In: *Physica Status Solidi (A) Applications and Materials Science* 214.12 (Dec. 2017). ISSN: 18626319. DOI: [10.1002/pssa.201700544](https://doi.org/10.1002/pssa.201700544).
- [18] H. Sai, T. Matsui, and K. Matsubara. “Stabilized 14.0%-efficient triple-junction thin-film silicon solar cell”. In: *Applied Physics Letters* 109.18 (Oct. 2016). ISSN: 00036951. DOI: [10.1063/1.4966996](https://doi.org/10.1063/1.4966996).
- [19] T. Matsui, K. Maejima, A. Bidiville, H. Sai, T. Koida, T. Suezaki, M. Matsumoto, K. Saito, I. Yoshida, and M. Kondo. “High-efficiency thin-film silicon solar cells realized by integrating stable a-Si:H absorbers into improved device design”. In: *Japanese Journal of Applied Physics* 54.8S1 (Aug. 2015), 08KB10. ISSN: 0021-4922. DOI: [10.7567/JJAP.54.08KB10](https://doi.org/10.7567/JJAP.54.08KB10). URL: <https://iopscience.iop.org/article/10.7567/JJAP.54.08KB10>.
- [20] J. Cashmore, M. Apolloni, A. Braga, O. Caglar, V. Cervetto, Y. Fenner, S. Goldbach-Aschemann, C. Goury, J. Hötzel, T. Iwahashi, J. Kalas, M. Kitamura, M. Klindworth, M. Kupich, G.-F. Leu, J. Lin, M.-H. Lindic, P. Losio, T. Mates, D. Matsunaga, B. Mereu, X.-V. Nguyen, I. Psimoulis, S. Ristau, T. Roschek, A. Salabas, E. Salabas, and I. Sinicco. “Improved conversion efficiencies of thin-film silicon tandem (MICROMORPH™) photovoltaic modules”. In: *Solar Energy Materials and Solar Cells* 144 (Jan. 2016), pp. 84–95. ISSN: 09270248. DOI: [10.1016/j.solmat.2015.08.022](https://doi.org/10.1016/j.solmat.2015.08.022).
- [21] S. De Wolf, A. Descoedres, Z. C. Holman, and C. Ballif. “High-efficiency Silicon Heterojunction Solar Cells: A Review”. In: *Green* 2.1 (Mar. 2012), pp. 7–24. ISSN: 1869-8778. DOI: [10.1515/green-2011-0018](https://doi.org/10.1515/green-2011-0018).
- [22] Q. Wang, E. Iwaniczko, J. Yang, K. Lord, and S. Guha. “High Quality Amorphous Silicon Germanium Alloy Solar Cells Made by Hot-wire CVD at 10 Å . . /s”. In: *MRS Proceedings* 664 (2001), A7.5. DOI: [10.1557/PROC-664-A7.5](https://doi.org/10.1557/PROC-664-A7.5).
- [23] R. E. I. Schropp. *Advances in solar cells made with hot wire chemical vapor deposition (HWCVD): superior films and devices at low equipment cost*. Tech. rep. 2002, pp. 17–25.
- [24] B. Korevaar, C. Smit, A. Petit, R. van Swaaij, and M. van de Sanden. “Integration of Expanding Thermal Plasma deposited Hydrogenated Amorphous Silicon in Solar Cells”. In: *MRS Proceedings* 715 (2002), A6.5. DOI: [10.1557/PROC-715-A6.5](https://doi.org/10.1557/PROC-715-A6.5).
- [25] C. Smit, A. Klaver, B. A. Korevaar, A. M. Petit, D. L. Williamson, R. A. Van Swaaij, and M. C. Van De Sanden. “High-rate deposition of microcrystalline silicon with an expanding thermal plasma”. In: *Thin Solid Films* 491.1-2 (Nov. 2005), pp. 280–293. ISSN: 00406090. DOI: [10.1016/j.tsf.2005.06.032](https://doi.org/10.1016/j.tsf.2005.06.032).
- [26] M. C. M. Van De Sanden, R. J. Severens, J. Bastiaanssen, and D. C. Schram. *High-quality a-Si:H grown at high rate using an expanding thermal plasma*. Tech. rep. 1997, pp. 719–722.
- [27] R. E. Schropp, C. H. Van Der Werf, M. Zeman, M. C. Van De Sanden, C. I. Spee, E. Middelmann, L. V. De Jonge-Meschaninova, P. M. Peters, A. A. Van Der Zijden, M. M. Besselink, R. J. Severens, J. Winkeler, and G. J. Jongerden. “Novel amorphous silicon solar cell using a manufacturing procedure with a temporary superstrate”. In: *Materials Research Society Symposium - Proceedings* 557 (1999), pp. 713–718. ISSN: 02729172. DOI: [10.1557/proc-557-713](https://doi.org/10.1557/proc-557-713).

- [28] J. S. Cashmore, M. Apolloni, A. Braga, O. Caglar, V. Cervetto, Y. Fenner, S. Goldbach-Aschemann, C. Goury, J. E. Hötzel, T. Iwahashi, J. Kalas, M. Kitamura, M. Klindworth, M. Kupich, G. F. Leu, J. Lin, M. H. Lindic, P. A. Losio, T. Mates, D. Matsunaga, B. Mereu, X. V. Nguyen, I. Psimoulis, S. Ristau, T. Roschek, A. Salabas, E. L. Salabas, and I. Sinicco. "Record 12.34% stabilized conversion efficiency in a large area thin-film silicon tandem (MICROMORPH™) module". In: *Progress in Photovoltaics: Research and Applications* 23.11 (Nov. 2015), pp. 1441–1447. ISSN: 1099159X. DOI: [10.1002/pip.2642](https://doi.org/10.1002/pip.2642).
- [29] *LG Electronics Enters Solar Business in North America*. Oct. 2010. URL: <https://www.achrnews.com/articles/115035-oct-26-2010-lg-electronics-enters-solar-business-in-north-america>.
- [30] *LG Solar Power Module*. Tech. rep. LG Electronics. URL: [https://www.lg.com/us/business/download/resources/BT00002151/BT00002151\\_418.pdf](https://www.lg.com/us/business/download/resources/BT00002151/BT00002151_418.pdf).
- [31] SHARP. *Sharp Launches Mass Production of 2nd-Generation Thin-Film Solar Cells Using Large-Size Glass Substrates*. Oct. 2008.
- [32] Kaneka. *Kaneka to Accelerate Development to Social Implementation of High-Performance Perovskite Solar Cells via the NEDO Green Innovation Fund*. Mar. 2022. URL: <https://www.kaneka.co.jp/en/topics/news/2022/enr2203162.html>.
- [33] NREL. *Thin-Amorphous Silicon Alloy Research Partnership; Final Technical Progress Report; 2 February 1995 - 28 February 1998*. American English. United States, 1998. URL: <http://docs.nrel.gov/docs/legosti/old/24723.pdf>.
- [34] Applied Materials. *Applied Materials Revolutionizes Solar Module Manufacturing with Breakthrough SunFab Thin Film Line*. Milan, Italy, July 2007. URL: <https://ir.appliedmaterials.com/news-releases/news-release-details/applied-materials-revolutionizes-solar-module-manufacturing>.
- [35] Oerlikon Solar. *Oerlikon Solar Breaking Two World Records: Lowest Module Production Cost and Highest Lab Cell Efficiency*. EN. Tech. rep. Oerlikon Solar, July 2010. URL: <https://www.oerlikon.com/en/about-us/media/press-releases/oerlikon-solar-breaking-two-world-records-lowest-module-production-cost-and-highest-lab-cell-efficiency/>.
- [36] NREL. *Research on High-Efficiency, Single-Junction, Monolithic, Thin-Film Amorphous Silicon Solar Cells, Phase II Annual Subcontract Report, 1 January 1985 - 31 January 1986*. American English. United States, 1986. URL: <https://research-hub.nrel.gov/en/publications/research-on-high-efficiency-single-junction-monolithic-thin-film--19/>.
- [37] M. Stuckelberger, R. Biron, N. Wyrsh, F.-J. Haug, and C. Ballif. "Review: Progress in solar cells from hydrogenated amorphous silicon". In: *Renewable and Sustainable Energy Reviews* 76. June 2016 (Sept. 2017), pp. 1497–1523. ISSN: 13640321. DOI: [10.1016/j.rser.2016.11.190](https://doi.org/10.1016/j.rser.2016.11.190).
- [38] J. Meier, J. Spitznagel, U. Kroll, C. Bucher, S. Faj, T. Moriarty, and A. Shah. "Potential of amorphous and microcrystalline silicon solar cells". In: *Thin Solid Films*. Vol. 451–452. Mar. 2004, pp. 518–524. DOI: [10.1016/j.tsf.2003.11.014](https://doi.org/10.1016/j.tsf.2003.11.014).
- [39] S. Benagli, D. Borrello, E. Vallat-Sauvain, J. Meier, U. Kroll, J. Hoetzel, J. Bailat, J. Steinhauser, M. Marmelo, G. Monteduro, and L. Castens. "High efficiency amorphous silicon devices on LP-CVD TCO prepared in industrial Kai-M R&D reactor high efficiency amorphous silicon devices on LPCVD-ZnO TCO prepared in industrial KAI TM-M R&D reactor". In: *24th European Photovoltaic Solar Energy Conference & Exhibition (2009)*, 3BO.9.3.
- [40] T. Matsui, H. Sai, T. Suezaki, M. Matsumoto, K. Saito, I. Yoshida, and M. Kondo. "Development of Highly Stable and Efficient Amorphous Silicon Based Solar Cells". In: *28th EU PVSEC*. Nov. 2013, pp. 2213–2217. DOI: [10.4229/28thEUPVSEC2013-3D0.7.2](https://doi.org/10.4229/28thEUPVSEC2013-3D0.7.2).
- [41] A. Lambertz, F. Finger, R. E. Schropp, U. Rau, and V. Smirnov. "Preparation and measurement of highly efficient a-Si:H single junction solar cells and the advantages of  $\mu\text{-SiOx:H}$  n-layers". In: *Progress in Photovoltaics: Research and Applications* 23.8 (Aug. 2015), pp. 939–948. ISSN: 1099159X. DOI: [10.1002/pip.2629](https://doi.org/10.1002/pip.2629).
- [42] K. Yamamoto. *Very Thin Film Crystalline Silicon Solar Cells on Glass Substrate Fabricated at Low Temperature*. Tech. rep. 10. 1999.

- [43] Y. Mai, S. Klein, R. Carius, H. Stiebig, L. Houben, X. Geng, and F. Finger. "Improvement of open circuit voltage in microcrystalline silicon solar cells using hot wire buffer layers". In: *Journal of Non-Crystalline Solids* 352.9-20 SPEC. ISS. (June 2006), pp. 1859–1862. ISSN: 00223093. DOI: [10.1016/j.jnoncrysol.2005.11.116](https://doi.org/10.1016/j.jnoncrysol.2005.11.116).
- [44] H. Sai, T. Koida, T. Matsui, I. Yoshida, K. Saito, and M. Kondo. "Microcrystalline silicon solar cells with 10.5% efficiency realized by improved photon absorption via periodic textures and highly transparent conductive oxide". In: *Applied Physics Express* 6.10 (Oct. 2013). ISSN: 18820778. DOI: [10.7567/APEX.6.104101](https://doi.org/10.7567/APEX.6.104101).
- [45] S. Hänni, G. Bugnon, G. Parascandolo, M. Boccard, J. Escarré, M. Despeisse, F. Meillaud, and C. Ballif. "High-efficiency microcrystalline silicon single-junction solar cells". In: *Progress in Photovoltaics: Research and Applications* 21.5 (Aug. 2013), pp. 821–826. ISSN: 10627995. DOI: [10.1002/pip.2398](https://doi.org/10.1002/pip.2398).
- [46] H. Sai, K. Saito, N. Hozuki, and M. Kondo. "Relationship between the cell thickness and the optimum period of textured back reflectors in thin-film microcrystalline silicon solar cells". In: *Applied Physics Letters* 102.5 (Feb. 2013), p. 053509. ISSN: 0003-6951. DOI: [10.1063/1.4790642](https://doi.org/10.1063/1.4790642).
- [47] H. Sai, T. Matsui, K. Matsubara, M. Kondo, and I. Yoshida. "11.0%-Efficient Thin-Film Microcrystalline Silicon Solar Cells With Honeycomb Textured Substrates". In: *IEEE Journal of Photovoltaics* 4.6 (Nov. 2014), pp. 1349–1353. ISSN: 2156-3381. DOI: [10.1109/JPHOTOV.2014.2355037](https://doi.org/10.1109/JPHOTOV.2014.2355037).
- [48] M. A. Green, K. Emery, Y. Hishikawa, W. Warta, and E. D. Dunlop. "Solar cell efficiency tables (Version 45)". In: *Progress in Photovoltaics: Research and Applications* 23.1 (2015). Cited by: 1546, pp. 1–9. DOI: [10.1002/pip.2573](https://doi.org/10.1002/pip.2573).
- [49] H. Sai, K. Maejima, T. Matsui, T. Koida, M. Kondo, S. Nakao, Y. Takeuchi, H. Katayama, and I. Yoshida. "High-efficiency microcrystalline silicon solar cells on honeycomb textured substrates grown with high-rate VHF plasma-enhanced chemical vapor deposition". In: *Japanese Journal of Applied Physics* 54.8S1 (Aug. 2015), 08KB05. ISSN: 0021-4922. DOI: [10.7567/JJAP.54.08KB05](https://doi.org/10.7567/JJAP.54.08KB05).
- [50] H. Sai, T. Matsui, H. Kumagai, and K. Matsubara. "Thin-film microcrystalline silicon solar cells: 11.9% efficiency and beyond". In: *Applied Physics Express* 11.2 (Feb. 2018), p. 022301. ISSN: 1882-0778. DOI: [10.7567/APEX.11.022301](https://doi.org/10.7567/APEX.11.022301).
- [51] M. A. Green, K. Emery, D. L. King, S. Igari, and W. Warta. "SHORT COMMUNICATION: Solar cell efficiency tables (version 25)". In: *Progress in Photovoltaics: Research and Applications* 13.1 (2005), pp. 49–54. DOI: <https://doi.org/10.1002/pip.598>.
- [52] J. Bailat, J.-B. Orhan, J. Steinhauser, L. Fesquet, J.-B. Orhan, Y. Djeridane, B. Wolf, P. Madliger, J. Steinhauser, S. Benagli, D. Borrello, L. Castens, G. Monteduro, M. Marmelo, B. Dehbozorgi, E. Vallat-Sauvain, X. Multone, D. Romang, J.-F. Boucher, J. Meier, U. Kroll, M. Despeisse, G. Bugnon, C. Ballif, S. Marjanovic, G. Kohnke, N. Borrelli, K. Koch, J. Liu, R. Modavis, D. Thelen, S. Vallon, A. Zakharian, and D. Weidman. "Recent Developments of High Efficiency Micromorph tandem solar cells in KAI-M PECVD reactors". In: *Proceedings of the 25th EU-PVSEC and 05th WC-PEC Conference*. Jan. 2010, pp. 2340–2343.
- [53] U. Kroll, J. Meier, L. Fesquet, J. Steinhauser, S. Benagli, J.-B. Orhan, B. Wolf, D. Borrello, L. Castens, Y. Djeridane, X. Multone, G. Choong, D. Domine, J.-F. Boucher, P.-A. Madliger, M. Marmelo, G. Monteduro, B. Dehbozorgi, D. Romang, E. Omnes, M. Chevalley, G. Charitat, A. Pomey, E. Vallat-Sauvain, S. Marjanovic, G. Kohnke, K. Koch, J. Liu, R. Modavis, D. Thelen, S. Vallon, A. Zakharian, and D. Weidman. "Recent Developments of High-Efficiency Micromorph Tandem Solar Cells in KAI-M/ Plasmabox PECVD Reactors". In: *Proceedings of the EU-PVSEC*. 2011, pp. 2340–2343. DOI: [10.4229/26thEUPVSEC2011-3B0.2.6](https://doi.org/10.4229/26thEUPVSEC2011-3B0.2.6).
- [54] A. Terakawa. "Review of thin-film silicon deposition techniques for high-efficiency solar cells developed at Panasonic/Sanyo". In: *Solar Energy Materials and Solar Cells* 119 (2013), pp. 204–208. ISSN: 09270248. DOI: [10.1016/j.solmat.2013.06.044](https://doi.org/10.1016/j.solmat.2013.06.044).
- [55] T. Matsui, H. Sai, K. Saito, and M. Kondo. "High-efficiency thin-film silicon solar cells with improved light-soaking stability". In: *Progress in Photovoltaics: Research and Applications*. Vol. 21. 6. Sept. 2012, pp. 1363–1369. DOI: [10.1002/pip.2300](https://doi.org/10.1002/pip.2300).

- [56] B. Stannowski, O. Gabriel, S. Calnan, T. Frijnts, A. Heidelberg, S. Neubert, S. Kirner, S. Ring, M. Zelt, B. Rau, J. H. Zollondz, H. Bloess, R. Schlatmann, and B. Rech. "Achievements and challenges in thin film silicon module production". In: *Solar Energy Materials and Solar Cells* 119 (2013), pp. 196–203. ISSN: 09270248. DOI: [10.1016/j.solmat.2013.06.043](https://doi.org/10.1016/j.solmat.2013.06.043).
- [57] M. A. Green, K. Emery, Y. Hishikawa, and W. Warta. "k Dunlop, ED So- lar cell efficiency tables (version 41)". In: *Progress in Photovoltaics: Research and Applications* 21 (2013), pp. 1–11.
- [58] M. Boccard, M. Despeisse, J. Escarre, X. Niquille, G. Bugnon, S. Hanni, M. Bonnet-Eymard, F. Meillaud, and C. Ballif. "High-stable-efficiency tandem thin-film silicon solar cell with low-refractive-index silicon-oxide interlayer". In: *IEEE Journal of Photovoltaics* 4.6 (2014), pp. 1368–1373. ISSN: 21563381. DOI: [10.1109/JPHOTOV.2014.2357495](https://doi.org/10.1109/JPHOTOV.2014.2357495).
- [59] K. Yamamoto, A. Nakajima, M. Yoshimi, T. Sawada, S. Fukuda, T. Suezaki, M. Ichikawa, Y. Koi, M. Goto, T. Meguro, T. Matsuda, M. Kondo, T. Sasaki, and Y. Tawada. "A high efficiency thin film silicon solar cell and module". In: *Solar Energy* 77.6 (Dec. 2004), pp. 939–949. ISSN: 0038092X. DOI: [10.1016/j.solener.2004.08.028](https://doi.org/10.1016/j.solener.2004.08.028).
- [60] A. Banerjee, T. Su, D. Beglau, G. Pietka, F. S. Liu, S. Almutawalli, J. Yang, and S. Guha. "High-efficiency, multijunction nc-Si:H-based solar cells at high deposition rate". In: *IEEE Journal of Photovoltaics* 2.2 (2012), pp. 99–103. ISSN: 21563381. DOI: [10.1109/JPHOTOV.2011.2180892](https://doi.org/10.1109/JPHOTOV.2011.2180892).
- [61] S. Kim, J. W. Chung, H. Lee, J. Park, Y. Heo, and H. M. Lee. "Remarkable progress in thin-film silicon solar cells using high-efficiency triple-junction technology". In: *Solar Energy Materials and Solar Cells* 119 (2013), pp. 26–35. ISSN: 09270248. DOI: [10.1016/j.solmat.2013.04.016](https://doi.org/10.1016/j.solmat.2013.04.016).
- [62] X. Multone, L. Lesquet, D. Borrello, D. Romang, G. Choong, E. Vallat-Sauvain, M. Charrière, A. Billet, J. F. Boucher, J. Steinhäuser, J. B. Orhan, R. Monnard, J. P. Cardoso, G. Charitat, B. Dehbozorgi, N. Guillot, G. Monteduro, M. Marmelo, R. Semenzi, S. Benagli, and J. Meier. "Triple-junction amorphous/microcrystalline silicon solar cells: Towards industrially viable thin film solar technology". In: *Solar Energy Materials and Solar Cells* 140 (Sept. 2015), pp. 388–395. ISSN: 09270248. DOI: [10.1016/j.solmat.2015.04.038](https://doi.org/10.1016/j.solmat.2015.04.038).
- [63] H. Sai, T. Matsui, T. Koida, K. Matsubara, M. Kondo, S. Sugiyama, H. Katayama, Y. Takeuchi, and I. Yoshida. "Triple-junction thin-film silicon solar cell fabricated on periodically textured substrate with a stabilized efficiency of 13.6%". In: *Applied Physics Letters* 106.21 (May 2015). ISSN: 00036951. DOI: [10.1063/1.4921794](https://doi.org/10.1063/1.4921794).
- [64] E. Yablonovitch. "Statistical ray optics". In: *J. Optical Society of America* 72.7 (1982), p. 899.
- [65] O. Isabella, J. Krč, and M. Zeman. "Modulated surface textures for enhanced light trapping in thin-film silicon solar cells". In: *Applied Physics Letters* 97.10 (Sept. 2010), p. 101106. ISSN: 0003-6951. DOI: [10.1063/1.3488023](https://doi.org/10.1063/1.3488023).
- [66] R. J. D. Tilley. *Colour and the Optical Properties of Materials*. Ed. by Second Edition. John Wiley & Sons, Ltd, 2011.
- [67] F. J. Haug, K. Söderström, A. Naqavi, and C. Ballif. "Resonances and absorption enhancement in thin film silicon solar cells with periodic interface texture". In: *Journal of Applied Physics* 109.8 (Apr. 2011). ISSN: 00218979. DOI: [10.1063/1.3569689](https://doi.org/10.1063/1.3569689).
- [68] P. Bermel, C. Luo, L. Zeng, L. C. Kimerling, J. D. Joannopoulos, C. Herzinger, B. Johs, W. McGahan, J. Woollam, W. Paulson, D. Fischer, S. Dubail, J. Selvan, N. P. Vaucher, R. Platz, C. Hof, U. Kroll, J. Meier, P. Torres, H. Keppner, N. Wyrsh, M. Goetz, and A. Shah. *ASTMG173-03, Standard Tables for Reference Solar Spectral Irradiances: Direct Normal and Hemispherical on 37 degree Tilted Surface*. Tech. rep. 1998, pp. 3323–3336. DOI: [10.1364/OA{\\\_}License{\\\_}v1{\#}VOR](https://doi.org/10.1364/OA{\_}License{\_}v1{\#}VOR).
- [69] A. Chutinan, N. P. Kherani, and S. Zukotynski. "High-efficiency photonic crystal solar cell architecture". In: *Optics Express* 17.11 (May 2009), p. 8871. ISSN: 1094-4087. DOI: [10.1364/OE.17.008871](https://doi.org/10.1364/OE.17.008871).
- [70] H. Sai, H. Fujii, K. Arafune, Y. Ohshita, Y. Kanamori, H. Yugami, and M. Yamaguchi. "Wide-angle antireflection effect of subwavelength structures for solar cells". In: *Japanese Journal of Applied Physics, Part 1: Regular Papers and Short Notes and Review Papers* 46.6 A (June 2007), pp. 3333–3336. ISSN: 00214922. DOI: [10.1143/JJAP.46.3333](https://doi.org/10.1143/JJAP.46.3333).

- [71] H. Sai, Y. Kanamori, K. Arafune, Y. Ohshita, and M. Yamaguchi. "Light trapping effect of submicron surface textures in crystalline Si solar cells". In: *Progress in Photovoltaics: Research and Applications* 15.5 (Aug. 2007), pp. 415–423. ISSN: 10627995. DOI: [10.1002/pip.754](https://doi.org/10.1002/pip.754).
- [72] C. Battaglia, C. M. Hsu, K. Söderström, J. Escarré, F. J. Haug, M. Charrière, M. Boccard, M. Despeisse, D. T. Alexander, M. Cantoni, Y. Cui, and C. Ballif. "Light trapping in solar cells: Can periodic beat random?" In: *ACS Nano* 6.3 (Mar. 2012), pp. 2790–2797. ISSN: 19360851. DOI: [10.1021/nn300287j](https://doi.org/10.1021/nn300287j).
- [73] F. J. Haug, A. Naqavi, and C. Ballif. "Diffraction and absorption enhancement from textured back reflectors of thin film solar cells". In: *Journal of Applied Physics* 112.2 (July 2012). ISSN: 00218979. DOI: [10.1063/1.4737606](https://doi.org/10.1063/1.4737606).
- [74] J. Schroeder and J. H. Rosolowski. "Light scattering in polycrystalline materials". In: *SPIE Emerging Optical Materials* 297 (1981), pp. 156–168.
- [75] M. H. Shachar and J. E. Garay. "An Analytical Model of Light Scattering by Birefringent Polycrystalline Dielectrics Using Perturbation of Maxwell's Equations". In: *Advanced Theory and Simulations* 6.12 (Dec. 2023). ISSN: 25130390. DOI: [10.1002/adts.202300332](https://doi.org/10.1002/adts.202300332).
- [76] S. Faÿ, J. Steinhauser, N. Oliveira, E. Vallat-Sauvain, and C. Ballif. "Opto-electronic properties of rough LP-CVD ZnO:B for use as TCO in thin-film silicon solar cells". In: *Thin Solid Films* 515.24 SPEC. ISS. (Oct. 2007), pp. 8558–8561. ISSN: 00406090. DOI: [10.1016/j.tsf.2007.03.130](https://doi.org/10.1016/j.tsf.2007.03.130).
- [77] H. Tan, E. Moulin, F. T. Si, J.-W. Schüttauf, M. Stuckelberger, O. Isabella, F.-J. Haug, C. Ballif, M. Zeman, and A. H. M. Smets. "Highly transparent modulated surface textured front electrodes for high-efficiency multijunction thin-film silicon solar cells". In: *Progress in Photovoltaics: Research and Applications* 23.8 (Aug. 2015), pp. 949–963. ISSN: 10627995. DOI: [10.1002/pip.2639](https://doi.org/10.1002/pip.2639).
- [78] D. Y. Kim, S. Hänni, J. W. Schüttauf, R. A. Van Swaaij, and M. Zeman. "Quantification of Valleys of Randomly Textured Substrates as a Function of Opening Angle: Correlation to the Defect Density in Intrinsic nc-Si:H". In: *ACS Applied Materials and Interfaces* 8.32 (Aug. 2016), pp. 20660–20666. ISSN: 19448252. DOI: [10.1021/acsami.6b03995](https://doi.org/10.1021/acsami.6b03995).
- [79] G. Yang, R. A. van Swaaij, H. Tan, O. Isabella, and M. Zeman. "Modulated surface textured glass as substrate for high efficiency microcrystalline silicon solar cells". In: *Solar Energy Materials and Solar Cells* 133 (Feb. 2015), pp. 156–162. ISSN: 09270248. DOI: [10.1016/j.solmat.2014.11.013](https://doi.org/10.1016/j.solmat.2014.11.013).
- [80] H. B. Li, R. H. Franken, J. K. Rath, and R. E. Schropp. "Structural defects caused by a rough substrate and their influence on the performance of hydrogenated nano-crystalline silicon n-i-p solar cells". In: *Solar Energy Materials and Solar Cells* 93.3 (Mar. 2009), pp. 338–349. ISSN: 09270248. DOI: [10.1016/j.solmat.2008.11.013](https://doi.org/10.1016/j.solmat.2008.11.013).
- [81] H. Sai, K. Maejima, T. Matsui, T. Koida, K. Matsubara, M. Kondo, Y. Takeuchi, S. Sugiyama, H. Katayama, and I. Yoshida. "Impact of front TCO layer in substrate-type thin-film microcrystalline silicon solar cells". In: *2015 IEEE 42nd Photovoltaic Specialist Conference (PVSC)*. IEEE, June 2015, pp. 1–6. ISBN: 978-1-4799-7944-8. DOI: [10.1109/PVSC.2015.7355677](https://doi.org/10.1109/PVSC.2015.7355677).
- [82] H. Sai, K. Maejima, T. Matsui, T. Koida, M. Kondo, S. Nakao, Y. Takeuchi, H. Katayama, and I. Yoshida. "High-efficiency microcrystalline silicon solar cells on honeycomb textured substrates grown with high-rate VHF plasma-enhanced chemical vapor deposition". In: *Japanese Journal of Applied Physics* 54.8S1 (Aug. 2015), 08KB05. ISSN: 0021-4922. DOI: [10.7567/JJAP.54.08KB05](https://doi.org/10.7567/JJAP.54.08KB05).
- [83] G. Li, Y. Zhou, and F. Liu. "Influence of textured c-Si surface morphology on the interfacial properties of heterojunction silicon solar cells". In: *Journal of Non-Crystalline Solids* 358.17 (Sept. 2012), pp. 2223–2226. ISSN: 00223093. DOI: [10.1016/j.jnoncrysol.2011.12.106](https://doi.org/10.1016/j.jnoncrysol.2011.12.106).
- [84] T. de Vrijer and A. H. M. Smets. "Advanced textured monocrystalline silicon substrates with high optical scattering yields and low electrical recombination losses for supporting crack-free nano- to poly-crystalline film growth". In: *Energy Science & Engineering* 9.8 (Aug. 2021), pp. 1080–1089. ISSN: 2050-0505. DOI: [10.1002/ese3.873](https://doi.org/10.1002/ese3.873).
- [85] M. Python, E. Vallat-Sauvain, J. Bailat, D. Dominé, L. Fesquet, A. Shah, and C. Ballif. "Relation between substrate surface morphology and microcrystalline silicon solar cell performance". In: *Journal of Non-Crystalline Solids* 354.19-25 (May 2008), pp. 2258–2262. ISSN: 00223093. DOI: [10.1016/j.jnoncrysol.2007.09.084](https://doi.org/10.1016/j.jnoncrysol.2007.09.084).

- [86] G. Bugnon, G. Parascandolo, T. Söderström, P. Cuony, M. Despeisse, S. Hänni, J. Holovský, F. Meillaud, and C. Ballif. “A New View of Microcrystalline Silicon: The Role of Plasma Processing in Achieving a Dense and Stable Absorber Material for Photovoltaic Applications”. In: *Advanced Functional Materials* 22.17 (Sept. 2012), pp. 3665–3671. ISSN: 1616301X. DOI: [10.1002/adfm.201200299](https://doi.org/10.1002/adfm.201200299).
- [87] G. Limodio, D. Bartesaghi, G. Padmakumar, D. Rajagopal, A. M. Shah, E. Hamers, and A. Smets. “Modulated surface texturing of temporary Al foils substrates for high-efficiency thin-film, flexible solar cells”. In: *Conference Record of the IEEE Photovoltaic Specialists Conference*. Institute of Electrical and Electronics Engineers Inc., June 2021, pp. 1103–1105. ISBN: 9781665419222. DOI: [10.1109/PVSC43889.2021.9518843](https://doi.org/10.1109/PVSC43889.2021.9518843).
- [88] S. C. Oh, B. J. Bae, K. Y. Yang, M. H. Kwon, and H. Lee. “Fabrication of aluminum nano-scale structures using direct-embossing with a nickel template”. In: *Metals and Materials International* 17.5 (Oct. 2011), pp. 771–775. ISSN: 15989623. DOI: [10.1007/s12540-011-1012-4](https://doi.org/10.1007/s12540-011-1012-4).
- [89] H. Tan, A. Furlan, W. Li, K. Arapov, R. Santbergen, M. M. Wienk, M. Zeman, A. H. M. Smets, and R. A. Janssen. “Highly Efficient Hybrid Polymer and Amorphous Silicon Multijunction Solar Cells with Effective Optical Management”. In: *Advanced Materials* 28.11 (Mar. 2016), pp. 2170–2177. ISSN: 15214095. DOI: [10.1002/adma.201504483](https://doi.org/10.1002/adma.201504483).
- [90] T. Todorov, T. Gershon, O. Gunawan, Y. S. Lee, C. Sturdevant, L. Y. Chang, and S. Guha. “Monolithic Perovskite-CIGS Tandem Solar Cells via in Situ Band Gap Engineering”. In: *Advanced Energy Materials* 5.23 (Dec. 2015). ISSN: 16146840. DOI: [10.1002/aenm.201500799](https://doi.org/10.1002/aenm.201500799).
- [91] S. Kang, R. Sharma, J. K. Sim, and C. R. Lee. “Band gap engineering of tandem structured CIGS compound absorption layer fabricated by sputtering and selenization”. In: *Journal of Alloys and Compounds* 563 (June 2013), pp. 207–215. ISSN: 09258388. DOI: [10.1016/j.jallcom.2013.02.112](https://doi.org/10.1016/j.jallcom.2013.02.112).
- [92] E. L. Unger, L. Kegelmann, K. Suchan, D. Sörell, L. Korte, and S. Albrecht. “Roadmap and roadblocks for the band gap tunability of metal halide perovskites”. In: *Journal of Materials Chemistry A* 5.23 (2017), pp. 11401–11409. ISSN: 20507496. DOI: [10.1039/c7ta00404d](https://doi.org/10.1039/c7ta00404d).
- [93] S. Guha, J. Yang, A. Banerjee, B. Yan, and K. Lord. “High quality amorphous silicon materials and cells grown with hydrogen dilution”. In: *Solar Energy Materials and Solar Cells* 78.1-4 (July 2003), pp. 329–347. ISSN: 09270248. DOI: [10.1016/S0927-0248\(02\)00441-5](https://doi.org/10.1016/S0927-0248(02)00441-5).
- [94] R. J. Koval, J. Koh, Z. Lu, L. Jiao, R. W. Collins, and C. R. Wronski. “Performance and stability of Si:H p-i-n solar cells with i layers prepared at the thickness-dependent amorphous-to-microcrystalline phase boundary”. In: *Applied Physics Letters* 75.11 (Sept. 1999), pp. 1553–1555. ISSN: 00036951. DOI: [10.1063/1.124752](https://doi.org/10.1063/1.124752).
- [95] O. Astakhov, R. Carius, F. Finger, Y. Petrusenko, V. Borysenko, and D. Barankov. “Relationship between defect density and charge carrier transport in amorphous and microcrystalline silicon”. In: *Physical Review B* 79.10 (Mar. 2009), p. 104205. ISSN: 1098-0121. DOI: [10.1103/PhysRevB.79.104205](https://doi.org/10.1103/PhysRevB.79.104205).
- [96] M. N. van den Donker, B. Rech, F. Finger, L. Houben, W. M. M. Kessels, and M. C. M. van de Sanden. “Deposition of highly efficient microcrystalline silicon solar cells under conditions of low H<sub>2</sub> dilution: the role of the transient depletion induced incubation layer”. In: *Progress in Photovoltaics: Research and Applications* 15.4 (June 2007), pp. 291–301. ISSN: 10627995. DOI: [10.1002/pip.743](https://doi.org/10.1002/pip.743).
- [97] M. N. van den Donker, S. Klein, B. Rech, F. Finger, W. M. M. Kessels, and M. C. M. van de Sanden. “Microcrystalline silicon solar cells with an open-circuit voltage above 600mV”. In: *Applied Physics Letters* 90.18 (Apr. 2007), p. 183504. ISSN: 0003-6951. DOI: [10.1063/1.2734375](https://doi.org/10.1063/1.2734375).
- [98] M. van den Donker, B. Rech, R. Schmitz, J. Klomfass, G. Dingemans, F. Finger, L. Houben, W. Kessels, and M. van de Sanden. “Hidden parameters in the plasma deposition of microcrystalline silicon solar cells”. In: *Journal of Materials Research* 22.7 (July 2007), pp. 1767–1774. ISSN: 0884-2914. DOI: [10.1557/jmr.2007.0226](https://doi.org/10.1557/jmr.2007.0226).
- [99] A. H. Smets, W. M. Kessels, and M. C. Van De Sanden. “The effect of ion-surface and ion-bulk interactions during hydrogenated amorphous silicon deposition”. In: *Journal of Applied Physics* 102.7 (2007). ISSN: 00218979. DOI: [10.1063/1.2786873](https://doi.org/10.1063/1.2786873).

- [100] A. H. M. Smets, T. Matsui, and M. Kondo. "High-rate deposition of microcrystalline silicon p-i-n solar cells in the high pressure depletion regime". In: *Journal of Applied Physics* 104.3 (Aug. 2008), p. 034508. ISSN: 0021-8979. DOI: [10.1063/1.2961334](https://doi.org/10.1063/1.2961334).
- [101] O. Vetterl, F. Finger, R. Carius, P. Hapke, L. Houben, O. Kluth, A. Lambertz, A. Möck, B. Rech, and H. Wagner. "Intrinsic microcrystalline silicon: A new materials for photovoltaics." In: *Solar Energy Materials & Solar Cells* 62.1/2 (2000), p. 97. ISSN: 09270248.
- [102] A. Shah, J. Meier, E. Vallat-Sauvain, N. Wyrsh, U. Kroll, C. Droz, and U. Graf. "Material and solar cell research in microcrystalline silicon". In: *Solar Energy Materials and Solar Cells* 78.1-4 (July 2003), pp. 469–491. ISSN: 09270248. DOI: [10.1016/S0927-0248\(02\)00448-8](https://doi.org/10.1016/S0927-0248(02)00448-8).
- [103] Y. Mai, S. Klein, R. Carius, J. Wolff, A. Lambertz, F. Finger, and X. Geng. "Microcrystalline silicon solar cells deposited at high rates". In: *Journal of Applied Physics* 97.11 (2005). ISSN: 00218979. DOI: [10.1063/1.1927689](https://doi.org/10.1063/1.1927689).
- [104] M. Kondo, M. Fukawa, L. Guo, and A. Matsuda. "High rate growth of microcrystalline silicon at low temperatures". In: *Journal of Non-Crystalline Solids* (2000), pp. 266–269.
- [105] B. Rech, T. Roschek, T. Repmann, J. Muller, R. Schmitz, and W. A. Appenzeller. "Microcrystalline silicon for large area thin film solar cells". Tech. rep. 2003, pp. 157–165.
- [106] B. Rech, T. Repmann, J. Hüpkes, M. Berginski, H. Stiebig, W. Beyer, V. Sittinger, and F. Ruske. "Recent Progress in Amorphous and Microcrystalline Silicon Based Solar Cell Technology". In: *20th European Photovoltaic Solar Energy Conference* (2005).
- [107] S. Shimizu, M. Kondo, and A. Matsuda. "A highly stabilized hydrogenated amorphous silicon film having very low hydrogen concentration and an improved Si bond network". In: *Journal of Applied Physics* 97.3 (Feb. 2005). ISSN: 00218979. DOI: [10.1063/1.1846132](https://doi.org/10.1063/1.1846132).
- [108] L. Houben, M. Luysberg, P. Hapke, R. Carius, F. Finger, and H. Wagner. "Structural properties of microcrystalline silicon in the transition from highly crystalline to amorphous growth". In: *Philosophical Magazine A: Physics of Condensed Matter, Structure, Defects and Mechanical Properties* 77.6 (1998), pp. 1447–1460. ISSN: 01418610. DOI: [10.1080/01418619808214262](https://doi.org/10.1080/01418619808214262).
- [109] M. Python, C. Ballif, F. Meillaud, O. Madani, and D. Domine. "Influence of the substrate geometrical parameters on microcrystalline silicon growth for thin-film solar cells". In: 93 (2009), pp. 1714–1720. DOI: [10.1016/j.solmat.2009.05.025](https://doi.org/10.1016/j.solmat.2009.05.025).
- [110] D. Y. Kim, R. Santbergen, K. Jäger, M. Sever, J. Krč, M. Topič, S. Hänni, C. Zhang, A. Heidt, M. Meier, R. A. Van Swaaij, and M. Zeman. "Effect of substrate morphology slope distributions on light scattering, nc-Si:H film growth, and solar cell performance". In: *ACS Applied Materials and Interfaces* 6.24 (Dec. 2014), pp. 22061–22068. ISSN: 19448252. DOI: [10.1021/am5054114](https://doi.org/10.1021/am5054114).
- [111] G. Padmakumar, M. Criel, T. Kashyap, F. Saitta, P. Perez-Rodriguez, R. A. C. M. M. van Swaaij, and A. H. M. Smets. "Superimposed Sacrificial Texturing to Enhance the Optical Performance in Thin Film Solar Cells". In: *Progress in photovoltaics* (Oct. 2025), (in production). DOI: [DOI:10.1002/pip.70046](https://doi.org/10.1002/pip.70046).
- [112] A. H. M. Smets, T. Matsui, and M. Kondo. "Infrared analysis of the bulk silicon-hydrogen bonds as an optimization tool for high-rate deposition of microcrystalline silicon solar cells". In: *Applied Physics Letters* 92.3 (Jan. 2008), p. 033506. ISSN: 0003-6951. DOI: [10.1063/1.2837536](https://doi.org/10.1063/1.2837536).
- [113] C. Smit, R. A. C. M. M. van Swaaij, H. Donker, A. M. H. N. Petit, W. M. M. Kessels, and M. C. M. van de Sanden. "Determining the material structure of microcrystalline silicon from Raman spectra". In: *Journal of Applied Physics* 94.5 (Sept. 2003), pp. 3582–3588. ISSN: 0021-8979. DOI: [10.1063/1.1596364](https://doi.org/10.1063/1.1596364).
- [114] R. C. Teixeira, I. Doi, M. B. Zakia, J. A. Diniz, and J. W. Swart. "Micro-Raman stress characterization of polycrystalline silicon films grown at high temperature". In: *Materials Science and Engineering: B* 112.2-3 SPEC. ISS. (Sept. 2004), pp. 160–164. ISSN: 09215107. DOI: [10.1016/j.mseb.2004.05.025](https://doi.org/10.1016/j.mseb.2004.05.025).
- [115] A. T. Voutsas, M. K. Hatalis, J. Boyce, and A. Chiang. "Raman spectroscopy of amorphous and microcrystalline silicon films deposited by low-pressure chemical vapor deposition". In: *Journal of Applied Physics* 78.12 (1995), pp. 6999–7006. ISSN: 00218979. DOI: [10.1063/1.360468](https://doi.org/10.1063/1.360468).

- [116] A. H. M. Smets, W. M. M. Kessels, and M. C. M. van de Sanden. "Vacancies and voids in hydrogenated amorphous silicon". In: *Applied Physics Letters* 82.10 (Mar. 2003), pp. 1547–1549. ISSN: 0003-6951. DOI: [10.1063/1.1559657](https://doi.org/10.1063/1.1559657).
- [117] T. de Vrijer, B. Bouazzata, and A. H. M. Smets. "Spectroscopic review of hydrogenated, carbonated and oxygenated group IV alloys". In: *Vibrational Spectroscopy* 121 (July 2022), p. 103387. ISSN: 09242031. DOI: [10.1016/j.vibspec.2022.103387](https://doi.org/10.1016/j.vibspec.2022.103387).
- [118] V. A. Burrows, Y. J. Chabal, G. S. Higashi, K. Raghavachari, and S. B. Christman. "Infrared spectroscopy of Si(111) surfaces after HF treatment: Hydrogen termination and surface morphology". In: *Applied Physics Letters* 53.11 (1988), pp. 998–1000. ISSN: 00036951. DOI: [10.1063/1.100053](https://doi.org/10.1063/1.100053).
- [119] S. Klein, F. Finger, R. Carius, and M. Stutzmann. "Deposition of microcrystalline silicon prepared by hot-wire chemical-vapor deposition: The influence of the deposition parameters on the material properties and solar cell performance". In: *Journal of Applied Physics* 98.2 (July 2005), p. 024905. ISSN: 0021-8979. DOI: [10.1063/1.1957128](https://doi.org/10.1063/1.1957128).
- [120] J. Meier, E. Vallat-Sauvain, S. Dubail, U. Kroll, J. Dubail, S. Golay, L. Feitknecht, P. Torres, S. Fay, D. Fischer, and A. Shah. *Microcrystalline/micromorph silicon thin-film solar cells prepared by VHF-GD technique*. Tech. rep. 2001, pp. 73–84.
- [121] T. Matsui, T. Fujibayashi, Y. Nasuno, H. Fukuhori, Y. Kanemitsu, M. Kondo, and a. Matsuda. "Impurity diffusion effect on p/i interface properties of p-i-n junction microcrystalline silicon solar cells". In: *3rd World Conference on Photovoltaic Energy Conversion, 2003. Proceedings of 2* (2003), pp. 1–4.
- [122] M. Stuckelberger, B. S. Park, G. Bugnon, M. Despeisse, J. W. Schüttauf, F. J. Haug, and C. Ballif. "The boron-tailing myth in hydrogenated amorphous silicon solar cells". In: *Applied Physics Letters* 107.20 (Nov. 2015). ISSN: 00036951. DOI: [10.1063/1.4935348](https://doi.org/10.1063/1.4935348).
- [123] E. Kawamura, V. Vahedi, M. A. Lieberman, and C. K. Birdsall. "Ion energy distributions in rf sheaths; review, analysis and simulation". In: *Plasma Sources Science and Technology* 8 (1999), R45–R64.
- [124] R. C. Ross and J. Jaklik. "Plasma polymerization and deposition of amorphous hydrogenated silicon from rf and dc silane plasmas". In: *Journal of Applied Physics* 55.10 (1984), pp. 3785–3794. ISSN: 00218979. DOI: [10.1063/1.332935](https://doi.org/10.1063/1.332935).
- [125] G. E. Jellison, V. I. Merkulov, A. A. Puretzy, D. B. Geohegan, G. Eres, D. H. Lowndes, and J. B. Caughman. *Characterization of thin-film amorphous semiconductors using spectroscopic ellipsometry*. Tech. rep. 2000, p. 6873.
- [126] T. de Vrijer, A. Ravichandran, B. Bouazzata, and A. H. M. Smets. "The impact of processing conditions and post-deposition oxidation on the opto-electrical properties of hydrogenated amorphous and nano-crystalline Germanium films". In: *Journal of Non-Crystalline Solids* 553 (Feb. 2021), p. 120507. ISSN: 00223093. DOI: [10.1016/j.jnoncrsol.2020.120507](https://doi.org/10.1016/j.jnoncrsol.2020.120507).
- [127] J. Hoetzel, O. Caglar, J. Cashmore, C. Goury, J. Kalas, M. Klindworth, M. Kupich, G.-F. Leu, M.-H. Lindic, P. Losio, T. Mates, B. Mereu, T. Roschek, and I. Sinicco. "Microcrystalline bottom cells in large area thin film silicon MICROMORPH™ solar modules". In: *Solar Energy Materials and Solar Cells* 157 (Dec. 2016), pp. 178–189. ISSN: 09270248. DOI: [10.1016/j.solmat.2016.05.043](https://doi.org/10.1016/j.solmat.2016.05.043). URL: <https://linkinghub.elsevier.com/retrieve/pii/S0927024816301507>.
- [128] P. Delli Veneri, P. Aliberti, L. V. Mercaldo, I. Usatii, and C. Privato. "Influence of microcrystalline silicon bottom cell on micromorph tandem solar cell performance". In: *Thin Solid Films* 516.20 (Aug. 2008), pp. 6979–6983. ISSN: 00406090. DOI: [10.1016/j.tsf.2007.12.032](https://doi.org/10.1016/j.tsf.2007.12.032).
- [129] S. Agbo, J. Krč, R. van Swaaij, and M. Zeman. "Optimization of the p-i interface properties in thin film microcrystalline silicon solar cell". In: *Solar Energy Materials and Solar Cells* 94.11 (Nov. 2010), pp. 1864–1868. ISSN: 09270248. DOI: [10.1016/j.solmat.2010.06.034](https://doi.org/10.1016/j.solmat.2010.06.034).
- [130] C. Droz, E. Vallat-Sauvain, J. Bailat, L. Feitknecht, J. Meier, and A. Shah. "Relationship between Raman crystallinity and open-circuit voltage in microcrystalline silicon solar cells". In: *Solar Energy Materials and Solar Cells* 81.1 (Jan. 2004), pp. 61–71. ISSN: 09270248. DOI: [10.1016/j.solmat.2003.07.004](https://doi.org/10.1016/j.solmat.2003.07.004).
- [131] D. Y. Kim, E. Guijt, R. A. Van Swaaij, and M. Zeman. "Development of a SiO<sub>x</sub>:H solar cells with very high Voc×FF product". In: *Progress in Photovoltaics: Research and Applications* 23.6 (June 2015), pp. 671–684. ISSN: 1099159X. DOI: [10.1002/pip.2581](https://doi.org/10.1002/pip.2581).

- [132] T. de Vrijer, D. van Nijen, H. Parasramka, P. A. Procel Moya, Y. Zhao, O. Isabella, and A. H. M. Smets. "The fundamental operation mechanisms of nc-SiO<sub>x</sub>:H based tunnel recombination junctions revealed". In: *Solar Energy Materials and Solar Cells* 236 (Mar. 2022). ISSN: 09270248. DOI: [10.1016/j.solmat.2021.111501](https://doi.org/10.1016/j.solmat.2021.111501).
- [133] M. Fischer, H. Tan, J. Melskens, R. Vasudevan, M. Zeman, and A. H. M. Smets. "High pressure processing of hydrogenated amorphous silicon solar cells: Relation between nanostructure and high open-circuit voltage". In: *Applied Physics Letters* 106.4 (Jan. 2015), p. 043905. ISSN: 0003-6951. DOI: [10.1063/1.4907316](https://doi.org/10.1063/1.4907316).
- [134] A. H. M. Smets and M. C. M. van de Sanden. "Relation of the Si-H stretching frequency to the nanostructural Si-H bulk environment". In: *Physical Review B* 76.7 (Aug. 2007), p. 073202. ISSN: 1098-0121. DOI: [10.1103/PhysRevB.76.073202](https://doi.org/10.1103/PhysRevB.76.073202).
- [135] H. W. Deckman, C. R. Wronski, H. Witzke, and E. Yablonovitch. "Optically enhanced amorphous silicon solar cells". In: *Applied Physics Letters* 42.11 (June 1983), pp. 968–970. ISSN: 0003-6951. DOI: [10.1063/1.93817](https://doi.org/10.1063/1.93817).
- [136] A. R. Pascoe, S. Meyer, W. Huang, W. Li, I. Benesperi, N. W. Duffy, L. Spiccia, U. Bach, and Y.-B. Cheng. "Enhancing the Optoelectronic Performance of Perovskite Solar Cells via a Textured CH<sub>3</sub>NH<sub>3</sub>PbI<sub>3</sub> Morphology". In: *Advanced Functional Materials* 26.8 (Feb. 2016), pp. 1278–1285. ISSN: 1616-301X. DOI: [10.1002/adfm.201504190](https://doi.org/10.1002/adfm.201504190).
- [137] C. Onwudinanti, R. Vismara, O. Isabella, L. Grenet, F. Emieux, and M. Zeman. "Advanced light management based on periodic textures for Cu(In,Ga)Se<sub>2</sub> thin-film solar cells". In: *Optics Express* 24.6 (Mar. 2016), A693. ISSN: 1094-4087. DOI: [10.1364/OE.24.00A693](https://doi.org/10.1364/OE.24.00A693).
- [138] X. Luo, H. Luo, H. Li, R. Xia, X. Zheng, Z. Huang, Z. Liu, H. Gao, X. Zhang, S. Li, Z. Feng, Y. Chen, and H. Tan. "Efficient Perovskite/Silicon Tandem Solar Cells on Industrially Compatible Textured Silicon". In: *Advanced Materials* 35.9 (Mar. 2023). ISSN: 0935-9648. DOI: [10.1002/adma.202207883](https://doi.org/10.1002/adma.202207883).
- [139] P. K. Gupta. *Non-crystalline solids: glasses and amorphous solids*. Tech. rep. 1996, pp. 158–164.
- [140] G. Padmakumar, A. Balaji, M. Criel, F. Saitta, G. Limodio, P. Perez Rodriguez, R. A. C. M. M. Van Swaaij, and A. H. M. Smets. "Engineering of Hexagonal Microtextures on Glass". In: *ACS Applied Optical Materials* 3.10 (Oct. 2025). DOI: [10.1021/acsaom.5c00328](https://doi.org/10.1021/acsaom.5c00328).
- [141] H. Park, S. M. Iftiqar, M. Shin, H. Kim, J. Jung, S. Kim, A. H. T. Le, Y. Kim, D. P. Pham, J.-S. Jeong, and J. Yi. "Fabrication of honeycomb textured glass substrate and nanotexturing of zinc oxide front electrode for its application in high efficiency thin film amorphous silicon solar cell". In: *Journal of Photonics for Energy* 7.2 (Apr. 2017), p. 025502. ISSN: 1947-7988. DOI: [10.1117/1.jpe.7.025502](https://doi.org/10.1117/1.jpe.7.025502).
- [142] P. I. Widenborg and A. G. Aberle. "Polycrystalline silicon thin-film solar cells on AIT-textured glass superstrates". In: *Advances in OptoElectronics* 2007 (2007), p. 24584. ISSN: 1687563X. DOI: [10.1155/2007/24584](https://doi.org/10.1155/2007/24584).
- [143] G. Yang, R. A. C. M. M. van Swaaij, O. Isabella, and M. Zeman. "A novel way of texturing glass for microcrystalline silicon thin film solar cells application". In: *Progress in Photovoltaics: Research and Applications* 23.10 (Oct. 2015), pp. 1283–1290. ISSN: 10627995. DOI: [10.1002/pip.2550](https://doi.org/10.1002/pip.2550).
- [144] H. Tan, E. Psomadaki, O. Isabella, M. Fischer, P. Babal, R. Vasudevan, M. Zeman, and A. H. M. Smets. "Micro-textures for efficient light trapping and improved electrical performance in thin-film nanocrystalline silicon solar cells". In: *Applied Physics Letters* 103.17 (Oct. 2013), p. 173905. ISSN: 0003-6951. DOI: [10.1063/1.4826639](https://doi.org/10.1063/1.4826639).
- [145] B. J. Wiley, D. Qin, and Y. Xia. *Nanofabrication at high throughput and low cost*. July 2010. DOI: [10.1021/nn101472p](https://doi.org/10.1021/nn101472p).
- [146] O. Kluth, G. Schöpe, J. Hüpkes, C. Agashe, J. Müller, and B. Rech. "Modified Thornton model for magnetron sputtered zinc oxide: film structure and etching behaviour". In: *Thin Solid Films* 442.1-2 (Oct. 2003), pp. 80–85. ISSN: 00406090. DOI: [10.1016/S0040-6090\(03\)00949-0](https://doi.org/10.1016/S0040-6090(03)00949-0).
- [147] M. L. Addonizio, L. Fusco, A. Antonaia, F. Cominale, and I. Usatii. "Optimization of surface morphology and scattering properties of TCO/AIT textured glass front electrode for thin film solar cells". In: *Applied Surface Science* 357 (Dec. 2015), pp. 651–658. ISSN: 01694332. DOI: [10.1016/j.apsusc.2015.09.073](https://doi.org/10.1016/j.apsusc.2015.09.073).

- [148] Corning Incorporated. *Semiconductor Glass Wafers Product Information Sheet*. Tech. rep. 2015.
- [149] Corning Incorporated. *Exceptional Dimensional Stability and Surface Quality in Thin, Large-Size Sheets*. Tech. rep. 2021.
- [150] O. Tuna, Y. Selamet, G. Ayguz, and L. Ozyuzer. "High quality ITO thin films grown by dc and RF sputtering without oxygen". In: *Journal of Physics D: Applied Physics* 43.5 (2010). ISSN: 00223727. DOI: [10.1088/0022-3727/43/5/055402](https://doi.org/10.1088/0022-3727/43/5/055402).
- [151] K. H. Patel and S. K. Rawal. "Influence of power and temperature on properties of sputtered AZO films". In: *Thin Solid Films* 620 (Dec. 2016), pp. 182–187. ISSN: 00406090. DOI: [10.1016/j.tsf.2016.08.073](https://doi.org/10.1016/j.tsf.2016.08.073).
- [152] M. Nisha, S. Anusha, A. Antony, R. Manoj, and M. K. Jayaraj. "Effect of substrate temperature on the growth of ITO thin films". In: *Applied Surface Science* 252.5 (Dec. 2005), pp. 1430–1435. ISSN: 01694332. DOI: [10.1016/j.apsusc.2005.02.115](https://doi.org/10.1016/j.apsusc.2005.02.115).
- [153] G. Frank and H. K6stlin. *Applied so Electrical Properties and Defect Model of Tin-Doped Indium Oxide Layers*. Tech. rep. 1982, pp. 197–206.
- [154] A. H. M. Smets. *Growth related material properties of hydrogenated amorphous silicon*. English. Technische Universiteit Eindhoven, 2002, p. 175. ISBN: 90-386-1969-3. DOI: [10.6100/IR556557](https://doi.org/10.6100/IR556557).
- [155] Jean M. Bennett and Lars Mattsson. *Introduction to Surface Roughness and Scattering*. Optical Society of America, 1989. ISBN: 1-55752-108-5. DOI: [10.1364/1557521085](https://doi.org/10.1364/1557521085).
- [156] K. Jäger, O. Isabella, L. Zhao, and M. Zeman. "Light scattering properties of surface-textured substrates". In: *physica status solidi (c)* 7.3-4 (Jan. 2010), NA–NA. ISSN: 18626351. DOI: [10.1002/pssc.200982695](https://doi.org/10.1002/pssc.200982695).
- [157] K. Jäger, O. Isabella, R. A. C. M. M. van Swaaij, and M. Zeman. "Angular resolved scattering measurements of nano-textured substrates in a broad wavelength range". In: *Measurement Science and Technology* 22.10 (Oct. 2011), p. 105601. ISSN: 0957-0233. DOI: [10.1088/0957-0233/22/10/105601](https://doi.org/10.1088/0957-0233/22/10/105601).
- [158] H. Scherg-Kurmes, S. Seeger, S. Körner, B. Rech, R. Schlatmann, and B. Szyszka. "Optimization of the post-deposition annealing process of high-mobility In2O3:H for photovoltaic applications". In: *Thin Solid Films* 599 (Jan. 2016), pp. 78–83. ISSN: 00406090. DOI: [10.1016/j.tsf.2015.12.054](https://doi.org/10.1016/j.tsf.2015.12.054).
- [159] C. Battaglia, L. Erni, M. Boccard, L. Barraud, J. Escarré, K. Sderstrm, G. Bugnon, A. Billel, L. Ding, M. Despeisse, F. J. Haug, S. D. Wolf, and C. Ballif. "Micromorph thin-film silicon solar cells with transparent high-mobility hydrogenated indium oxide front electrodes". In: *Journal of Applied Physics* 109.11 (June 2011). ISSN: 00218979. DOI: [10.1063/1.3592885](https://doi.org/10.1063/1.3592885).
- [160] S. Fay, L. Feitknecht, R. Schlüchter, U. Kroll, E. Vallat-Sauvain, and A. Shah. "Rough ZnO layers by LP-CVD process and their effect in improving performances of amorphous and microcrystalline silicon solar cells". In: *Solar Energy Materials and Solar Cells* 90.18-19 (Nov. 2006), pp. 2960–2967. ISSN: 09270248. DOI: [10.1016/j.solmat.2006.06.003](https://doi.org/10.1016/j.solmat.2006.06.003).
- [161] M. L. Addonizio and C. Diletto. "Doping influence on intrinsic stress and carrier mobility of LP-MOCVD-deposited ZnO:B thin films". In: *Solar Energy Materials and Solar Cells* 92.11 (Nov. 2008), pp. 1488–1494. ISSN: 09270248. DOI: [10.1016/j.solmat.2008.06.013](https://doi.org/10.1016/j.solmat.2008.06.013).
- [162] A. Krywonos, J. E. Harvey, and N. Choi. *Linear systems formulation of scattering theory for rough surfaces with arbitrary incident and scattering angles*. Tech. rep. 2011.
- [163] K. Jäger, R. A. C. M. M. van Swaaij, and M. Zeman. "The Scalar Scattering Theory: A Multi-Functional Tool for Optimizing Scattering in Thin-Film Silicon Solar Cells". In: *Renewable Energy and the Environment Optics and Photonics Congress*. Washington, D.C.: OSA, 2012, PT3C.7. ISBN: 978-1-55752-952-7. DOI: [10.1364/PV.2012.PT3C.7](https://doi.org/10.1364/PV.2012.PT3C.7).
- [164] A. H. Smets, W. M. Kessels, and M. C. Van de Sanden. "Temperature dependence of the surface roughness evolution during hydrogenated amorphous silicon film growth". In: *Applied Physics Letters* 82.6 (Feb. 2003), pp. 865–867. ISSN: 00036951. DOI: [10.1063/1.1543237](https://doi.org/10.1063/1.1543237).
- [165] Hecht Eugene. *Optics*. English. 4th ed. San Francisco, CA 94111: Addison Wesley, 2002. ISBN: 0-321-18878-0.

- [166] A. Larena, F. Millán, G. Pérez, and G. Pinto. *Effect of surface roughness on the optical properties of multilayer polymer films*. Tech. rep. 2002.
- [167] A. Larena, G. Pinto, and F. Millán. *Using the Lambert-Beer law for thickness evaluation of photoconductor coatings for recording holograms*. Tech. rep. 1995, pp. 407–411.
- [168] H. Sai, T. Matsui, K. Saito, M. Kondo, and I. Yoshida. “Photocurrent enhancement in thin-film silicon solar cells by combination of anti-reflective sub-wavelength structures and light-trapping textures”. In: *Progress in Photovoltaics: Research and Applications* 23.11 (Nov. 2015), pp. 1572–1580. ISSN: 10627995. DOI: [10.1002/pip.2594](https://doi.org/10.1002/pip.2594).
- [169] S. Guha, J. Yang, and B. Yan. “High efficiency multi-junction thin film silicon cells incorporating nanocrystalline silicon”. In: *Solar Energy Materials and Solar Cells* 119 (2013), pp. 1–11. ISSN: 09270248. DOI: [10.1016/j.solmat.2013.03.036](https://doi.org/10.1016/j.solmat.2013.03.036).
- [170] H. Park and D. Kim. “Influence on the Haze Effect of Si Thin-Film Solar Cell on Multi-Surface Textures of Periodic Honeycomb Glass”. In: *Transactions on Electrical and Electronic Materials* 22.1 (Feb. 2021), pp. 80–90. ISSN: 20927592. DOI: [10.1007/s42341-020-00263-3](https://doi.org/10.1007/s42341-020-00263-3).
- [171] G. Padmakumar, F. Saitta, P. Sluijs, R. Boekhof, L. v. der Poll, N. van Sielhoff, K. Sreejith, P. P. Rodriguez, L. Mazzarella, T. Savenije, T. d. Vrijer, R. Vasudevan, M. E. Makkaoui, H. Lifka, E. Hamers, and A. H. Smets. “Progress in the research on the performance, processing and reliability of lightweight and flexible thin-film PV foils at TUDelft”. In: *2025 IEEE 53rd Photovoltaic Specialists Conference (PVSC)*. IEEE, June 2025, pp. 1124–1126. ISBN: 979-8-3315-3444-8. DOI: [10.1109/PVSC59419.2025.11133203](https://doi.org/10.1109/PVSC59419.2025.11133203).
- [172] K. H. Kim, S. Kasouit, E. V. Johnson, and P. Roca I Cabarrocas. “Substrate versus superstrate configuration for stable thin film silicon solar cells”. In: *Solar Energy Materials and Solar Cells* 119 (2013), pp. 124–128. ISSN: 09270248. DOI: [10.1016/j.solmat.2013.05.045](https://doi.org/10.1016/j.solmat.2013.05.045).
- [173] F. J. Haug and C. Ballif. *Light management in thin film silicon solar cells*. Mar. 2015. DOI: [10.1039/c4ee03346a](https://doi.org/10.1039/c4ee03346a).
- [174] M. Python, D. Dominé, T. Söderström, F. Meillaud, and C. Ballif. “Microcrystalline silicon solar cells: Effect of substrate temperature on cracks and their role in post-oxidation”. In: *Progress in Photovoltaics: Research and Applications* 18.7 (Nov. 2010), pp. 491–499. ISSN: 10627995. DOI: [10.1002/pip.956](https://doi.org/10.1002/pip.956).
- [175] G. Yue, L. Sivec, J. M. Owens, B. Yan, J. Yang, and S. Guha. “Optimization of back reflector for high efficiency hydrogenated nanocrystalline silicon solar cells”. In: *Applied Physics Letters* 95.26 (2009). ISSN: 00036951. DOI: [10.1063/1.3279143](https://doi.org/10.1063/1.3279143).
- [176] V. Naresh and N. Lee. “A Review on Biosensors and Recent Development of Nanostructured Materials-Enabled Biosensors”. In: *Sensors* 21.4 (Feb. 2021), p. 1109. ISSN: 1424-8220. DOI: [10.3390/s21041109](https://doi.org/10.3390/s21041109).
- [177] A. N. Koya, J. Cunha, T. L. Guo, A. Toma, D. Garoli, T. Wang, S. Juodkazis, D. Cojoc, and R. Proietti Zaccaria. “Novel Plasmonic Nanocavities for Optical Trapping-Assisted Biosensing Applications”. In: *Advanced Optical Materials* 8.7 (Apr. 2020), p. 1901481. ISSN: 21951071. DOI: [10.1002/adom.201901481](https://doi.org/10.1002/adom.201901481).
- [178] Y. Geng, J. H. Jang, K. G. Noh, J. H. Noh, J. P. Lagerwall, and S. Y. Park. “Through the Spherical Looking-Glass: Asymmetry Enables Multicolored Internal Reflection in Cholesteric Liquid Crystal Shells”. In: *Advanced Optical Materials* 6.1 (Jan. 2018), p. 1700923. ISSN: 21951071. DOI: [10.1002/adom.201700923](https://doi.org/10.1002/adom.201700923).
- [179] L. Li, H. Lin, S. Qiao, Y.-Z. Huang, J.-Y. Li, J. Michon, T. Gu, C. Alosno-Ramos, L. Vivien, A. Yadav, K. Richardson, N. Lu, and J. Hu. “Monolithically integrated stretchable photonics”. In: *Light: Science & Applications* 7.2 (Oct. 2017), p. 17138. ISSN: 2047-7538. DOI: [10.1038/lsa.2017.138](https://doi.org/10.1038/lsa.2017.138).
- [180] Z. Li, S. Li, and T. Ma. “Using Photonic Glasses as Colored Covers for Solar Energy Harvesting”. In: *Advanced Optical Materials* 11.5 (Mar. 2023), p. 2202370. ISSN: 2195-1071. DOI: [10.1002/adom.202202370](https://doi.org/10.1002/adom.202202370).

- [181] C. Pan, K. Chen, B. Liu, L. Ren, J. Wang, Q. Hu, L. Liang, J. Zhou, and L. Jiang. "Fabrication of micro-texture channel on glass by laser-induced plasma-assisted ablation and chemical corrosion for microfluidic devices". In: *Journal of Materials Processing Technology* 240 (Feb. 2017), pp. 314–323. ISSN: 09240136. DOI: [10.1016/j.jmatprotec.2016.10.011](https://doi.org/10.1016/j.jmatprotec.2016.10.011).
- [182] G. Yang, R. A. van Swaaij, H. Tan, O. Isabella, and M. Zeman. "Modulated surface textured glass as substrate for high efficiency microcrystalline silicon solar cells". In: *Solar Energy Materials and Solar Cells* 133 (Feb. 2015), pp. 156–162. ISSN: 09270248. DOI: [10.1016/j.solmat.2014.11.013](https://doi.org/10.1016/j.solmat.2014.11.013).
- [183] O. Isabella, J. Krč, and M. Zeman. "Modulated surface textures for enhanced light trapping in thin-film silicon solar cells". In: *Applied Physics Letters* 97.10 (Sept. 2010), p. 101106. ISSN: 0003-6951. DOI: [10.1063/1.3488023](https://doi.org/10.1063/1.3488023). URL: <http://aip.scitation.org/doi/10.1063/1.3488023>.
- [184] M. Despeisse, C. Battaglia, M. Boccard, G. Bugnon, M. Charrière, P. Cuony, S. Hänni, L. Löfgren, F. Meillaud, G. Parascandolo, T. Söderström, and C. Ballif. "Optimization of thin film silicon solar cells on highly textured substrates". In: *physica status solidi (a)* 208.8 (Aug. 2011), pp. 1863–1868. ISSN: 18626300. DOI: [10.1002/pssa.201026745](https://doi.org/10.1002/pssa.201026745). URL: <http://doi.wiley.com/10.1002/pssa.201026745>.
- [185] L. Fejes Tóth. *Regular Figures*. Elsevier, 2014. ISBN: 9780080100586. DOI: [10.1016/C2013-0-01735-5](https://doi.org/10.1016/C2013-0-01735-5).
- [186] T. C. Hales. "The Honeycomb Conjecture". In: *Discrete & computational geometry* 25 (Jan. 2001), pp. 1–22.
- [187] T. De Vrijer, M. Wiering, D. Van Nijen, G. Padmakumar, S. Sambamurthy, G. Limodio, and A. H. Smets. "The optical performance of random and periodic textured mono crystalline silicon surfaces for photovoltaic applications". In: *EPJ Photovoltaics* 13 (2022). ISSN: 21050716. DOI: [10.1051/epjpv/2022021](https://doi.org/10.1051/epjpv/2022021).
- [188] S. Y. Chou, P. R. Krauss, and P. J. Renstrom. "Nanoimprint lithography". In: *Journal of Vacuum Science & Technology B: Microelectronics and Nanometer Structures Processing, Measurement, and Phenomena* 14.6 (Nov. 1996), pp. 4129–4133. ISSN: 1071-1023. DOI: [10.1116/1.588605](https://doi.org/10.1116/1.588605).
- [189] R. E. Russo, X. Mao, J. Yoo, and J. Gonzalez. "Laser ablation". In: *Laser-Induced Breakdown Spectroscopy*. Elsevier, 2007, pp. 41–70. DOI: [10.1016/B978-0-12-818829-3.00003-4](https://doi.org/10.1016/B978-0-12-818829-3.00003-4).
- [190] W. M. Moreau. *Semiconductor Lithography*. Boston, MA: Springer US, 1988. ISBN: 978-1-4612-8228-0. DOI: [10.1007/978-1-4613-0885-0](https://doi.org/10.1007/978-1-4613-0885-0).
- [191] L. J. Guo. "Nanoimprint Lithography: Methods and Material Requirements". In: *Advanced Materials* 19.4 (Feb. 2007), pp. 495–513. ISSN: 0935-9648. DOI: [10.1002/adma.200600882](https://doi.org/10.1002/adma.200600882).
- [192] H. Hauser, B. Michl, S. Schwarzkopf, V. Kübler, C. Müller, M. Hermlle, and B. Bläsi. "Honeycomb texturing of silicon via nanoimprint lithography for solar cell applications". In: *IEEE Journal of Photovoltaics* 2.2 (2012), pp. 114–122. ISSN: 21563381. DOI: [10.1109/JPHOTOV.2012.2184265](https://doi.org/10.1109/JPHOTOV.2012.2184265).
- [193] D. Eisenhauer, H. Sai, T. Matsui, G. Köppel, B. Rech, and C. Becker. "Honeycomb micro-textures for light trapping in multi-crystalline silicon thin-film solar cells". In: *Optics Express* 26.10 (May 2018), A498–A507. ISSN: 10944087. DOI: [10.1364/oe.26.00a498](https://doi.org/10.1364/oe.26.00a498).
- [194] Y. Wang, C. Ke, T. Wu, X. Zhao, and R. Wang. "Nanosecond laser texturing with hexagonal honeycomb micro-structure on Titanium for improved wettability and optical properties". In: *Optik* 192 (Sept. 2019), p. 162953. ISSN: 00304026. DOI: [10.1016/j.ijleo.2019.162953](https://doi.org/10.1016/j.ijleo.2019.162953).
- [195] W. Ehrfeld and A. Schmidt. "Recent developments in deep x-ray lithography". In: *Journal of Vacuum Science & Technology B: Microelectronics and Nanometer Structures Processing, Measurement, and Phenomena* 16.6 (Nov. 1998), pp. 3526–3534. ISSN: 1071-1023. DOI: [10.1116/1.590490](https://doi.org/10.1116/1.590490).
- [196] K. Kovačević, Y. Zhao, P. Procel, L. Cao, L. Mazzarella, and O. Isabella. "Interdigitated-back-contacted silicon heterojunction solar cells featuring novel MoO<sub>x</sub>-based contact stacks". In: *Progress in Photovoltaics: Research and Applications* 33.1 (Jan. 2025), pp. 209–218. ISSN: 1062-7995. DOI: [10.1002/pip.3812](https://doi.org/10.1002/pip.3812).
- [197] H. Miyajima and M. Mehregany. "High-aspect-ratio photolithography for MEMS applications". In: *Journal of Microelectromechanical Systems* 4.4 (1995), pp. 220–229. ISSN: 10577157. DOI: [10.1109/84.475549](https://doi.org/10.1109/84.475549).

- [198] J. Zhao, A. Wang, M. A. Green, and F. Ferrazza. "19.8% efficient "honeycomb" textured multicrystalline and 24.4% monocrystalline silicon solar cells". In: *Applied Physics Letters* 73.14 (1998), pp. 1991–1993. ISSN: 00036951. DOI: [10.1063/1.122345](https://doi.org/10.1063/1.122345).
- [199] Jianhua Zhao, Aihua Wang, P. Campbell, and M. Green. "A 19.8% efficient honeycomb multicrystalline silicon solar cell with improved light trapping". In: *IEEE Transactions on Electron Devices* 46.10 (1999), pp. 1978–1983. ISSN: 00189383. DOI: [10.1109/16.791985](https://doi.org/10.1109/16.791985).
- [200] E. Manea, E. Budianu, M. Purica, I. Cernica, and F. Babarada. "Technological process for a new silicon solar cell structure with honeycomb textured front surface". In: *Solar Energy Materials and Solar Cells* 90.15 (Sept. 2006), pp. 2312–2318. ISSN: 09270248. DOI: [10.1016/j.solmat.2006.03.036](https://doi.org/10.1016/j.solmat.2006.03.036).
- [201] V. Sahu, R. V. Vardhan, P. Dewangan, Y. K. Srivastava, and P. Pal. "Wet bulk micromachining of Borofloat glass towards the fabrication of through-holes in different concentrations of hydrofluoric acid". In: *International Journal of Applied Glass Science* (Oct. 2025). ISSN: 20411294. DOI: [10.1111/ijag.70004](https://doi.org/10.1111/ijag.70004).
- [202] V. Sahu, P. Dewangan, R. V. Vardhan, P. K. Menon, and P. Pal. "Fabrication of microchannels and through-holes in Borofloat glass using Cr thin film with positive photoresist as the masking layer through wet etching". In: *Materials Today Communications* 41 (Dec. 2024). ISSN: 23524928. DOI: [10.1016/j.mtcomm.2024.110352](https://doi.org/10.1016/j.mtcomm.2024.110352).
- [203] H. Park and D. Kim. "Influence on the Haze Effect of Si Thin-Film Solar Cell on Multi-Surface Textures of Periodic Honeycomb Glass". In: *Transactions on Electrical and Electronic Materials* 22.1 (Feb. 2021), pp. 80–90. ISSN: 20927592. DOI: [10.1007/s42341-020-00263-3](https://doi.org/10.1007/s42341-020-00263-3).
- [204] H. Sai, K. Saito, and M. Kondo. "Enhanced photocurrent and conversion efficiency in thin-film microcrystalline silicon solar cells using periodically textured back reflectors with hexagonal dimple arrays". In: *Applied Physics Letters* 101.17 (Oct. 2012), p. 173901. ISSN: 0003-6951. DOI: [10.1063/1.4761956](https://doi.org/10.1063/1.4761956).
- [205] Z. Ge, H. Yang, L. Li, a. -, J.-S. Lim, R. Prasanna Venkatesh, J.-G. Park -, A. Pacco, and S. Halder. *The evolution of Silicon wafer cleaning technology*. Tech. rep. 1990, p. 1887.
- [206] MicroChemicals GmbH. *Chapter 01 MicroChemicals ®-Fundamentals of Microstructuring Substrate Preparation*. Tech. rep. 2010. URL: [www.microchemicals.com/downloads/application\\_notes.html](http://www.microchemicals.com/downloads/application_notes.html).
- [207] Robert H Collins and Frank T Deverse. *Process for improving photoresist adhesion*. 1970.
- [208] MicroChemicals GmbH. *Chapter 01 MicroChemicals ®-Fundamentals of Microstructuring Softbake*. Tech. rep. 2010. URL: [www.microchemicals.com/downloads/application\\_notes.html](http://www.microchemicals.com/downloads/application_notes.html).
- [209] Merck Performance Materials GmbH. *Technical Data Sheet AZ 5214 E Photoresist*. Tech. rep.
- [210] Y. He, W. Hu, and B. Cui. "Effect of Triton X-100 surfactant and agitation on tetramethylammonium hydroxide wet etching for microneedle fabrication". In: *Journal of Vacuum Science & Technology B* 42.5 (Sept. 2024), p. 053002. ISSN: 2166-2746. DOI: [10.1116/6.0003852](https://doi.org/10.1116/6.0003852).
- [211] Shubhava, A. Jayarama, G. K. Kannarpady, S. Kale, S. Prabhu, and R. Pinto. "Chemical etching of glasses in hydrofluoric Acid: A brief review". In: *Materials Today: Proceedings*. Vol. 55. Elsevier Ltd, 2022, pp. 46–51. DOI: [10.1016/j.matpr.2021.12.110](https://doi.org/10.1016/j.matpr.2021.12.110).
- [212] MicroChemicals GmbH. *Chapter 01 MicroChemicals ®-Fundamentals of Microstructuring Wet chemical etching - basics*. Tech. rep. Jan. 2010. URL: [www.microchemicals.com/downloads/application\\_notes.html](http://www.microchemicals.com/downloads/application_notes.html).
- [213] Park Hyeongsing, Hyun Cho Jae et al, Jun Hee Jung, Pham Phong Duy, Anh Huy Tuan Le, and Junsin Yi. "A Review of Wet Chemical Etching of Glasses in Hydrofluoric Acid based Solution for Thin Film Silicon Solar Cell Application (1)". In: *Current Photovoltaic Research* 3 (2017), pp. 75–82.
- [214] Rohm and Haas Electronic Materials. *MEGAPOSIT™ SPR™3000 SERIES PHOTORESIST For Microlithography Applications*. Tech. rep. 2006.
- [215] Microchemicals GmbH. *Chapter 01 MicroChemicals ® - Fundamentals of Microstructuring Reflow of Photoresist*. Tech. rep. Jan. 2010. URL: <https://www.microchemicals.com/downloads/Application-Notes/>.

- [216] MicroChemicals GmbH. *Chapter 01 MicroChemicals ®-Fundamentals of Microstructuring Hardbake, Reflow and DUJ Hardening*. Tech. rep. 2010. URL: [www.microchemicals.com/downloads/application\\_notes.html](http://www.microchemicals.com/downloads/application_notes.html).
- [217] H. K. Jang, Y. D. Chung, S. W. Whangbo, T. G. Kim, C. N. Whang, S. J. Lee, and S. Lee. "Effects of chemical etching with nitric acid on glass surfaces". In: *Journal of Vacuum Science & Technology A: Vacuum, Surfaces, and Films* 19.1 (Jan. 2001), pp. 267–274. ISSN: 0734-2101. DOI: [10.1116/1.1333087](https://doi.org/10.1116/1.1333087).
- [218] Z. Zhu, Y. Chen, Z. Xu, Z. Yu, X. Luo, J. Zhou, Y. Tian, and L. Jiang. "Super-spreading on superamphiphilic micro-organized nanochannel anodic aluminum oxide surfaces for heat dissipation". In: *iScience* 24.4 (Apr. 2021), p. 102334. ISSN: 25890042. DOI: [10.1016/j.isci.2021.102334](https://doi.org/10.1016/j.isci.2021.102334).
- [219] M. Chodkowski, K. Terpiłowski, and S. Pasieczna-Patkowska. "Fabrication of transparent polysiloxane coatings on a glass support via the sol-gel dip coating technique and the effect of their hydrophobization with hexamethyldisilazane". In: *Physicochemical Problems of Mineral Processing* 56 (2020), pp. 76–88. ISSN: 16431049. DOI: [10.37190/ppmp/126806](https://doi.org/10.37190/ppmp/126806).
- [220] P. M. Dentinger and J. W. Taylor. "Importance of chemistry at the resist-wafer interface for mechanical and lithographic adhesion". In: ed. by D. E. Seeger. May 1996, pp. 249–260. DOI: [10.1117/12.240476](https://doi.org/10.1117/12.240476).
- [221] K. Jäger, U. Aeberhard, E. Alarcon Llado, B. Bläsi, S. Burger, B. Ehrler, W. Favre, A. Fejfar, T. Gageot, I. Gordon, H. Helmers, O. Höhn, O. Isabella, M. Jošt, M. Ledinský, J. Mandal, P. Manley, D. Muñoz, Z. Omair, J. C. Ortiz Lizcano, U. W. Paetzold, A. P. Raman, H. Sai, R. Saive, M. Schmid, E. Yablonovitch, and C. Becker. "Optics for terawatt-scale photovoltaics: review and perspectives". In: *Advances in Optics and Photonics* 17.1 (Mar. 2025), p. 185. ISSN: 1943-8206. DOI: [10.1364/AOP.530556](https://doi.org/10.1364/AOP.530556).
- [222] J. Zhao, A. Wang, P. Campbell, and M. A. Green. *A 19.8% Efficient Honeycomb Multicrystalline Silicon Solar Cell with Improved Light Trapping*. Tech. rep. 10. 1999.
- [223] G. Yang, R. A. C. M. M. van Swaaij, O. Isabella, and M. Zeman. "A novel way of texturing glass for microcrystalline silicon thin film solar cells application". In: *Progress in Photovoltaics: Research and Applications* 23.10 (Oct. 2015), pp. 1283–1290. ISSN: 10627995. DOI: [10.1002/pip.2550](https://doi.org/10.1002/pip.2550).
- [224] K. Söderström, F. J. Haug, J. Escaró, O. Cubero, and C. Ballif. "Photocurrent increase in n-i-p thin film silicon solar cells by guided mode excitation via grating coupler". In: *Applied Physics Letters* 96.21 (May 2010). ISSN: 00036951. DOI: [10.1063/1.3435481](https://doi.org/10.1063/1.3435481).
- [225] H. Sai, K. Saito, and M. Kondo. "Investigation of textured back reflectors with periodic honeycomb patterns in thin-film silicon solar cells for improved photovoltaic performance". In: *IEEE Journal of Photovoltaics* 3.1 (2013), pp. 5–10. ISSN: 21563381. DOI: [10.1109/JPHOTOV.2012.2213800](https://doi.org/10.1109/JPHOTOV.2012.2213800).
- [226] Y. Saito and T. Kosuge. "Honeycomb-textured structures on crystalline silicon surfaces for solar cells by spontaneous dry etching with chlorine trifluoride gas". In: *Solar Energy Materials and Solar Cells* 91.19 (Nov. 2007), pp. 1800–1804. ISSN: 09270248. DOI: [10.1016/j.solmat.2007.06.009](https://doi.org/10.1016/j.solmat.2007.06.009).
- [227] H. Sai, T. Matsui, A. Bidiville, T. Koida, Y. Yoshida, K. Saito, and M. Kondo. *Light Management Using Periodic Textures for Enhancing Photocurrent and Conversion Efficiency in Thin-Film Silicon Solar Cells*. Tech. rep. 2013.
- [228] K. Jäger, O. Isabella, L. Zhao, and M. Zeman. "Light scattering properties of surface-textured substrates". In: *physica status solidi (c)* 7.3-4 (Jan. 2010), pp. 945–948. ISSN: 18626351. DOI: [10.1002/pssc.200982695](https://doi.org/10.1002/pssc.200982695).
- [229] C. Battaglia, L. Erni, M. Boccard, L. Barraud, J. Escarré, K. Sderstrm, G. Bugnon, A. Billel, L. Ding, M. Despeisse, F. J. Haug, S. D. Wolf, and C. Ballif. "Micromorph thin-film silicon solar cells with transparent high-mobility hydrogenated indium oxide front electrodes". In: *Journal of Applied Physics* 109.11 (June 2011). ISSN: 00218979. DOI: [10.1063/1.3592885](https://doi.org/10.1063/1.3592885).
- [230] S. Olibet, C. Monachon, A. Hessler-Wyser, E. Vallat-Sauvain, S. De Wolf, L. Fesquet, J. Damon-Lacoste, and C. Ballif. *Textured Silicon Heterojunction Solar Cells With Over 700mV Open Circuit Voltage Studied by Transmission Electron Microscopy*. Tech. rep.
- [231] C. Kothandaraman, T. Tonon, C. Huang, and A. E. Delahoy. *Improvement of a-Si:H p-i-n devices using zinc oxide-based back-reflectors*. Tech. rep.

- [232] K. Jäger, G. Köppel, M. Hammerschmidt, S. Burger, and C. Becker. “On accurate simulations of thin-film solar cells with a thick glass superstrate”. In: *Optics Express* 26.2 (Jan. 2018), A99. ISSN: 10944087. DOI: [10.1364/oe.26.000a99](https://doi.org/10.1364/oe.26.000a99).
- [233] H. K. Raut, V. A. Ganesh, A. S. Nair, and S. Ramakrishna. *Anti-reflective coatings: A critical, in-depth review*. Oct. 2011. DOI: [10.1039/c1ee01297e](https://doi.org/10.1039/c1ee01297e).
- [234] T. K. Chong, J. Wilson, S. Mokkalapati, and K. R. Catchpole. “Optimal wavelength scale diffraction gratings for light trapping in solar cells”. In: *Journal of Optics* 14.2 (2012). ISSN: 20408986. DOI: [10.1088/2040-8978/14/2/024012](https://doi.org/10.1088/2040-8978/14/2/024012).
- [235] C. Haase and H. Stiebig. “Thin-film silicon solar cells with efficient periodic light trapping texture”. In: *Applied Physics Letters* 91.6 (2007). ISSN: 00036951. DOI: [10.1063/1.2768882](https://doi.org/10.1063/1.2768882).
- [236] B. Yang and M. Lee. “Fabrication of honeycomb texture on poly-Si by laser interference and chemical etching”. In: *Applied Surface Science* 284 (Nov. 2013), pp. 565–568. ISSN: 01694332. DOI: [10.1016/j.apsusc.2013.07.134](https://doi.org/10.1016/j.apsusc.2013.07.134).
- [237] J. W. Goodman. *Introduction to Fourier Optics*. 4th ed. New York, NY 10004-1562: W. H. Freeman and Company, 2017. ISBN: 978-1-319-15304-5.
- [238] E. Vallat-Sauvain, J. Bailat, J. Meier, X. Niquille, U. Kroll, and A. Shah. “Influence of the substrate’s surface morphology and chemical nature on the nucleation and growth of microcrystalline silicon”. In: *Thin Solid Films* 485.1-2 (Aug. 2005), pp. 77–81. ISSN: 00406090. DOI: [10.1016/j.tsf.2005.03.017](https://doi.org/10.1016/j.tsf.2005.03.017).
- [239] O. Vetterl, A. Lambertz, A. Dasgupta, F. Finger, B. Rech, O. Kluth, and H. Wagner. “Thickness dependence of microcrystalline silicon solar cell properties”. In: *Solar Energy Materials and Solar Cells* 66.1-4 (Feb. 2001), pp. 345–351. ISSN: 09270248. DOI: [10.1016/S0927-0248\(00\)00193-8](https://doi.org/10.1016/S0927-0248(00)00193-8).
- [240] H. Sai, K. Maejima, T. Matsui, T. Koida, K. Matsubara, M. Kondo, Y. Takeuchi, S. Sugiyama, H. Katayama, and I. Yoshida. “Impact of front TCO layer in substrate-type thin-film microcrystalline silicon solar cells”. In: *2015 IEEE 42nd Photovoltaic Specialist Conference (PVSC)*. IEEE, June 2015, pp. 1–6. ISBN: 978-1-4799-7944-8. DOI: [10.1109/PVSC.2015.7355677](https://doi.org/10.1109/PVSC.2015.7355677).
- [241] T. de Vrijer, S. Miedema, T. Blackstone, D. van Nijen, C. Han, and A. H. Smets. “Application of metal, metal-oxide, and silicon-oxide based intermediate reflective layers for current matching in autonomous high-voltage multijunction photovoltaic devices”. In: *Progress in Photovoltaics: Research and Applications* 30.12 (Dec. 2022), pp. 1400–1409. ISSN: 1099159X. DOI: [10.1002/ppp.3600](https://doi.org/10.1002/ppp.3600).
- [242] F. Saitta, G. Padmakumar, P. P. Rodriguez, A. Wilson, P. Gonugunta, P. R. Anusuyadevi, R. Santbergen, and A. H. Smets. “Room-Temperature Sputtered SnO<sub>2</sub>-Based Thin Films as Earth-Abundant Transparent Conductive Oxides for Photovoltaic Applications”. In: *ACS Applied Electronic Materials* 7.20 (Oct. 2025), pp. 9489–9504. ISSN: 26376113. DOI: [10.1021/acsaelm.5c01650](https://doi.org/10.1021/acsaelm.5c01650).
- [243] T. De Vrijer, M. Wiering, D. Van Nijen, G. Padmakumar, S. Sambamurthy, G. Limodio, and A. H. Smets. “The optical performance of random and periodic textured mono crystalline silicon surfaces for photovoltaic applications”. In: *EPJ Photovoltaics* 13 (2022). ISSN: 21050716. DOI: [10.1051/epjpv/2022021](https://doi.org/10.1051/epjpv/2022021).
- [244] A. Perot and C. Fabry. “On the Application of Interference Phenomena to the Solution of Various Problems of Spectroscopy and Metrology”. In: *The Astrophysical Journal* 9 (Feb. 1899), p. 87. ISSN: 0004-637X. DOI: [10.1086/140557](https://doi.org/10.1086/140557).
- [245] M. Rajibul Islam, M. Mahmood Ali, M. H. Lai, K. S. Lim, and H. Ahmad. *Chronology of fabry-perot interferometer fiber-optic sensors and their applications: A review*. Apr. 2014. DOI: [10.3390/s140407451](https://doi.org/10.3390/s140407451).
- [246] J. Müller, B. Rech, J. Springer, and M. Vanecek. “TCO and light trapping in silicon thin film solar cells”. In: *Solar Energy* 77.6 (Dec. 2004), pp. 917–930. ISSN: 0038092X. DOI: [10.1016/j.solener.2004.03.015](https://doi.org/10.1016/j.solener.2004.03.015).
- [247] F. Saitta, P. Kalpoe, V. Ahluwalia, G. Padmakumar, P. P. Rodriguez, G. Limodio, R. Santbergen, and A. H.M. Smets. “De-coupling of optical and electrical properties in front TCO using the bilayer concept for thin-film solar cells”. In: *Solar Energy Materials and Solar Cells* 290 (Sept. 2025). ISSN: 09270248. DOI: [10.1016/j.solmat.2025.113723](https://doi.org/10.1016/j.solmat.2025.113723).

- [248] S. Neubert, S. Ring, F. Welker, S. Götzendörfer, F. Ruske, B. Stannowski, R. Schlatmann, and B. Rech. "Very thin, highly-conductive ZnO:Al front electrode on textured glass as substrate for thin-film silicon solar cells". In: *physica status solidi (RRL) – Rapid Research Letters* 8.1 (Jan. 2014), pp. 44–47. ISSN: 1862-6254. DOI: [10.1002/pssr.201308195](https://doi.org/10.1002/pssr.201308195).
- [249] J.-W. Schuttauf, G. Bugnon, M. Stuckelberger, S. Hanni, M. Boccard, M. Despeisse, F.-J. Haug, F. Meillaud, and C. Ballif. "Thin-Film Silicon Triple-Junction Solar Cells on Highly Transparent Front Electrodes With Stabilized Efficiencies up to 12.8%". In: *IEEE Journal of Photovoltaics* 4.3 (May 2014), pp. 757–762. ISSN: 2156-3381. DOI: [10.1109/JPHOTOV.2014.2307162](https://doi.org/10.1109/JPHOTOV.2014.2307162).
- [250] P.A. Losio, O. Caglar, J. S. Cashmore, J. E. Hötzel, S. Ristau, J. Holovsky, Z. Remes, and I. Sinicco. "Light management in large area thin-film silicon solar modules". In: *Solar Energy Materials and Solar Cells* 143 (Aug. 2015), pp. 375–385. ISSN: 09270248. DOI: [10.1016/j.solmat.2015.07.018](https://doi.org/10.1016/j.solmat.2015.07.018).
- [251] J. Wu, Z. Wang, F. Chen, Q. Shen, and L. Zhang. "Chemical evolution of target surfaces during RF magnetron sputtering and its effect on the performance of TCO films". In: *Applied Surface Science* 493 (Nov. 2019), pp. 665–672. ISSN: 01694332. DOI: [10.1016/j.apsusc.2019.07.021](https://doi.org/10.1016/j.apsusc.2019.07.021).
- [252] G. T. Chavan, Y. Kim, M. Q. Khokhar, S. Q. Hussain, E. C. Cho, J. Yi, Z. Ahmad, P. Rosaiah, and C. W. Jeon. *A Brief Review of Transparent Conducting Oxides (TCO): The Influence of Different Deposition Techniques on the Efficiency of Solar Cells*. Apr. 2023. DOI: [10.3390/nano13071226](https://doi.org/10.3390/nano13071226).
- [253] P. Babal, J. Blanker, R. Vasudevan, A. H. M. Smets, and M. Zeman. "Microstructure analysis of n-doped nc-SiO:H reflector layers and their implementation in stable a-Si:H p-i-n junctions". In: *2012 38th IEEE Photovoltaic Specialists Conference*. IEEE, June 2012, pp. 000321–000326. ISBN: 978-1-4673-0066-7. DOI: [10.1109/PVSC.2012.6317627](https://doi.org/10.1109/PVSC.2012.6317627).
- [254] G. Padmakumar, A. Balaji, F. Saitta, P. Perez-Rodriguez, R. A. van Swaaij, and A. H. Smets. "Hexagonal microtextured glass to achieve high optical performance in thin-film silicon solar cells". In: *Solar Energy* 306 (Mar. 2026). ISSN: 0038092X. DOI: [10.1016/j.solener.2025.114292](https://doi.org/10.1016/j.solener.2025.114292).
- [255] S. E. Han and G. Chen. "Toward the lambertian limit of light trapping in thin nanostructured silicon solar cells". In: *Nano Letters* 10.11 (Nov. 2010), pp. 4692–4696. ISSN: 15306984. DOI: [10.1021/nl1029804](https://doi.org/10.1021/nl1029804).
- [256] T. Gessert, J. Burst, X. Li, M. Scott, and T. Coutts. "Advantages of transparent conducting oxide thin films with controlled permittivity for thin film photovoltaic solar cells". In: *Thin Solid Films* 519.21 (Aug. 2011), pp. 7146–7148. ISSN: 00406090. DOI: [10.1016/j.tsf.2011.01.143](https://doi.org/10.1016/j.tsf.2011.01.143).
- [257] J. Bailat, D. Dominé, R. Schlüchter, J. Steinhauser, S. Faÿ, F. Freitas, C. Bücher, L. Feitknecht, X. Niquille, T. Tschanner, A. Shah, and C. Ballif. "High-efficiency p-i-n microcrystalline and micromorph thin film silicon solar cells deposited on LPCVD ZnO coated glass substrates". In: *IEEE 4th World Conference on Photovoltaic Energy Conversion 2* (2006), pp. 1533–1536.
- [258] K. Maejima, T. Koida, H. Sai, T. Matsui, K. Saito, M. Kondo, and T. Takagawa. "Influences of deposition temperature on characteristics of B-doped ZnO films deposited by metal-organic chemical vapor deposition". In: *Thin Solid Films* 559 (May 2014), pp. 83–87. ISSN: 00406090. DOI: [10.1016/j.tsf.2013.11.137](https://doi.org/10.1016/j.tsf.2013.11.137).



# A

## Spatial distribution of angles in random textures

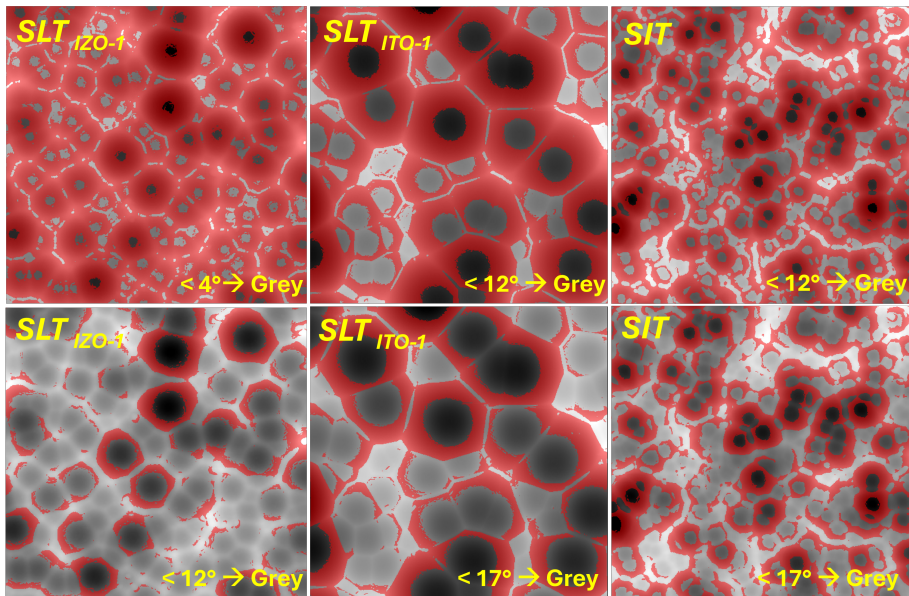


Figure A.1.: Colour map of surface normal distribution curves of  $SLT_{ITO}$ ,  $SLT_{IZO}$  and  $SIT$  in terms of angle.

## Influence of TCO thickness on fringes in solar cell reflection data

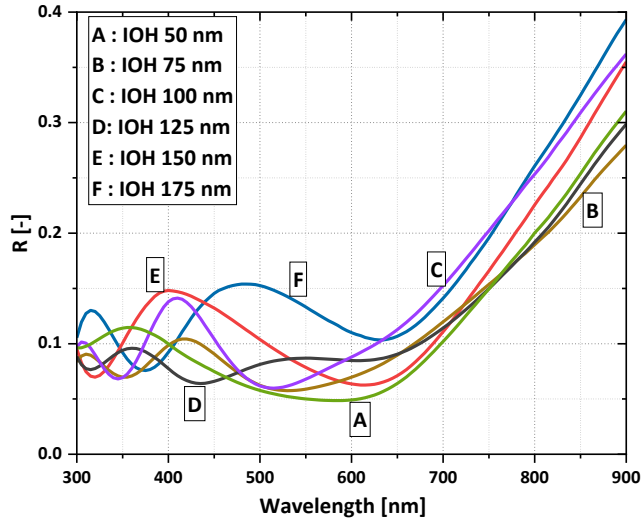


Figure A.2.: Reflectance curves of solar cells in superstrate configuration air/ glass/ IOH/ silicon solar cell/ silver fabricated on textured glass with various IOH thickness.

## n-k data of layers used in solar cells

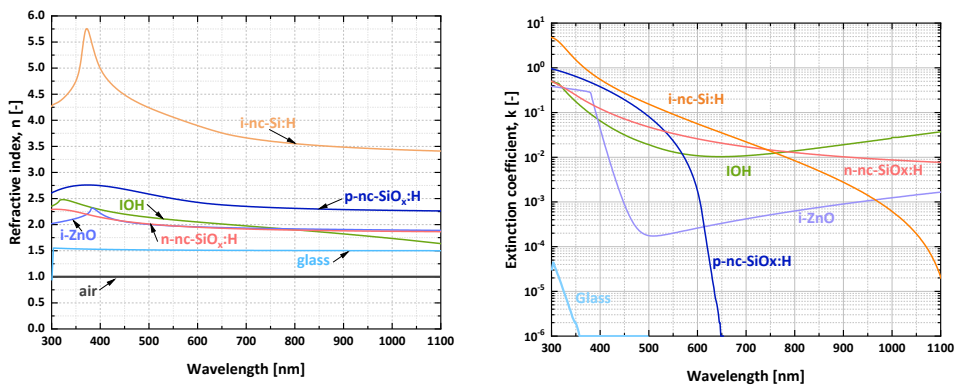


Figure A.3.: Refractive index ( $n$ ) and extinction coefficient ( $k$ ) of different layers used in the solar cells in the paper.

## External parameters of best performing cells on each superstrate

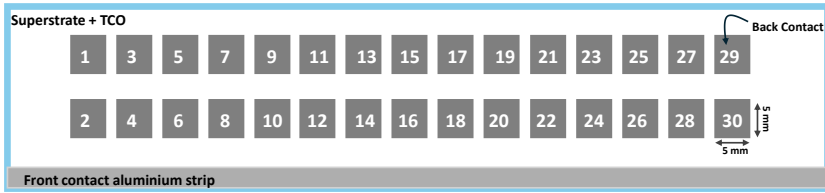


Figure A.4.: Distribution of defined cells over the area of the superstrate

Sample	$J_{sc}$ [mA/cm <sup>2</sup> ]	$V_{oc}$ [mV]	FF [%]	Eff. [%]	$R_s$ [Ω.cm <sup>2</sup> ]	$R_p$ [kΩ.cm <sup>2</sup> ]	Cell Number
<i>SLT<sub>ITO</sub></i>	27.35	544	64.9	9.66	7.9	3.34	<b>28</b>
	27.07	540	65.1	9.52	8.6	3.00	<b>4</b>
	26.92	543	64.7	9.46	10.6	3.65	<b>9</b>
	27.67	545	63.6	9.59	10.4	2.06	<b>14</b>
	28.13	551	62.6	9.70	10.0	2.30	<b>26</b>
	26.55	538	63.6	9.09	13.4	3.24	<b>11</b>
	26.79	540	62.1	8.98	11.9	3.38	<b>23</b>
	26.39	534	62.2	8.77	13.6	3.17	<b>6</b>
	27.00	533	61.6	8.86	10.8	1.27	<b>18</b>
	27.32	533	61.4	8.94	12.3	3.11	<b>13</b>
	Avg ± SD	27.12 ± 0.52	540 ± 6	63 ± 1	9.2 ± 0.4	11 ± 2	2.8 ± 0.8

<b>Sample</b>	$J_{sc}$ [mA/cm <sup>2</sup> ]	$V_{oc}$ [mV]	FF [%]	Eff. [%]	$R_s$ [Ω.cm <sup>2</sup> ]	$R_p$ [kΩ.cm <sup>2</sup> ]	Cell Number
<i>SLT<sub>IZO</sub></i>	23.98	532	61.1	7.79	12.2	1.61	<b>21</b>
	23.89	531	60.9	7.73	12.5	2.56	<b>15</b>
	24.50	536	59.7	7.84	12.4	1.49	<b>14</b>
	24.58	538	58.7	7.76	13.8	1.65	<b>22</b>
	23.49	532	59	7.37	14.0	1.77	<b>18</b>
	24.60	537	58.4	7.71	13.5	1.66	<b>11</b>
	24.51	542	57.6	7.65	15.1	1.87	<b>16</b>
	24.92	533	58	7.70	14.6	1.61	<b>20</b>
	24.91	531	57.5	7.61	14.9	1.58	<b>3</b>
	24.60	532	56.7	7.42	16.1	1.60	<b>17</b>
Avg ± SD	24.40 ± 0.46	534 ± 4	58 ± 1	7.6 ± 0.2	14 ± 1	1.7 ± 0.3	
<b>SIT</b>	28.81	548	65.6	10.36	8.7	2.64	<b>10</b>
	26.62	545	65.8	9.55	6.9	2.98	<b>12</b>
	27.96	541	65.9	9.97	7.3	3.15	<b>28</b>
	26.40	545	65.4	9.41	8.6	2.53	<b>17</b>
	28.63	547	64.7	10.13	8.3	2.42	<b>8</b>
	28.54	549	63.3	9.92	10.0	2.38	<b>30</b>
	27.22	540	64.2	9.44	8.4	3.11	<b>23</b>
	27.51	536	64.3	9.48	8.9	2.60	<b>19</b>
	25.56	544	63.2	8.79	10.8	2.73	<b>11</b>
	26.78	542	62.4	9.06	11.9	2.46	<b>9</b>
Avg ± SD	27 ± 1	544 ± 4	64 ± 1	9.6 ± 0.5	9 ± 1	2.7 ± 0.3	
<b>FLAT</b>	23.18	528	56.7	6.94	12.7	1.08	<b>26</b>
	22.38	523	56.3	6.59	13.1	1.04	<b>8</b>
	22.81	526	55.7	6.68	13.0	1.00	<b>13</b>
	19.62	522	55.7	5.70	14.9	1.05	<b>6</b>
	23.12	517	55.8	6.67	14.5	1.11	<b>28</b>
	22.14	521	55.1	6.35	13.3	0.91	<b>23</b>
	21.71	519	55.3	6.23	13.8	0.96	<b>14</b>
	21.46	516	55.3	6.12	13.6	0.95	<b>18</b>
	22.50	523	54.5	6.41	14.3	1.00	<b>4</b>
	22.90	519	54.7	6.50	13.6	0.93	<b>10</b>
Avg ± SD	22 ± 1	521 ± 3	55.5 ± 0.7	6.4 ± 0.4	13.7 ± 0.7	1.0 ± 0.1	

Table A.1.: Performance of top ten solar cells on each sample - performance is sorted based on largest to smallest value of  $V_{oc} \times FF$ .  $J_{sc}$  values are obtained from the WACOM solar simulator. Efficiencies (Eff.) tabulated are also calculated based on these  $J_{sc}$  and are not corrected for EQE measurement.

# B

## Surface angle distribution and surface steepness

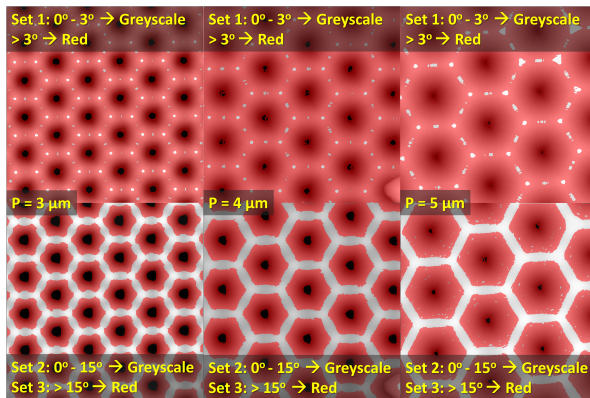


Figure B.1.: Regions on hexagonal craters with particular angles.

## Dimensions of hexagonal texture surface and unit shape

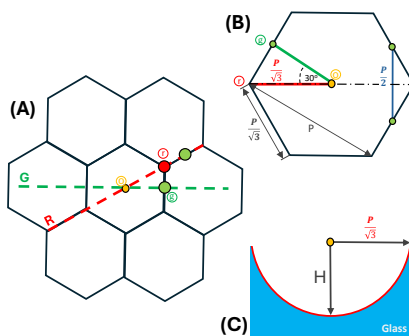
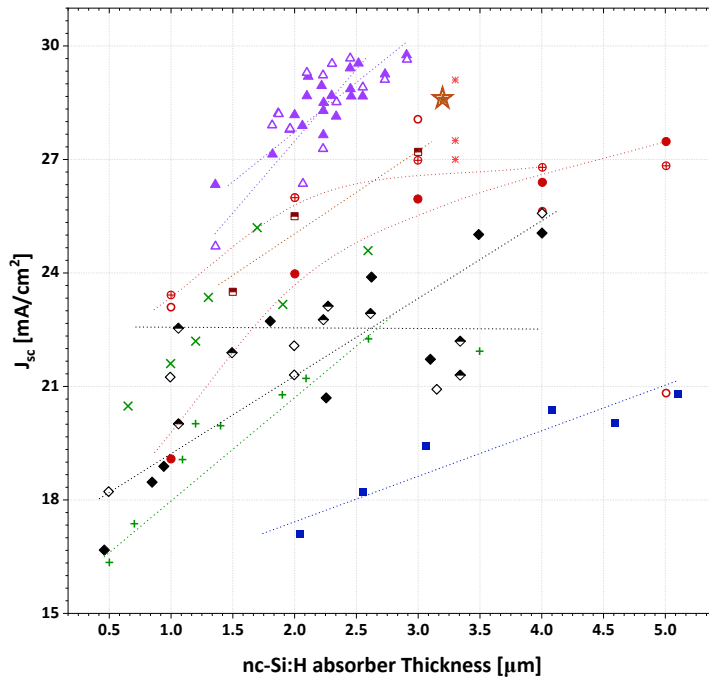


Figure B.2.: (A) R-axis and G-axis on an area tessellated with hexagons. (B) Dimensions of a hexagonal unit cell in terms of periodicity, P. (C) Height of a hexagonal crater.

## External Parameters of nc-Si:H single junction solar cells as a function of absorber thickness

B

- ▲ nip ITO as TCO ARC H. Sai , et al., IEEE 42nd PVSC 345-351 (2015)
- △ nip BZO as TCO ARC 345-351 (2015)
- × pin Klein, et al., J.Appl. Physics 98, 024905 (2005)
- + nip
- nip T. de Vrijer, et al., PiP . 1400-1409 (2022)
- pin EG H. Tan, et al., Appl. Phys. Lett. 103,173905 (2013)
- pin EAZO
- ⊕ pin MST
- ◆ nip (SC = 6%) O. Vetterl, et.al., Sol. Energy Mat. and Sol. Cells 66, 345-351 (2001)
- ◇ pin (SC = 6%)
- ◆ nip (SC = 5%)
- nip ZIT glass G. Yang, et al., PiP. 1283-1290 (2015)
- × pin Z5 45min ARC Hänni, et al., PiP 821-826 (2015)
- ★ pin nc-Si:H on hexagonal microtextured glass without ARC



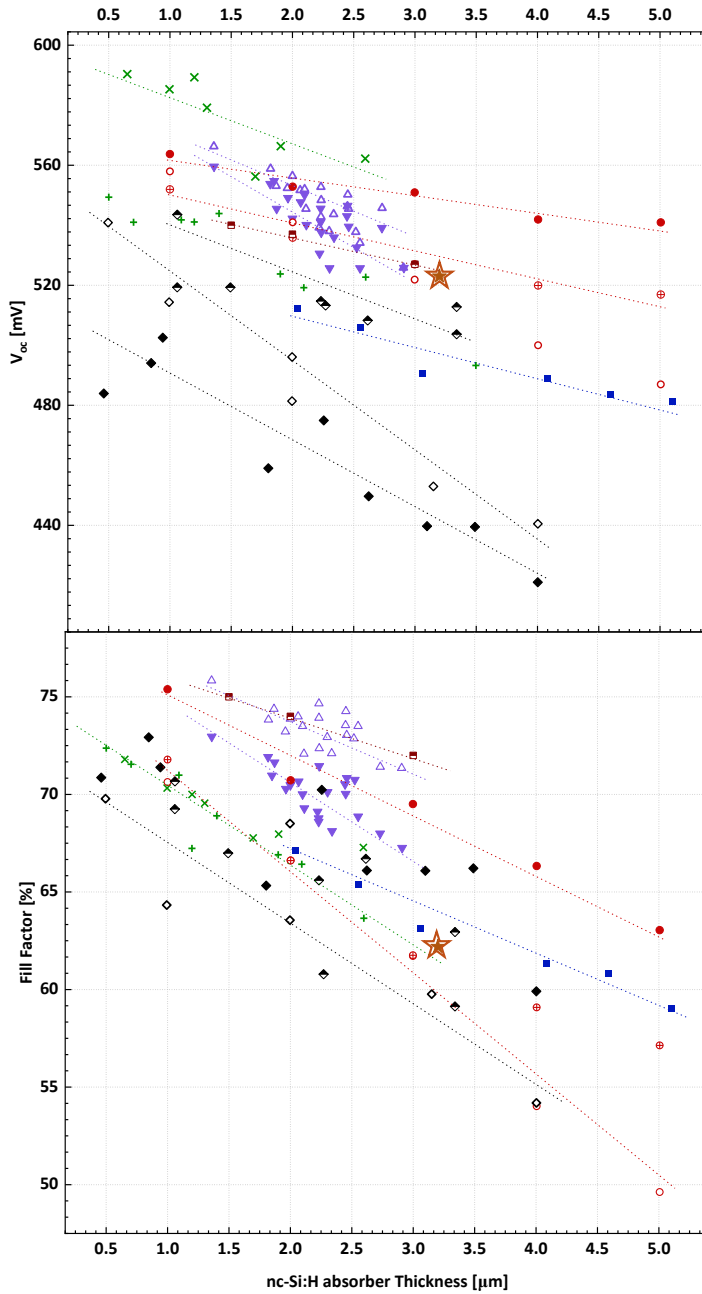


Figure B.4.: Open circuit voltage and fill factor of nc-Si:H single junction solar cells as a function of absorber thickness

## Surface profile of hexagonal microtextures - Circle fit

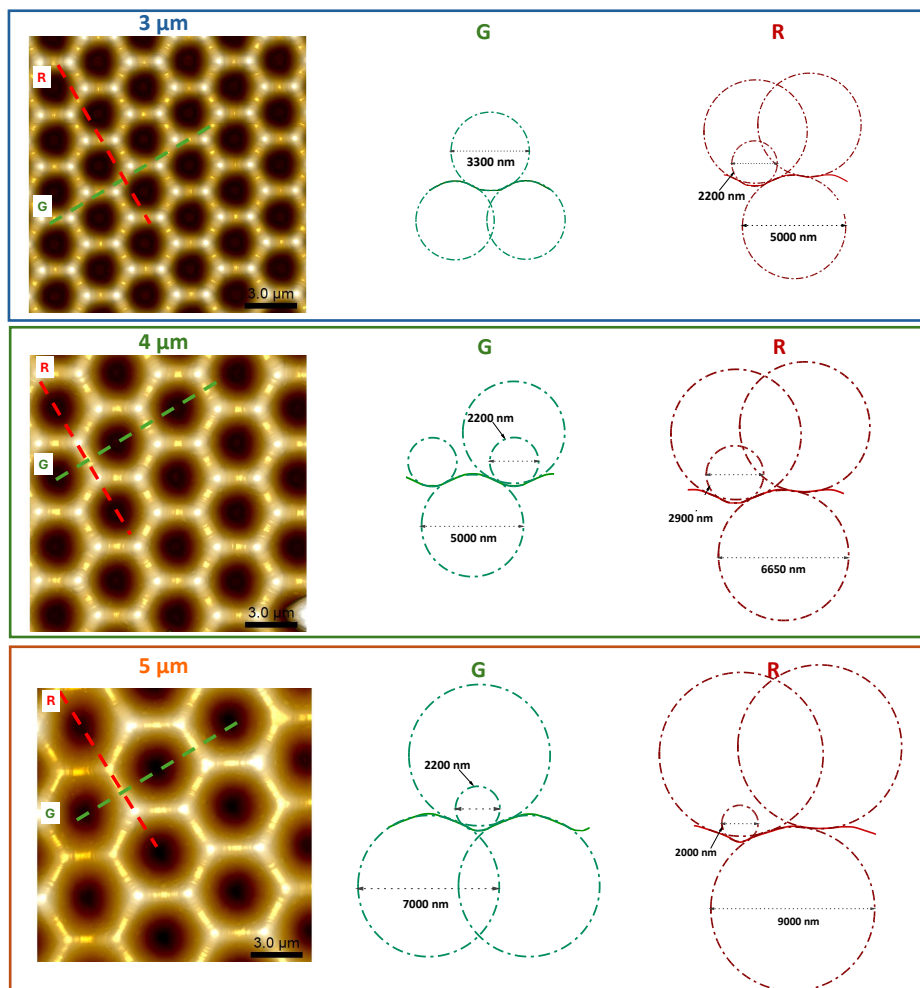


Figure B.5.: Top to bottom rows: AFM data visualised for 3 μm, 4 μm, and 5 μm periodicity hexagons. Additionally, the corresponding extracted surface profiles for the G and R axes are provided in the next columns. The profiles are to scale 1:1. The dash-dot circles are extrapolated arcs used to fit the profiles. All unique diameters are marked once (the adjacent non-marked circles are the same).

## Near-field and Far-field diffraction patterns - Python simulated

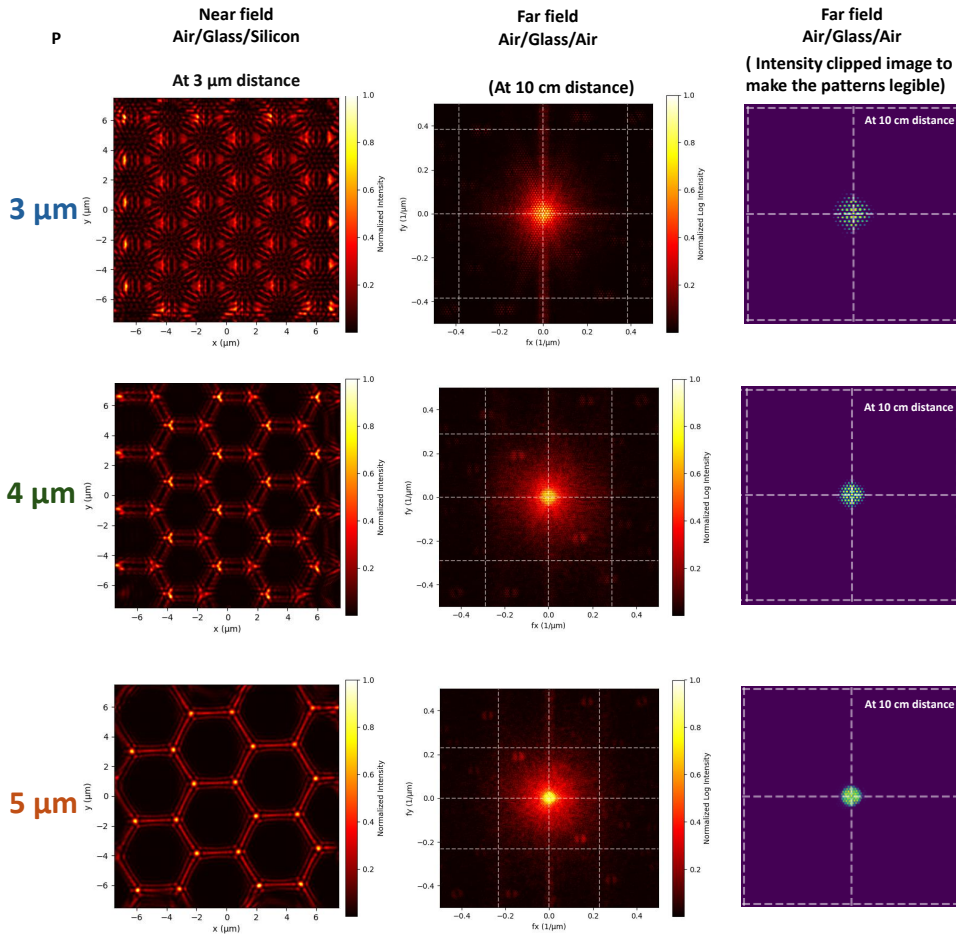


Figure B.6.: Simplified simulation of near-field and far-field diffraction patterns for honeycomb textures using Python computation library (SciPy). The 2D grating data is loaded from AFM scans. Illumination of the grating is done with  $635\ \text{nm}$  red light. The near-field diffraction patterns are performed in a system consisting of glass (with a refractive index of 1.5 at  $600\ \text{nm}$ ), a hexagonal texture, and a  $4\ \mu\text{m}$  thick silicon layer (refractive index of 3.8 at  $635\ \text{nm}$ ). The Angular Spectrum Method is used in constructing the near-field diffraction patterns. The far-field diffraction patterns are simulated in a system consisting of glass (with a refractive index of 1.5 at  $635\ \text{nm}$ ), a hexagonal texture, and air (refractive index of 1.0 at  $635\ \text{nm}$ ). A fast Fourier transform is performed to generate the far-field pattern.



# Acknowledgements

I extend my deepest gratitude to everyone who contributed to the success of this project. Your support was invaluable throughout this journey. I would like to acknowledge financial and technical support from Lift PV B.V., Arnhem, The Netherlands (formerly HyET Solar B.V).

## **I am profoundly grateful to:**

My first promoter, Arno, first and foremost, for the opportunity given to me to undertake this PhD. I consider myself genuinely lucky to work under your inspiring mentorship and genuine dedication to science. I sincerely thank you for the freedom that you gave me throughout the 4 years of my PhD. Academically and socially, you are the person who has had the most significant influence on me over the past four years. On multiple occasions, you have shown me how to prioritise human values over all else in decision-making.

My second promoter, Rene, for his critical insights into scientific thinking and invaluable guidance with my research. Your insightful feedback has been crucial in shaping my research papers. I admire you immensely for the remarkable lecturer you are.

All my close-to-heart supervisors. It was my genuine pleasure. Gianluca - Boss, you were my peacekeeper. I thank you immensely for encouraging me to take up an academic position. Your calm presence and positive demeanour have greatly enriched my experience during my master's thesis and the first year of my PhD. I still miss you in our group. Paula - you are an exceptional supervisor-friend; you granted me complete independence in my experiments while providing steadfast encouragement. I cherish the coffee breaks and conversations we had. You saw me confused, stressed, proud, and excited over the past three years. Sreejith - the first reader of my papers, one of the best humans I have seen, you played one of the biggest parts in my journey. I greatly value you. Thierry, my former supervisor and beloved friend, I thank you from the bottom of my heart for equipping me with the necessary knowledge at the beginning of my PhD trajectory. I cherish the deep conversations we had, the opinions we shared and the ideas we discussed. To my surprise, I seldom found disagreements in views, which is extremely rare for me.

My brilliant MSc students - Matthias, Aravind, Olav, Shriram, Kang Po Wang, Sriram, Seyed, and Tanya, whom I had the privilege of supervising. We worked together towards this, and that indeed made our collaboration both productive and enjoyable. Thank you for being an integral part of this journey. My smart colleague and friend Federica, who has shared this PhD journey with me from the very beginning. We've celebrated successes, endured challenges, and grown together, and I'm so thankful to have had you in my team throughout these four years.

Dr Shubhendu Guha - Former Chairman, United Solar Ovonic LLC, and Dr Edward Hammers-former CTO of HyET Solar, for their valuable insights into research approaches and experimental design. I also extend my gratitude to Dr. Jimmy Melskins and Dr. Ravi Vasudevan for their scientific input as part of the HyET solar collaboration.

The PVMD members — Olindo, Miro, Arthur, Yifeng, Brian, Sebastian, Hesan, Ivan, Luana, Patrizio, Alestair, David, Rudi, Malte, Paul, Mirco, Robin, Peer, Urvashi, Liqi and Carlos— for their expertise and contributions, which significantly enriched this project. I consider myself truly lucky to be surrounded by the PVMD technical team for their expertise and timely support. Particularly Martijn for helping me immensely during the initial stages of my PhD. Stefaan and Tim for helping me with the measurements - particularly, I would like to thank you for the setup that helped me measure AID. Bernardus - for the punctual assistance and the new software that made my life way easier. Engin - I thank you, my valued coffee companion and friend. I cherish the daily conversations over '1 notification - coffee ???'. Also, for all the moments that you stepped in to help me with Zorro. I also thank the EKL staff, Johannes and Daniel, for their help in developing my proficiency with Photolithography.

My office family: Sreejith, Federica, Haoxu, and Johnathan. LB.02.480, and the cookies shared will always hold a special place in my heart. My 'next door' office mates, Katarina, Yingwen, Alex and Sowmya. The knock-knock-knock followed by "yeesss" always led to long conversations. To Devika and Rik, my steadfast conference companions, you guys made my conference experiences ever memorable. To my friends Kristin, Dipanjan and Daphne, you people made my summer school unforgettable.

My friends in Delft: Aswin George- for our philosophical discussions about anything under the sun. Kamath and RV - for the constructive discussions we had over the past 6 years, we might have made the best political panellists. Gopal, Jitin, Sreeja, Mahesh and Gary - for all the gatherings and fun over the years. Akshay, Sam and Gokul - for the footballing lessons. Sandra-Thank you for unending 'dude-stories'. Vijesh, Nithya and Aswathy - for all the good moments. Preetha, Saran, Bharath and Aarathi- for the Onam and Vishu every year, Karthik and Vidhya - for being such caring and warm friends. My PhD colleagues, Prateek and Sarika, for their timely help and discussions. Our Football team - CFC, and cricket team - C<sup>3</sup> Delft.

My best friends, who have stood by me through thick and thin - Bijin, Radhika, JK, and Alana. To all my friends back home, for those deep and caring conversations: Dhanya, Alenso, Sreejith, Antony, Ajith, Jusaila and Ghoshettan. Their support, encouragement, and cherished moments of friendship provided me with the strength and inspiration throughout this journey. To my dear friends, Nisha, Sarath and Bibin, who are no longer with us but whose presence in my life was profoundly impactful. Although they are deeply missed, their memory continues to guide and motivate me.

My companion Ganesh, some people become family with time.

My brothers, Aravind and Liju.

My Family: Achan for teaching me that the only thing that matters in life is how good a human I am, for developing my understanding of sound political principles and democratic values. You didn't just share opinions -you showed me how to question, listen, and form my own views. I'm really grateful that you encouraged me to care about the world and to believe my voice matters. Amma -for her lifelong mentorship. She taught me the value of persistence in the face of setbacks and anchored me with the confidence to stay true to my principles throughout this doctoral pursuit. You taught me that doing things with heart and honesty is most important. Indu chechi, Kannan chettan, Adithi - For the genuine support and love you have given me throughout this journey. Maluamma, Achan and Adithya - for your warmth, for always checking in, and for

making me feel that I was never alone in this process. Your support made a difference.

The love of my life, Mwalutty. These four years were a struggle. This degree is yours as much as it is mine. We witnessed happiness, tears, stress, laughter, and sacrifices over the course of the four years. We made it :). 'A book for the shelf' .

Govind

7<sup>th</sup> October 2025



# List of Publications

## First-authored peer-reviewed journal articles

1. **G. Padmakumar**, M. Criel, T. Kashyap, F. Saitta, P. Perez-Rodriguez, R.A.C.M.M. van Swaaij, A.H.M Smets, "Superimposed Sacrificial Texturing to Enhance the Optical Performance in Thin Film Solar Cells" *Progress in Photovoltaics*, **34**, 465–481, 2026  
DOI: 10.1002/pip.70046
2. **G. Padmakumar**, A. Balaji, M. Criel, F. Saitta, G. Limodio, P. Perez-Rodriguez, R.A.C.M.M. van Swaaij, A.H.M. Smets, "Engineering of Hexagonal Microtextures on Glass" *ACS Applied Optical Materials*, **3(10)**, 2360-2372, 2025  
DOI: 10.1021/acsaom.5c00328
3. **G. Padmakumar**, A. Balaji, F. Saitta, P. Perez-Rodriguez, R.A.C.M.M. van Swaaij, A.H.M. Smets, "Hexagonal Microtextured Glass to Achieve High Optical Performance in Thin-Film Silicon Solar Cells" *Solar Energy*, **(306)C**, 2026, 114292  
DOI: 10.1016/j.solener.2025.114292
4. **G. Padmakumar**, F. Saitta, K.P. Sreejith, P. Perez-Rodriguez, R.A.C.M.M. van Swaaij, A.H.M. Smets, "Mitigating the Interference Effects Induced by Optical Cavities in Superstrate Thin Film Silicon Multi-junction Solar Cells" *Solar Energy*, **311**, 2026, 114537  
DOI: 10.1016/j.solener.2026.114537
5. **G. Padmakumar**, O. Eringfeld, S.M. Ghayeni, S.M. Karthikeyan, T. De Vrijer, F. Saitta, P. Perez-Rodriguez, R.A.C.M.M. van Swaaij, A.H.M. Smets, "Optimisation of Amorphous and Microcrystalline Silicon in VHF Deposition Conditions"  
*manuscript in preparation*

## Co-authored peer-reviewed journal articles

1. F Saitta, **G. Padmakumar**, P. Perez-Rodriguez, A. Wilson, P. Gonugunta, P.R. Anusuyadevi, R. Santbergen, A.H.M. Smets, "Room-Temperature Sputtered SnO<sub>2</sub>-Based Thin Films as Earth-Abundant Transparent Conductive Oxides for Photovoltaic Applications" *ACS Applied Electronic Materials*  
DOI: 10.1021/acsaelm.5c01650
2. F Saitta, **G. Padmakumar**, P. Perez-Rodriguez, P. P. Moya, R. Santbergen, A.H.M. Smets, "Time-Efficient, Accurate and Experimentally Grounded Optical Modelling of Multiscale-Textured Thin-Film Solar Cells" *Global Challenges*, 10(no.1), 2026: e00448  
DOI: 10.1002/gch2.202500448
3. K.P Sreejith, V. Venkatesh, **G. Padmakumar**, A.H.M. Smets, "Comprehensive Glare Hazard Analysis of Ethylene Tetrafluoroethylene (ETFE) Based Frontsheet for Flexible Photovoltaic Applications" *IEEE Journal of Photovoltaics*, 14(6), 930-936, 2024  
DOI: 10.1109/jphotov.2024.3463961

4. F. Saitta, P. Kalpoe, V. Ahluwalia, **G. Padmakumar**, P. Perez Rodriguez, G. Limodio, R. Santbergen, A.H.M. Smets, “De-coupling of optical and electrical properties in front TCO using the bilayer concept for thin-film solar cells” *Solar Energy Materials and Solar Cells*, 290, 113723  
DOI: 10.1016/j.solmat.2025.113723
5. T. de Vrijer, M. Wiering, D. van Nijen, **G. Padmakumar**, S. Sambamurthy, G. Limodio, and A.H.M. Smets “The optical performance of random and periodic textured monocrystalline silicon surfaces for photovoltaic applications” *EPJ Photovoltaics* 13, 23, 2022  
DOI: 10.1051/epjpv/2022021

## Conference Contributions

1. **Govind Padmakumar**, A. Balaji, F. Saitta, P. Perez-Rodriguez, A.H.M. Smets, “Honeycomb Textures on Glass for Solar Cells in Superstrate Configuration”, in *43rd European Photovoltaic Solar Energy Conference and Exhibition (EUPVSEC43)*, Bilbao, Spain, September 2025
2. **Session Chair**, Advanced Conversion Devices - Thin films and new concepts in *43rd European Photovoltaic Solar Energy Conference and Exhibition (EUPVSEC-43)*, Bilbao, Spain, September 2025
3. **Govind Padmakumar**, A. Balaji, M. Criel, T. Kashyap, F. Saitta, G. Limodio, P. Perez-Rodriguez, A.H.M. Smets, “Processing Methods to Texture Glass for Enhanced Optical Performance in Thin Film Solar Cells ” in *52nd IEEE Photovoltaic Specialist Conference (PVSC-52)*, Seattle, USA, June 2024
4. **Govind Padmakumar**, F. Saitta, G. Limodio, P. Perez-Rodriguez, T. de Vrijer, E. Hamers, A.H.M Smets “Use of Germanium in multi-junction solar cells: A case study on spectral utilisation in multi junctions” in *41st European Photovoltaic Solar Energy Conference and Exhibition (EUPVSEC41)*, Lisbon, Portugal, September 2023
5. **Govind Padmakumar**, G. Limodio, T. de Vrijer, F. Saitta, E. Hamers, A.H.M Smets “Use of back reflectors in multi junction solar cells: A case study on tandem configuration cells ” in *33rd International Photovoltaic Science and Engineering Conference (PVSEC-33)*, Nagoya, Japan, November 2022

## Other Contributions to Conferences

1. **Govind Padmakumar**, F. Saitta, P. Sluijs, R. Boekhof, L. van der Poll, N. van Sielthout, K.P. Sreejith, P. Perez-Rodriguez, L. Mazzarella, T. Savenije, T. de Vrijer, R. Vasudevan, M. El Makkaoui, H. Lifka, E. Hamers, A.H.M Smets<sup>1</sup> “Progress in the research on the performance, processing and reliability of lightweight and flexible thin-film PV foils at TUDelft” in *43rd European Photovoltaic Solar Energy Conference and Exhibition (EUPVSEC-43)*, Bilbao, Spain, September 2025

---

<sup>1</sup>Corresponding author.

2. **Govind Padmakumar**, F. Saitta, P. Sluijs, R. Boekhof, L. van der Poll, N. van Sijlfhout, K.P. Sreejith, P. Perez-Rodriguez, L. Mazzarella, T. Savenije, T. de Vrijer, R. Vasudevan, M. El Makkaoui, H. Lifka, E. Hamers, A.H.M Smets<sup>1</sup> “Progress in the research on the performance, processing and reliability of lightweight and flexible thin-film PV foils at TUDelft” in *53rd IEEE Photovoltaic Specialist Conference (PVSC-53)*, Montreal, Canada, June 2025
3. G. Limodio<sup>1</sup>, D. Bartesaghi, **G. Padmakumar**, D. Rajagopal, A.M. Shah, E. Hamers, A.H.M Smets “Modulated surface texturing of temporary Al foils substrates for high-efficiency thin-film, flexible solar cells ” in *48th IEEE Photovoltaic Specialist Conference (PVSC-48)*, Virtual conference, June 2021
4. F Saitta<sup>1</sup>, P Kalpoe, **G Padmakumar**, P Perez-Rodriguez, G Limodio, R. Santbergen, A.H.M Smets “Transparent Conductive Oxide Bi-Layer as Front Contact for Multijunction Thin-Film Silicon Solar Cells” in *50th IEEE Photovoltaic Specialists Conference (PVSC-50)*, 1-3
5. F Saitta<sup>1</sup>, A Balaji, V Ahluwalia, **G Padmakumar**, P Perez-Rodriguez, R. Santbergen, A.H.M Smets “Novel Transparent Conductive Oxide Bilayer Designs for Thin-Film Silicon Solar Cells” in *52nd IEEE Photovoltaic Specialist Conference (PVSC-52)*, 0766-0768
6. K.P Sreejith<sup>1</sup>, P. Sluijs, V. Venkatesh, N. Zeiher, **G. Padmakumar**, A.H.M Smets “Screening of Defects Responsible for Hotspot Formation in Amorphous Silicon Foils by Electroluminescence Imaging” in *52nd IEEE Photovoltaic Specialist Conference (PVSC-52)*, 1302-1302

---

<sup>1</sup>Corresponding author.

# Curriculum Vitae

**Govind Padmakumar** was born in Kerala, India, on 6<sup>th</sup> of November 1994. He earned his B.Tech. (Honours) degree in Mechanical Engineering from Mahatma Gandhi University, Kerala, in 2016. Following his graduation, he joined Tata Consultancy Services in Bangalore, India, where he worked as a Systems Engineer, developing expertise in mechanical design and analysis tools from 2016 to 2019. His early academic achievements include a research fellowship in physics by the Council of Scientific and Industrial Research (CSIR), India and a 97<sup>th</sup> percentile score in the Graduate Aptitude Test in Mechanical Engineering (GATE).



In 2019, Govind moved to the Netherlands to pursue an M.Sc. in Sustainable Energy Technologies at Delft University of Technology. His master's studies were complemented by a research and development internship at LiFT PV B.V., where he later completed his master's thesis on the fabrication of high-efficiency solar cells on flexible superstrates.

In 2022, he continued in the Photovoltaic Materials and Devices (PVMD) group at Delft University of Technology to pursue a PhD under the supervision of Prof. Arno Smets. His work was carried out in close collaboration with LiFT PV B.V., with a prime focus on the Engineering of different front textures for thin-film silicon solar cells that are transferable to an aluminium substrate.

Govind's professional philosophy revolves around the idea that meaningful progress lies in creating solutions that not only advance technology but also respect and restore the balance of our environment.

## Contact

Email: [govind.padmakumarsudha@gmail.com](mailto:govind.padmakumarsudha@gmail.com)

LinkedIn: <https://www.linkedin.com/in/govind-padmakumar/>

